UNIVERSITÀ
DEGLI STUDI
DI PADOVA

TESI DI DOTTORATO

Sede Amministrativa: Universitá degli Studi di Padova

CISAS - Centro di Ateneo Studi e Attivitá Spaziali 'G. Colombo'

SCUOLA DI DOTTORATO DI RICERCA IN SCIENZE TECNOLOGIE E MISURE PER LO SPAZIO
INDIRIZZO: SCIENZE E TECNOLOGIE PER APPLICAZIONI SATELLITARI E AERONAUTICHE
CICLI XXVII

ANALYSIS OF INNOVATIVE SCENARIOS AND KEY TECHNOLOGIES TO PERFORM ACTIVE DEBRIS REMOVAL WITH SATELLITE MODULES

Direttore della scuola: Ch.mo Prof. Giampiero Naletto
Coordinatore di indirizzo: Ch.mo Prof. Giampiero Naletto
Supervisore: Ch.mo Prof. Alessandro Francesconi

Dottorando: Livia Savioli

To my math teacher Sandra Canova.
She tought me how to love math and science.
If I am following my dreams
it is also thanks to her!

To my parents and my brother,
you are the fixed stars in the sky of my life!

Contents

Sommario **xi**

Abstract **xiii**

1 Space Debris **1**
1.1 Introduction . . . 1
1.2 Space debris environment . . . 4
1.3 Mitigation Measures and International Guidelines . . . 10
1.3.1 Postmission Disposal of Space Structures . . . 10
1.3.2 Survival of Debris From Earth Atmospheric Reentry . . . 13
1.4 Active Debris Removal to preserve the space environment . . . 13
1.4.1 ADR: enabling technologies and challenges . . . 14
1.5 Thesis objectives and outline . . . 15

2 ADR multi-mission concept and modular removers architecture **19**
2.1 ADR: state of the art . . . 19
2.2 ADR multi-mission concept . . . 21
2.2.1 De-orbiting technologies . . . 22
2.2.2 Drag augmentation devices . . . 23
2.2.3 Propulsion . . . 24
2.2.4 Electrodynamic tethers . . . 27
2.3 Remover kits modular architecture . . . 28
2.3.1 Drag sail unit sizing . . . 28
2.3.2 Electric propulsion unit sizing . . . 30
2.3.3 Hybrid propulsion unit sizing . . . 30
2.3.4 Electrodynamic tether unit sizing . . . 34
2.3.5 Main bus unit sizing . . . 34

3 Mission analysis and results **35**
3.1 Orbital regions of interest and potential targets . . . 35
3.2 Models for de-orbiting operations . . . 41
3.2.1 De-orbiting through drag augmentation devices . . . 41
3.2.2 De-orbiting through propulsive devices . . . 44
3.2.3 De-orbiting through electrodynamic tethers . . . 47
3.3 Model for controlled re-entry of space debris . . . 51
3.4 Model for multiple transfers optimization . . . 53
3.5 Mission Analysis and Results . . . 56
3.5.1 Case study #1: mission analysis . . . 56
3.5.2 Case study #1: results . . . 60
3.5.3 Case study #2: mission analysis . . . 66
3.5.4 Case study #2: results . . . 69
3.5.5 Case study #3: mission analysis . . . 73
3.5.6 Case study #3: results . . . 77
3.6 Risk assessment evaluation . . . 82
3.6.1 Electric propulsion: risk assessment . . . 82

3.6.2 Electrodynamic tether: risk assessment 83

4 Capture interface for uncooperative objects **87**
4.1 On-orbit capture of uncooperative objects 87
4.2 Capture interface concept 89
4.2.1 Morphing capabilites 89
4.2.2 Shape Memory Polymers (SMP): overview and main applications 90
4.2.3 Adhesion capabilities 100
4.2.4 Electroadhesion 100
4.2.5 Thermal model 107
4.3 Prototypes realization and testing 107
4.3.1 Prototype # 1: design and realization 108
4.3.2 Prototype # 1: tests and results 109
4.3.3 Prototype # 2: design and realization 116
4.3.4 Prototype # 2: tests and results 116

5 Final conclusions and future work **131**

Appendix A Solar radiation pressure perturbation **135**

Bibliography **139**

Acknowledgements **149**

List of Figures

1.1 Evolution of the space environment form the beginning of the space activity, at different epochs. (*Credits: NASA*). 1
1.2 Space debris protected zones [2]. 3
1.3 Space Debris growth and composition of the space objects sent in orbit from as of October 2012 (*Courtesy of ESA, Space Debris section [15]*). 4
1.4 Number of objects re-entered on the Earth, from the beginning of the space activities in 1957 to 2013 (*courtesy of the Center for Orbital and Reentry Debris Studies [16]*) 5
1.5 Current distribution of space objects according to their origin (data from [3] and [23]). . . 6
1.6 Orbital distribution of space objects (data from [8]). 6
1.7 10 worst satellite breakups events (credits NASA [19]). 7
1.8 Spatial density of catalogued objects after the disruption of the CHinese satellite Fengyun-1C in 2007 [24]. 8
1.9 Spatial density of catalogued objects after Cosmos-Iridium collision in 2009 [25]. 9
1.10 This plot shows the number of catalogued objects luanched in space form the beginning of the space activities. It is evident the sudden increase occured afetr the two collissional events in 2007 and 2009. It can be also seen a change in slope of the debris growth trend line due to the adoption of mititgation measures starting from the '90s (*credits by NASA*). 9
1.11 Disposal regions and storage orbit options for post-mission disposal (NASA 1995) [10] . . 11
1.12 Effective number of LEO objects, 10 cm and larger, from the LEGEND simulations based on the *no new launches* assumption. The plot is taken from REF, where Monte Carlo runs were performed to simulate the future projection parts of the curves (years 20062205). It is evident that the increase in the total number of objects would be mainly caused by the increase due to collisional events between objects already in orbit (*intacts are rocket bodies and spacecraft that have not experienced breakups* [28]. 14
1.13 Simulated LEO population growth as a function of time and removal rates. 90% PMD indicates common adopted postmission disposal (PMD) measures with 90% success rate (red line). ADR2020/02 means active debris removal starts from the year 2020 and the removal rate is two objects per year. ADR2020/05 means active debris removal starts from the year 2020 and the removal rate is five objects per year ([12]). 15
1.14 Simulated LEO population growth as a function of time and starting epoch. 90% PMD indicates common adopted postmission disposal (PMD) measures with 90% success rate. Two different strating epoch are considered ADR2020/05 and ADR2060/05, both with a removal rate of five debris per year. ([12]). 16

2.1 ADR mission concepts: (i) *single vehicle mission* (a single large satellite is responsible of both orbital transfers and de-orbiting manoeuvres); (ii) *multiple vehicles mission* (distinct vehicles are employed for orbital transfers and de-orbiting operations). 20
2.2 Examples of inflatable drag augmenation devices: GOLD - Gossamer Orbit Lowering Device [50] (on the left), and the inflatable structure mounted on board the French MICROSCOPE satellite [51] (on the right). 23
2.3 Examples of non-inflated drag augmentation devices: a typical drag sail, supported by four rigid booms aling the diagonals (on the left, artist's concept of NanoSail-D [52]); an appendage deployed from one side of the spacecraft (on the right, QSat-EOS post mission configuration with extended sail [53]) 23

2.4 Density variation, in kg/m^3, between an altitude of 600 km and 1000 km, estimated through the exponential model described in section 3.2.1. 24
2.5 Thrusters characterisitcs [55] 25
2.6 Electric Thrusters Performances 26
2.7 Working principle of Electrodynamic Tether [70] 27
2.8 EDT system developed by JAXA [71] 28
2.9 Example of the de-orbiting kit modular architecture 28
2.10 Example of CTM (*Collapsible Tube Mast*) boom (on the left), and CM (*Coilable Mast*) truss, (on the right) [74]. 29
2.11 Specific impulse for a hybrid rocket composed by 85% HTP as oxidizer and HTPB as solid fuel, with 10 bar of combustion pressure and different expansion ratio ε. 31
2.12 Mass of the hybrid propulsive unit for the controlled re-entry in function of the system mass (debris + de-orbiting kit). 32

3.1 Orbital regions of interest for ADR in LEO 36
3.2 Upper stages in Sun-Synchronous orbits [94]. 37
3.3 Number of debris in each selected orbital band. 39
3.4 Distribution of the debris according to their mass range. 40
3.5 Atmospheric density model [101] 44
3.6 Inward spiral trajectory followed during a continuous low thrust maneouvre 45
3.7 System of reference and satellite orbit [102]. 48
3.8 De-orbiting time evaluated with the first order equation IGRF 1x1 (blue line) and third order equation IGRF 3x3 (green line). 50
3.9 Controlled re-entry orbital parameters. 53
3.10 Scheme of the procedure implemented to determine the optimum sequence of orbital transfers that minimize the total ΔV budget, and so, the propellant mass required to de-orbit a set of five selected debris within 1 year. For each set of 5 debris, the total number of possible combination is 5!. For each sequence i ($\sqrt{seq.i}$ in the figure) four orbital transfers are performed. For each orbital transfer j ($\sqrt{j}$ in the figure) it is determined the time required for the RAAN alignment and the consequent ΔV, that is the sum of the ΔV for the RAAN alignment, if required, for the orbital transfer and the rendezvous maneouvre. The total ΔV budget for the i-th sequence is the sum of the ΔV determined for each transfer j, as well as the total maneouvre time is the sum of the time for the RAAN alignment, the otbital transfer and the rendezvous manoeuvre of each transfer j. 55
3.11 Example of a de-orbiting kit composed by both drag sail unit and electric propulsion units. An hybrid rocket (schematically represented in yellow) is foreseen for the controlled re-entry. 58
3.12 Scheme of the code developed and implemented in *Matlab* to analyse the ADR scenario emphCase study #1 59
3.13 Intermediate altitude that allows a natural re-entry of the debris within 25 years, reached after the propulsive phase, in function of the number of propulsive units (propulsion only scenario). 61
3.14 Total orbital lifetime in case of de-orbiting performed by means of propulsion only 61
3.15 *Debris #1.* Total mass of the de-orbiting kits and total de-orbiting time: comparison between de-orbiting by means of propulsion only and combined maneouvre drag sail + electric propulsion ($A_{sail} = 10\ m^2$). 63
3.16 *Debris #2.* Total mass of the de-orbiting kits and total de-orbiting time: comparison between de-orbiting by means of propulsion only and combined maneouvre Drag sail + electric propulsion ($A_{sail} = 10\ m^2$). 63
3.17 *Debris #3.* Total mass of the de-orbiting kits and total de-orbiting time: comparison between de-orbiting by means of propulsion only and combined maneouvre Drag sail + electric propulsion ($A_{sail} = 30\ m^2$). 64
3.18 *Debris #4.* Total mass of the de-orbiting kits and total de-orbiting time: comparison between de-orbiting by means of propulsion only and combined maneouvre Drag sail + electric propulsion ($A_{sail} = 30\ m^2$). 64

3.19 *Debris #5.* Total mass of the de-orbiting kits and total de-orbiting time: comparison between de-orbiting by means of propulsion only and combined maneouvre Drag sail + electric propulsion ($A_{sail} = 30\ m^2$). 65

3.20 *Debris #6.* Total mass of the de-orbiting kits and total de-orbiting time: comparison between de-orbiting by means of propulsion only and combined maneouvre Drag sail + electric propulsion ($A_{sail} = 30\ m^2$). 65

3.21 Remover mass fraction, in percentage, respect to the debris mass. As it can be observed, the mass of the remover is, in most of the cases, less then 15% of the debris mass 66

3.22 Scheme of the code developed and implemented in *Matlab* to analyse the ADR scenario *Case study #2* 69

3.23 Total orbital lifetime in case of de-orbiting performed by means of propulsion only 71

3.24 Total orbital lifetime in case of de-orbiting performed by means of propulsion only 72

3.25 Inert-to-propellant mass fraction of hybrid rocket systems for $M_{pay} = 1000\,kg$ and variable ΔV. 76

3.26 Total number and total mass for each kit required for population deorbiting. 77

3.27 *Orbital band h = 960 km, i = 64°.* Total mass of the de-orbiting kit required to de-orbit a debris in function of its mass, when electric propulsion (blue), electrodynamic tether (green) and hybrid propulsion (magenta) are employed (on the left). Total de-orbiting time with electric propulsion (blue) and electrodynamic tether (green) (on the right). Hybrid propulsion is not reported since the orbital lifetime is very small and not visible ompared to the one obtained with the previous technologies: it is simply the semi-period of the transfer elliptical orbit. 78

3.28 *Orbital band h = 830 km, i = 71°.* Total mass of the de-orbiting kit required to de-orbit a debris in function of its mass, when electric propulsion (blue), electrodynamic tether (green) and hybrid propulsion (magenta) are employed (on the left). Total de-orbiting time with electric propulsion (blue) and electrodynamic tether (green) (on the right). Hybrid propulsion is not reported since the orbital lifetime is very small and not visible ompared to the one obtained with the previous technologies: it is simply the semi-period of the transfer elliptical orbit. 79

3.29 *Orbital band h = 740 km, i = 74°.* Total mass of the de-orbiting kit required to de-orbit a debris in function of its mass, when electric propulsion (blue), electrodynamic tether (green) and hybrid propulsion (magenta) are employed (on the left). Total de-orbiting time with electric propulsion (blue) and electrodynamic tether (green) (on the right). Hybrid propulsion is not reported since the orbital lifetime is very small and not visible ompared to the one obtained with the previous technologies: it is simply the semi-period of the transfer elliptical orbit. 79

3.30 *Orbital band h = 920 km, i = 82°.* Total mass of the de-orbiting kit required to de-orbit a debris in function of its mass, when electric propulsion (blue), electrodynamic tether (green) and hybrid propulsion (magenta) are employed (on the left). Total de-orbiting time with electric propulsion (blue) and electrodynamic tether (green) (on the right). Hybrid propulsion is not reported since the orbital lifetime is very small and not visible ompared to the one obtained with the previous technologies: it is simply the semi-period of the transfer elliptical orbit. 80

3.31 *Orbital band h = 800 km, i = 99°.* Total mass of the de-orbiting kit required to de-orbit a debris in function of its mass, when electric propulsion (blue), electrodynamic tether (green) and hybrid propulsion (magenta) are employed (on the left). Total de-orbiting time with electric propulsion (blue) and electrodynamic tether (green) (on the right). Hybrid propulsion is not reported since the orbital lifetime is very small and not visible ompared to the one obtained with the previous technologies: it is simply the semi-period of the transfer elliptical orbit. 80

3.32 Number of the de-orbiting kits, for each orbital band, required to de-orbit a debris in a specific mass range. 81

3.33 Total mass (blue) injected in orbit depending on the technology employed. The mass is evaluated considering the number of debris in each mass range for each orbital band; the mass of the de-orbiting kit is multiplied for each number and then all the values obtained for the same mass range are summed over the five orbital bands. In the same way it is evaluated the number of units injected in orbit (green) for each de-orbiting technology. . . 82
3.34 Tape tether geometry and reference frame (left); edge impact (right). A and B are the axis of the elliptic impact damage 84
3.35 Total number of debris critical impacts per unit length for Al1100 (left) and PEEK (right), in function of the orbit altitude (250, 500, 750, 1000, 1250, 1500 [km]), inclination (0, 50, 90 [°]) and epoch (2016, 2021, 2027). The impact flux is provided for maximum debris size equal to 10 cm [109]. 85

4.1 On-OrbitServicing concepts: (a) ESA - ISS by ESA (*credit: ESA*), (b) SpaceX Dragon captured by the ISS robotic arm (*credit: NASA*), (c) ETS - VII by Jaxa [122], (d) Orbital Express by DARPA (*credit: Vacco*), (e) TECSAS of DLR, CSA and RKA [123] and (f) DEOS by DLR [124]. 88
4.2 Drastic change in the Youg's modulus of a SMP, where temperature is the external stimulus [146]. 90
4.3 *Shape Memory Effect* cycle [145]. 92
4.4 Illustration of the shape memory cycle [148]: stress/temperature plane (on the left), stress/strain plane (in the middle), and strain/temperature plane (on the right). 92
4.5 Schematics of the typical structures of a polymer network that is (a) physically cross-linked network; (b) chemically cross-linked network. 94
4.6 Example of SME at molecular scale: the crosslinks allow to maintain the deformed shape when the material is cooled, and they act as springs, recalling the chains to their original place, when the material is heated again, determinng the recovery of the permanent shape. 95
4.7 Example of terrestrial and space applications where SMP are employed: (a) biomedial application for surgical operations, (b) comfort devices, like matress or cuscions fillings, (c) supporting devices for post-surgical rehabilitation, (d)(e)(f) possible configurations with adaptabe wings, (g) deployable structures for space applcations, (h) technical textures for space suits. 97
4.8 Comparison of chemical compositions, physical, and material properties of porous SMP materials reported in the literature [148]. 98
4.9 Comparison of chemical compositions, physical, and material properties of porous SMP materials reported in the literature [148]. 99
4.10 Scheme of an electroadhesive interface [164]. 100
4.11 Scheme of an electroadhesive interface. 101
4.12 Example of interdigitated electrodes geometry (a) and equivalent rectangular electrodes configuration (b). In (c) it is represented the typical electroadhesive layer employed in climbing robots, with the interdigitated configuration. 102
4.13 Simulation models of electrodes patterns used in [167] to optimize electrostatic adhesive geometries. 103
4.14 Example of interdigitated electrodes geometry (a) and equivalent rectangular electrodes configuration (b). 104
4.15 Interdigitated configuration considered to determine the adhesion performances in [168]. . 105
4.16 Comparison between the normal adhesion pressure evaluated with the capacitor theory and with the model developed by Koh in [168]. 105
4.17 Shear adhesion pressures measured on different materials [159]. 106
4.18 Electrodes configurations. 109
4.19 Electrodes final configuration. It is also shown how the connection as resistor (red line) and capacitors (blue line) was realised. 110
4.20 Experimental setup to test electroadhesion on Prototype # 1. The setup consisted of: a DC-DC high voltage amplifier (E101CT, $EMCO^{TM}$ High Voltage), a $FUTEK^{TM}$ load cell, a linear stage ($Zaber^{TM}$). 110
4.21 Adhesion shear pressure obtained with Prototype # 1. 111

4.22 Thermal test exeprimental setup. The test setup consisted of: the electro-adhesive sample and a humidity and temperature sensor. An ATX power supply was employed to supply the required power, using the 3.3V output line. 112
4.23 Thermal model validation through experimental data. The red line rapresents the values predicted by the developed model, while the blue line are the experimental data. 113
4.24 Images of the deformed polymer, after the cooling phase (left side) and after 30 minutes (right side); the polymer is the black thin layer, indicated by the red arrows in the pictures. No relevant differences can be observed regarding the strain recovery of the material. . . . 115
4.25 Electro-adhesive layers. On the left, the sample with electrodes otained from a conductive fabric texture; on the right, the layer with the electrodes made fabricating a conductive silicone in laboratory. 117
4.26 Morphing electro-adhesive sample with electrodes made of conductive fabric. The electro-adhesive interface was connected to the polymeric foam support through a thin layer of TC-5005. 117
4.27 Experimental setup to test normal adhesion and morphing capabilities of Prototype # 2. The test setup consisted of: a supporting structure, a DC-DC high voltage amplifier, a linear stage, a load cell and a conductive plate (steel). An enlargement of the linear stage, the load cell and the steel plate assemply, and the sample is shown in (b). 119
4.28 Influence of a mechanical pre-load on the normal adhesion performances when no voltage is applied. 120
4.29 Percentage increase of the adhesion force as the mechanical re-load is increased. 120
4.30 Normal adhesion pressure obtained on a steel plate, and electrodes made of conductive fabric. The blue bars rapresent the dry-adhesion pressure (no voltage applied). The red and violet bars are the adhesion pressures obtained applying respectively 2.5 kV and 4.5 kV continously; the green and light blue bars are the adhesion pressures achieved removing the voltage 30 s before the activation of the linear stage for the detachment. 122
4.31 Comparison between theoretical normal adhesion pressure estimated through Equations 4.8 and 4.10 and experimental data obtained with 1.5 N of mechanical preload. As it can be observed, theoretical models underestimate the adhesion pressure achievable. This could depends on the presence of the silicone layer, responsible of some adhesion phenomenon that are not taken into account in analytical models, such as the Wan der Waals interactions that arise at the contact interface. 123
4.32 Normal adhesion pressure obtained on a steel plate, and electrodes made of conductive silicone. The blue bars rapresent the dry-adhesion pressure (no voltage applied). The red and violet bars are the adhesion pressures obtained applying respectively 2.5 kV and 4.5 kV continously; the green and light blue bars are the adhesion pressures achieved removing the voltage 30 s before the activeton of the linear stage for the detachment. 123
4.33 Comparison between the normal adhesion pressure obtained with a linear speed of 100 $\mu m/s$ and 500 $\mu m/s$. 125
4.34 Comparison between the normal adhesion pressure obtained with a linear speed of 800 $\mu m/s$ and 500 $\mu m/s$. 126
4.35 Example of a complete morphing test cycle: two peaks can be observed, the first referred to the detachment from the steel plate and the second one form the external surface of the irregularities, washers in this case. 128
4.36 Surface irregularities: on the right, it is shown the steel plate with two washers, 1.7 mm hugh, attached on it; on the left the washers are replaced with two nuts, 4.65 mm high. . 128
4.37 Normal adhesion pressure obtained with two washers to simulate macroscopical irregularities on the steel plate. 128
4.38 Normal adhesion pressure obtained with two nuts to simulate macroscopical irregularities on the steel plate. 129
4.39 Normal adhesion pressure obtained with no irregularities on the surface of the steel plate. 129

A.1 Angle of eclipse 136
A.2 Schematic representation of the effect of solar radiation pressure on satellites in circular orbits. The integration terms are obtained form the figure. 137

List of Tables

2.1 Main Bus mass budget 34

3.1 Selected debris for the mission analysis: main orbital parameters (initial altitude and inclination), mass and A/m ratio. 58
3.2 Mass budget of the main bus unit, drag sail unit and electric propulsion unit employed in case study #1. The subsystems of the main bus unit, and the relative mass, are indicated in 2.1, section 2.3.5 58
3.3 De-orbiting by means of drag sail only: results. The table shows the remover configuration, the remover mass fraction (%) and the total de-orbiting time for a given sail area. 60
3.4 Mass of the hybrid unit required to perform a controlled re-entry from an altitude of 250 km, in function of the final mass of the de-orbited system. In the second column it is reported the percentage of the hybrid unit mass respect to the final system mass. 66
3.5 Set of homogeneous debris selected among the thrid stages in the SSO band. 68
3.6 Set of eterogeneous debris selected among the debris in the SSO band. 68
3.7 Mass budget of the main bus unit, electric propulsion unit and electro-dynamic tether unit. The mass of the main bus unit, of the electric propulsion unit and of the electrodynamic tether unit were estimated according to the sizing procedure presented in sections 2.3.5, 2.3.2 and 2.3.4 respectively. 68
3.8 Number of units assembled and de-orbiting kit mass ratio. in percentage, for a de-orbiting performed by means of electric propulson (EP) and electrodynamic tether (EDT) for the debris selected in SSO. 71
3.9 Difference, in percentage, between the de-orbiting kit mass (left column) and de-orbiting time (right) obtained with electrc propulsion and electrodynamic tether (electrodynamic tether as reference). 71
3.10 Examples of the most efficient multiple transfers. The ΔV budget required for multiple orbital transfers is always significant and this implies a large mass of the propulsion system required to accomplish the entire mission: the mass could be of the order of some tons, depending on the maneouvres required for each sequence of debris. 72
3.11 SNECMA PPS-1350 performances 74
3.12 Mass budget of the electric propulsion unit, the hybrid propulsion unit and the electro-dynamic tether unit. The mass of the electric propulsion unit and of the electrodynamic tether unit were estimated according to the sizing procedure presented in section 2.3.2 and 2.3.4 respectively. The mass of the hybrid unit was the result of an optimization procedure presented in this section. 74
3.13 Candidate deorbiting kits for a nominal payload mass of 1000 kg and quantification of total items for the relevant debris population. L/D_{in} and OF ratio are characteristics of the hybrid rocket derived by the sizing procedure; M_i and M_{prop} are the inert mass and the propellant mass respectively; $\dot{m_{ox}}$ is the oxidizer flow rate. The last two columns represent the total mass and the total number of unit inserted in orbit, as the ΔV provided by each single unit is varied from 200 m/s to 900 m/s. 76
3.14 Mission parameters considered for impact flux calculation. All orbits are circular. 83

4.1 Geometric and electrical characteristics of the conductive path realised for Prototype #1. 109
4.2 Regime temperatures reached during each one of the three heating cycles. 112
4.3 Properties of the SMP employed to test the morphing capabilities. 114

4.4 % increase in normal adhesion pressure respect to dry-adhesion condition, when 1-5 N, 5 N and 10 N of pre-load are applied at 2.5 kV and 4.5 kV (electrodes in conductive fabric). The greater increase is registered at low mechanical pre-loads, while the electrostatic effect decreases for higher pre-loads. 121
4.5 % increase in normal adhesion pressure respect to dry-adhesion condition, when 1-5 N, 5 N and 10 N of pre-load are applied at 2.5 kV and 4.5 kV (electrodes in conductive silicone). The greater increase is registered at low mechanical pre-loads, while the electrostatic effect decreases for higher pre-loads. 124
4.6 % difference in normal adhesion pressure at 100 $\mu m/s$ respect to 500 $\mu m/s$ speed condition. As it can be observed, it was registered a decrease in the adhesion force measured as the speed of the linear stage was decreased from 500 $\mu m/s$ to 100 $\mu m/s$. 124
4.7 % difference in normal adhesion pressure at 100 $\mu m/s$ respect to 500 $\mu m/s$ speed condition. As it can be observed, it was registered an increase in the adhesion force measured as the speed of the linear stage was increased from 500 $\mu m/s$ to 800 $\mu m/s$. 127

Sommario

Sará sicuramente capitato qualche volta di guardare il cielo stellato e di scorgere un piccolo puntino luminoso che si muoveva come un aeroplano, ma senza lampeggiare come di solito fanno le luci degli aerei: si trattava di un satellite. É sempre affascinante pensare che ci sono oggetti che orbitano continuamente attorno alla Terra, cosí distanti da noi. Forse, non é cosí noto che ce ne sono davvero tanti...migliaia...17,000 quelli pi vicini alla Terra per la precisione. É difficile immaginare come cosiťanti oggetti possano orbitare senza toccarsi o scontrarsi tra loro. Fin dall'inizio delle attivitá spaziali nel 1957, un'enorme quantitá di oggetti é stata lanciata o rilasciata in orbita, e pensando che lo spazio sia cosí illimitato da poter contenere ogni cosa, tutti questi oggetti sono stati abbandonati in orbita. Il risultato é stato la creazione di un gran numero di detriti che hanno iniziato a rappresentare una minaccia per le future missione spaziali. Recenti studi hanno rivelato che se proprie contromisure non saranno adottate per ridurre la creazione di ulteriori detriti in orbita, come per esempio satelliti non operativi e stadi orbitali, l'ambiente spaziale potrebbe rimanere stabile solo per i prossimi 20 o 30 anni. Oltre tale termine, potrebbero verificarsi eventi di collisioni in cascata tra gli oggetti attualmente in orbita causando un rapido aumento del numero di detriti, anche nel caso irrealistico di un completo arresto dei lanci. Questo fenomeno autosostenuto, noto come *Sindrome di Kessler*, potrebbe impedire qualsiasi altra missione nello spazio. Nonostante a partire dagli anni '90 siano state proposte misure di mitigazione per limitare la generazione di detriti in orbita, esse si sono rivelate insufficienti per garantire una stabilitá a lungo termine dell'ambiente spaziale. L'unico modo di intervenire é l'implementazione, in parallelo, di missioni di rimozione attive dei detriti spaziali (in inglese Active Debris Removal - ADR). L'efficacia di tali missioni é stata dimostrata, ma ci sono ancora numerose questioni che devono essere affrontate per poterle applicare nella realtá. Da un lato, l'efficienza dei possibili scenari di missione deve essere investigata in modo da individuare le soluzioni migliori. Dall'altro lato ci sono ancora diverse questioni tecnologiche particolarmente critiche, specialmente riguardo la cattura dei detriti, che sono essenzialmente oggetti non cooperativi e quindi non predisposti per essere catturati.

La ricerca sviluppata nel presente lavoro di tesi é stata focalizzata su due degli aspetti principali legati all'ADR: I) analisi di missione di ADR e II) sviluppo di una tecnologia chiave per l'ADR; nel caso specifico, di un'interfaccia deformabile adesiva per la cattura di oggetti non-cooperativi.

É stato considerato uno scenario di missione basato sull'impiego di veicoli distinti per l'esecuzione dei trasferimenti orbitali e delle manovre di de-orbiting. In particolare, un veicolo di grandi dimensioni per i primi e propri kits di de-orbiting per le seconde. La soluzione innovativa sviluppata é stata l'adozione di strutture modulari per la realizzazione dei kits di de-orbiting: esse consistono nell'assemblare un certo numero di unitá base di microsatelliti, equipaggiate con specifici sistemi di de-orbiting; il numero di unitá assemblate dipende dalle caratteristiche del detrito, in termini di massa e altezza iniziale, e dalla particolare tecnologia di de-orbiting. Uno scenario di questo tipo comporta una maggiore efficienza, affidabilitá e flessibilitá. Sono inoltre previsti vantaggi in termini di costo e di massa, con la possibilitá di impiegare economie di scala grazie alla standardizzazione delle unitá impiegate.
Nello studio sono state considerate quattro soluzioni di de-orbiting: vele per l'aumento del drag, propulsione elettrica, filo elettrodinamico (electrodynamic tether) e propulsione ibrida. Diversi scenari di missione sono stati analizzati per determinare le caratteristiche delle soluzioni adottate, in termini di massa del sistema di de-orbiting e di tempo totale di manovra. Per ogni tecnologia é stata dimensionata una unitá microsatellite elementare. Inoltre, é stata anche implementata una procedure di ottimizzazione di trasferimenti orbitali multipli per minimizzare la massa del sistema propulsive richiesto. Sono state poi individuate cinque bande orbitali in cui attuare l'ADR, caratterizzate da detriti con masse tra 800 kg e

11 tonnellate, e altezze tra gli 800 km e i 1000 km.
Le analisi hanno rivelato che le vele per incrementare il drag atmosferico, pur essendo soluzioni a basso costo e semplici, non sono adeguate per la rimozione di detriti massivi in orbite elevate perché richiederebbero dimensioni troppo elevate con un aumento della possibilitá di collisioni durante la fase di de-orbiting. La propulsione elettrica e il filo elettrodinamico sono entrambe soluzioni promettenti per l'ADR: per detriti con massa minore di 2000 kg le due tecnologie sono comparabili, sia in termini di massa del sistema di rimozione, sia di tempo di de-orbiting. Per detriti piú massivi, con massa maggiore di 2000 kg, il filo elettrodinamico é piú vantaggioso in termini di massa, ma richiede tempi di de-orbiting molto maggiori rispetto alla propulsione elettrica. La probabilitá di avere impatti con detriti fino a 10 cm di diametro é risultata maggiore del limite suggerito nel NASA-STD-8719.14 di 0.001. Nel caso della propulsione elettrica invece, si é ottenuto un rischio di collisioni catastrofiche trascurabile. La propulsione ibrida é risultata la soluzione piú svantaggiosa in termini di massa, ma é quella che consente il de-orbiting in tempi piú ridotti.

La seconda parte dell'attivitá di ricerca é focalizzata sullo sviluppo di un'interfaccia deformable adesive che potrebbe essere impiegata come end-effector di un meccanismo robotico per la cattura di oggetti non-cooperativi. Due diverse tecnologie sono state considerate per lo studio: polimeri a memorie di forma, per la capacitá di adattarsi a forme differenti, e l'elettroadesione per l'adesione mediante forze elettrostatiche. Due prototipi sono stati realizzati e testati.
Dai test é emerso che sia un precarico meccanico che le forze elettrostatiche contribuiscono ad aumentare l'adesione. Si sono ottenuti livelli di pressione normale di adesione dell'ordine di 0.55 kPa - 1.4 kPa senza forze elettrostatiche, con variazione del precarico meccanico tra 1.5N e 10 N. L'adesione aumenta in presenza di forze elettrostatiche, variando tra 1.4 kPa e 1.8 kPa per diverse condizioni di precarico meccanico e voltaggio applicato per generare le forze elettrostatiche. Le forze di adesione ottenute variano tra 3.5 N e 11.5 N. Sono stati eseguiti anche dei test che prevedevano la deformazione del supporto per verificare la capacitá di deformazione e adesione in presenza di irregolaritá macroscopiche sulla superficie dell'oggetto da catturare. Tali test hanno dimostrato che la presenza di un supporto polimerico tipo schiuma puó essere vantaggioso nel caso di cattura di oggetti irregolari, in quanto consente di adeguarsi alla forma della superficie dell'oggetto e aderire anche in presenza di irregolaritá. In questo modo l'efficacia della soluzione proposta é stata confermata.

Abstract

It has surely happened sometimes to look at the night sky and catch sight of a small, brighting spot moving like an airplane, but without flashing as usually airplane lights do: it was a satellite. It is always amazing to think that there are objects that continously orbit around Earth, so far from us. Maybe, it is not well-known that they are a lot...thousands...more or less 17,000 those closer to the Earth, to be precise. It is difficult to imagine how so much objects can orbit without touching or colliding each other. From the beginning of the space activities in 1957, an enormous number of objects have been sent or released in space, and thinking that space is so limitless that it could contain everything, all these objects have been abandoned in orbit. The result has been the creation of a great quantity of debris that have began to represent a serious threat for future space missions. Recent studies revealed that if no countermeasures are going to be adopted to reduce the generation of debris in orbit, like for example spent spacecraft and orbital stages, the space population could remain stable only for the next 20 - 30 years. Beyond that, collisional cascade events between objects already in orbit will cause a rapidly increase of debris, even in case of a complete hault of launches. This self-sustained phenomenon, known as *Kessler Syndrome*, would prevent any other human access to space. Although from '90s, mitigation measures have been proposed to limit the generation of debris in orbit, they appeared to be insufficient to guarantee a long term stability of the space environment. The only way to intervene would be the implementation, in parallel, of active debris removal (ADR) missions. The effectiveness of such kind of missions has been demonstrated, but there are numerous aspects that have to be solved yet in order to make them feasible in the near future. On one hand new mission studies and analyses are required to identify the most efficient ADR scenarios. On the other hand, there are several technological issues that are particularly critical, espacially as regards the capture of space debris, that are essentially un-cooperative objects and so, not-specially-prepared to be grasped.

The research developed in this thesis deals with two of the main aspects related to active debris removal: I) ADR mission analysis, II) developement of an enabling technology for ADR; in the specific case, the development of a morphing adhesive interface to capture uncooperative ojects.

A *multiple vehicles scenario*, where orbital transfers and de-orbiting operations are accomplished by distinct vehicles (a space tug for the former, proper de-orbiting kits for the latter), is selected for the analysis. The innovative solution proposed is the employemnt of modular structures as de-orbiting kits, constructed by assembling a certain number of microsatellite elementary units, equipped with proper de-orbiting devices; the number of assembled units depends on the characteristics of the debris, in terms of mass and initial orbit, as well as to the specific de-orbiting technology selected. An increased mission efficiency, reliablity and flexibility are expected from the adoption of such approach. Costs and mass savings can be also expected, as well as economy of scale, thanks to the standarization of the units employed.
Four de-orbiting solutions are implemented in the analysis: drag sails, electric propulsion, electrodynamic tethers, hybrid propulsion. Different mission scenarios are analysed, to determine the performances of each solution, in terms of de-orbiting kit mass and total de-orbiting time. For each de-orbiting technlogy, a proper base unit is determined. An optimization procedure to perform multiple orbital transfers and, hence, minimize the mass of the propulsion system of the space tug, is also performed. Five orbital bands are identified as priority regions, where debris have mass between 800 kg and 11 tons and orbits between 800 km and 1000 km.
The analyses revealed that, although drag sails are low-cost and simple solutions, they are not suitable to de-orbit massive debris from high altitudes since very large sails could be required, with consequent

high risk of collisions during the de-orbiting phase. Electric propulsion and electrodynamic tethers are both promising solutions for ADR: for debris with mass $\leq$ 2000 kg they are comparable, both in terms of de-orbiting kit mass and total de-orbiting time. For more massive debris, mass $\geq$ 2000 kg, electrodynamic tethers performes better from the remover mass point of view, but higher de-orbiting time is required compared to electric propulsion. Risks assessment evaluation revealed that in this case the probability for the electrodynamic tethers to be damaged in consequence of collisional events with debris up to 10 cm exceeded the limit of 0.001 indicated in the NASA-STD-8719.14. The risk analyses conducted for electric propulsion, on the other hand, did not reveal any risk of catastrophic collision during the de-orbiting manoeuvre. Hybrid propulsion resulted the most massive solution among those implemented, but it represents the fastest solution in terms of de-orbiting time.

The second part of the research activity is focused on the development of a morphing adhesive interface to be intagrated as end effect of a robotic mechanisms to allow the capture of uncooperative objects. Two technologies are investigated in the realization of the interface: shape memory polymers, for the morphing behaviour, and electroadhesion for the adhesion capabilities. Two prototypes are then developed and tested. It is observed that mechanical pre-load as well as electrostatic force increase the normal adhesion performances of the realised interface. Normal adhesion pressures can vary between 0.55 and 1.4 kPa without the contribution of electrostatic forces, as the mechanical pre-load is varied between 1.5 N and 10 N. The adhesion pressure increases in presence of electrostatic forces, varying between 1.40 kPa and 1.80 kPa for different mechanical pre-load and voltage conditions. The forces achievable range between 3.5 N and 11.5 N. Morphing tests are also performed to verify the morphing-adhesive capabilities of the developed interface. The tests demonstrates taht the presence of a foam substrate could be advantageous as regards the capture of uncooperative objects, allowing a good compliance between two contact surfaces even in presence of macroscopical irregularities, enhancing the adhesion between them. The effectivness of the proposed morphing-adhesive interface is then demonstrated.

Chapter 1

Space Debris

1.1 Introduction

The launch of Sputnik-1 in 1957 marked the beginning of space race: from that date it has been a never-ending succession of launches and space missions that has led to populate the regions around the Earth, from low altitudes of 200 km, crossed by the International Space Staion ISS, to higher orbits at 35000 km, where geosynchronous satellites are sent. The exponential rate of this growth is well represented in Figure 1.1, where it is shown, through a sequence of images, the evolution of the space environment around the Earth at different epochs from the beginning of the space activity.

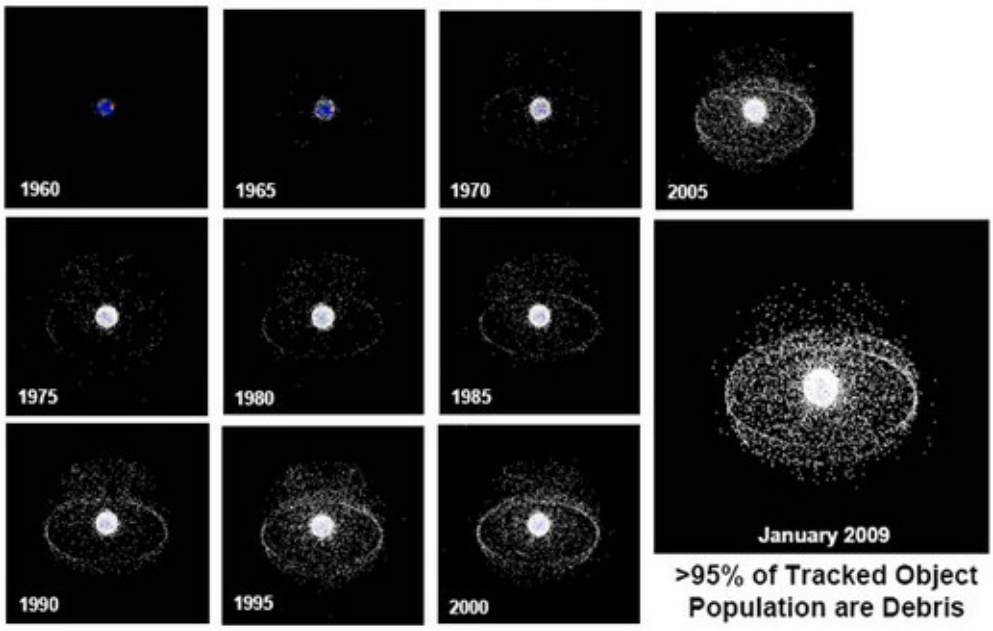

Figure 1.1: Evolution of the space environment form the beginning of the space activity, at different epochs. (*Credits: NASA*).

Apart some satellites sent in particular orbits, the greatest part of the objects has been concentrated in two main orbital regions: the first region corresponds to the Low Earth orbits (LEO), whose altitude is spread between 200 km and 2000 km, and the second one coincides with Geosynchronous orbits (GEO) at a mean altitude of 35000 km. The most significant fact that emerges from the picture is that the greatest part of the objects launched or generated in orbit through mission operations, over the years, is still there. While a deeper description of the space debris environment will be presented in the next sections, what it is important to highlight here is that only 6% of these objects are still operational satellites, while the remaining 94% re-enter in the group of the well-known space debris [1], [2] [3]. The

first example of space debris is Vanguard I, launched in 1958 and not yet re-entered (the Sputnik-1, the first satellite sent in orbit, re-entered after three months from its launch); it is the most long-lived satellite and represent the oldest space objects still in orbit. Over the years, only few objects, placed in orbits low enough, have naturally re-entered in the atmosphere thanks to the effect of the atmospheric drag, but most of them are destined to remain in space for hundreds, or even thousand years, since no disposal devices were provided to move them away from orbit after the end of their operational life. According to the general definition proposed by the Inter-Agency Space Debris Coordination Committee (IADC) and explained in the *Position Paper on Orbital Debris* [4], space debris are all "*non-functional objects with no reasonable expectation of assuming or resuming its original function or any other function for which it is or can be expected to be authorized, including fragments and thereof*". This definition includes all non-operational satellites, spent rocket bodies, materials released during planned space operations and fragments generated by satellites and upper stage breakup due to accidental explosions or collisions. The main problem related with these objects is that they continually pass through the orbital regions typical of functional satellites, representing a threat for possible catastrophic events that could prevent the continuation of their mission. The issues related to the crowding of the near Earth orbital environment and the possible consequences on its evolution were first theorized by Donald Kessler and Burton Cour-Palais in 1977; one year later they published the paper *Collision frequency of Artificial Satellites: The Creation of Debris Belt* [5] in which they postulated that in few decades the space population would have become *self-regenerative* and on-orbit collisions would have become the primary source of new debris due to collisions between satellites, both active or inactive, fragments and old payloads and rocket motors. Such arguments were not a simple theory: examples of catastrophic events in orbit really happened over the years. The first accidental explosion of the DELTA second stage, happened in 1973 [6], had shown the potentialities in the creation of thousands of space debris as consequence of such events, and posed the attention to the need to control the generation of space debris and to study their potential effects on space operations. The first step in the recognition of the space debris problem was done in 1980 [2] when the International Astronautical Federation addressed the issue of debris management in GEO; one year later it was published the document *Position Paper on Space Debris* by the American Institute of Aeronautics and Astronautics (AIAA). NASA' s efforts to reduce further fragmentation, such as DELTA second stage explosion, one of the most notably on-orbit break-up event, led to a policy based on the development and adopton of some mitigation measures that aim to regulate the generation of debris during orbital operations and to prevent orbital accidents, for example removing the residual propellant from spent stages. International space agencies will be later invited to share and follow these measures working together to preserve the space environment. For about ten years space debris had represented an issue to be considered, but no significant improvements were really done regarding the space activities: no de-orbiting devices were installed on board satellites and no much attention was dedicated to limit the release of debris during orbital operations. An impulse arrived in 1990, when Donald Kessler published the paper *Collisional Cascading: The Limits of Population Growth in Low-Earth Orbits* [7]: he designed the evolution of the space debris environment as a cascading process in which the growth of space debris was described as a self-sustained phenomenon, triggered by initial collisions between intact objects and ultimately sustained by collisions between small fragments. This processes, that could not be stopped once began, could make some regions in LEO unsafe for long time. This phenomenon became known as *The Kessler Syndrome*. In light of these theory, in the early 1990s, the International Academy of Astronautics (IAA) convened a group of 13 orbital debris specialists in order to investigate the status of the near Earth man-made objects population and to predict its evolution and effects on future space operations to find confirmation to such theory [8].

As result of this investigation, in 1993 the first *Position Paper on Orbital Debris* [4] (updated version) outlined a general overview of the space debris situation and clearly conveyed the urgency of adopting mitigation measures to control the growing of objects in near Earth orbital regions. The most important consideration reported in the document was that "*without changes to the way many space missions are performed, near-Earth space will become so cluttered by debris that routine operations will be severely hampered*" ([4], p. 14) . In the same year the Inter-Agency Space Debris Coordination Committee (IADC) was founded as an international governmental agency for the worldwide coordination of activities related to the issues of man-made and natural debris in space. The primary purposes of the IADC were, and still are, to exchange information on space debris research activities between member space agencies (ESA, NASA, JAXA, ROSAVIAKOSMOS, ASI, DLR, UKSpace, CNSA, CNES, BNSC, NSAU, CSA and ISRO) to facilitate opportunities for cooperation in space debris research, to review the progress of

ongoing cooperative activities, and to identify debris mitigation options [9].

Since 1994, space debris issue has been an agenda item of the Scientific and Technical Subcommittee of the United Nations Committee on the Peaceful Uses of Outer Space (UNCOPUOS) [2]. Space debris environment was beginning to be considered one of the long-term objective in space mission planning. In the following years, several reports have been published related to near-Earth environment, and alternative solutions for mitigation have been proposed. In 1995 the *Safety Standard Guidelines and Assessment Procedures for Limiting Orbital Debris* [10], published by NASA, provided specific guidelines and methods to comply with the NASA policy to mitigate orbital debris generation. This represented an important document related with space debris issue because, for the first time, it was established a shared behaviour to prevent debris generation starting from mission definition. Two main solutions were proposed: debris prevention, for future space activities, and debris removal, to regulate the removal of those objects that will never re-enter or re-orbit by their own. In 2000, exactly seven years after the initial treatise, an updated version of *IAA Position Paper on Orbital Debris* was approved [8]. After the realization of the obstacles related to cost and technological effectiveness and feasibility of active removal of space debris, the report concentrated on means to reduce or eliminate the creation of orbital debris.

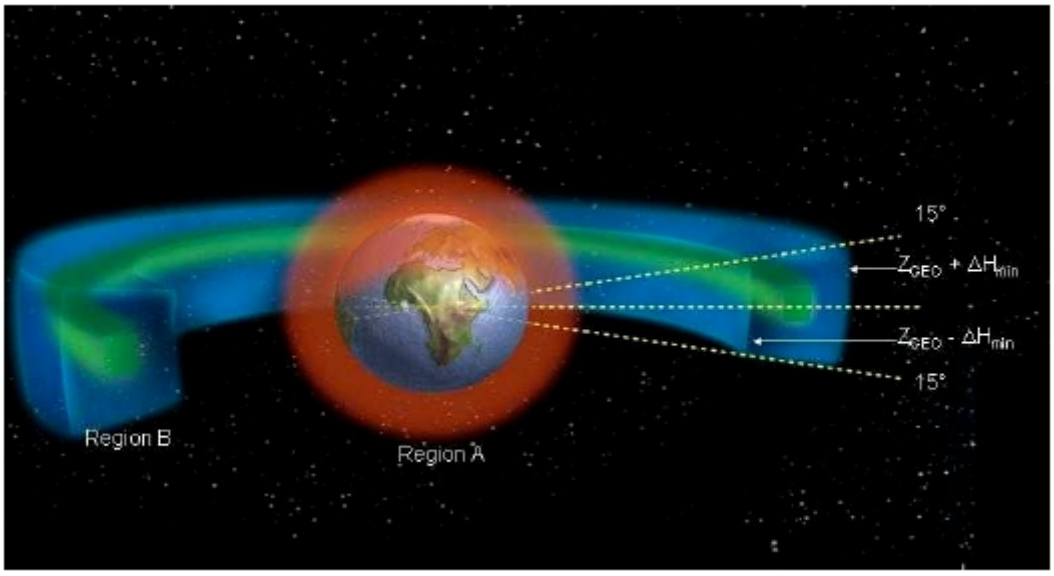

Figure 1.2: Space debris protected zones [2].

In 2005, the *Position Paper Space Debris Mitigation, Implementing Zero Debris Creation Zones* [2], published by ESA, introduced the concept of '*protected regions*' for Low Earth Orbit (LEO) up to 2,000 km in altitude and about the geostationary altitude in bands extending 200 km above and below 35,678 km altitude as well as plus and minus 15 degrees in latitude (Figure 1.2). The paper promoted *'zero debris creation within the protected zones'* and indicated, as an interim step to consider in the mitigation issue, 'zero long lived debris creation within the protected zones'.

Nowadays, mitigation measures only appear insufficient to ensure a long term stability of the space environment and the development and implementation of techniques for active debris removal (ADR) is one of the immediate future challenges in the space field [11] [12] [13]. Space debris environment remain one of the principle issue in future space activities. The international collaboration between countries in cleaning space from debris is one of the main hallmarks of President Obama's new National Space Policy, announced on June, 2010 [14] . Cleaning space from debris is the only way to ensure the possibility for continuing space missions in future. The next shared objective is to make the aforementioned guidelines, that are non-binding at the moment, a customary international law to be applied in space activities.

1.2 Space debris environment

Space debris, in general, include both natural meteoroids and objects generated by human space activity. Natural meteoroids cannot be actively controlled and, most of them, are very small in size. They represent a severe threat for orbiting satellites and the adoption of proper external structure is the only means to protect by accidental catastrophic collisions with these objects . The issue is different for man-made space debris. From the beginning of the space activities, with the launch of Sputnik-1 in 1957, the number of objects sent in orbit has esponentially increased, as it is shown in Figure 1.3. Of these objects, only a very small quantity, compared to the quantity sent in orbit in the same periods, re-entered back on the Earth (Figure 1.4), and this trend has slowed down in the last decades, determining a consequent increase of debris left in orbit.

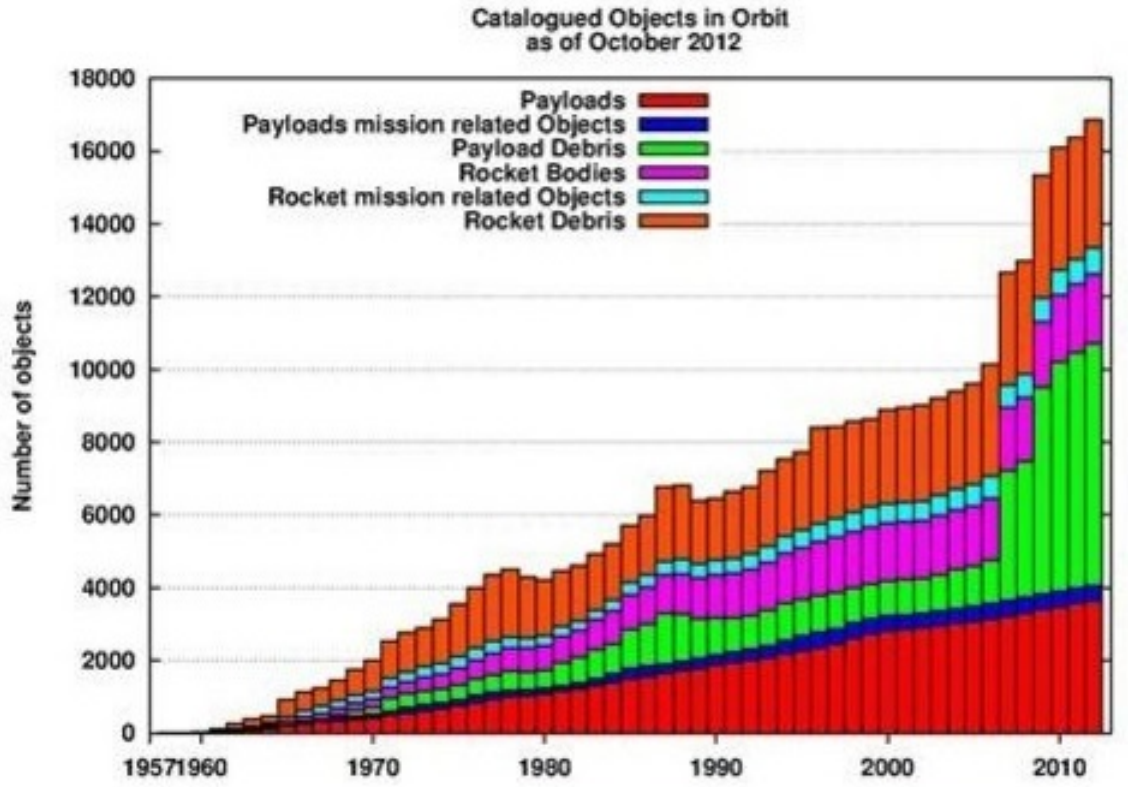

Figure 1.3: Space Debris growth and composition of the space objects sent in orbit from as of October 2012 (*Courtesy of ESA, Space Debris section [15]*).

According to their size, space debris can be classified in two main classes [17] large objects, such as spent spacecraft and rocket stages, whose population is small in absolute term, but large relative to their masses; and small objects that are the results of explosions or collisions, whose size is similar to that of micrometeoroids. The interaction between these two classes of debris is the main cause of the growth of debris population in LEO and GEO.
Since the problem of space debris became one the most important issue at the attention of the space community, there has been the necessity of tracking the objects in orbit and classify them by their mass, size and orbital regions. The most important data set is the NASA Satellite Situation Report (SSR) together with the Two Line Element (TLE) catalogue of the US Strategic Command. They are based on observation data and orbit determination from the US Space Surveillance Network (SSN) [18] [19] [20]. The SSN generally considers objects larger than 10 cm in average cross section [18] [20] [21] [22], that is the limiting size due to limitations in the sensitivities of SSN radars and telescope. This means that a great number of small debris has not been catalogued and, thus, the dimension of space debris population is well underestimated. The space debris population is then characterised by the following ojects [21]:

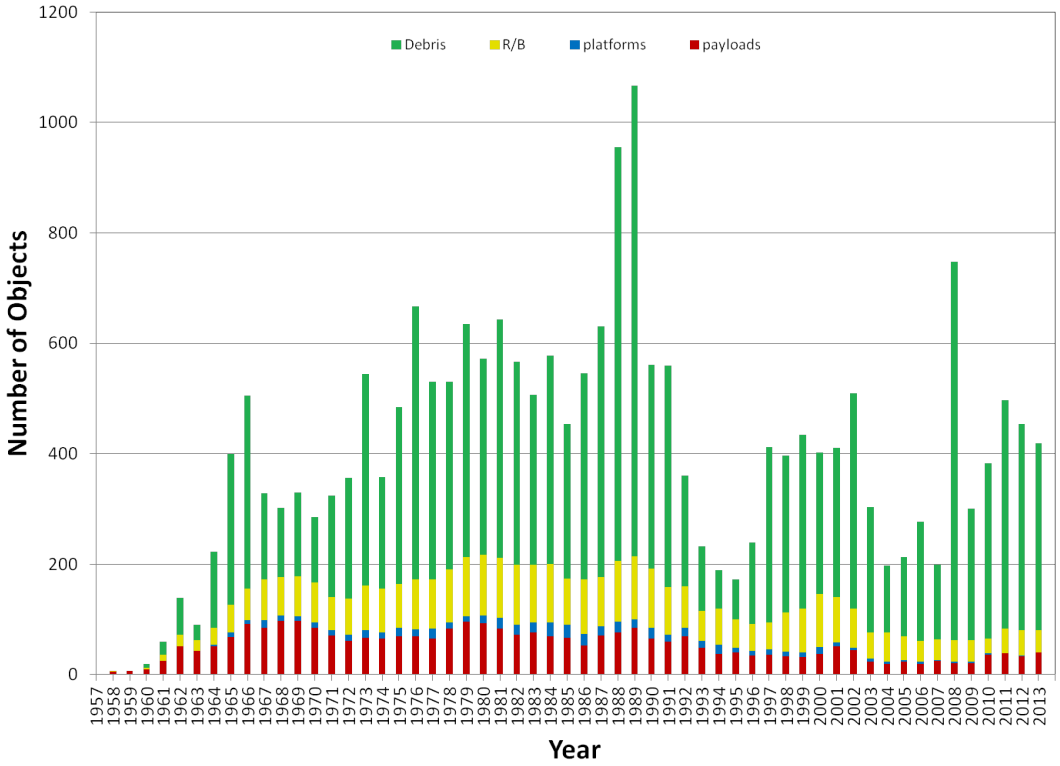

Figure 1.4: Number of objects re-entered on the Earth, from the beginning of the space activities in 1957 to 2013 (*courtesy of the Center for Orbital and Reentry Debris Studies [16]*)

- spent intact satellites;
- rocket bodies;
- mission related debris
- fragments of intact satellites resulting from accidental or intentional explosions and collisions;
- solid rocket motors exhaust products;
- ejecta from micro-particles impacts with intact satellite and fragment surfaces;
- paint flakes.

Presently (September 2014), there are about 17,127 catalogued objects in orbit [3]. Figure 1.5 shows the distribution according to their nature. Approximately 3,965 are intact satellites; 1,344, which corresponds to 7% of the entire population, are operational payloads, while 2,621, about the 15% of the entire population, are spent intact objects. The remaining 78% comprehends rocket bodies and fragments of different nature: 11% are rocket bodies, 11% mission related debris and the great amount, and 56% are fragments due to breakup events, accidental or intentional collisions or explosions [23]. In Figure 1.6 it is represented the distribution in the three main orbital bands; as it can be observed, most of the objects, about 73%, are concentrated in LEO regions, where also the largest amount of mass can be found, while 8% are in GEO and 19% are in MEO [8].

The LEO environment is the most crowded, since some orbits are particularly advantageous for several purpose (communications, Earth observations, investgations related to the magnetic or th gravitational field, ...). The most populated orbits are concentrated at some altitudes and inclination; three of them, listed below, stand out among the other, and represent the most critical for tow main reasons: the first and the last one are foreseen to be the orbits where the largest number of catastrophic collissions will occure in the next 200 years, while the second one correspond to the sunsynchronous orbit (SS), one of the most used type of orbits becasue of its well known advanatges [27].

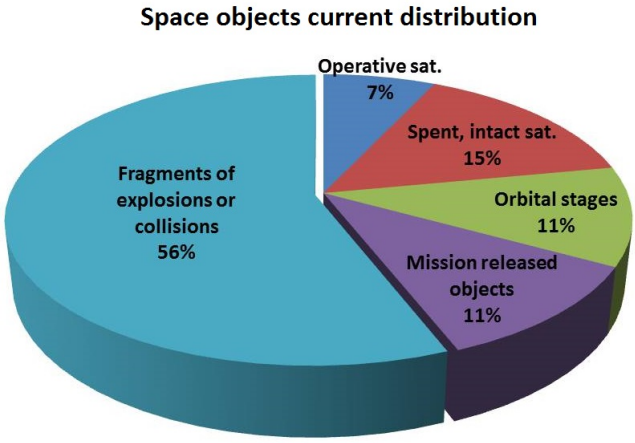

Figure 1.5: Current distribution of space objects according to their origin (data from [3] and [23]).

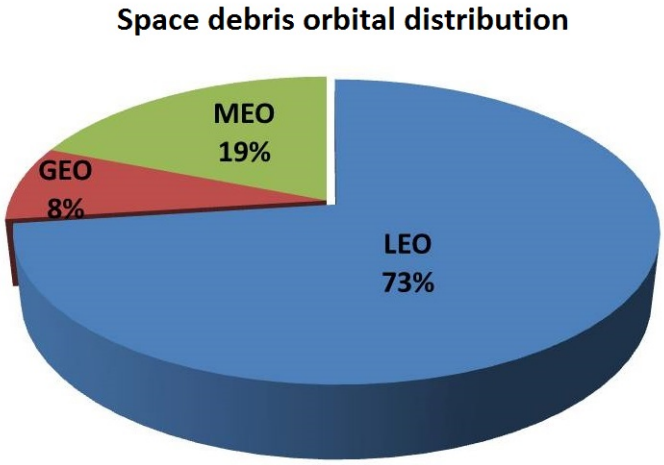

Figure 1.6: Orbital distribution of space objects (data from [8]).

1. Altitude: $1000km \pm 100km$; inclination: $82° \pm 1°$;
2. Altitude: $800km \pm 100km$; inclination: $99° \pm 1°$;
3. Altitude: $850km \pm 100km$; inclination: $71° \pm 1°$.

General information about the main characteristics of the space debris population can be found in [19]. Spent satellites can be extremely variable in size: picosats and microsats may be small, weighting few kilograms, while massive objects can be between 500 and 8000 kilograms, and represent critical targets for accidental collisions. Also rocket bodies can be variable in size, as small as 100 kilograms, to even 11 tons. More than 30% of the launch vehicles used in the history remain in orbit for years, without re-entering the Earth. Mission related debris are usually objects generated in the first days of first few weeks of orbital operations, during satellite-deployment processes; they are mainly sensors and engine covers, straps, spring, yo-yo despin weights, frequently used between 1960s and 1970s. Some mitigation measures adopted later limited the creation of this kind of debris. Fragments are usually generated by three main events: anomalous events, explosions or collisions; most of them are accidental and occur at the end of the operative life. Once again, international measures adopted aimed to limit or eliminate any risk of satellite fragmentation.

	Common Name	Owner	International Designator	Cataloged Debris*	Debris in Orbit*	Year of Breakup	Altitude of Breakup	Cause of Breakup
	Fengyun-1C	China	199-025A	3218	2989	2007	850 km	Intentional Collision
	Cosmos 2251	Russia	1993-036A	1559	1371	2009	790 km	Accidental Collision
	STEP 2 Rocket Body	USA	1994-029B	710	58	1996	625 km	Accidental Explosion
	Iridium 33	USA	1997-051C	567	487	2009	790 km	Accidental Collision
	Cosmos 2421	Russian	2006-025A	509	0	2008	410 km	Unknown
	SPOT 1 Rocket Body	France	1986-091C	492	32	1986	805 km	Accidental Explosion
	OV 2-1 / LCS 2 Rocket Body	USA	1965-082DM	473	35	1965	740 km	Accidental Explosion
	Nimbus 4 Rocket Body	USA	1970-025C	375	245	1970	1075 km	Accidental Explosion
	TES Rocket Body	India	2001-049D	370	111	2001	670 km	Accidental Explosion
	CBERS 1 Rocket Body	China	1999-057C	343	178	2000	740 km	Accidental Explosion

Figure 1.7: 10 worst satellite breakups events (credits NASA [19]).

According to the information collected by scientists, one-third of the debris in Earth orbit generated from just ten satellites breakups, shown in Figure 1.7. Fortunately most of them had fallen out of orbit and re-entered in the atmosphere. Until 2007, most of fragmentation events had been accidental: the first one confirmed between two catalogued objects happened in 1996, when the gravity-gradient attitude control boom of the French satellite CERISE was damaged by a fragment from an ARIANE rocket body. But there has been two quite significant on-orbit collision events that caused a visible, sudden increase of the debris population: the first one represents the first intentional breakup ever: it was a demonstration mission occurred on January 11th, 2007, where the Chinese FENGYUN-1C satellite was disrupted by an interceptor missile, and created about 2,500 catalogued small objects, most of which are still in orbit [24].

The second was an accidental hypervelocity collision between two satellites, COSMOS and IRIDIUM, one of which was still operational (IRIDIUM), occurred on February 10th, 2009. By June 2012 the U.S. Space Surveillance Network had cataloged 598 pieces of debris associated with Iridium and 1,603 pieces from Cosmos [19]. The increase of debris after these events is well shown in Figures 1.8 and 1.9. As of July 2012, nearly three and a half years after the event, 90% of the debris from the collision was still in orbit around Earth. In both cases, the debris clouds spread over the most frequented orbits, between 750 km and 900 km, posing further potential threats for every spacecraft in LEO.

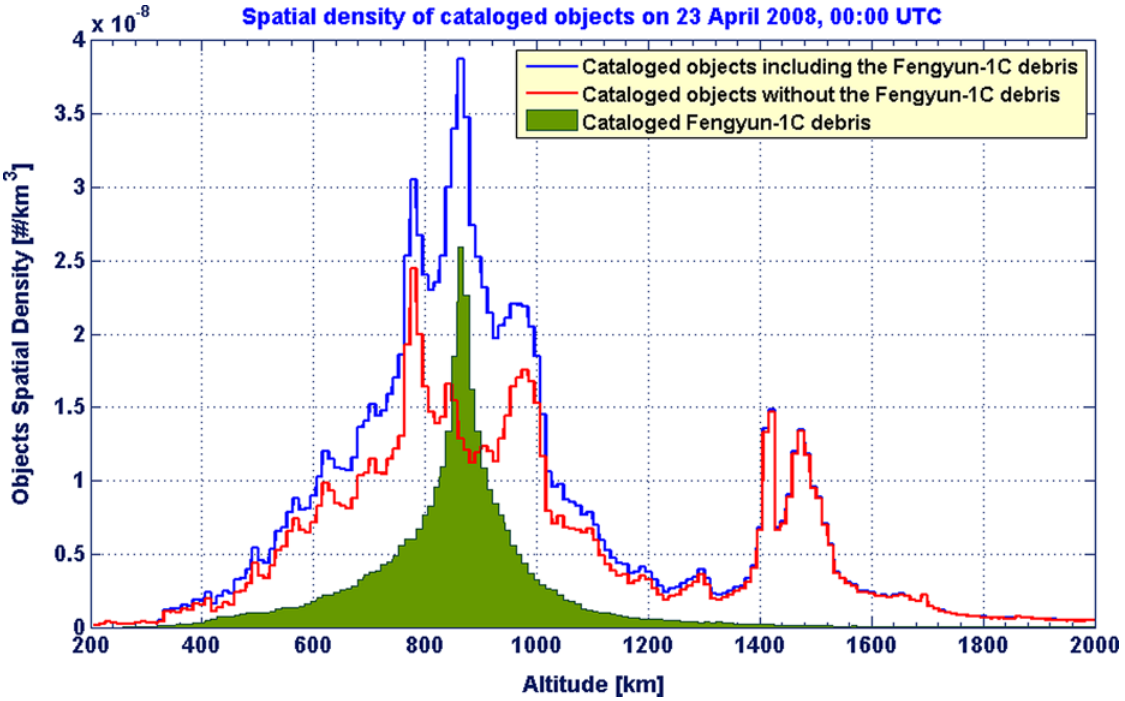

Figure 1.8: Spatial density of catalogued objects after the disruption of the CHinese satellite Fengyun-1C in 2007 [24].

While accidental collisions cannot be controlled, some mitigation measures have been adopted to prevent on-orbit explosions, such as the passivation of the upper stages at the end of mission completion, and they resulted successfully [19].. Solid motors exhaust products are mainly large quantities of aluminium oxide particles ejected during thrust and after shut down, that could remain in orbit. Starting from the early 1990s, NASA and DOD collaborated with MIT Lincoln Laboratories in a project that aimed to detect particles smaller than 10 cm, of the order of about 5 mm. This allowed to discover new kinds of debris, especially at orbits of 65° of inclination and 900-1000 km of altitude. There appeared to be more than 100000 particles, like metallic spheres, larger than 5 mm. After some investigations, it was discovered that they were droplets of sodium potassium from Soviet spacecraft nuclear reactors. The particles larger than a centimetre could represent a mission-terminating threat to satellites below 850 km, as well as to human spaceflight. Some impacts with these particles have been registered also on the International Space Station, although no catastrophic consequences occurred. After these discoveries, sodium potassium as coolant has not been used anymore on board [19].. Paint flakes derive from the covers used on the walls of spacecraft for thermal control. Even though they could not seem a potential threat for spacecraft, they could cause damages that could become dangerous for the survivability of the hit structures. In 1983, a 3-millimeter wide, 4-millimeter deep crater was discovered in a window of the space shuttle Challenger, following its STS-7 mission. Such a crater may not seem large; and since the windows on the shuttle were three layers deep, it wasnt a threat on reentry. But the danger increased for launch: because the launch environment was much more severe, even a crater that small could have had unwanted consequences for subsequent missions [19].

Figure 1.10 shows how the debris population has increased over the years, from the beginning of the space activity. From this picture it emerges the most relevant events that signed important moments concerning the space debris issue. It is clear the fast increase of objects that have been inserted in

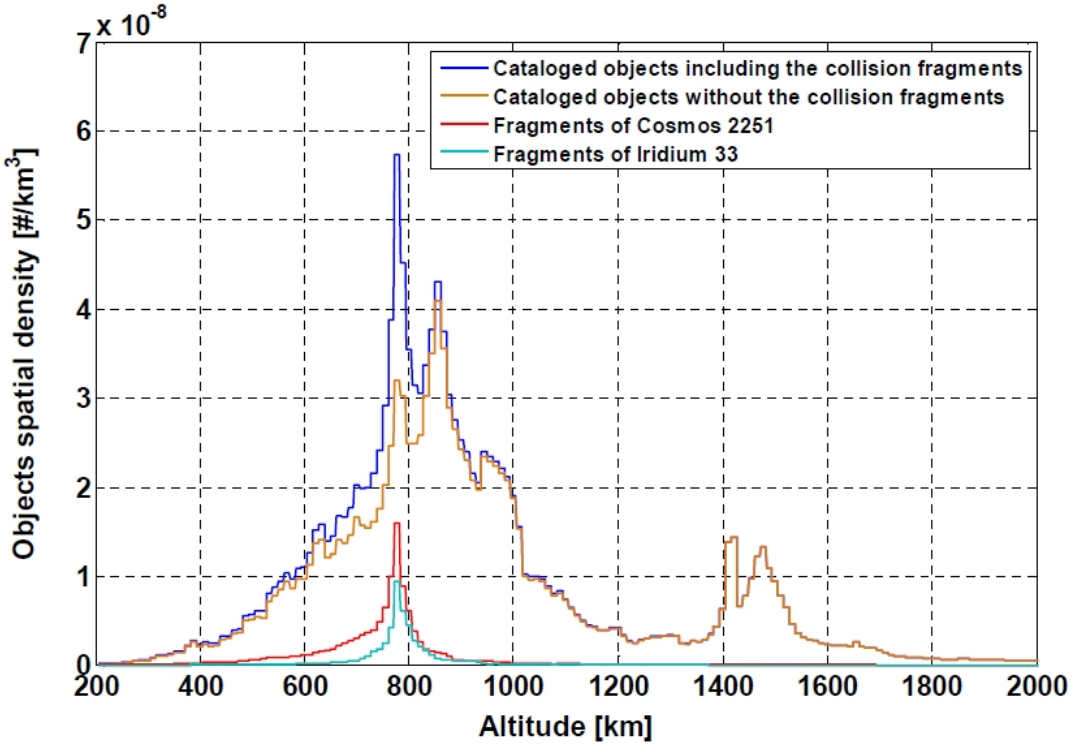

Figure 1.9: Spatial density of catalogued objects after Cosmos-Iridium collision in 2009 [25].

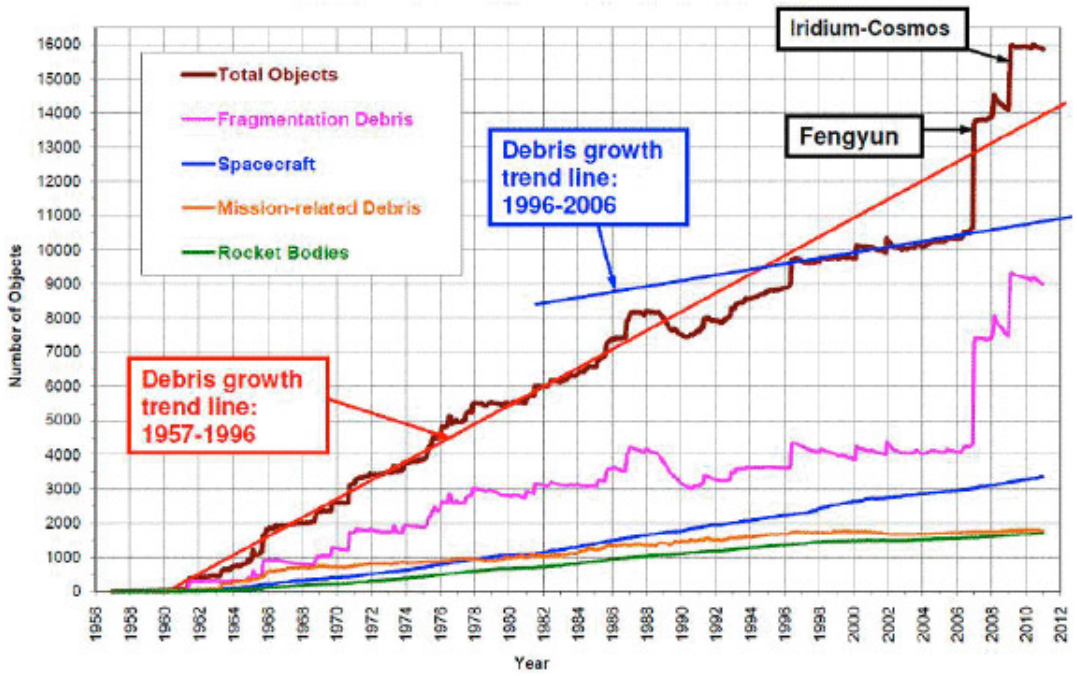

Figure 1.10: This plot shows the number of catalogued objects luanched in space form the beginning of the space activities. It is evident the sudden increase occured afetr the two collissional events in 2007 and 2009. It can be also seen a change in slope of the debris growth trend line due to the adoption of mititgation measures starting from the '90s (*credits by NASA*).

orbit since the beginning; and as was pointed out earlier, while the trend of satellites, rocket bodies and mission released objects are almost the same, the greater contribution to the debris population comes from fragmentation events. Three main facts can be highlighted form the picture; the most evident are the two collisional events described earlier, whose drastic effect is shown by two almost vertical lines in the graph. The third fact regards the change in slope of the debris growth trend lines in the periods 1957 1996 and 1996 2006, mainly due to the change in slope of the mission released objects and fragmentation debris lines. This phenomenon can be mainly attributed to the definition of some mitigation measures that were published for the first time between 1993 and 1995, and that are well explained in the document *NASA-STD-8719.14A, Process for Limiting Orbital Debris* [26] which is the latest updated version (2011). In the next section, the most relevant guidelines concerning the removal, active or passive, of space debris are presented.

1.3 Mitigation Measures and International Guidelines

In April of 1993 NASA issued the *NASA Management Instruction (NMI) 1700.8, Policy to Limit Orbital Debris Generation*, which outlined a formal assessment of the potential to generate orbital debris. Two years later, in 1995, the standard *NSS 1740.14 Guidelines and Assessment Procedures for Limiting Orbital Debris* [10] was published as a companion to *NIM 1700.8*. After the review and acceptance of the U.S. Air Force, they became the U.S. government guidelines, that dictated the principal means for controlling the increase of orbital debris. According to the latest version of *NASA-STD-8719.14A* [26], the most relevant guidelines that involve debris disposal are presented as follows. The debris limitation is articulated in the following areas (taken form the document [26]):

- Limiting the generation of debris associated with normal space operations;
- Limiting the probability of impact with other objects in orbit;
- Limiting the consequences of impact with existing orbital debris or meteoroids;
- Limiting the debris hazard posed by tether systems;
- Depleting onboard energy sources after completion of mission;
- Limiting orbital lifetime in LEO after mission completion or maneuvering to a disposal orbit; and
- Limiting the human casualty risk from space system components surviving reentry as a result of postmission disposal.

The measures about the *limiting orbital lifetime in LEO after mission completion or maneuvering to a disposal orbit* have been considered of particular interest for the present work.

1.3.1 Postmission Disposal of Space Structures

As indicated in the document NASA-STD 8719.14 [26], spacecraft disposal can be accomplished by one of the following three methods:

- Atmospheric reentry,
- Maneuvering to a storage orbit, or
- Direct retrieval.

Atmospheric re-entry is in general a viable option for debris that orbit in LEO, where the effects of atmospheric drag are stronger. Manoeuvering to a storage orbit is in general applied to objects with a perigee altitude above 2000 km; it should be selected a storage orbit with a perigee altitude above 2500 km and an apogee altitude lower belowe 35288 km, that is the altitudeof GEO, or an orbit with a perigee altitude above the GEO altitude by a distance of at least 300 km above or below GEO. A scheme of the possible storage orbital regions is shown in Figure 1.11. The direct retrieval was considered an hipotheticl solution that would have not generally been adopted due to logistical constraints, cost, and crew safety. It has to be highlighted that the greater part of the measures suggested refer to missions that had been going to be developed after the realization of such document; they didn't refer directly to objects sent

in orbit in previous epochs. This aspect has particularly changed in the last few years. Some studies revealed that the adoption of the mitigation measures only is not enough to preserve the safety of the space environment and missions of active debris removal (ADR) are extremely important for the future space activities. The development of complementary technologies is required to adapt such measures to old debris and allow their retrieval through ADR missions. In any case, ADR missions should be planned considering the International Guidelines (IG) defined in the document.

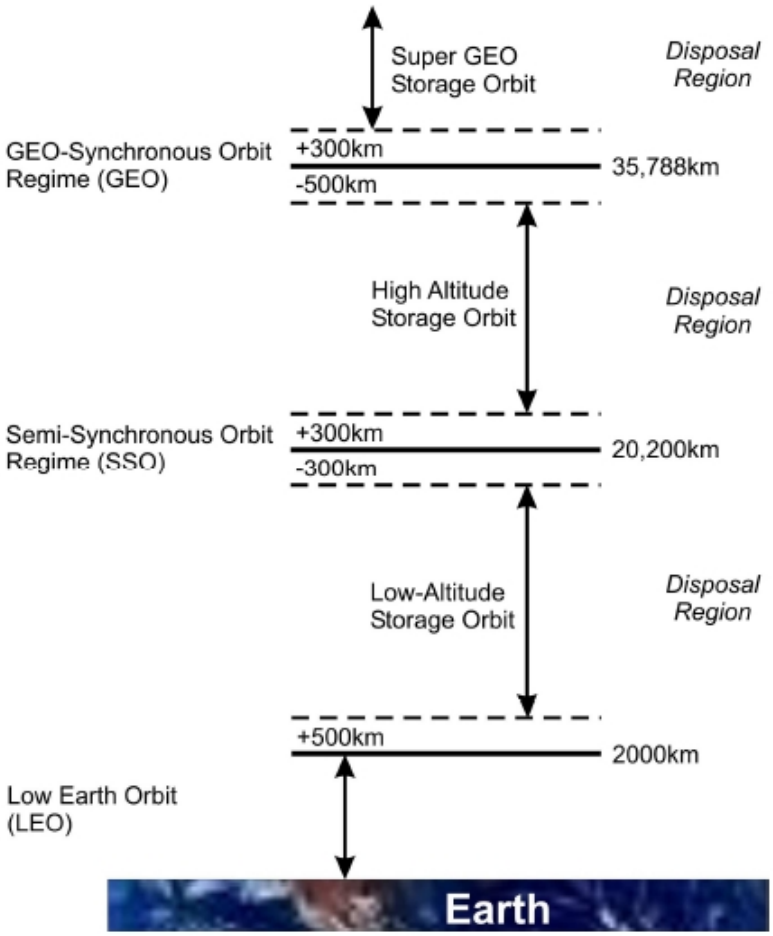

Figure 1.11: Disposal regions and storage orbit options for post-mission disposal (NASA 1995) [10]

In the present work, the atmospheric re-entry options and direct retrieval, and the correlated requirements have been considered for the implementation of the ADR scenarios analysis. The most relevant conditions that were assumed for our analysis are sumarised below, as they are written in the NASA-STD 8719.14 [26].

Requirement 4.6-1. Disposal for space structures in or passing through LEO

" A spacecraft or orbital stage with a perigee altitude below 2,000 km shall be disposed of by one of the following three methods (Requirement 56557):

a Atmospheric reentry option:

- Leave the space structure in an orbit in which natural forces will lead to atmospheric reentry within 25 years after the completion of mission but no more than 30 years after launch. If drag enhancement devices are to be used to reduce the orbit lifetime, it should be demonstrated that such devices will significantly reduce the area-time product of the system or will not cause spacecraft or large debris to fragment if a collision occurs while the system is decaying from orbit.

- Maneuver the space structure into a controlled de-orbit trajectory as soon as practical after completion of mission.

b Storage orbit option: Maneuver the space structure into an orbit with perigee altitude greater than 2000 km and apogee less than GEO - 500 km;

c Direct retrieval: Retrieve the space structure and remove it from orbit within 10 years after completion of mission.

Rationale for the aformentioned requirement

a The intent of Requirement 4.6-1a is to remove spacecraft and orbital stages in LEO from the environment in a reasonable period of time. The 25-year removal time from LEO limits the growth of the debris environment over the next 100 years, while limiting the cost burden to LEO programs. The 30-year limit recognizes a mean mission lifetime in LEO of five years. Missions with longer anticipated durations should plan on using disposal orbit lifetimes of less than 25 years. Spacecraft and orbital stages in mission orbits with mean altitudes below 600 km will usually have orbital lifetimes less than 25 years and will likely, therefore, automatically satisfy this requirement. This requirement will have the greatest impact on programs with mission orbit perigee altitudes above 700 km, where objects can remain in orbit for hundreds of years if abandoned at EOM (End Of Mission).

b The 25-year criterion of Requirement 4.6-1a is a maximum value, and, if possible, spacecraft and orbital stages use all available capabilities to minimize the time spent in LEO disposal orbits. For example, orbital stages have often used residual propellants to reduce orbital lifetimes to very short periods, only months or a few years.

c ...

d If disposal by controlled reentry into the atmosphere is chosen, the trajectory must be designed to ensure that the space structure does not skip in the upper regions of the atmosphere. Therefore, the effective perigee of the reentry trajectory should be no higher than 50 km.

e In Requirement 4.6-1c only 10 years is allowed for planned retrieval after completion of the mission, which is shorter than the 25 years for orbital decay and atmospheric reentry in Requirement 4.6-1a. Retrieval may leave the space system in a higher altitude orbit where, in general, there is a higher probability per unit time that the system will be involved in a collision fragmentation, whereas transfer to an orbit with reduced lifetime lowers the perigee of the final orbit and reduces the probability per unit time that the system will be a source of collision fragments. To balance the risk of the system creating collision debris, the allowed period of time is therefore less for a system waiting to be retrieved.

f ... ”

Some *Methods to Assess Compliance* in particular refer to the necessity to evaluate the collission risks probability and the exhecution of controlled re-entry maneouvres when drag augmentation devices are employed:

- ” Drag augmentation devices, such as inflatable balloons, increase the area-to-mass ratio of a space structure and, consequently, reduce its orbital lifetime. However, the use of such a device results in a larger collision cross-section, thereby increasing the probability of a collision during natural orbital decay. The increased collision probability should be documented in the ODAR/EOMP. This assessment needs to include the probable consequence of a hypervelocity impact between a resident space object, operational or non-operational, and the drag augmentation device.

- Space structures using atmospheric drag and reentry for postmission disposal need to be evaluated for survival of structural fragments to the surface of the Earth. ”

1.3.2 Survival of Debris From Earth Atmospheric Reentry

" This section is dedicated to measures relative to the controlled or uncontrolled re-entry of space structures. The following considerations take into account the possibility that fragments survived to the impact with the atmosphere and set some requirements to consider in the design of the controlled re-entry orbit. These requirements should be applied to all spacecraft and launch vehicles returning to the surface of the Earth from an altitude of greater than 100 km. The potential for human casualty is assumed for any object with an impacting kinetic energy in excess of 15 J.

a Performing a controlled reentry. Maneuver the structure at EOM to a reentry trajectory with an effective perigee altitude no higher than 50 km to control the location of the reentry and ground impact points.

b Using materials that are less likely to survive reentry, which is also known as design to demise. Thermophysical and physical material properties of the space structure components, such as thermal conductivity, specific heat capacity, heat of fusion, melt temperature, heat of ablation, and density, have a significant effect on reentry survivability. In general, materials with high melting temperatures, such as titanium, beryllium, and stainless steel, are more likely to survive than materials with low melting temperatures like aluminum. However, the configuration of the component is also very important.

c Causing a structure to break up immediately prior to reentry. If the components of a space structure can be exposed individually to the environment prior to structural breakup altitude at about 80 km, then additional heating will take place, facilitating component demise. In the extreme, a deliberate detonation of the space structure (see Section 4.4) before normal breakup would not only expose the components sooner, but also create a large number of smaller debris more susceptible to demise. Such a breakup would normally take place at an altitude below 120 km, which would prevent any debris from remaining in orbit. "

1.4 Active Debris Removal to preserve the space environment

Although the international agreement and the adoption of mitigation measures after 1996, debris created with past space missions has begun to represent a threat for the future space environment. In 1990 Donald Kessler already predicted a worrisome situation anticipating the effects of the Kessler Syndrome [7]; unfortunately, the mitigation measures formulated and adopted later had not solved the problem completely and some more recent studies, started around 2005, have demonstrated that, even though no further space launches will be conducted, the debris population would remain relatively stable only for the next 20-30 years. Beyond that, collisional cascade events between objects already in orbit will cause a rapidly increase of debris, generating the self-sustained phenomenon anticipated by Kessler and preventing any other space activity. Debris population would be destined to increase, as shown in Figure 1.12, without any possibility of control [11] [12] [13] [28].

Since the problem is mainly related to objects already in orbit, the shared point of view is that the situation could get better if, in parallel to mitigation measures, direct retrievals of space debris will be implemented to reduce the number of debris currently in orbit [11] [13] [12] [28]. These missions are well-known as Active Debris Removal (ADR) missions. Their effectiveness have been investigated by several researchers, focusing mainly to LEO regions which represent the most crowded orbits and where a rapid intervention is more needed. Simulations were performed considering business-as-usual scenario (BAU), where launches and explosions reflects the traffic model of the last 8 years without any mitigation measure, and scenarios where ADR measures were implemented [11] [12] [22] [28]. The analysis revealed a fast non-linear increase in the next 200 years in the BAU scenario, while in cases where ADR was simulated, the growth of debris population was checked, demonstrating the effectiveness of removal measures. As it can be observed in Figure 1.14, a removal rate of at least five debris per year is required to make ADR really effective. Lower removal rates would not be sufficient to stabilize the population growth in longterm. Also the starting epoch of ADR plays a relevant role [12] [27]: as it can be observed from Figure 1.13, ADR missions implemented from 2060 appear to be less efficient than mission begun in 2020. If ADR is delayed too much in future, the space environment could progressively worsen instead of taking benefits from its implementation.

All these aspects underline the urgency to implement such kind of missions, but there are still several challenges and limitations to be faced in order to perform ADR on orbit.

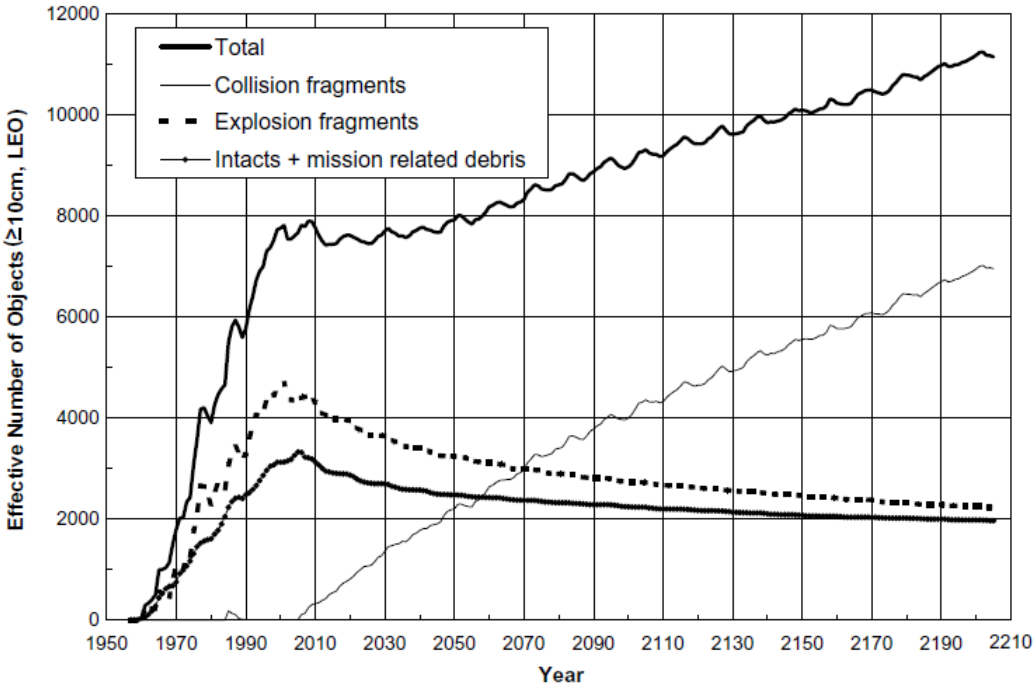

Figure 1.12: Effective number of LEO objects, 10 cm and larger, from the LEGEND simulations based on the *no new launches* assumption. The plot is taken from REF, where Monte Carlo runs were performed to simulate the future projection parts of the curves (years 20062205). It is evident that the increase in the total number of objects would be mainly caused by the increase due to collisional events between objects already in orbit (*intacts are rocket bodies and spacecraft that have not experienced breakups* [28].

1.4.1 ADR: enabling technologies and challenges

ADR missions represent a new kind of missions that has never been implemented in orbit yet. Up to now, the main objectives of launching in space were for scientific, commercial or even military purpose (universe investigation, telecommunication, Earth studies, phenomenon mapping as gravity gradient or Earth magnetic field, surveillance,); on the contrary, ADR aims to remove objects from orbit, since they do not have any functional capability and they are not going to re-enter. The effectiveness of implementing ADR has been demonstrated, but there are numerous aspects that have to be solved in order to make it feasible in the near future. On one hand new mission studies and analysis are required to identify the most efficient scenarios according to the characteristics of the targets to be removed: proper mission scenarios should be further investigated to determine the most efficient ways to intervene in orbit as regards both the orbital transfers to reach each debris and the de-orbiting phase itself. In particular, as regards the de-orbiting, several solutions have been proposed so far: drag sails or faoms, to increase the effect of atmospheric drag, propulsive devices such as chemical rockets or even electrical, tethered systems, in particular electrodynamic tethers that take advantage from the interation with the Earth's magnetic field, ion beams, and some others. Although some of these technologies have already been space qualified, such as propulsion, the others are still under investigation. The effectiveness of the ADR missions depends mainly on which one of these technologies is employed. On the other hand, there are several technological issues that are particularly critical, espacially as regards the capture of un-cooperative and not-specially-prepared objects, like space debris. The main problem with such kind of objects is that they are out of any kind of control and they do not have any suitable feature that could act as anchor point to allow a solid grasp during a capture manoeuvre. These aspects involve several critical issues in different fields: improvements are required for the relative navigation in the approaching phase, vision based systems capable to determine the status of the debris (intact, damaged) and to identify proper anchor points, attitude control devices capable to control each phase of the manoeuvre (contact phase, post capture phase), capture devices, which represent maybe the most critical issue. The

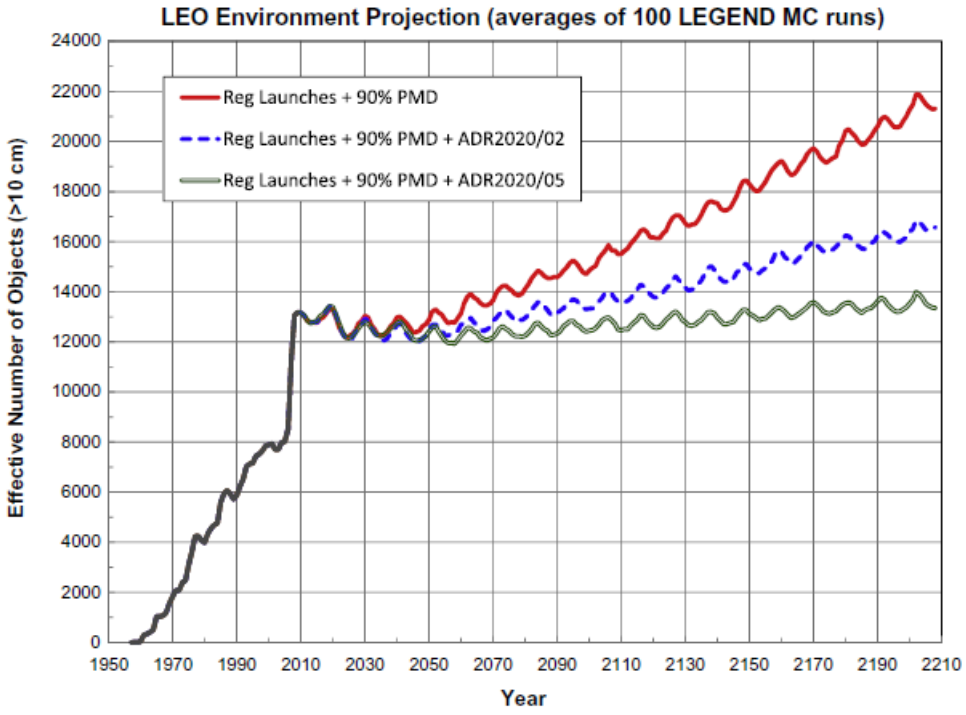

Figure 1.13: Simulated LEO population growth as a function of time and removal rates. 90% PMD indicates common adopted postmission disposal (PMD) measures with 90% success rate (red line). ADR2020/02 means active debris removal starts from the year 2020 and the removal rate is two objects per year. ADR2020/05 means active debris removal starts from the year 2020 and the removal rate is five objects per year ([12]).

most critical issues concern the capability to capture or create a solid conection with objects of unknown shapes and external features, the dynamic control of objects with unknown motion during the capture phase and the stabilization of the coupled motion once the object has been captured, all aspects that are typical in the capture of space debris.

1.5 Thesis objectives and outline

The present thesis is focused on two main aspect of the ADR:

- analysis of possible innovative ADR mission scenarios;
- analysis and development of a capture interface to be employed in an end-effector of a robotic device to allow the capture of un-cooperative objects.

The innovative idea proposed for the mission analysis is the employment of modular de-orbiting kits. It was observed that the debris population is extremely heterogenous, in terms of mass and orbital altitude, and proper removal vehicles could be required according to these parameters. The modular architecture makes possible to build different de-orbiting kits by simply assembling a certain number of base units, previously sized, each one dedicated to a specific operation. The number of units depends on the de-orbiting technology selected to accomplish the ADR mission, as well as the the characteristics of the debris (mass and initial orbit). In this way, each de-orbiting kit is tailored to each target debris, and it is possible to change the de-orbiting perfomances varying the number and the type of assembled units, with also the possibility of hybrid solutions. As basic units, the microsatellite class appeared to be an effective option: microsatellites have become increasingly popular in recent years as they offer signicant cost savings and are generally more affordable for a large variety of commercial applications, allowing to increase the mission efficiency respect to previous monolithic concepts. All these aspects seem to be

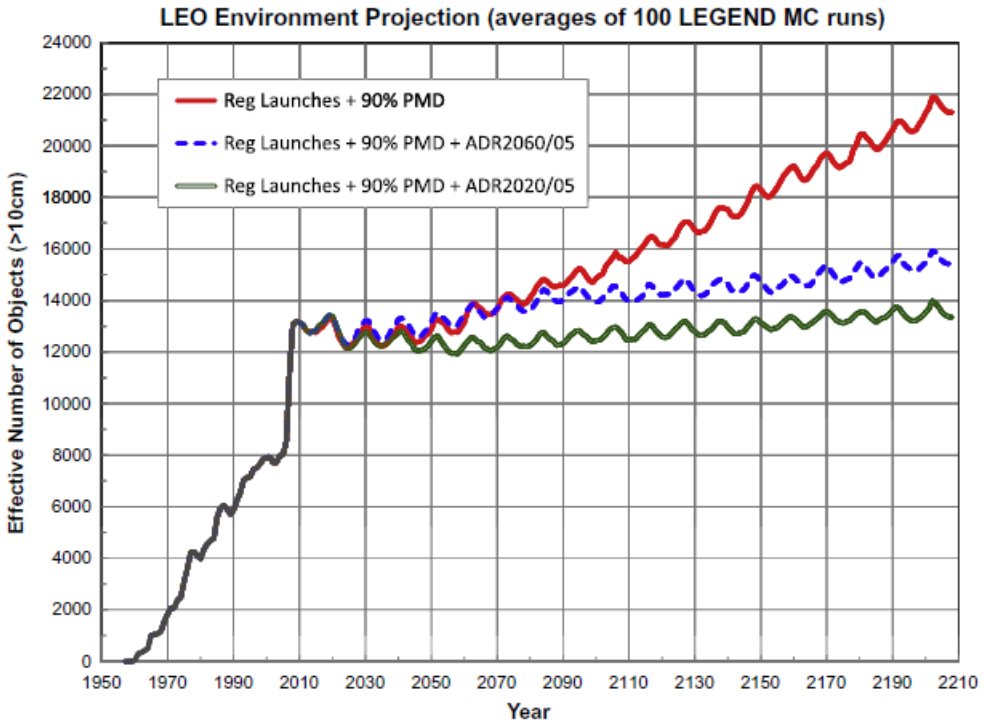

Figure 1.14: Simulated LEO population growth as a function of time and starting epoch. 90% PMD indicates common adopted postmission disposal (PMD) measures with 90% success rate. Two different strating epoch are considered ADR2020/05 and ADR2060/05, both with a removal rate of five debris per year. ([12]).

advnatageous for ADR mssions. With this approach, orbital transfers and de-orbiting operations can be accomplished independently by separated vehicles, increasing the mission efficiency, reliability and flexibility. The vehicle dedicated to the orbital transfers is not affected by the debris mass, allowing significant mass savings for its sizing. Moreover, optimizing the sequence of multiple transfers, i.e. minimizing the ΔV budget required to remove a certain number of debris per mission, it is possible to optimize the total mass of the propulsive system of the transfer vehicle. In this work, three de-orbiting solutions were chosen for the analysis: drag sails, propulsion and electrodynamic tethers. Two kinds of propulsive options were implemented: electric propulsion and hybrid propulsion. Proper base units were sized according to each one of the technologies selected. Then, three different ADR scenarios were considered to determine the most suitable de-orbiting solution, in terms of de-orbiting kit mass and total de-orbiting time, according to the debris orbit and mass:

- the first one focused on the preliminary analysis of the modular architecture, through the comparison of two de-orbiting solutions, drag sails and electric propulsion;
- the second one was split in two aspect: the first one was the comparison between electric propulsion and the electrodynamic tether, and the optimization of a multiple transfers manoeuvre, accomplished to bring each de-orbiting kit to the correspondent selected debris. The debris selected for this analysis belonged to the same orbital region;
- the third analysis focused on the perfomances comparison of electric propulsion, hybrid propulsion and electrodynaimc tether, considering all the critical orbital bands where ADR is more urgent.

The second part of the activity focused on the study and development of a capture interface where morphing and adhesive capablities are combined in a single smart system. This work answered to the need of proper capture devices that could allow to adhere to a wide variety of surfaces and objects, regardless their shapes, external features, surface irregularities and materials. Two main technologies were

selected for this study: the adhesion was make possible thanks to the generation of electrostatic forces between the developed interface and the object's surface; the basic principle is called *electro-adhesion*. The morphing behaviour was allowed thanks to a particular class of polymeric materials, belonging to the thermoplastic class, known as *shape memory polymer*. They are materials characterised by a drastic change in their mechanical properties when subject to the effect of an external stimulus. This change in the mechanical properties allows an easier deformation of the material and the maintainance of the deformed shape under certain conditions, as well as to restore the orginal shape, under other conditions. This cycle will be better explained in Chapetr 4. In our case, the main mechanical property was the elastic modulus, and the external activator was heat. The innovative idea is the dual employment of the electric components in both a capacitive way, for the generation of the electrostatic forces needed for the electro-adhesion, and as resistors, to generate the electric power required to perform the shape memory cycle.

In sumary, the thesis is organized in the following sections:

- **Chapter 2: ADR multi-mission concept and modular removers architecture.**
  The chapter presents at the beginning a brief overview on the state of the art on the actual ADR mission concepts, highlighting their fields of application (i.e. type of debris and orbits) and the main limitations. The ADR multi-mission concept and the modular architecture implemented are then described. According to the de-orbiting technologies selected for the analysis, i.e. drag sails, propulsion (electric and hybrid) and electrodynamic tethers, the preliminary sizing of each unit is described in detail.
- **Chapter 3: Mission analysis and results.**
  In this chapter the analytical models developed and the procedures defined to determine the performances in each ADR scenario are described in details. For each de-orbiting solution, a proper analytical model was developed to determine the remover configuration, i.e. the number of units and the total remover mass, in function of the mass and the initial orbit of the debris. Other models were then developed for complementary manoeuvres and aspects, such as the controlled re-entry of space debris, the optimization of the multiple orbital transfers and the risks assessment evaluation. A section is also dedicated to the description of the orbital regions and the potential targets selected for the analysis. Three ADR scenario are then presented: this first one is based on the comparison between electric propulsion and drag sails. Three main manoeuvres are considered: I) de-orbiting through drag sails only, II) de-orbiting through electric propulsion only, and III) de-orbiting through a combined maneouvre with drag sails and electric propulsion. Some preliminary conclusions on the modular architecture approach can be also derived. In the second scenario, a specific orbital region, the SSO (Sun-Synchronous Orbits), is selected. Electric propulsion and electro-dynamic tethers are compared in terms of remover mass and de-orbiting time. A multiple transfers maneouvre analysis is also implemented to give an examle of optimization procedure to determine the mass of the propulsion system required for the transfer vehicle. The third scenario involves all the debris belonging to all the orbital bands identified. The comparison is made considering electric propulsion, electro-dynamic tethers and hybrid propulsion. For each scenario the results are then presented, as well as a risk assessment evaluation for the third scenario.
- **Chapter 4: Technological development: morphing adhesive capture interface.** This chapter is dedicated to the development of the capture interface. The main concept is presented, as well as a detailed description of the technologies employed and main working principles. Two prototypes were realised and are described. Finally, the test procedures and the results concerning the morphing and the adhesive capabilities obtained with these prototypes are presented. This part of the activity was performed thanks to a collaboration with the MENRVA Research Group at Simon Fraser University - Burnaby (Vancouver) where the PhD candidate spent 9 months.
- **Chapter 5: Conclusions and future work.**
  The main results of the PhD activity are presented in this last chapter, as well as future development that could improve the work presented in this thesis.

Chapter 2

ADR multi-mission concept and modular removers architecture

2.1 ADR: state of the art

In this section, some of the ADR concepts studied so far are presented to give a brief overview of the state of the art as regards ADR and to highlight in which aspects the concept proposed in this work is innovative compared to them. In general, two main post-mission disposal are considered: de-orbiting, active or passive, and re-orbiting. In a de-orbiting manoeuvre, the orbit of an object is lowered in order to accelerate natural re-entry, or induce controlled re-entry, and reduce the orbital lifetime; in case of re-orbiting, the targets are inserted into disposal orbits, most known as graveyards orbits (GYO), that are regions where spacecraft are intentionally placed at the end of their operational life, few hundred kilometers above, or sometimes below, the common operational orbits. In general de-orbiting manoeuvres are performed in LEO, where the re-entry of satellites and debris is facilitated by atmospheric drag. In GEO, because of high altitudes, re-entry is not an effective option and the general solution adopted is the re-orbiting in graveyard orbits, usually at $\pm$ 300 km respect GEO altitude. In geostationary orbits (GEO) the risk of collision is lower and impacts result to be less destructive because the satellites all move in the same direction and at similar speeds [29]. The space environment at these altitudes is more stable and the debris situation appears to be of at least two orders of magnitude less severe than in LEO; in any case, in a more far future, it will may be necessary to completely remove these spent satellites and upper stages also from GEO. In both cases, de-orbiting and re-orbiting, proper mission scenarios should be defined and analysed to determine the main driving parameters that affects mission efficiency and costs, and the technological developments or improvements required to make feaible such kind of missions. The present work focused mainly on LEO regions, so only de-orbiting scenarios were investigated.

An ADR mission is characterised by two man phases:

I orbital transfers, to rendezvous with target debris and perform capture operations;

II de-orbiting operations, to lower the debris orbit and allow its re-enter.

These two manoeuvres can be accomplished in different ways, from which several mission scenarios can be defined and analysed. From a literary research [30] [31] [32] [33] [34] it emerged that two main mission concepts prevail regarding ADR. We decided to define them as*single vehicle missions* and *multiple vehicles missions*. The distinction is based on the way wherein orbital transfers and de-orbiting operations are carried out. A *single vehicle mission* is characterisd by the employment of a single, large satellite, which is responsible of both orbital transfers and the real de-orbiting operations. On the contrary, in a *multiple vehicles scenario* orbital transfers and de-orbiting operations are independent and carried out by distinct vehicles: a large satellite accomplishes orbital manoeuvres to reach the target debris, while proper autonomous de-orbiting kits (DKs) are mounted on the debris or grasp it, if predisposed, and perform the de-orbiting operations. The DKs can be equipped with different de-orbiting devices, although in most of the concepts, they are auxiliary propulsion units. A schematic rapresentation of the ADR mission concepts is shown if Figure 2.1.

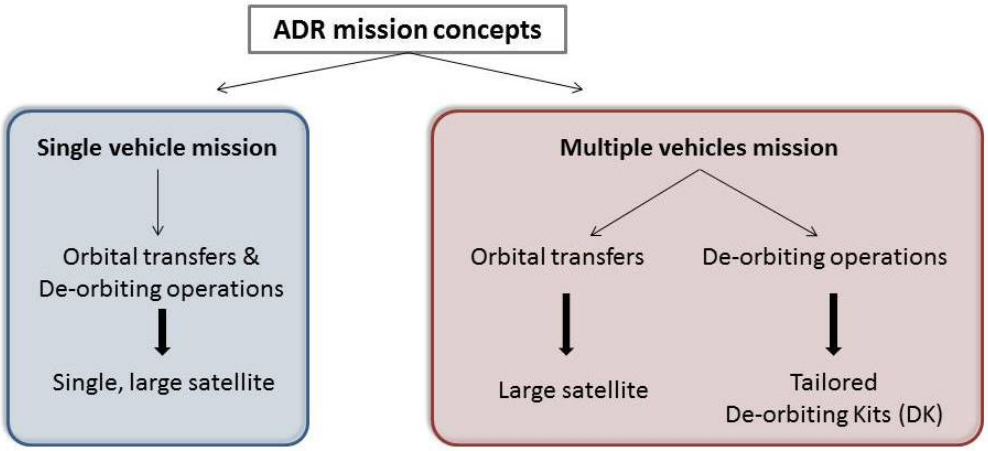

Figure 2.1: ADR mission concepts: (i) *single vehicle mission* (a single large satellite is responsible of both orbital transfers and de-orbiting manoeuvres); (ii) *multiple vehicles mission* (distinct vehicles are employed for orbital transfers and de-orbiting operations).

An example of single vehicle mission is represented by the ESA ROGER concept (RObotic GEostationary orbit Restorer): it consists of a single big satellite able to accomplish several removals in a single mission. Two competitive teams, ASTRIUM and QinetiQ Team, are working on two different configurations, where the differences are not only in the spacecraft, but mainly in the means used to capture the target satellite as well as in the de-orbiting technologies implemeted [35]. The configuration proposed by the QinetiQ Team is based on a spacecraft (1450 kg at launch) with a single capture mechanism constituted by a telescopic boom subsystem and a tentacles subsystem [35]. In this case, a vision based system is used to identify the best location of grabbing. After the capture of the debris, the satellite is expected to move towards the GYO where the debris is released. The vehicle then transfers to another orbit to accomplish the same operations with another debris. In ths case only one capture device is used. Four SPT electric thrusters are used for GTO GEO transfers and for re-orbiting, with a significant propellant gain due to the high specific impulse of this kind of thrusters. The consfiguration proposed by ASTRIUM is slightly different: it based on a single satellites with multiple de-orbiting devices. It is equipped with 20 throw-nets of 9 kg [36]; each net is supposed to enclose the debris and pull it in a graveyard orbit (GYO); the extending cable is then severed, leaving the debris in GYO. The satellite is expected to have a mass of 3500 kg. The propulsion system is sized in order to guarantee the required amount of propellant, about 2700 kg, for the orbital transfers to reach the debris [35]. Even though these concepts are mainly designed for re-orbiting operations in GEO, the same concept can be applied for LEO regions, with the difference that the debris orbit would be lowered to enhance the re-enter in the atmosphere. Propulsion and tethered systems represent two of the most common solutions usually proposed in several ADR mission concepts. While propulsion is an already space qualified technology, tether systems require further improvements to be employed in such kind of missions, although they represent a very promising propellantless solution for ADR.

Another example of a single vehicle scenario is proposed by Quinlan [34]. Chemical propulsion was chosen for both the orbital transfers and the de-orbiting operations, while the debris population considered for the analysis was limited to 91 debris, with masses in the range 1000 kg 3000 kg, in the inclination bands 70° - 75°, 80° - 85°, 95° - 100° and altitudes 700km - 850km, 950km - 1000km and 1450km - 1500km. The servicing satellite was supposed to remove five debris in one year, performing both the orbital transfers and the de-orbiting operations. Considering the sets of five debris in the entire population (91 debris) with the lowest δV, it resulted that for almost all of them the system mass, i.e. the mass of the servicing satellite for each set of five debris, was below 1000 kg, well within the mass limitations of conventional launch systems. Several aspects that could significantly affect the design of the satellite were not considered in this paper: from the analysis conducted in the present thesis, it will be demonstrated that phasing and timing manoeuvres, not included in the paper, could have a high impact

on the period of the entire mission as well as on the propellant mass budget when too long phasing period could be required and active orbital manoeuvres are needed to ensure the removal of a set of debris within one year. Furthermore, the debris population is quite limited, only 91 debris in a small mass range, while it will be showed how the effective debris population is much larger and then, more massive systems could be required.

An example of *multiple vehicles mission* analysis was proposed by Castronuovo [33]. In the scenario presented in the paper, a serving vehicle is supposed to accomplish orbital transfers, while proper de-orbiting kits are mounted on the target debris through a robotic arm. In the paper, the debris population is limited to the objects in SSO that are upper stages with masses between 65kg and 3800 kg. The objective of the analysis was the minimization of the δV required to accomplish five orbital transfers in each single mission, determining the optimal combination of semimajor axis, inclination and RAAN during the transfer manoeuvre. A solid state propellant (chemical propulsion) was selected to provide the required Δv to lower the perigee of the target debris. The propellant mass was then estimated for each object selected. The final results were that with a platform of a wet mass of 2000 kg and a dry mass of 600 kg, 35 R/B could be de-orbited in SSO within 7 years, with 8 refuelling operations.

As it emerges from the mission concepts described, most of the works considered only how the de-orbiting operations are performed, but no specific designs of the de-orbiting kits were presented. Furthermore, the debris population is often limited to a small range of debris, for which the solutions proposed appear to be more efficient and feasible.
In the present work a *multiple vehicles mission* was selected. An innovative solution related to the de-orbiting kits is proposed, as well as a more precise sizing of possibile de-orbiting units. Further improvements are also developed concernong the orbital transfers. The analysis is conducted considering the entire debris population, that is characterised by a wide range of masses, from 800 kg to 11 tons, and orbital bands.

2.2 ADR multi-mission concept

The debris population is extremely heterogenous in terms of mass of the debris and orbital bands. This implies that for each object could be required a specific de-orbiting vehicle properly sized, depending on the de-orbiting solution adopted. This procedure could be quite complex considering the great number of debis and their distribution. The innovative idea introduced with the present work is the employemnt of modular structures as de-orbiting kits (DKs), where a certain number of microsatellite elementary units, equipped with specific de-orbiting devices, are assembled together according the characteristics of the debris to dispose. In this way, proper removal vehicles could be tailored for the entire population simply varying the number and/or type of assembled units. The second relevant aspect that characterised the ADR analysis perfomed in the present thesis is the tasks separation between orbital transfers and de-orbiting operations. A servicing vehicle, indicated as *space tug*, is responsible of the orbital transfers, while the de-orbiting kits perform the de-orbiting operations.

Several advatages are expected related to the adoption of the *multiple vehicles* approach and the modular architecture for the DKs:

- **High fault tolerance and mission reliability**
  the failure of one DK does not compromise the entire mission: other DKs are available for the other debris; a new DK could be sent in orbit later with other DKs. In a *single vehicle missions* the failure of the main spacecraft could determine the failure of the entire mission;
- **System flexibility**
  The removers modular architecture implies a high system flexibility, thanks to the possibility of tailoring each de-orbiting package according to the characteristics of the debris to deorbit;
- **System scalability**
  The modular architecture makes the concept scalable and adaptable both to large and small objects, varying the number and/or the size of each unit;

- **Mass and costs savings**
  Mass and costs savings can be foreseen, with respect to missions with a single, large spacecraft, since each modular system is properly sized depending on the associated debris, allowing to reduce the resources needed for the orbital transfers from one debris to the following, as well as those dedicated to the de-orbiting operations; furthermore, more removal units could be launched in orbit every year thanks to the reduced dimensions of each remover, considering also piggyback solutions, when available; finally the standardization of the modules employed to build the de-orbiting kits allows to apply economy of scale, increasing the economic benefits of the developed concept;

- **Optimization of the orbital manoeuvres**
  the separation between orbital transfers and de-orbiting manoeuvres allows to optimize independently both of them

- **System improvements**
  It was observed that over the last few years there has been an increasing trend to move the attention from monolithic large satellites to fragmented, modular structures composed by subunits, each one dedicated to specific functions (communication, propulsion, attitude control, power,), simplifying the maintenance of the satellites, improving the performances and extending the orbital lifespan.

Mission operations

The mission is considered to start with both the space tug and the DKs already in orbit and docked together. Assuming a removal trend of 5 objects per year, that is the minimum removal trend suggested by previous studies [11], it is supposed that five DKs are launched already assembled in a single large structure. The entire system is then transferred by the space tug to each selected debris, following an optimized path. At the end of each tranfer, the DK is detached from the structure. The execution of the capture operations was not considered in this part of the analysis. It was simply assumed that each DK was independent and able to capture and stabilise the debris to perform de-orbiting operations. An alternative way is proposed for example in [33], where the space tug capture and stabilise the debris through a robotic arm, and then attaches the DK on it. These operations do not affect the mission analysis, so no more investigations were performed on this aspect. Once the DK is released, the space tug transfers the remaining kits to the subsequent targets.

2.2.1 De-orbiting technologies

Three main de-orbiting technologies were selected for the mission analysis: drag sails, propulsion (electric and hybrid) and electrodynamic tethers. All these technologies are suitable to be carried onboard microsatellites thanks to their limited mass. According to each technology, a proper base unit was sized, considering the main components of each subsystem and limiting the entire unit mass to 100 kg, that is the typical size of microsatellites.
Several missions, already performed or under development, foresee the employment of drag sails, and the systems developed so far were considered as reference to estimate the mass of the drag sail microsatellite unit [37] [38]. Several micro-propulsion devices have been studied and developed in recent years for micro-satellites applications [39] [40] [41]. For this particular study, two types of propulsive solutions were adopted: electric propulsion and hybrid propulsion. Among all the possible thruster solutions available, electric propulsion appeared to be the most suitable to perform active debris removal through spacecraft belonging to microsatellite size [42]. An electric propulsive unit was sized considering two different thrusters available on the market and whose performances are known, the BUSEK-BHT-200 [43] [44] and the SNECMA PPS-1350 [45] [46] [47], that fit with the microsatellite size requirement, in order to give different alternatives according to the solutions currently available. Hybrid propulsion was employed to simulated the de-orbiting manoeuvre as well as a controlled re-entry manoeuvre. In this case, a proper thruster was developed in both cases; in particular, for the de-orbiting unit, an optimizing proceudre was developed to determine the optimum unit size to minimize the number of hybrid units, and hence the total mass, to be sent in orbit to remove the entire debris population. Finally, as regards

the electrodynamic tether, an already developed electro-dynamic tether unit was adopted, according to some previous studies [48].

2.2.2 Drag augmentation devices

Drag augmentation devices can be divided in inflatable devices, like balloons [49] [50] or inflated appendices [51], and non-iflatable devices, such as *drag sails*, that are supported by rigid structures. Examples of inflatable devices are shown in Figure 2.2, while typical drag sails are depicted in Figure 2.3.

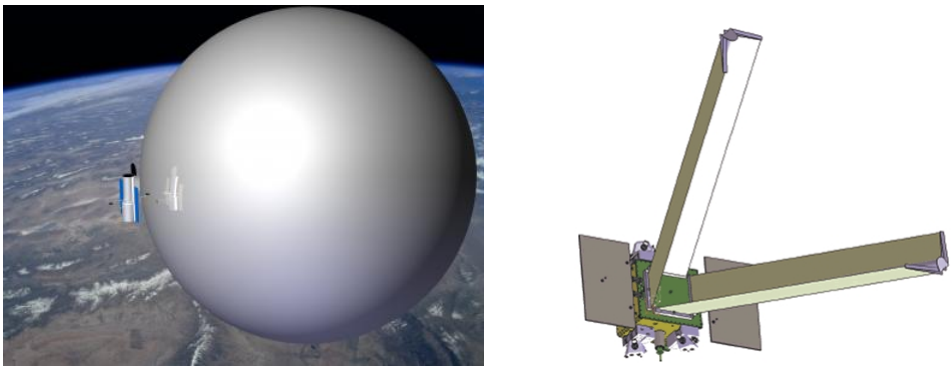

Figure 2.2: Examples of inflatable drag augmenation devices: GOLD - Gossamer Orbit Lowering Device [50] (on the left), and the inflatable structure mounted on board the French MICROSCOPE satellite [51] (on the right).

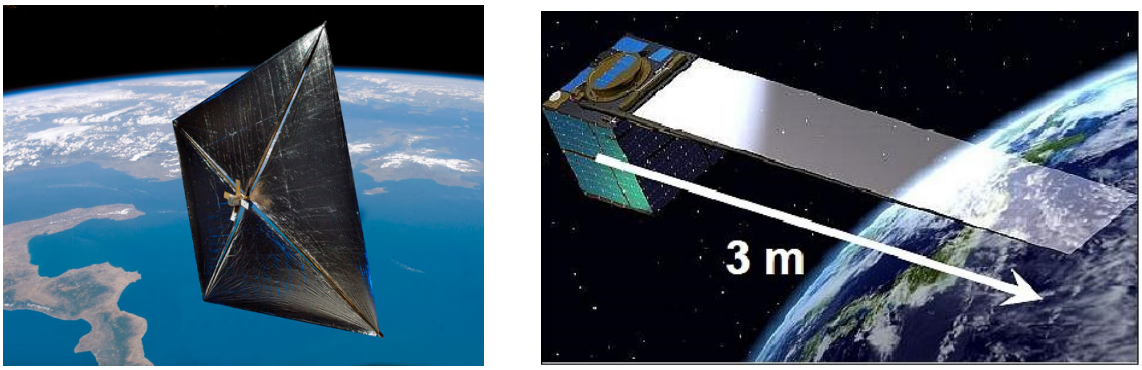

Figure 2.3: Examples of non-inflated drag augmentation devices: a typical drag sail, supported by four rigid booms aling the diagonals (on the left, artist's concept of NanoSail-D [52]); an appendage deployed from one side of the spacecraft (on the right, QSat-EOS post mission configuration with extended sail [53])

The main advantages of drag augmentation devices are the relative semplicity and the very low wheight, which make them particularly attractive for ADR. They are considered the principle mean of de-orbiting for small satellites, from 1 kg to few hundreds kilograms. An example is MICROSCOPE [51] (see Figure 2.2 on the right), a 120 kg satellite sent in a sunsynchronous polar orbit at 730 km altitude. Two 4.5 kg wings made of an aluminized Kapton membrane (100 g/m^2 density) will be deployed by a central inflatable mast at the end of its operational life, providing a total mean drag surface of only 6.3 m^2; the deorbit assembly is quite light, about 12 kg. As reference example, a 0.15 m^2 area enables a 1-unit CubeSat to be de-orbited within 25 years from a maximum altitude of 910 km [38]. The main drawback is that the effectiveness of such devices significantly decreases as the altitude and the mass of the object increases: in comparison with the previous example, a drag sail of about 20 m^2 should be required to de-orbit a satellite belonging to the microsatellite class (100 kg) from the same altitude of 910 km, while the size increases to 42 m^2 (almost double) if the altitude is risen to 1000 km. The greater part of the debris, selected as primary targets for ADR, orbits at altitudes between 800 km and

1000 km, and has masses between 1000 kg and 11000 kg. The estimated area of a drag augmentation device required to help the natural decay within 25 years, as indicated by International Guidelines, could become incredibly high for these objects, even of the order of some hundreds square meters. The drag force, which acts on the de-orbiting object, is determined by the atmospheric density. The atmospheric density is not constant and depends on several parameters. It decreases with the orbital altitude and it is deeply influenced by the solar flux and the geomagnetic activity. A typical reference model, that allows to calculate the drag force with a good approximations, is the exponential model. The variation of the density with the altitude is depicted in Figure 2.4, from 600 km to 1000 km.

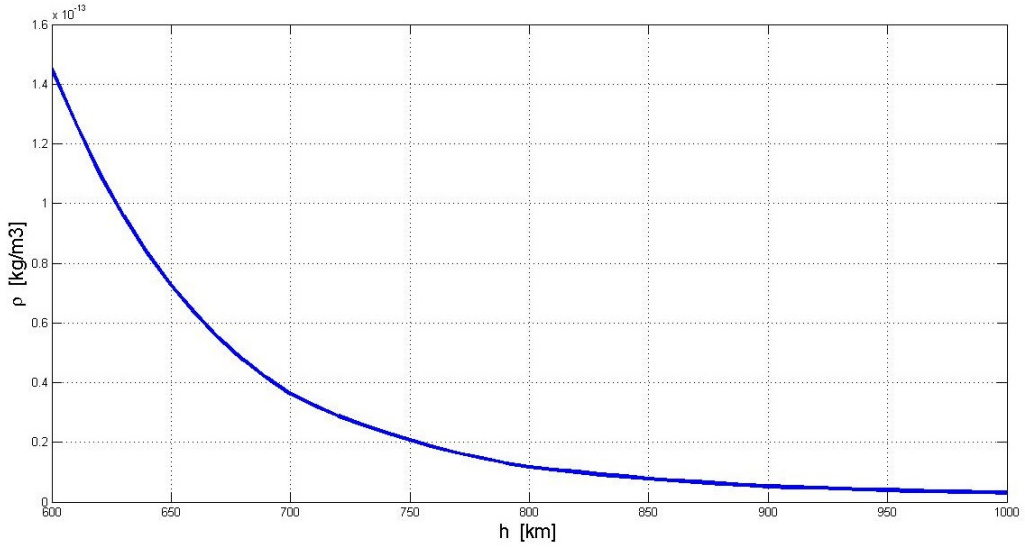

Figure 2.4: Density variation, in kg/m^3, between an altitude of 600 km and 1000 km, estimated through the exponential model described in section 3.2.1.

As it can be seen, the density drops down quite fastly with the altitude, and, as consequence, the drag force. It was estimated, through the developed model in section 3.2.1, that for debris with mass in the range [1000 - 10000] kg the drag area required to de-orbit from 800 km to 250 km lies in the range [61 - 610] m^2; simply increasing the altitude at 900 kg, for the same masses, the area results between [180 - 1800] m^2 while it becomes [415 - 4150] m^2 from 1000 km. Drag sails of such dimensions could present several problems, from the structural point of view as well as the high collission risks due to the resulting large cross sectional area.

No on-orbit demonstrations of the deployment of drag augmentation devices have been performed so far, although several missions, especially those where cubesats are employed, foresee the employment of drag sails as de-orbiting devices at the end of the operational life [37] [38] [51]. An on-ground deployment test of a 20x20 m^2 square sail was already performed at the German Aerospace Centre(DLR) in 1999 [54], but no on-orbit tests were performed.

2.2.3 Propulsion

Propulsion rapresents, at the moment, the most space qualified technology, among all the solutions proposed, that could be immediately employed for ADR. Several propulsion systems are available for end-of-life de-orbiting [55], such as cold gas, solid, monopropellant and bipropellant liquid, hybrid propulsion, various electric thrusters such as ion, hall, and field emission electric, and pulsed plasma thrusters, each one with proper pro and cons, as summarised in Figure 2.5

Chemical propulsion is the most used propulsion solution employed in space missions. It represents a very competitive option to be adopted for de-orbiting in future missions: both spacecraft and rocket stages are always equipped with chemical propulsion systems onboard, and only an additional propellant mass could be required to de-orbit at the end of operations, without increasing the dry mass of the system. Another advantage of chemical propulsion is the very low transfer time that reduce significantly the risk

	Advantages	Disadvantages
Cold Gas	• Simple • Low system cost • Reliable • Safe	• Extremely low Isp • Moderate impulse capability • Low density • High pressure
Mono Propellant	• Wide thrust range • Modulable • Proven	• Low Isp • (mostly) toxic fuels
Bi-Propellant (storable)	• Wide thrust range • Modulable • Proven	• Complex • Costly • Heavy • Toxic
Solid Propulsion	• Simple • Reliable • Low cost • High density • Low structural index	• One thruster per burn • Total Impulse fix • Currently not qualified for long-term space application
Hybrid Propulsion	• Simple • Modulable • Low cost • Reliable	• Not qualified • Lack of suitable oxidizer for long-term mission
Electrical Propulsion	• Very high Isp	• Low thrust • Complex • Long maneuver time • Power consumption

Figure 2.5: Thrusters characterisitcs [55]

of collision during the de-orbiting manoeuvre. The main drawback of chemical propulsion is due to the lowest specific impulse that characterises such systems. This implies the need of high propellant mass to transfer massive debris to lower orbits. For future space missions this means that satellites should store onboard, for the entire mission duration, significant additional mass of propellant that will be used only at the end of the operational life. Analogous conclusions can be derived in case of de-orbiting the present space debris. Very massive propulsion units could be required to de-orbit debris from the most critical altitudes; just to give an idea, taking as reference example a liquid bipropellant N2O2/MMH, with Isp and inert-mass-fraction respectively 300 s and 0.17 (from historical data [56] [57]), 102 kg of propellant mass and a total system mass of 131 kg would be required to de-orbit a 1000 kg debris from 800 km to 250 km (controlled re-entry not included). For more massive debris at higher altitudes, the mass of the propulsion devices would be even higher.
Good competitors to classic solid propulsion systems could be electric thrusters and hybrid rockets.

Electric propulsion

Electric propulsion is now a mature and widely used technology on spacecraft. Russian satellites have used electric propulsion for decades. As of 2013, over 200 spacecraft operated around the world use electric propulsion for stationkeeping, orbit raising, or primary propulsion [58]. Electric propulsion offers several advantages. The first one is the high specific impulses achievable with such technology, that are around 1000 - 3000 s [56] [57], one order of magnitude greater than chemical rockets. This implies lower propellant mass to produce the same overall effect, i.e. a particular increase in spacecraft velocity. Electric thrusters also give the ability to regulate the force applied to the spacecraft very accurately, making it possible to control the spacecrafts position and orientation along its orbit with incomparable precision. From the safety point of view, electric thrusters appear to be less dangerous than chemical

rockets: the propellants used are not higly inflamable like in chemical rockets and the risk of accidental, catastrophic explosions is much lower [59]. One of the main drawbacks is that the mass flows are very low, and hence only small thrust forces can be provided, resulting in longer maneouvre time. Electric thruster are, anyway, able to operate continously for ver long periods, months or even years, rapresenting the most suitable solution for interplanetary missions where the target can sometimes be reached more quickly than with chemical propulsion [59]. Electric thruster require proper power systems to provide the power needed for their functioning. The main power source employed are solar panels, although some other power sources, more efficient, could be considered, such as nuclear generators. This aspect is another drawback of such technology, since the inert mass could become a significant amount of the entire mass budget. Today, the main applications of electric propulsion are on geostationary telecommunication satellites, such as the ESA's ARTEMIS, where electric thrusters are used both to transfer the satellite from its initial transfer orbit to the nominal one around the Earth and for attitude control during the operational lifetime (10-15 years), by compensating for the gravitational perturbations induced by the Earth, the Moon and the Sun. The use of electric propulsion on a modern telecommunications satellite easily provides a saving of more than 20% in the initial launch mass [59]. Electric propulsion is used as primary source of thrust in two famous ESA's missions: SMART-1 and Bepi-Colombo, to the Moon and the planet Mercury, respectively. SMART-1 employs the SNECMA PPS-1350 electric thruster, with a specific impulse of 1600 s and capable of 99 mN thrust. The electric propulsion subsystem has a weight of 29 kg with a peak power consumption of 1200W [59].

However, it is not so easy to reduce the size of such systems, maintaining the same performances of bigger devices, since the dimension of the components influence the overall performances. In Figure 2.6 the main electric systems developed and the correspondents performances are reported. Micro-electric thrusters appears to be a promising solution for ADR, thanks to the propellant mass savings due to the high specific impulse that allow to size more compact propulsion systems. Even though an increase in the total mass is determined by the power plant, the propellant savings, with respect to chemical propulsion, for the same mission parameter are more advantageous and can justify the adoption of such technology. Among all the possible types of micro-electric thrusters, ion and plasma thruster appear to be the most suitable for ADR [42], where moderate ΔV are required to lower the orbits, because of the higher levels of thrust and specific impulse provided respect to other thrusters (see Figure 2.6) . More flexibility is also allowed, thanks to the possibility of employing arrays of thrusters that operate at the same time, increasing the total thrust achievable and reducing, in this way, the total de-orbiting time. Several electric propulsion devices have been scaled to be employed in microsatellites [39] [40] [41].

Type	Thrust Range (mN)	Specific Impulse (sec)	Thruster Efficiency[b] (%)	Thrust Duration	Typical Propellants	Kinetic Power per Unit Thrust (W/mN)
Resistojet (thermal)	200–300	200–350	65–90	Months	NH_3,N_2H_4,H_2	0.5–6
Arcjet (thermal)	200–1000	400–1000	30–50	Months	H_2,N_2,N_2H_4,NH_3	2–3
Ion engine	0.01–200	1500–5000	60–80	Months	Xe,Kr,Ar	10–70
Solid pulsed plasma (PPT)	0.05–10	600–2000	10	Years	Teflon	10–50
Magnetoplasma dynamic (MPD)	0.001–2000	2000–5000	30–50	Weeks	Ar,Xe,H_2,Li	100
Hall thruster	0.01–2000	1500–2000	30–50	Months	Xe,Ar	100
Monopropellant rocket[a]	30–100,000	200–250	87–97	Hours or minutes	N_2H_4	

Figure 2.6: Electric Thrusters Performances

Hybrid propulsion

The work presented in this thesis concerning hybrid propulsion was developed by Filippo Maggi (SPLAb, Politecnico of Milano); the treatise is taken from an internal report [60]. The results reported in the correspondent sections were used as input for the mission analysis that will be developed in Chapter 3. As reported by Maggi [60], among the possibilities offered by the chemical propulsion, hybrid rocket technology can represent a valuable option for several missions. Intrinsically safe with a negligible propellant TNT equivalence, claimed as a green propulsion solution, relatively cheap and simple solution from the construction point of view, hybrid propulsion can grant specific impulse which are comparable to storable liquids [61] [62] [63]. In general, selected additives can be introduced for the increment of specific impulse

or ballistic properties, producing specific effects also on other material properties [64] [65] [66] [67]. In common hybrid rockets, storable or cryogenic liquid oxidizer is injected in a combustion chamber, in contact with the fuel grain, where a turbulent and diffusive boundary layer combustion sets on. The simplest possible shape is represented by a center-perforated cylinder. In this case, the combustion takes place in the internal channel which changes its diameter in time. Multi-channel options are also possible. For small systems, blow-down pressurization and constant mass flow rate valve can be used producing a shift in the oxidizer-to-fuel ratio and a variation of the regression rate due to the change of fuel grain size [68] [69]. At the moment, no specific hybrid propulsion thrusters have been developed and tested for microsatelite applications. In this work, it is proposed a preliminary study of a possible system suitable for this kind of satellites.

2.2.4 Electrodynamic tethers

An electrodynamic tether is a system based on the interaction between a conductive wire and the Earth's magnetic field. The principle of *electrodynamic tether* is illustrated in Figure 2.7:

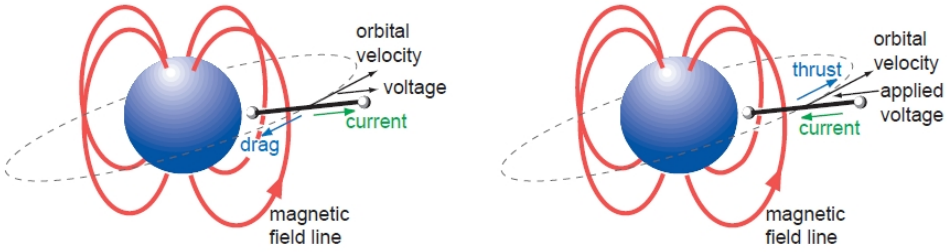

Figure 2.7: Working principle of Electrodynamic Tether [70]

A long tether of conducting wire is extended from a spacecraft and, under the influence of gravity gradient forces, the structure tends to orient itself along the local vertical direction. The orbital motion of the system across the geomagnetic field generates a voltage along the tether; a pair of plasma contactors are collocated at either ends of the tether for collecting and emitting electrons. The induced voltage produced drives current up the tether, closing the circuit via the ambient plasma. The interaction between the current and Earth's magnetic field generates a Lorentz force along the wire which could act as a drag force (Figure 2.7, on the left), opposite to flight direction, reducing the orbital lifetime by dissipating orbital energy, or as a thrust force that raises the orbit of the tether system (Figure 2.7, on the right), according with the voltage applied to the tether [70]. The efficiency of this technology decreases with $1/r^3$, where r is the radius of the orbit, and it is strictly related to the inclination of the orbit. The Japan Aerospace Exploration Agency (JAXA) has proposed an active debris removal system based on EDT technology [71] , named *Space Debris Micro-Remover (SDMR)*: it consists of a small spacecraft, capable of piggyback launch with other payloads, equipped with a release mechanism that ends with a robotic arm. A space debris, identified as target of the removal operation, is captured through this robotic arm and the EDT fixed at the base of the arm is extended, lowering the orbit of the object. The small satellite acts itself as the tip mass of the tether and de-orbits with the debris. A picture of the system is shown in figure 2.8.

According with the policy of mitigate the growth of space debris in future missions, also Tethers Unlimited, Inc has developed an EDT-based system for LEO satellite disposal [70]. This product, called *Terminator Tether* consist of a small, lightweight, low-cost device that will be attached to satellites and upper stages before launch. Deployed at the end of mission operations, the drag force generated along the tether, due to the interaction with geomagnetic filed, accelerate the natural re-entry of the object.
Electrodynamic tethers represent a promising, low-cost concept for satellite orbit rising, propellantless manoeuvres and end-of-life de-orbit for LEO satellites. One of the main issues concerning the employment of such technology is related to its vulnerability to the space environment: the risk of collisins, during the de-orbiting phase, could be very high, and the tether could be severly damaged, determining the failure of the mission. Further investigations are still required to implement this technology to ADR.

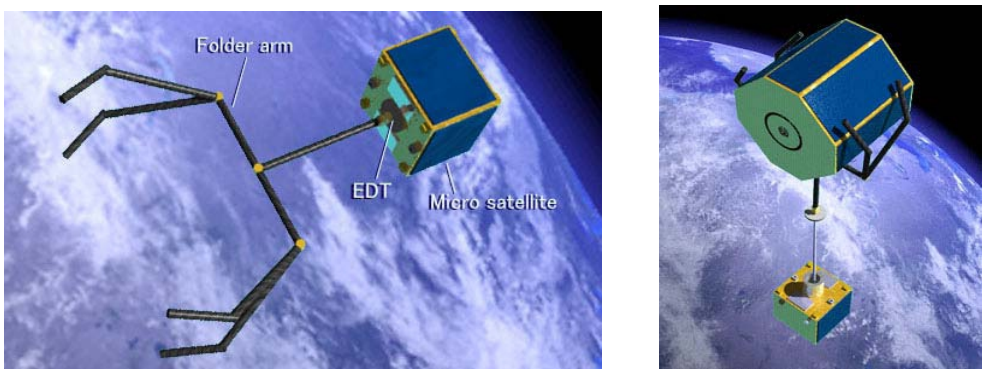

Figure 2.8: EDT system developed by JAXA [71]

2.3 Remover kits modular architecture

The innovative idea of the ADR mission analysis performed in this work is the employment of a modular architecture for the de-orbiting kits. Each remover is the result of the aggregation of a certain number of elementary microsatellite units. Each type of unit is fully autonomous in terms of power generation. Five main units were identified and designed, according to the de-orbiting technologies selected for our stidy. These units are: 1) a drag sail unit (DSU); 2) an electric propulsion unit (EPU); 3) two hybrid propulsion unit (HPU), one for a controlled re-entry and one for an entire de-orbiting manoeuvre; 4) an electrodynamic tether unit (EDTU); and finally 5) a main bus, with the main auxiliary subsystems (capture device, ADC, navigation, telecom, power, ...)

An example of the implemented modular architecture is shown in Figure 2.9

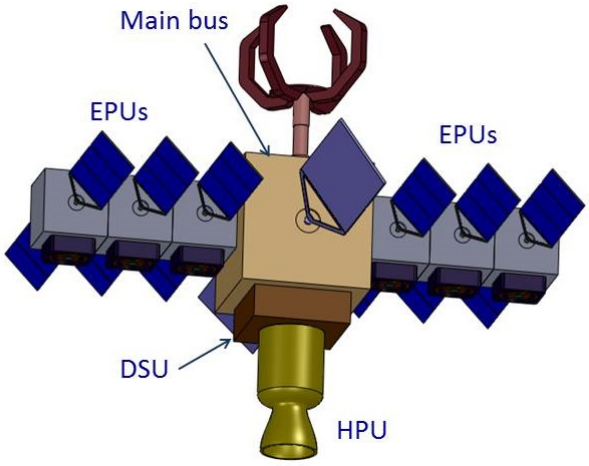

Figure 2.9: Example of the de-orbiting kit modular architecture

For each de-orbiting technology, a basic unit was identified; then, it was determined the number of units needed to de-orbit each debris with a specific technology, according to the object mass and initial altitude (altitude, inclination). Finally, the remover mass, the de-orbiting time and the total mass injected in orbit in each mission scenario considered were compared to determine the more effective way to accomplish an ADR mission. A maximum mass of each main unit was limited to ∼100kg, the typical size of a microsatellite. The sizing procedure for each unit is described in details in the next sections.

2.3.1 Drag sail unit sizing

The total mass of the drag sail unit (DSU) was estimated considering the contribution of five main elements: 1) the sail itself; 2) the booms that support the sail; 3) the canister that host the supporting

structures; 4) the case where the entire system is stowed (sail plus deployment devices); 5) safety margins for the structures and other miscellaneous. Modern sail designs make use of thin films of Mylar or Kapton, which are lightweight and space proven, coated with about 500 angstroms of aluminum. Their density is around 1400 kg/m^3. Kapton has a Young's modulus around 3 GPa and a tensile strength around 241 MPa [72]. Thin films are available (25.4 μm), with an areal density (defined as the total material mass divided by the material area) of about 11 g/m^2. These represent reasonable values according to the examples employed in real missions, and it was assumed for the preliminary sizing of the drag sail unit. Known the areal density of the sail ρ_s and its area A_s , the mass of the sail was determned as

$$m_{sail} = \rho_s A_s \tag{2.1}$$

Usually, the sail is supported by lightweight structures, like trusses or booms. For the sail design, a typical square geometry was chosen, with the supporting structure along the diagonals and connected in the middle. Among the most common configurations available, two were chosen in this design: the Collapsible Tube Mast (CTM) and the Coilable Mast (CM), resectively a boom and a truss structure [73] [74]. CTM is derived by the STEM configuration, and is constructed from two STEM-like elements with the free edges bonded together. The resulting double Ω section can then be flattened and wrapped around a spool in a similar manner to the STEM systems. Examples of such kind of deployable structures are represented in Figure 2.10.

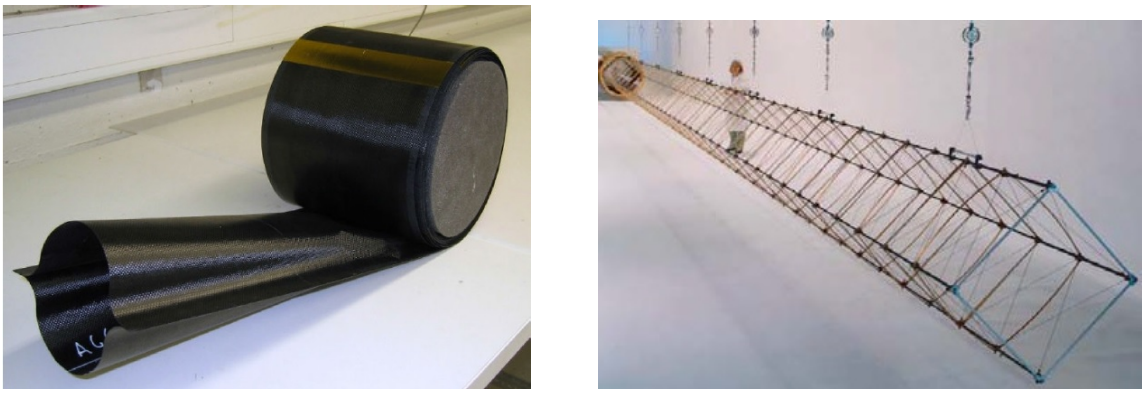

Figure 2.10: Example of CTM (*Collapsible Tube Mast*) boom (on the left), and CM (*Coilable Mast*) truss, (on the right) [74].

CTM are efficient in kind of storage volume, structural efficient thanks to their closed cross section that leads to higher strength and those made in CFRP are thermally neutral. It can be determined a linear density around 0.1 kg/m [75]. The Coilable Mast is a truss structure usually composed of three longerons braced by other members. By coiling the longerons the whole truss can be wound into a shortened package which typically measures around 2% of the deployed length [76]. The linear density is lower than the CTM structure, being around 0.05 kg/m. A typical example of this truss is shown in Figure 2.10 (on the right).

Both CTM and CM require casings over and above the quoted weights, but these casings can be made of very lightweight materials as they are only minimally structural. Considering four radial booms, the length of each boom can be reasonably estimated as:

$$l = \frac{\sqrt{(2)}}{2}\sqrt{A_s} \tag{2.2}$$

The total mass of the supporting structure is the product of this length and the linear density of CTM and CM. The mass of the canister that host the supporting structres, CTM or Coilable Mast, was estimated as 25% of the boom mass for CTMs and 33% of the truss mass for Coilable Mast. The case which accommodates both the booms and the sail is sized assuming a square based cuboid. The square platform is determined assuming that coilable booms can be contracted to 2% [76] of their deployed length at constant diameter, and that four spooled CTMs can be arranged into a square with an edge length equal to 4.5% of their deployed length (engineering assumptions). The height of the square based cuboid which accommodates the booms is assumed 1.5 time the diameter of the deployed structure.

Considering a sail storage volume five times the volume of the sail material V_s and the square base A_{base} is maintained, the height of the sail case is calculated as:

$$h_s = \frac{5V_s}{2}\sqrt{A_{base}} \tag{2.3}$$

The case is made of Kevlar epoxy, with a density of 1400 kg/m^3 and a thickness of 1 mm [33]. A mass penalty of 25% of the overall mass was assumed for the other systems (actuators, power, electronic,). A further margin of 10% was also considered. The mass of the drag device was then calculated as the mean value between the mass in case of CTM and the mass with CM, to consider an intermediate representative value for different supporting structure. In any case, the difference in mass due to the employment of different technologies for the supports do not have any significant influence on the de-orbiting performance of the drag device, being very light elements.
This preliminary design shows how drag sails could appear very attracting technologies to be employed in microsatellites units, being the mass of such vehicles limited to a maximum of 100 kg. In the further mission analysis, several drag sails were sized varying the area between 10 and 30 square metres. The mass in each case was determined with the procedure above.

2.3.2 Electric propulsion unit sizing

The total mass of the electric propulsive unit (EPU) was estimated as the sum of five main contributions: 1) the thruster mass, that is a constant value, provided by the supplier once the type of thruster has been chosen; 2) the mass of the power plant; 3) the mass of the tank where the propellant is stored 4) the propellant mass, estimated according to the debris mass and initial orbit; 5) a margin for the structures and devices needed for the thruster functioning (harness, valves, auxiliary components, ...). Solar panels and rechargable batteries were chosen as power source to supply the power needed to ensure the functioning of the thruster during the entire de-orbiting manoeuvre. The mass of the power plant, comprehensive of the solar panels, rechargeable batteries and harness, was determined according to the procedure reported in [57]. A GaAs triple junction technology was selected for the solar panels (efficiency 0.26 [77]); the inherent degradation was set at 0.77, the power loss due to time at 0.92, with swivelling panels the incident angle is always 0. As regards the batteries, Litio-ion type was selected, with specific energy density of 120 Wh/kg, depth of discharge (DOD) of 0.60 and one effective cell. The harness contribution was set at 15% of the total mass of the power plant, as suggested in [57]. The mass of the tank was estimated considering the formula reported in [57] for the thickness of a spherical tank:

$$t_{thick} = \frac{p * R_i}{\sigma_{adm}} * SF \tag{2.4}$$

where p is the storage pressure, set at 70 bar as typical storage pressure for Xenon in electric propulsive applications, R_i is the internal radius of the tank, σ_{adm} is the ultimate tensile strength, assumed 900 MPa for Ti6Al4V, the typical material used for tanks in space applications [57]. The propellant mass was estimated assuming a total mass of the EPU of 100 kg, that is the typical mass for microsatellites. The density was calculated according to the following equation:

$$\rho_{Xe} = \frac{p_{Xe}}{R_{Xe} * T_{Xe}} * Z \tag{2.5}$$

where p_{Xe} is the storage pressure (70 bar), T_{Xe} is the storage temperature (10°C) and Z = 0.21 is the compressibility factor used when real gases relations are required. Through a Matlab code, where all the mass contributions were taken into account, the maximum propellant mass allowed in each unit was estimated and used to calculate the correspondent total impulse to verify it was lower than the total impulse supplied by the thruster. The structures and miscellaneous were computed as 14% of the mass of the entire unit (design assumption). It was verified that for electric thrusters the inert to mass ratio results quite high compared to chemical propulsion : this is one of the disadvantages of the electric propulsion, where the inert mass has a dominant role due to the complexity of the systems required [56].

2.3.3 Hybrid propulsion unit sizing

Hybrid propulsion was selected for two different orbital manoeuvres: the controlled re-entry and the de-orbiting. Two hybrid units were then designed. On one hand, a specific hybrid rocket was sized for

the controlle re-entry. On the other hand, an optimization procedure was developed to determine the most efficient unit size to de-orbit the greater part of the entire debris population. All the information that are going to be presenetd in this section are taken from the Internal Report [60] by Filippo Maggi.

Hybrid unit for controlled re-entry

The controlled re-entry maneuver was supposed to be accomplished by one single firing. The entire maneouvre was supposed to be performed with a hybrid rocket engine whose propellant was characterised by a concentration of 85% of HTP (High Test Peroxide) and HTPB as solid fuel. HTP has the benefit of being a high density liquid (here assumed about 1.39 g/cm^3), advantageous for missions that require compact designs; there are still some open issues as regards the storability for long-term missions [56]. HTPB is a standard elastomer, commonly used in propulsion industry, whose typical density is about 0.92 g/cm^3. It was assumed a combution pressure of 10 bar and the specific impulse I_{sp} was evaluated for different expansion ratio of the nozzle between 40 and 100. Computations were performed with the NASA CEA software [78] and the results are plot in Figure 2.12.

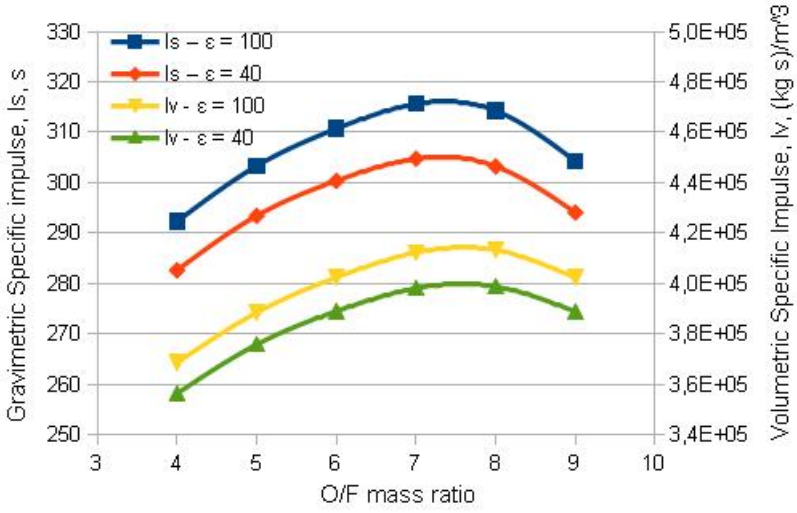

Figure 2.11: Specific impulse for a hybrid rocket composed by 85% HTP as oxidizer and HTPB as solid fuel, with 10 bar of combustion pressure and different expansion ratio ε.

The mass budget of the unit was computed, as usual in propulsion, through the Tsiolkovsky equation:

$$\Delta V = I_{sp} g_0 ln \frac{M_i}{M_f} \tag{2.6}$$

The propellant mass can be estimated from the final mass of the system at the end of the re-entry maneouvre (debris + chaser + rocket after burnout) as follows:

$$M_p = M_f (e^{\frac{\Delta V}{g_0 I_{sp}}} - 1) \tag{2.7}$$

The total mass of the unit for the controlled re-entry is plot, in Figure 4.1, in function of the total mass of the de-orbitied system. Figure **??** is in logarithmic scale, while Figure **??** is an enlargement of Figure **??** for system mass between 0 kg and 1000 kg. Inert masses represent a preliminary evaluation of fuel case, nozzle, pressuring tank, pressuring gas, and oxidizer tank, all built in aluminum. The ratio O/F = 7 is a condition that grants the minimum weight. Known the final mass of the system, i.e. debris mass + de-orbiting kit mass, it is possible to estimate the total mass of the hybrid unit required for the ceontrolled re-entry manoeuvre.

In order to support the data obtained so far, a comparison was performed with an AIAA paper which carries on an optimal design for a similar configuration but different mission [79].

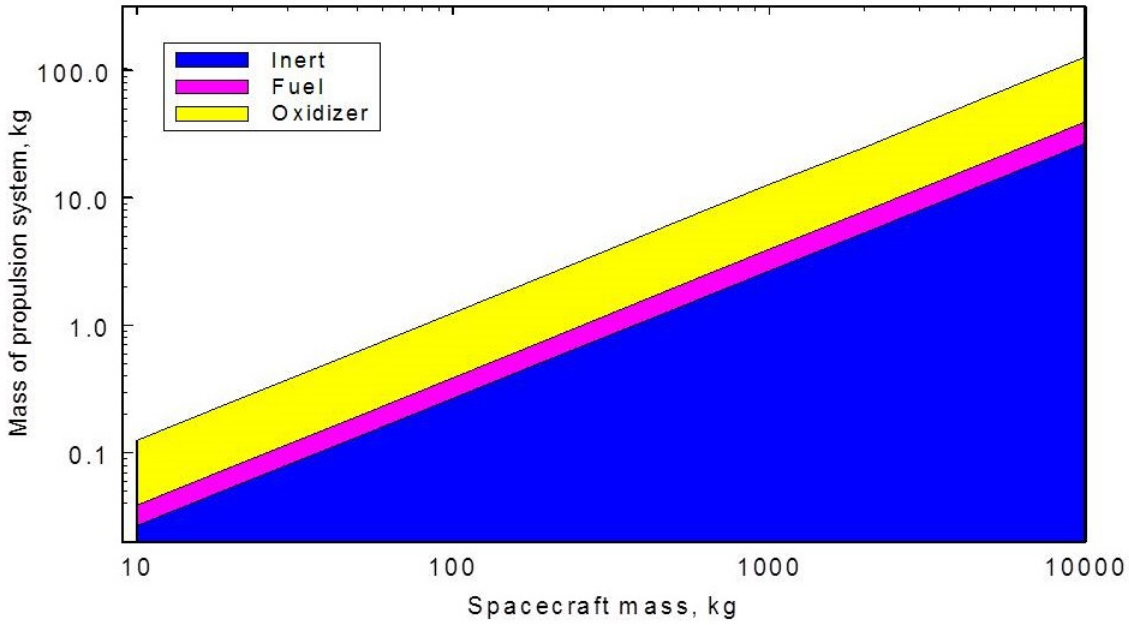

Figure 2.12: Mass of the hybrid propulsive unit for the controlled re-entry in function of the system mass (debris + de-orbiting kit).

Hybrid unit for de-orbiting manoeuvre

The design of the hybrid rocket unit results in intermingled constraints related to instantaneous oxidizer-to-fuel mass ratio, relevant specific impulse, variable regression rate, in conjunction with grain geometry, oxidizer mass flow rate, combustion pressure or designed ΔV. The main issue consists of the mass flow rate which cannot be fixed or controlled as a free parameter but it results in a nonlinear function of the oxidizer mass flow rate and of the internal burning surface. The use of non-liquefying fuels such as HTPB or PE grants in general better mechanical properties but introduces the complexity of managing a slow regression rate. The construction of a generic de-orbiting kit based on hybrid rocket technology must take into account for the fraction of inert mass to be introduced in the design. Deorbiting missions do not need high level of ΔV, in comparison to launch systems or other high-power applications. That is, we may expect that the fraction of inerts can be strongly dependent on the mission itself since some components do not fully scale with system size or other design parameters (e.g. thickness of pressure vessels will have a minimum thickness for technological reasons). Statistic studies for masses of in-space hybrid rockets do not exist yet even though parametric optimizations were found in the open literature and were consulted as a baseline [80] [81] along with standard design textbooks [56] [82]. The construction of hybrid rockets inherits aspects from both solid and liquid propulsion. That is, oxidizer tank, injection plate and blow-down pressurization are common to liquid systems whereas several aspects of combustion chamber and grain design address solid rocket technology. For the present design approach some arbitrary choices have been done in order to fix some variables. Considering that the deorbiting kit will operate in space, the expansion ratio of the nozzle was fixed to $\varepsilon = 100$, as a compromise between size and performance. HTP oxidizer (High test peroxide, 90% H_2O_2, $\rho_{ox} = 1390kg/m^3$ [83]) was considered, due to storability. HTPB (Hydroxy-terminated polybutadiene, $\rho_f = 920kg/m^3$, [65]) was assumed as a fuel. The initial combustion chamber pressure was also fixed to 10 bar, after some considerations on performance, combustion properties and weight which follow hereafter. From thermochemical considerations, frozen specific impulse is mainly driven by the ratio

$$\sqrt{\frac{T_C}{M_m}} \tag{2.8}$$

and can be computed as a function of characteristic velocity c^*, of thrust coefficient C_F and of standard gravity g_0 with the formula

$$I_{sp} = \frac{c^* * C_F}{g_0} \tag{2.9}$$

Once the combustion chamber pressure is above 5 bar, it is unlikely to expect dramatic increments of performance due to the variation of the combustion parameters and the same consideration can be done for c^*. In the present case the computation of the thrust coefficient C_F (Equation 2.10) depends only on nozzle area ratio ε and on specific heat ratio γ which is only negligibly dependent on combustion pressure.

$$C_F = \sqrt{\frac{2\gamma^2}{\gamma-1}\left(\frac{2}{\gamma+1}\right)^{\left(\frac{\gamma-1}{\gamma}\right)}\left(1-\left(\frac{p_e}{p_c}\right)^{\frac{\gamma-1}{\gamma}}\right)} + \varepsilon\frac{p_e - p_a}{p_c} \tag{2.10}$$

In fact, the discharge occurs in vacuum and the ratio P_e/P_c (exit-to-combustion chamber pressure) turns to be dependent on γ and ε again. For a matter of simplicity and lack of specific data, c^* efficiency is set to unity, though it may be lower and strongly design-dependent. That is, from the performance point of view there is no reason to increase the combustion pressure since parametric analyses showed that the overall system tends to become heavier due to pressure vessel thickness. However, pressure cannot be kept too low due to combustion issues. On one side, despite the regression rate on hybrid rockets is generally dependent on the oxidizer mass flux $G_o x$ through the formula $r_f = aG_o^n x$,there are conditions where the behavior detaches from the classical diffusion-limited regime, occurring at high and low mass flow rates where the pressure dependence can become important ([84]). Finally, lower pressure reduces the reaction rate of combustion processes and should be carefully considered, in order to prevent a reduction of rocket efficiency [85]. These specific aspects depend on the oxidizer-fuel couple and were not fully addressed in this design, mainly due to the lack of specific experimental or modelling data. The computation of inert mass fraction comprised two titanium spherical tanks respectively for the oxidizer and for the blow-down pressurization system based on nitrogen initially stored at 150 bar, one cylindrical aluminum combustion chamber ended by two half spheres, an aluminum injection plate, one nozzle as well as piping and skirt (assumed as 10% of the inert mass). Vessel thickness was computed by assuming a safety coefficient of 2 and an oxidizer design pressure of $P_{tank} = P_c/0.4$, consistent with the choice of Casalino and Pastrone [80]. Minimum thickness of 2 mm is imposed on the wall vessels. The parameter is empirically derived comparing with available catalogues and data [86] [87] [88]. For grain design, a simple center-perforated cylinder is assumed. Initial oxidizer-to-fuel ($OF = \dot{m}_{ox}/\dot{m}_f$) ratio and initial length-to-internal diameter (K = L/Din) ratio were considered, along with ballistic information of the specific propellant and a constant oxidizer mass flow rate. Given such constraints, a nonlinear relation can be derived (Equation 2.11) to be solved for grain length L.

$$\dot{m}_f = \frac{\dot{m_{ox}}}{OF} = \frac{a\pi L^2}{k}\left(\frac{4k^2}{\pi L^2}\dot{m}_{ox}\right)^n \rho_f \tag{2.11}$$

Once propellant mass M_prop is known from Tsiolkovski equation (Equation 2.12), also external grain diameter D can be evaluated, being the fuel density $_f$ a known quantity.

$$\Delta V = I_{sp} g_0 \log\frac{M_i + M_{pay} + M_{prop}}{M_i + M_{pay}} \tag{2.12}$$

However, mass budget cannot abstain from the a-priori knowledge of the effective specific impulse, resulting from the average of the instantaneous I_{sp}, and from the inert mass M_i, both dependent from the geometry of the rocket. For this reason, a double nested iterative procedure is set up for the definition of these quantities. Once the HTPB/HTP propellant is selected, the design is fully determined when initial OF ratio, initial $L = D_{in}$ ratio, payload mass, oxidizer mass flow rate, and ΔV are fixed. In this work, mission specific ΔV is a parameter of investigation. All geometric and performance data, such as regression rate, thrust or geometry, depend on the other parameters.

2.3.4 Electrodynamic tether unit sizing

The EDT unit was estimated to have a mass between 50 kg and 70 kg depending on the mass of the debris to deorbit: 50 kg was assumed for objects below 4000 kg, while 70 kg for the more massive objects. The unit includes the tether, tip mass and all the mechanisms necessary for the deployment and control of the system dynamics after deployment [89].

2.3.5 Main bus unit sizing

The total mass of the main bus unit was determined as the sum of XX main subsystems: 1)the Attitude Determination and Control Subsystem (ADCS), 2) the Telemetry, Tracking and Command subsystem (TT& C), 3) the Command and Data Handling subsystem (C& DH), 4) the power sybsystem; 5) the capture device; 6) a margin for the structures and thermal devices. The mass of each subsystem was estimated according to historical data reported in [57] referring to the typical subsystems mounted on board microsatellites. For the ADCS a three axis control was assumed, considering four reaction wheels, each one with mass lower than 5 kg, three torqrods, for a total mass lower than 2 kg, and four wide-angle coarse sun-sensors, with mass lower than 1 kg. The total mass of the ADCS was set around 18 kg. For the TT&C it was assumed a typical Ku-band communication subsystem, composed by transponders, antennas and filters/switch diplexers, for a total mass of about 13 kg. A combined system (Command and Telemetry) was considered for the C & DH subsystem, with a mass of about 5 kg. The mass of the power subsystem was determined from the solar panels sizing for a total power of 250 W, obtaining a total mass around 5 kg. Since no references were available as concerns the capture device, and the design was not the objective of this part of the work, it was assumed a mass equal to 20% of the entire microsatellite mass. A safety margin to take into account structure and other miscellaneous was set at 17%. The overall mass budget for the main bus resulted around 55 kg. The value obtained with this sizing procedure are comparable with other mass budgets relative to already developed microsatellite systems [90] [91] [92].

Main Bus mass budget

Subsystem	**Mass [kg]**
ADCS	18
TT& C	13
C& DH	5
Power	5
Capture device	20%
Safety margin	17%
TOTAL mass	~ 55

Table 2.1: Main Bus mass budget

Chapter 3

Mission analysis and results

In the present work, a *multiple vehicles* approach was considered (details in section 2.1). The mission analysis focused on four main aspects:

1. de-orbiting manoeuvres;
2. controlled re-entry for space debris;
3. multiple transfers operations;
4. risk assessment.

The main objective of point 1) was to analyse the de-orbiting phase according to the removal technologies selected and to determine the number of microsatellite units to assemble in order to de-orbit a specific debris within 25 years, as suggested by the International Guidelines. The number of units varied depending on the de-orbiting technology implemented and the characteristics of the selected debris in terms of mass and initial altitude. Four removal solutions were considered: drag sails, electric propulsion, hybrid propulsion and electrodynamic tethers; solid chemical propulsion was excluded since high propellant mass was expected due to the low specific impulse typical of such kind of rockets. Different removal scenarios were considered and proper analytical models were developed and used to determine the number of units, and hence the remover mass, and the orbital lifetimes for each de-orbiting option.
Controlled re-entry manoeuvres were also foreseen at the end of the de-orbiting manoeuvres, at an altitude of about 250 km. In case of space debris, the controlled re-entry is performed to limit the number of fragments that can survive at the impact, and to direct the remaining fragments, if survived, to uninhabited area in order to avoid any damage to people and structures on the ground. The manoeuvre consists of inserting the object in a re-entry orbit such that the flight path angle at the crossing with the atmopshere (usually set at 120 km) is within a specific range.
An optimizing procedure was developed to determine the most effective way to perform multiple orbital transfers with a single vehicle: considering a removal trend of 5 debris per year (as suggeseted in [11] [12] [28]), the objective was to determine the best sequnce of debris to rendezvous with in order to minimize the ΔV budget required to reach all the debris in a single mission, with no refuelling operations.
Finally, a preliminary risk assessment was performed to complete the analysis. The collisison risk probability was estimated in case of de-orbiting with electric propulsion and electrodynamic tether, which are more vulnerable to the space environment because of the longer de-orbiting time (months or even years) respect to hybrid propulsion. No risk assessment was foreseen in case of drag sail since this solution appeared not suitable for the characteristics, in terms of initial orbit and mass, of the priority targets selected for ADR.
In the following sections, the models and procedures developed are presented in more detail.

3.1 Orbital regions of interest and potential targets

The distribution of the space objects in the near Earth regions has been well characterized in previous works [4] [2] [8]. Between 500 and 1100 km several altitude-inclination bands where efficient active debris removal might be carried out were identified. According to these studies, three in particular were recognized as the most critical [8] [27] and were characterized by the following altitudes and inclinations:

1. Altitude: $1000km \pm 100km$; inclination: $82° \pm 1°$;
2. Altitude: $800km \pm 100km$; inclination: $99° \pm 1°$;
3. Altitude: $850km \pm 100km$; inclination: $71° \pm 1°$.

Although these previous studies, a deeper research was conducted, starting from the literary data reported in the on-line NORAD catalogue [93], to better characterise how the current debris population is distributed in the near Earth orbits. The objective was to identify the nature of the objects that can be found in each band, required for the mission analysis that will be presented later. According to this overview, seven orbital bands, between 500 km and 1100 km, were identified as very densely populated zones:

1. Altitude: $950km \pm 100km$; inclination: $64° \pm 1°$;
2. Altitude: $850km \pm 100km$; inclination: $71° \pm 1°$;
3. Altitude: $750km \pm 100km$; inclination: $74° \pm 1°$.
4. Altitude: $600km \pm 100km$; inclination: $82° \pm 1°$.
5. Altitude: $900km \pm 100km$; inclination: $82° \pm 1°$.
6. Altitude: $1000km \pm 100km$; inclination: $90° \pm 1°$.
7. Altitude: $800km \pm 100km$; inclination: $99° \pm 1°$.

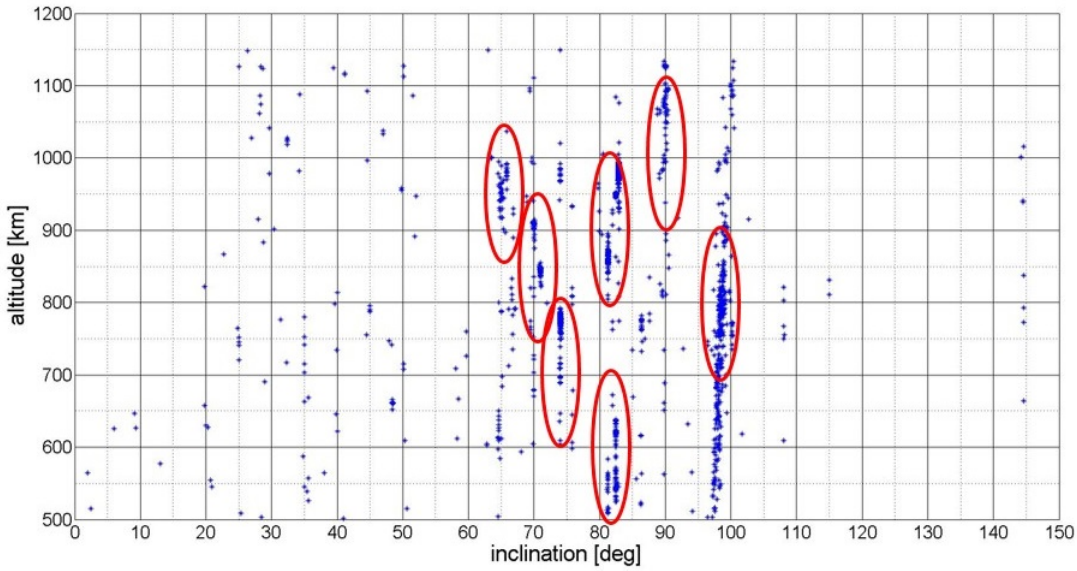

Figure 3.1: Orbital regions of interest for ADR in LEO

Bands from 1 to 6 are characterized by a rather homogeneous distribution of debris, as regards the mass and nature of the objects: they are primarily orbital stages and satellites forming different constellation, such as COSMOS and METEOR. COSMOS satellites can be found in all these bands, with masses that range between 700 kg and 6000 kg, while METEOR satellites are widely distributed in the fifth band, with masses between 1400 kg and 3300 kg. SL-8 orbital stages (1400 kg) are present in small number in the first orbital region, while they represents the greater part of the debris population in the third and fifth band; SL-16 stages (8300 kg) and few SL-12 (11000 kg) can be found in the second band; finally, a large number of SL-3 (1440 kg) and SL-14 (1407 kg) is concentrated in the fifth band. The sixth band is mainly characterized by small satellites, with masses between 1 and 100 kg, and by few SCOUT-A (1275 kg) and THOR ABLESTAR rocket bodies (600 kg). In contrast with this homogeneous

distribution, the last band, which correspond to the sun-synchronous orbits (SSO), is extremely heterogeneous, with a wide range of debris in terms of types and masses, varying from small satellites, such as cubesats, to massive satellites and orbital stages, such as Envisat (8100 kg) and Ariane and CZ rocket bodies (1400 kg 4000 kg).
An accurate investigation on the debris population in SSO was conducted by Carmen Pardini and reported in [94]: as of 19 February 2013, there were 192 spacecraft and 74 upper stages, excluding classified objects, with mean altitudes between 700 and 1100 km [95]. According to a survey carried out by the Union of Concerned Scientists [96], the operational satellites should be about 90, so the total number of potential targets to be removed is around 175. But contrary to the situation prevailing in most of the other crowded altitude-inclination bands, spacecraft and upper stages in sun-synchronous orbits are extremely heterogeneous, with the full range of models and masses represented [97]. Abandoned satellites, for instance, include both cubesats and the 8 metric tons Envisat. This means that a specific debris removal option might be used only a relatively limited number of times. However, some families of upper stages might offer attractive targets for removal, as can be seen in Figure 3.2. Being a potential source of many breakup fragments posing an additional collision risk, the targets for active removal should be large intact objects in crowded LEO regions characterized by a substantial orbital lifetime. They can be ranked according to $P_c \times M^{0.75}$, where P_c represents the overall catastrophic breakup probability of the object during its orbital lifetime, M is the dry mass and the exponent reproduces the trend of the cumulative number of collisional fragments according to the NASA standard breakup model [98].

Upper Stage	No.	Dry Mass (kg)	Mean Altitude (km)	Inclination (°)
Agena D stage	3	673	784-1067	99.9-100.0
Altair stage	1	30	717	98.1
Ariane 1 H8	1	1450	786	98.8
Ariane 4 H10	5	1800	756-786	98.3-98.8
Ariane 5 EPS	1	3600	770	98.2
Burner 2 stage	17	116	707-836	97.5-99.1
CZ-2 2nd stage	4	4000	727-827	98.1-98.3
CZ-4 3rd stage	10	1000	717-918	98.2-99.4
Delta 2nd stage	6	820	708-942	96.5-99.6
Dnepr-1 3rd stage	10	2356	758-991	97.4-98.6
H-2 2nd stage	2	2700	785-1081	98.5-98.8
Molniya 3rd stage	1	879	802	98.7
PSLV 4th stage	5	920	713-835	98.4-98.9
Rokot Briz KM	1	1420	901	99.5
Scout 4th stage	2	25	754-1012	97.8-99.5
Taurus 4th stage	1	203	725	99.2
Vostok 2nd stage	2	1440	885-889	99.2-99.5
Zenit 2nd stage	2	8300	805-994	98.3-99.1

Figure 3.2: Upper stages in Sun-Synchronous orbits [94].

According to the previous considerations, only objects with mass greater than 800 kg and altitude above 700 km were considered for the mission analysis, reducing the number of orbital regions of interest to the following five bands:

1. Altitude: $950km \pm 100km$; inclination: $64° \pm 1°$;
2. Altitude: $850km \pm 100km$; inclination: $71° \pm 1°$;
3. Altitude: $750km \pm 100km$; inclination: $74° \pm 1°$.
4. Altitude: $900km \pm 100km$; inclination: $82° \pm 1°$.
5. Altitude: $800km \pm 100km$; inclination: $99° \pm 1°$.

Figure 3.3 shows the distribution of the debris population, divided in ten classes of mass, for each orbital band, while Figure 3.4 represents the totality of objects with mass in the same range, regardless the orbital band. As it can be observed, the greater part of the debris, estimated as the 78%, is characterised by a mass between 800 kg and 2000 kg; except for some more massive debris, it can be concluded that most of the debris that orbits in LEO have mass below 4000 kg. This represents a significant aspect for the implementation of ADR mission, since similar removal strategies could be employed for a large part of the targets selected.

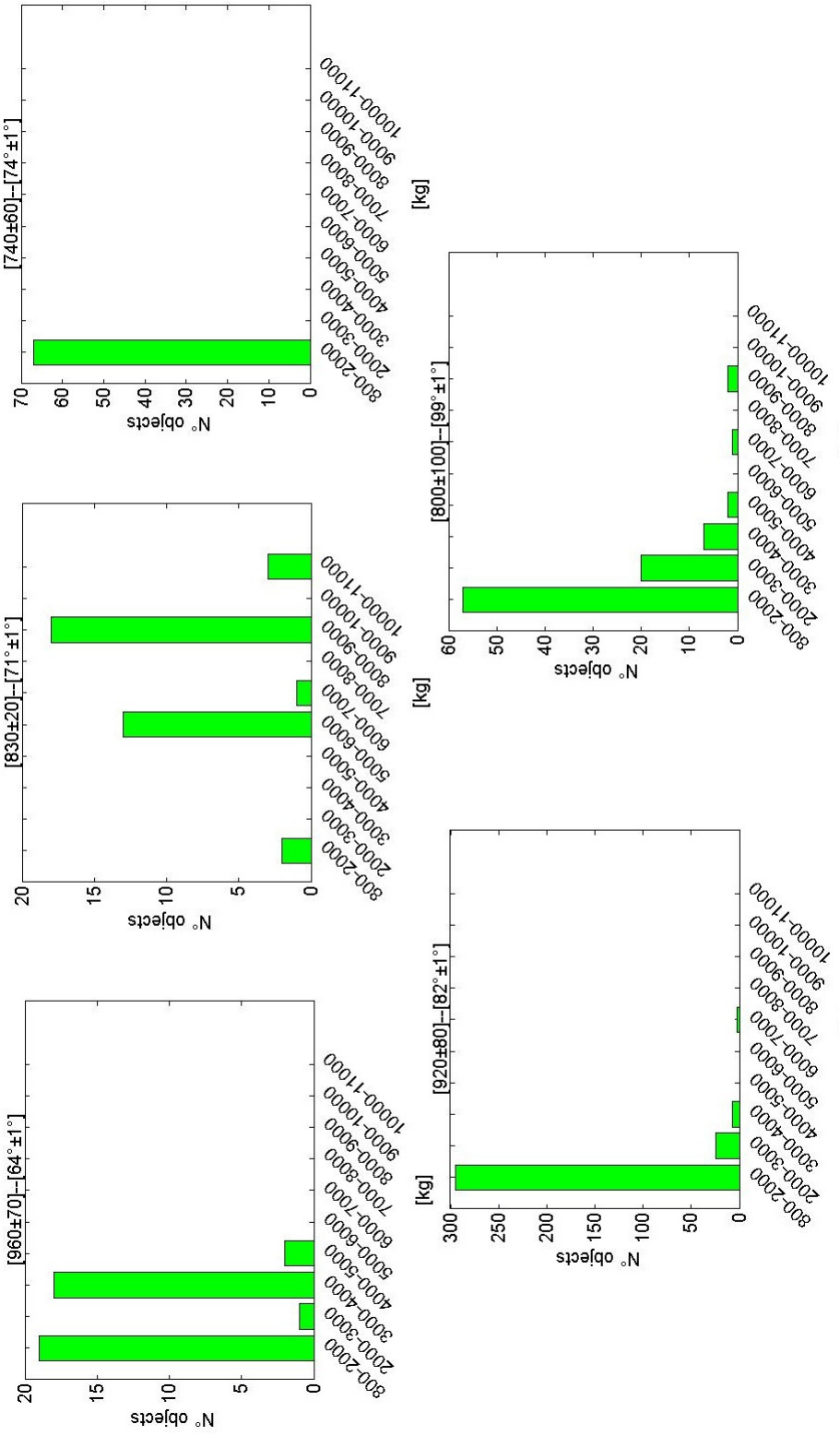

Figure 3.3: Number of debris in each selected orbital band.

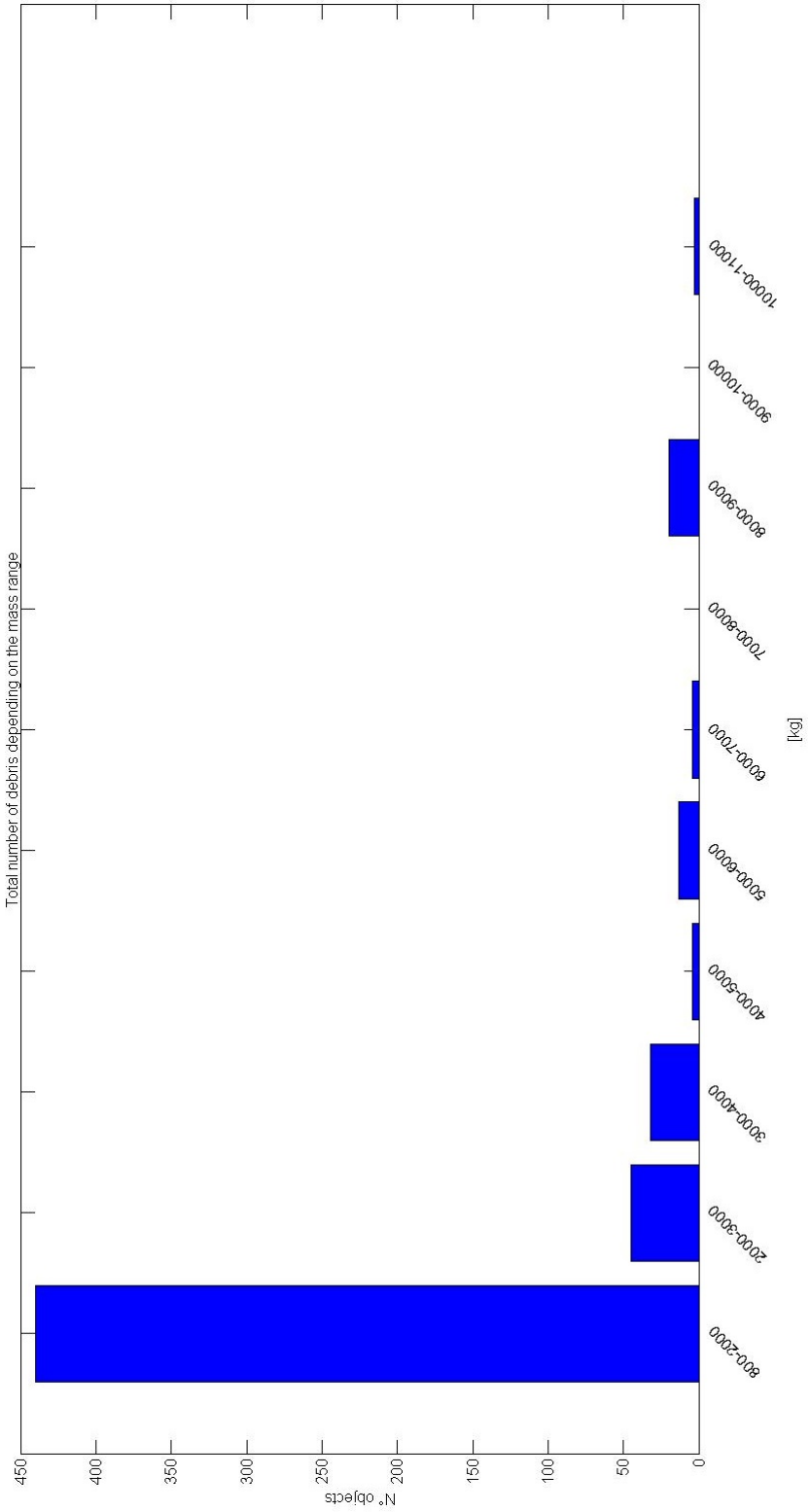

Figure 3.4: Distribution of the debris according to their mass range.

3.2 Models for de-orbiting operations

Some simplifing hypothesis are adopted:

- the manouevres are performed as sequences of circular orbits in case of drag, eletric propulsion and electrodynamic tether; the typical impulsive manoeuvre is considered for hybrid propulsion;
- central gravitational attraction is assumed;
- it is considered a still atmosphere, so drag and electric propulsion manoeuvres are not affected by rotational components of the atmosphere;
- solar radiation pressure and third body perturbation are neglected: they are both negligible in LEO respect to the other effects that act on the satellite due to the de-orbiting systems

The magnitude of the acceleration due to solar radiation pressure is of the order of $10^{-6} m/s^2$; as reported in [57], '*below 800 km altitude, acceleration from drag is greater than that from solar radiation pressure; above 800 km, acceleration from solar radiation pressure is greater*". Anyway, it was demonstrated that for circular orbits the effect of solar radiation pressure is null if integrated on the entire orbit (Appendix A), so it can be neglected in drag effect calculations also for orbits higher than 800 km. Concering propulsion, the thrust force available varies from few tens of mN to several N for electric propulsion, according to the specific kind of electric thruster considered; for hybrid propulsion, the thrust force is of the order of several kN [57]; in both cases, the thrust force is higher than the effect of solar radiation pressure. On the other hand, the main effects of third body perturbation are secular changes of right ascension of the ascending node, argument of perigee and mean anomaly; furthermore, for nearly circular orbits, e^2 is almost zero and the resulting error is of the order e^2 [57]. These parameters were not considered in the development of analytical models, and hence also third body perturbations could be neglected.

Three main analytical models were developed and implemented in the mission analysis:

I De-orbiting through drag augmentation devices;

II De-orbiting through propulsion devices (in case of electric thruster);

III De-orbiting through electrodynamic tethers.

3.2.1 De-orbiting through drag augmentation devices

In this section it is developed and presented an analytical model to determine the de-orbiting time, given the sail area and the debris mass. The output will be then compared with the limit of 25 years indicated in the NASA-STD 1740.14 [10] to verify if the mission scenario is compliant with the guidelines. The model takes into account the characteristics of the de-orbiting kit (numer of units assmebled) and the correspondent mass. The starting point is the equation relative to orbital specific energy:

$$E = -\frac{\mu}{2a} \tag{3.1}$$

where:
μ is the Earth's gravitational parameter (398600 km^3/s^2);
a is the semimajor axis of the orbit.

Differentiating, the orbital energy variation per unit mass results:

$$dE = \frac{\mu}{2a^2} da \tag{3.2}$$

and the istantaneous power is:

$$\frac{dE}{dt} = \frac{\mu}{2a^2} \frac{da}{dt} \tag{3.3}$$

Orbital energy variation due atmospheric drag equals work due to drag forces along the orbit:

$$dE = \frac{F_D}{m} ds \tag{3.4}$$

The power dissipated per unit mass by aerodynamic forces is:

$$\frac{dE}{dt} = \frac{F_D}{m}\frac{ds}{dt} = \frac{F_D}{m} v_{rel} \tag{3.5}$$

Considering the hypothesis of circular orbits and rotation of the atmosphere negligible yields:

$$v_{rel} = na \tag{3.6}$$

$$\frac{dE}{dt} = \frac{F_D}{m} na \tag{3.7}$$

where n is the mean motion.

Substituting this expression in the derivative of orbital energy, results:

$$\frac{da}{dt} = \frac{2a^2}{\mu}\frac{dE}{dt} = \frac{2a^2}{\mu}\frac{F_D}{m} na \tag{3.8}$$

The aerodynamic forces per unit mass can be expressed as:

$$\frac{F_D}{m} = -\frac{1}{2}\rho\frac{c_D A}{m} v_{rel}^2 = -\frac{1}{2}\rho\frac{c_D A}{m}(na)^2 \tag{3.9}$$

where:
ρ is the atmospheric density;
c_D is the drag coefficient(it can be adopted $c_D = 2$);
A is the cross-sectional area of the satellite;
m is the total mass of the object;
$c_D A/m$ represents the ballistic coefficient of the satellite.

Substituting in (3.8):

$$\frac{da}{dt} = -\frac{2a^2}{\mu}\frac{1}{2}\rho\frac{c_D A}{m}(na)^2 na \tag{3.10}$$

For circular orbits:

$$\mu = n^3 a^2 \tag{3.11}$$

$$n = -\frac{2\pi}{T} = \frac{\sqrt{\mu}}{a^3} \tag{3.12}$$

so:

$$\frac{da}{dt} = -a^2 n\rho\frac{c_D A}{m} \tag{3.13}$$

$$da = -a^2 n\rho\frac{c_D A}{m} dt \tag{3.14}$$

Equation (3.14) cannot be directly integrated to determine the total orbital decay in function of the total manoeuvre time. This is due to atmospheric density, which varies with altitude, epoch and solar activity [99].
According with King-Hele theory [100], assuming small orbital decay for single orbit, semimajor axis can be considered constant; adopting an exponential model of atmospheric density, Equation 3.14 can be solved as follows:

$$\int_{1orb} da = \int_0^T -a^2 n\rho\frac{c_D A}{m} dt \tag{3.15}$$

which yields:

$$\Delta a_{1orb} = -2\pi a^2 \frac{C_D A}{m}\rho \tag{3.16}$$

This expression, valid for circular orbits, allows to calculate the orbital decay for a single orbit. The total orbital decay can be obtained in an iterative way.
Initial objective was to determine the size of a sail to de-orbit a satellite starting from a specific altitude, assuring an orbital lifetime of 25 years. Equation 3.16 does not allow in any way to determine an analytical expression for this purpose.

To solve the problem it has been considered an equation in which density is calculated as a mean value in the altitude range where the manoeuvre takes place. After few passages, equation (3.10) can be written as follows:

$$\frac{da}{\rho\sqrt{a}} = -\sqrt{\mu}\frac{c_D A}{m}dt \tag{3.17}$$

Considering a manoeuvre from an initial orbit with semimajor axis a_i to a final orbit with semimajor axis a_f, the integral expression becomes:

$$\int_{a_i}^{a_f} \frac{da}{\rho\sqrt{a}} = \int_0^{t_f} -\sqrt{\mu}\frac{c_D A}{m}dt \tag{3.18}$$

where t_f represent the istant at which manoeuvre ends.
The calculus of the mean value of density requires a more in-depth study.

Several density models have been developed in the past four decades, with typical uncertainties of 10-20% at low altitudes and more at higher altitudes [99]. These uncertainties are mainly due to solar flux and geomagnetic activity, whose intensity is difficult to predict.
Solar flux is usually represented through the parameter $F_{10.7}$, which correspond to the wavelength, expressed in cm, of the incoming solar radiation. It is characterised by a 11-years cycle, with smaller fluctuations due to Earth's rotation, 27-day solar-rotation cycle, seasonal/semi-annual variations.
Solar flux influences satellite orbital lifetime, accelerating natural re-entry during periods of high activity, and slowing it down during periods of lower activity.
For our analysis, it has been chosen an exponential model, a simple static model which considers moderate solar activity and assumes an exponentially density decay with increasing altitude, according to:

$$\rho = \rho_0 e^{-\frac{h-h_0}{H}} \tag{3.19}$$

where:
h_0 and ρ_0 are reference values;
H is a scale height.

These values are tabulated for several altitude ranges in figure 3.5.

Taking the atmospheric density out of the integral in the equation 3.18, an analytical expression for the orbital lifetime can be approximated through the following equation:

$$\Delta t \cong \frac{2m(\sqrt{a_i} - \sqrt{a_f})}{\sqrt{\mu}c_D A}\overline{(\frac{1}{\rho})} \tag{3.20}$$

The mass m in the previous equation correspond to the entire mass of the system that is de-orbited, i.e. the mass of the debris plus the mass of the de-orbiting kits, and it can be written as:

$$m = m_{deb} + M_{DK} = m_{deb} + m_{bus} + \sum n_{DKi} m_{DKi} \tag{3.21}$$

where:
m_{deb} is the mass of the debris;
m_{bus} is the mass of the main bus unit;
M_{DK} is the total mass of the de-orbiting kit, i.e. the de-orbiting kit with all the units assembled;

Altitude h [km]	Base Altitude h_0 [km]	Nominal Density ρ_0 [kg/m^3]	Scale Height H [km]	Altitude h [km]	Base Altitude h_0 [km]	Nominal Density ρ_0 [kg/m^3]	Scale Height H [km]
0 – 25	0	1.225	7.249	150 – 180	150	2.070×10^{-9}	22.523
25 – 30	25	3.899×10^{-2}	6.349	180 – 200	180	5.464×10^{-10}	29.740
30 – 40	30	1.774×10^{-2}	6.682	200 – 250	200	2.789×10^{-10}	37.105
40 – 50	40	3.972×10^{-3}	7.554	250 – 300	250	7.248×10^{-11}	45.546
50 – 60	50	1.057×10^{-3}	8.382	300 – 350	300	2.418×10^{-11}	53.628
60 – 70	60	3.206×10^{-4}	7.714	350 – 400	350	9.158×10^{-12}	53.298
70 – 80	70	8.770×10^{-5}	6.549	400 – 450	400	3.725×10^{-12}	58.515
80 – 90	80	1.905×10^{-5}	5.799	450 – 500	450	1.585×10^{-12}	60.828
90 – 100	90	3.396×10^{-6}	5.382	500 – 600	500	6.967×10^{-13}	63.822
100 – 110	100	5.297×10^{-7}	5.877	600 – 700	600	1.454×10^{-13}	71.835
110 – 120	110	9.661×10^{-8}	7.263	700 – 800	700	3.614×10^{-14}	88.667
120 – 130	120	2.438×10^{-8}	9.473	800 – 900	800	1.170×10^{-14}	124.64
130 – 140	130	8.484×10^{-9}	12.636	900- 1000	900	5.245×10^{-15}	181.05
140 – 150	140	3.845×10^{-9}	16.149	1000 -	1000	3.019×10^{-15}	268.00

Figure 3.5: Atmospheric density model [101]

n_{DKi} is the number of units equipped with the i-th de-orbiting device;
m_{DKi} is the mass of the unit equipped with the i-th de-orbiting device.

When only a drag sail is employed for the de-orbiting phase, the number of de-orbiting units assembled is always 1, regardless the size of the sail, since an increase in size (mainly the total area) of such device does not determine a great increase in the total mass of the unit, that is always lower than 100 kg for the considered ADR scenarios.

The most important parameter that influence the de-orbiting time is the *Ballistic coefficient*, which is mainly related to the A/m ratio, as well as the drag coefficient:

$$C_B = \frac{C_D * A}{m} \tag{3.22}$$

where:
C_D is the drag coefficient, a dimensionless parameter that reflects satellite's susceptibility to drag forces;
A is the cross-sectional are, the satellite surface projected in a plane perpendicular to the velocity vector;
m is the mass of the entire de-orbitied system.

The drag coefficient C_D was set equal to 2.2 in the calculations, even though more accurate values can be considered if higher estimations are required. The Ballistic coefficient is usually the reference parameter to determine the orbital lifetime of an object given its orbital parameters. It can be observed that increasing the cross sectional area, without rising the mass of the system too much, implies a reduction of the ballistic coefficient and, thus, of the orbital lifetime.

3.2.2 De-orbiting through propulsive devices

Two different approached were considered to analyse a propulsive de-orbiting manoeuvre performed through an electric thruster:

1. final orbit achievable for a given propellant mass;
2. propellant mass required to achieve a pre-set final orbit.

In both case, the objective is to determine the number of propulsive units required to accomplish the selected manoeuvre.

Final orbit achievable for a given propellant mass

Assuming thrust vector parallel to the position vector along the orbit, orbital energy variation due to thrust can be expressed as:

$$dE = \frac{F_p}{m} ds \tag{3.23}$$

The istantaneous power dissipated per unit mass, assuming circular orbit, is:

$$\frac{dE}{dt} = \frac{F_p}{m} \frac{ds}{dt} = \frac{F_p}{m} na \tag{3.24}$$

From propulsion, thrust force is equals to:

$$F_p = \dot{m} I_{sp} g_0 = \frac{dm}{dt} I_{sp} g_0 \tag{3.25}$$

Substituting in equation (3.24), yields:

$$\frac{dE}{dt} = \frac{dm}{dt} \frac{I_{sp} g_0}{m} na \tag{3.26}$$

Considering equations (3.3) and (3.26), the orbital decay rate results:

$$\frac{da}{dt} = \frac{2a^2}{\mu} \frac{dE}{dt} = \frac{2a^2}{\mu} \frac{dm}{dt} \frac{I_{sp} g_0}{m} na \tag{3.27}$$

and after few passages, it obtains:

$$da = \frac{2a^{3/2} I_{sp} g_0}{\sqrt{\mu}} \frac{dm}{m} \tag{3.28}$$

In case of electric propulsion, the de-orbiting phase is characterised by a low-thrust continuous manoeuvre, which leads to an inward spiral trajectory, shown in Figure 3.6.

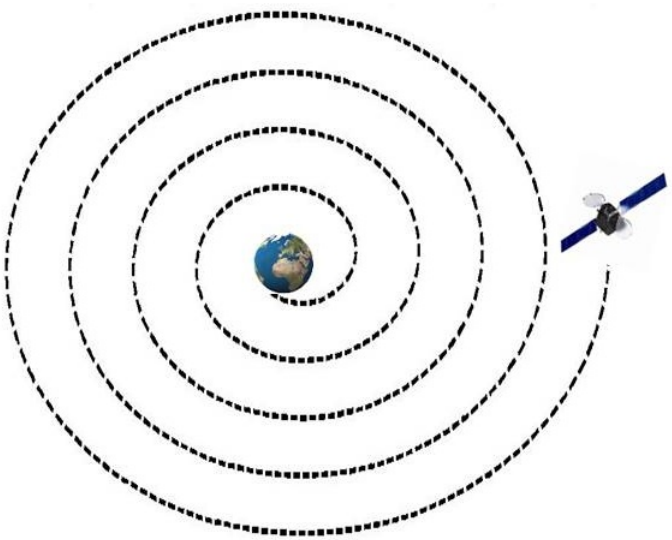

Figure 3.6: Inward spiral trajectory followed during a continuous low thrust maneouvre

The mass of the system varies continuously as the semimajor axis is lowered. Hence, Equation (3.28) can be directly integrated separating the variables and considering a manoeuvre from an initial orbit of semimajor axis a_i to a final orbit of semimajor axis a_f.

$$\int_{a_i}^{a_f} \frac{1}{a^{3/2}} da = \int_{m_i}^{m_f} \frac{2I_{sp}g_0}{\sqrt{\mu}} \frac{dm}{m} = \frac{2I_{sp}g_0}{\sqrt{\mu}} \int_{m_i}^{m_f} \frac{dm}{m} \tag{3.29}$$

where m_i and m_f represent initial mass of the system before and after the propulsive phase. Solving, it yields:

$$\left[-\frac{2}{\sqrt{a}}\right]_{a_i}^{a_f} = \left[\frac{2I_{sp}g_0}{\sqrt{\mu}} \ln(m)\right]_{m_i}^{m_f} \tag{3.30}$$

$$\ln\left(\frac{m_f}{m_i}\right) = \left(\frac{1}{\sqrt{a_i}} - \frac{1}{\sqrt{a_f}}\right) \frac{\sqrt{\mu}}{I_{sp}g_0} \tag{3.31}$$

The final mass of the system, at the end of the manoeuvre, is:

$$m_f = m_i \exp\left[\frac{\sqrt{\mu}}{I_{sp}g_0} \left(\frac{1}{\sqrt{a_i}} - \frac{1}{\sqrt{a_f}}\right)\right] \tag{3.32}$$

and the propellant mass results:

$$m_{prop} = m_i - m_f = m_i \left\{1 - \exp\left[\frac{\sqrt{\mu}}{I_{sp}g_0} \left(\frac{1}{\sqrt{a_i}} - \frac{1}{\sqrt{a_f}}\right)\right]\right\} \tag{3.33}$$

After some passages, the final orbit can be determined through the following equation:

$$a_f = \left(\frac{1}{\frac{1}{\sqrt{a_i}} - \frac{I_{sp}g_0}{\sqrt{\mu}} ln\left(1 - \frac{m_{prop}}{m_i}\right)}\right)^2 \tag{3.34}$$

Propellant mass for a given ΔV

When the final orbit is known, and then the ΔV budget can be easily evaluated, the equations implemented to analyse the propulsive manoeuvre can be derived from the basic equations of propulsion. In a low thrust manoeuvre, the ΔV required to lower the orbit from an initial altitude h_i to a final one h_f can be calculated through equation 3.35:

$$\Delta V = \sqrt{\frac{\mu}{a_f}} - \sqrt{\frac{\mu}{a_i}} \tag{3.35}$$

where μ is the Earth parameter and is equal to 398600 km^3/s^2, a_i and a_f are respectively the initial and final orbital radius. In LEO, this value is very close to the ΔV calculated in case of an impulsive manoeuvre. The number of microsatellite units required to de-orbit a specific debris can be determined, once the propulsive unit mass is known, comparing the previous ΔV with the one obtained through the Tsiolkowky equation:

$$\Delta V = I_{sp}g_0 \log \frac{m_i}{m_f} \tag{3.36}$$

where m_i and m_f are the initial and final mass of the entire system respectively. As it can be observed, this is the same equation that was derived analitically in the previous model for a low thrust manoeuvre. So it can be concluded that for a continous manoeuvre the propellant mass can be derived directly from the the tsiolkowsky equation, when the ΔV budget is known, and viceversa.

In both models, the initial mass, the final mass and the propellant mass of the de-orbited system (debris + DK) are:

$$m_i = m_{deb} + n_p m_{EPU} = m_{deb} + n_p(m_{EPUin} + m_{EPUp}) \tag{3.37}$$

$$m_f = m_{deb} + n_p(m_{EPU} - m_{EPUp}) = m_{deb} + n_p m_{EPUin} \tag{3.38}$$

$$m_{prop} = n_{EPU} m_{EPUp} \tag{3.39}$$

where m_{deb} is the debris mass, n_{EPU} is the number of propulsive units, m_{EPU} is the mass of the single unit, m_{EPUin}m is the inert mass of the unit and m_{EPUp} is the propellant mass stored in a single unit.

Substituting these expressions in equations 3.34 and 3.36, it is obtained:

$$a_f = \left(\frac{1}{\frac{1}{\sqrt{a_i}} - \frac{I_{sp} g_0}{\sqrt{\mu}} ln\left(1 - \frac{n_{EPU} m_{EPUp}}{m_{deb} + n_p m_{EPU}}\right)} \right)^2 \tag{3.40}$$

$$\Delta V = I_{sp} g_0 \ln \frac{m_{deb} + n_p(m_{EPUin} + m_{EPUp})}{m_{deb} + n_p m_{EPUin}} \tag{3.41}$$

Varying the number of assembled propulsive units, the final altitude achievable can be determened through equation 3.40, while solving respect to n_p, the total number of EPU required to de-orbit a debris of mass m_{deb} from an initial altitude h_i to a final orbit h_f, and then the total mass of the de-orbiting kit, can be estimated through equation 3.41.

Considering negligible the propellant mass ejected during the manoeuvre with respect to the entire system mass, the total de-orbiting time can be estimated, in both cases, from the following equation:

$$\Delta t = \frac{m_i \Delta V}{n_p F} \tag{3.42}$$

where F is the thrust provided by each thruster. The total thrust when two or more units are assembled together, can become:

$$F_{tot} = n_{EPU} F \tag{3.43}$$

if it is supposed that all thrusters work simultaneously during the de-orbiting manoeuvre.

3.2.3 De-orbiting through electrodynamic tethers

The arguments of the present section are taken from an internal report [102] by Denis Zanutto, in collaboration with Prof. Enrico Lorenzini. The model developed in the document was implemented in the mission analysis to determine the de-orbiting performances, in terms of orbital lifetime, when an electrodynamic tether (EDT) is employed. The only parameter to be determined in case of de-orbiting through EDT is the total de-orbiting time; only one EDT unit is sufficient to de-orbit a target debris. As anticipated in section 2.2.4, the working principle of an EDT is based on the interaction between the bare EDT and the Earth magnetic field, as the tether orbits in LEO. As reported in [102], one important feature is that the performances of the EDT strongly depend on the inclination of the orbit, i.e. the magnitude of the deorbiting force is roughly proportional to the square of the local magnetic field component $B_\perp$ along the normal to the orbit. This means that longer deorbiting times are required when EDTs operate at higher inclinations, in the range between $[80; 120]\, deg$. The model implemented in our analysis was based on three main assumptions: gravity-gradient stabilized tether, i.e. always aligned along the local vertical, sequence of circular inclined low earth orbits and average electric current equal to short circuit one [102]. The main systems of reference and orbital parameters are shown in Figure 3.7.

A detalied description of the mathematical passages can be found in [89]. We report just the final expression for the tangential component of the Lorentz force acting on the tether:

$$F = -I_{av} B_\perp L \tag{3.44}$$

where I_{av} is the average current that flows along the tether, $B_\perp$ is the local magnetic field components orthogonal to the orbital plane and L is the tether length. For an ideally designed tether it is obtained:

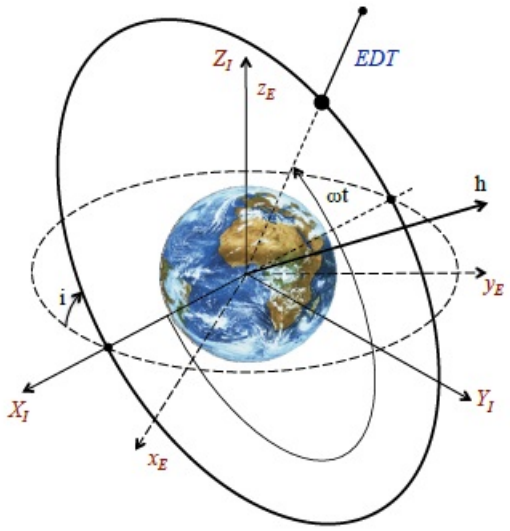

Figure 3.7: System of reference and satellite orbit [102].

$$F \approx \sigma A v {B_\perp}^2 L \tag{3.45}$$

where σ is the tether electrical conductivity (for Aluminum $\sigma = 5.84e-71/\Omega m$)) and A is the cross sectional area of the tether.

The de-orbiting of a massive object could require long time, from weeks to even years. For this reason it can be considered an avarage value $\overline{F}$ of the istantaneous force F computed on one Earth rotation period.

$$\overline{F} = \frac{\int_0^{2\pi\Omega_E} F dt}{2\pi\Omega_E} \tag{3.46}$$

where Ω_E is the Earth rotational velocity.

Substituting the previous equation in the Gauss planetary equation that expresses the evolution of the semimajor axis over the time (3.8), and neglecting any other additional perturbation force, it can be obtained:

$$\frac{da}{dt} = \frac{2a^2 v}{\mu} \frac{\overline{F}}{m_{tot}} \tag{3.47}$$

where a is the semimajor axis, v is the satellite velocity, μ is the Earth gravitational parameter ($398600\ km^3/s^2$) and m_{tot} is the total mass of the de-orbited system, i.e. the mass of the debris plus the mass of the de-orbiting kit. Assuming a sequence of circular orbits, the semimajor axis can be substituted by the orbital radius (as previously done for the atmospheric drag model) and the equation can be written as follows:

$$\frac{dr}{dt} = -\frac{2r\sigma A L B_\perp}{m_{tot}} \tag{3.48}$$

The total re-entry time can be evaluated as:

$$\Delta t = \int_{r_0}^{r_f} \frac{m_{tot}}{2r\sigma A L B_\perp} dr \tag{3.49}$$

The previous equation can be solved evaluating the average value of the square of $B_\perp$. A direct integration is not possible and two different integrations are required, the first respect to the orbital motion, and the second respect to the Earth's rotation. The final equation is a function of the orbital altitude and the inclination, expressed by proper coefficients k the former and a cosine function the latter. These coefficients are in the form $k_{i,j}$, where i represent the order of approximation considered and j is

the multiplier of the inclination in the cosine function. The perpendicular component $B_\perp$ of the magnetic field can be evaluated directly from the International Geomagnetic Reference Field (IGRF) model, which provides the expression of the magnetic field potential as a series expansion. Increasing the order of the expansion, a more accurate expression of the de-orbiting time can be obtained. Here we report only the expression of the first order and third order equations, that will be used in the analysis. The integral expression for the de-orbiting time estimated with a first order approximation for the IGRF model is:

$$\Delta t_{1x1} = \int_{r_0}^{r_f} \frac{m_{tot}}{2r\sigma AL} \frac{1}{k_{10} + k_{12} * cos(2i)} dr \tag{3.50}$$

which, once integrated, gives:

$$\Delta t_{1x1} = -\frac{4msc}{(2\sigma AL)} \frac{1}{k_{10} + k_{12} * cos(2i)} \frac{r_f^6 - r_i^6}{6R_E^6}; \tag{3.51}$$

The coefficients $k_{10} and k_{12}$ can be represented by the following equations:

$$k_{10} = \frac{1}{4}\left(\frac{R_E}{r}\right)^6 (2g_{10}^2 + g_{11}^2 + h_{11}^2)$$
$$k_{12} = \frac{1}{4}\left(\frac{R_E}{r}\right)^6 (2g_{10})^2 - g_{11}^2 - h_{11}^2)$$

where the terms $g_{n,m}$ and $h_{n,m}$ are the Schimdt-normalized coefficients that compare in the expression used to evaluate the magnetic field potential with IGRF model. The expression for orbital decay evaluated at the third order is:

$$\Delta t_{3x3} = \int_{r_0}^{r_f} \frac{m_{tot}}{2r\sigma AL} \frac{1}{k_{30} + k_{32} * cos(2i) k_{34} * cos(4i) k_{36} * cos(6i)} dr \tag{3.52}$$

The integral provides the following expression:

$$\Delta t_{3x3} = \Delta t_1 + \Delta t_2 + \Delta t_3 \tag{3.53}$$

Each term Δt_i can be expressed in function of the Schimdt-normalized coefficients evaluated for a series expansion stopped at the third order:

$$\Delta t_1 = \frac{6(A_2^2 - A_1 A_3) R_E^4 r^2 - 3A_1 A_2 R_E^2 r^4 + 2A_1^2 r^6}{12 A_1^3 R_E^6}$$
$$\Delta t_2 = \frac{6(A_2^4 - 4A_1 A_2^2 A_3 + 2A_1^2 A_3^2) tan^{-1}\left[\frac{A_2 R_E^2 + 2A_1 r^2}{R_E^2 \sqrt{4A_1 A_3 - A_2^2}}\right]}{2A_1^4 \sqrt{4A_1 A_3 - A_2^2}}$$
$$\Delta t_3 = \frac{A_2(2A_1 A_2 - A_2^2) ln\left[A_3 R_E^4 + A_2 R_E^2 r^2 + A_1 r^4\right]}{4A_1^4}$$

where

$$
\begin{aligned}
A_1 &= \frac{1}{4}(2g_{10}^2 + g_{11}^2 + h_{11}^2 + (2g_{10}^2 - g_{11}^2 - h_{11}^2)cos(2*i)) \\
A_2 &= \frac{9}{32} * (2g_{20}^2 + 8g_{21}^2 + 20g_{22}^2 - 2g_{10}g_{30} - g_{11}g_{31} + 8h_{21}^2 + 20h_{22}^2 - h_{11}h_{31}) \\
&+ \frac{3}{16}(3g_{21}^2 - 12g_{22}^2 - 4g_{10}g_{30} - 3g_{11}g_{31} + 3*h_{21}^2 - 12*h_{22}^2 - 3h_{11}h_{31})cos(2i) \\
&- \frac{3}{32}(6g_{20}^2 - 12g_{21}^2 + 12g_{22}^2 + 10g_{10}g_{30} - 15g_{11}g_{31} - 12h_{21}^2 + 12h_{22}^2 - 15h_{11}h_{31})cos(4i); \\
A_3 &= \frac{9}{1024}(118g_{30}^2 + 559g_{31}^2 + 6700g_{32}^2 + 27900g_{33}^2 + 559h_{31}^2 + 6700h_{32}^2 + 27900h_{33}^2) \\
&+ \frac{9}{2048} * (106g_{30}^2 - 13g_{31}^2 + 3700g_{32}^2 - 40500g_{33}^2 - 13h_{31}^2 + 3700h_{32}^2 - 40500h_{33}^2)cos(2i) \\
&+ \frac{45}{1024}(2g_{30}^2 - 43g_{31}^2 + 580g_{32}^2 - 1260g_{33}^2 - 43h_{31}^2 + 580h_{32}^2 - 1260h_{33}^2)cos(4i) \\
&+ \frac{67}{2048}(2g_{30}^2 - 9g_{31}^2 + 36g_{32}^2 - 36g_{33}^2 - 9h_{31}^2 + 36h_{32}^2 - 36h_{33}^2)cos(6i);
\end{aligned}
$$

The approximated orbital lifetimes evaluated with the two previous equation are represented in Figure 3.8, for an object of 1000 kg of mass, de-orbited from an initial altitude of 1000 km to a final one at 250 km; the tether was assumed 5 km long, with the conductive wire made of aluminum. As it emerged, the divergence between the two plots increases for inclinations between 80° and 110°, that represent the inclinations where the orthogonal component of the magnetic field is minimum and more critical to determine, and where the performances of the EDT worsen. This phenomenon is of particular interest for the mission analysis since one of the most crowded and critical regions for ADR, the SSO, is at $99° \pm 1°$ and the EDT could not be so efficient to remove the objects that lie in this orbital band.

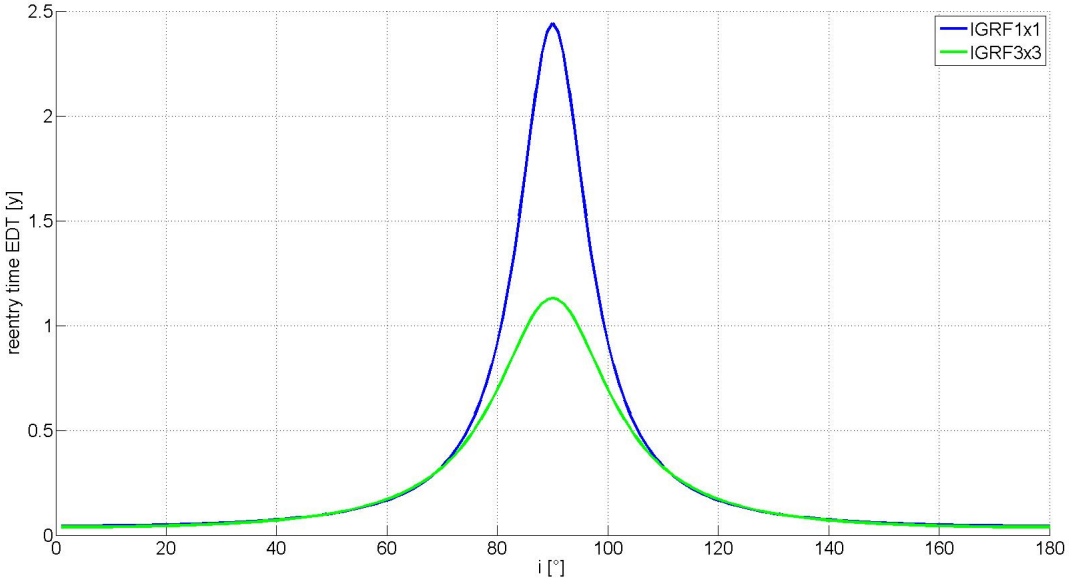

Figure 3.8: De-orbiting time evaluated with the first order equation IGRF 1x1 (blue line) and third order equation IGRF 3x3 (green line).

In the mission analysis, the equation at the third order of approximation was implemented, to obtain more accurate and precise results.

3.3 Model for controlled re-entry of space debris

The safe re-entry of man-made objects launched in space has represented an important issue since the beginning of the space activity. The first example of an object that re-enetered is Sputnik-1, the first ever satellite sent in space in 1957 by the Soviets: it was a pressurized aluminum sphere of 58 cm of diameter and it burned up at the re-entry, after three months of acitivity. In that case no debris reached the ground and this event didn't represent an hazardous to people. It was not the case for the Sputnik IV in 1962, which re-enetered the Earth's atmopshere over North America and many fragments of the re-entering debris ended their orbits over the state of Wisconsin [103]. A large fragment, of about 10 kg, impacted in the city of Manitowoc, and many other smaller fragments, of about 1/8 inch in diameter, were found on the roof of the church annex. The only damage reported was the impact impression left on the street, while no loss of life was recorded. A similar event happened with the re-enter of the Skylab in 1979: due to some problems occured during the launch phase, it had not been possible to put the satellite in its nominal orbit and it decayed faster than how it had been foreseen. Even though the experts had previously estimated the impact area, the satellite broke up in several parts much more later than expected, and this moved the landing area predicted [103]. Significant damages were, on the contrary, registered with the re-entry of COSMOS 954, the first nuclear powered satellite, in 1978 [103]: the uncontrolled re-entry of such object required several millions of dollars to locate and recover the radioactive debris produced, with the consequent problems related to contamination effects. By April 1972, there were 44 reported instances where man-made objects impacted the Earth, and in 1991 more than 14,417 decays/re-entries had been recorded [103].
In light of these number, it is clear how the safety in the re-entry operations of space objects represents a critical aspect to be considered. This is even more important if the treatment is extended to manned vehicles, where the safe return of the crew is the primary requirement to be answered.

An uncontrolled re-entry takes place when an object re-enters the atmosphere without any kind of control. In this case the main effect is the disintegration of the system, and most of the times, the generation of fragments that fall on the ground, becoming potential hazardaous for people and properties. This is what happened in the past with Skylab, COSMOS and many other spacecraft that re-entered with no control. Uncontrolled re-entry is typical for space debris, that are unrecoverable systems without any operational capability. The flight path angle in this case is very small, few degrees, and predictions of the impact area and fragments dispersion are affected by significant uncertainties [104]. Several studies have been conducted by NASA, ESA and other organizations, to develop methods and tools for predicting and analyzing debris reentry and ground risk assessment [105] [106].

In case of debris, five potentially hazardous events have been identified to conduct a re-entry safety analysis [104]:

1. Inert debris striking people or structures housing people;
2. Blast waves form explosive debris striking structures orimpacting in the immediate proximity of people or structures housing people;
3. Explosions producing blast waves affecting people in building at some distance as a result of distant focusing overpressure;
4. Toxic emissions from impacting burning propellant, a deflagration on impact or from normally thrusting vehicles;
5. Thermal hazards from solid propellant firebrands or liquid propellant fireballs.

A detailed treatise of atmospheric re-entry of space debris can be found in [104]. We report here the most significant aspects useful for our analysis. As the object lower its orbit due to gravity and drag effect, the heating increases determining, eventually, the fail of the materials with low melting points. It has been observed that magnesium and aluminum fail at approximately 78 km altitude, and being the main materials space debris are made of, this cause a catastrophic breakup of the objects. At this altitude the major breakeup events are mainly independent of vehicle attitude and rates, diameter, shape, and the flight path angle is usually between -0.3 °and -1.5 °(the flight path angle is negative because the veichle is moving from the apogee to the perigee of the re-entering orbit). The high heating rates and the aerodynamic forces that causes the thermal melting and fragmentation and the mechanical fracture are the

primary sources of external destruction. Other destruction sources can derive from internal components, such as propellants tanks with residual fuel or pressurized vessels that, releasing the explosive gases may lead to an explosive destruction. All the fragments continue their fall independently; most of the objects made in aluminum melts away, even though some fragments with low melting points can survive because the were released in the first part of the re-entering trajectory, when high temperatures were not reached yet. Objects made of high melting points like titanium, glass and steel often survive the impact, generating frament of different size that fall on the ground. Fragmentation events and probability to survive the impact are very difficult to predict. From theory, it is known that re-entry heating rates are approximately proportional to the velocity cubed and inversely related to the radius of curvature. The "footprint", i.e. the area where the debris are predictied to occur, should be limited to few hundreds of km^2, but it is difficult to foreseen for uncontrolled re-entries [104].

Dealing with active debris removal, although space debris do not have controlling capabilities during the atmospheric re-entry, it was considered the possibility to perform a kind of controlled re-entry through a propulsive unit, properly designed for this purpose. In this case, the term *controlled re-entry* does not refer to the tipologies of controlled manoeuvres where the re-entering vehicle was able to control the flight in the atmosphere; in case of space debris the main objective is to enter the atmosphere in a way that maximize the probability of disintegration of the debris, or in a specific position along the disposal orbit in order to confine the "footprint" in a limited pre-determined area.

In the NASA-STD-8719.14 *Processing for Limiting Orbital Debris* [26] some general guidelines are reported as regards the controlled re-entry of space debris. We report the main istances that were considered in the mission analysis to size the hybrid unit required to perform the controlled re-entry.

I *If disposal by controlled reentry into the atmosphere is chosen, the trajectory must be designed to ensure that the space structure does not skip in the upper regions of the atmosphere. Therefore, the effective perigee of the reentry trajectory should be no higher than 50 km.*

II *For controlled reentry, the selected trajectory shall ensure that no surviving debris impact with a kinetic energy greater than 15 joules is closer than 370 km from foreign landmasses, or is within 50 km from the continental U.S., territories of the U.S., and the permanent ice pack of Antarctica (Requirement 56627).*

III *For controlled reentries, the product of the probability of failure of the reentry burn (from Requirement 4.6-4.b) and the risk of human casualty assuming uncontrolled reentry shall not exceed 0.0001 (1:10,000) (Requirement 56628).*

The altitude at which the fragmentation events begin is usually set at 120 km. In [107] it is also suggested that, from simulations predicting the destruction of the spacecraft during the re-entry, the flight path angle at the altitude of 120 km should be in the range [-1.5 °, -2.5 °], depending on the initial orbit at which the re-entry burn is applied. Studies conducted in the same paper revealed that very small satellites burn up during re-entry for all initial conditions, so controlled re-entry can be exclued for these objects; for heavy satellites the probability that part of the spacecraft survive at the impact with the atmosphere is high, but a controlled re-entry manoeuvre could allow to predict and limit the footprint of the residual fragments; finally, for medium-size satellites it depends on the initial conditions whether they could reach the ground in large fragments or not. In the last two cases, the compliance with re-entry requirements state in the NASA-STD-8719.14T [10] can be evaluated through proper software, such as DAS.

In our analysis, according to the previous considerations, a preliminary estimation of the size deorbiting kit required for the controlled re-entry, when necessary, was performed with the following assumption:

I perigee of the re-entry orbit = 0 km;

II the altitude at which the encounter with the atmosphere is evaluated is set at 120 km

III the flight path angle at 120 km should be $\leq -1°$;

IV the spacecraft is supposed to move along a circular orbit before the burn.

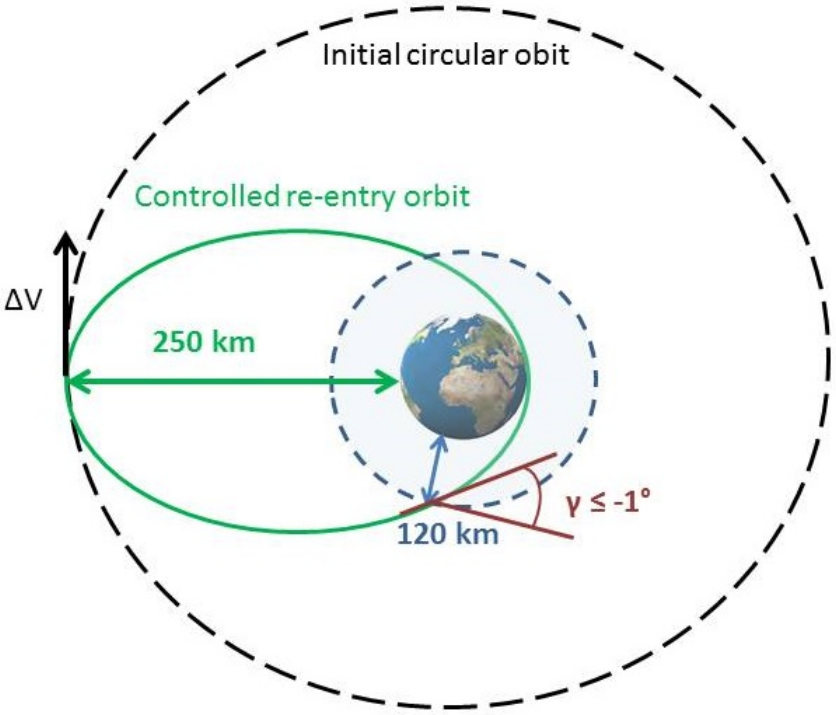

Figure 3.9: Controlled re-entry orbital parameters.

The previous parameters define the characteristics of the re-entry orbit, shown in Figure 3.9: it is an ellipse, with the perigee on the Earth (h = 0 km) and an apogee altitude at 250 km, leading to a flight path angle of $-1.1°$. The ΔV budget for the re-entry manoeuvre is evaluated at the apogee of the re-entry orbit, according to the typical equation of astrodynamics, and it results about 75 m/s:

$$V_c = \sqrt{\frac{\mu}{R_A}} = 7.755 km/s \tag{3.54}$$

$$V_t = \frac{h_t}{R_A} = 7.680 km/s \tag{3.55}$$

$$\Delta V = |V_c - V_t| = 75 m/s \tag{3.56}$$

The hybrid unit for the controlled re-entry will be determined through the graphs reported in section 2.3.4, which give the total mass of the propulsive unit, sized to provide the required ΔV, in function of the total mass of the de-orbited system at the end of the de-orbiting phase (so only inert mass is considered, while the propellant mass for the de-orbiting is excluded).

3.4 Model for multiple transfers optimization

This section is focused on the procedure implemented to determine the preliminary size of the propulsive system needed for the space tug to accomplish multiple transfers in a single mission. Some basic assumptions were made. A removal trend of at least five objects per year was considered, being the trend suggested by previous researches [11] as the minimum number to make ADR effective. Since it is well known that orbital changes in inclination require high ΔV budgets, with consequent high propellant mass for the propulsion system, the manoeuvres were supposed to take place between objects orbiting in the same orbital band as regards the inclination; in the specific case, the procedure was implemented for debris in the SSO, where the inclination range is $99° \pm 1°$. A chemical propulsion technology, based on liquid bipropellants N2O4/MMH, was considered for the space tug. This system was selected since it

appeared to be one of the better solutions, among those available in chemical propulsion, for the specific impulse and the inert lass fraction. Electric propulsion could be an alternative solution, advantageous for the propellant savings that implies thanks to its high specific impulses; however longer transfer times should be expected, increasing the mission duration and decreasing the annual removal rate. In our case, according to [57], the system was characterised by a specific impulse I_{sp} of 300 s and an inert mass fraction f_{inert} of 0.17. The total mass budget was estimated through a routine implemented in *Matab*. The equations used were derived by the basic equations of chemical propulsion:

$$MR = e^{\frac{\Delta v}{I_{sp} g_0}} \tag{3.57}$$

$$\frac{m_{prop}}{m_{pay}} = \frac{(MR-1)(1-f_{inert})}{(1-f_{inert}MR)} \tag{3.58}$$

$$f_{inert} = \frac{m_{inert}}{m_{inert}+m_{prop}} \tag{3.59}$$

where ΔV is the velocity required for the orbital transfer, m_{prop} is the propellant mass, m_{pay} is the mass of the entire system of de-orbiting kits trasnfered to each debris. A safety margin of 10% was considered in the total mass budget. The procedure implemented was articulated in the following steps: once proper de-orbiting kits are determined for each target debris and the removal sequence is defined, and so all the ΔV required in each transfer, the set of equations is solved considering as payload mass the mass of the de-orbiting kits that are effectively transfered in each manoeuvre. Starting from the last trasnfer, m_{pay} is the mass of the last de-orbiting kit that is released; known the ΔV the required propellant mass for the manoeuvre is determined through equation 3.58 and then the inert mass through equation 3.59. The total mass is the sum of these two contributions. The procedure is then repeated backward, considering in each step the mass of the payload as:

$$(m_{pay})_i = \sum_{i=4}^{1} [(m_{DK})_5 + (m_{DK})_i + (m_{prop})_{i+1}] \tag{3.60}$$

The final mass of the propulsive system is the sum of the inert mass and the propellant mass obtained in each step.

In order to minimize the total mass odf the space tug, the sequqnce of orbital transfers should be optimized, which is translated in the minimization of the ΔV budget necessary to accomplish the entire mission. Since all the targets lied in the same SSO region, the altitude and inclination variations did not affect significantly the total ΔV; more critical were the changes in terms of RAAN. Several sets of five objects were considered and a *Matlab* code was developed to determine the best sequence of multiple orbital transfers. This part of the activity was developed in collaboration with Prof. Lorenzini.
The structure of the procedure is schematically presented in Figure 3.10. The sequence should be completed within one year. It was set, for each target, a time interval for each rendezvous and capture manoeuvre of about 15 days. The remaining time for the orbital transfers was then 290 days. In order to consider the advantage derived by the natural alignment of the RAAN, that could allowed significant propellant savings in the final mass budget, it was fixed a maximum time limit within the alignment should take place. If the time of the natural alignment is exceeded, an impulsive manoeuvre is foreseen. Considering that an impulsive manouvre is usually fast, and in the best case scenario where natural alignment is possible for all the debris, the maximum time allowed for this operation, for each debris, is 72 days. The total ΔV budget for each orbital sequence is the sum of three main components: 1) the ΔV for the RAAN alignment, when required; 2) the ΔV for the orbital transfer to approach the debris orbit; 3) the ΔV to rendezvous with the target debris. The total number of possible combination of five objects, and then the number of possible sequences, is 5!. The output of the code is the minimum ΔV budget, among all the possible combination evaluated. This value, and the single ΔV evaluated in the correspondent sequence of orbital transfers, are then used to estimate the mass budget for the space tug.

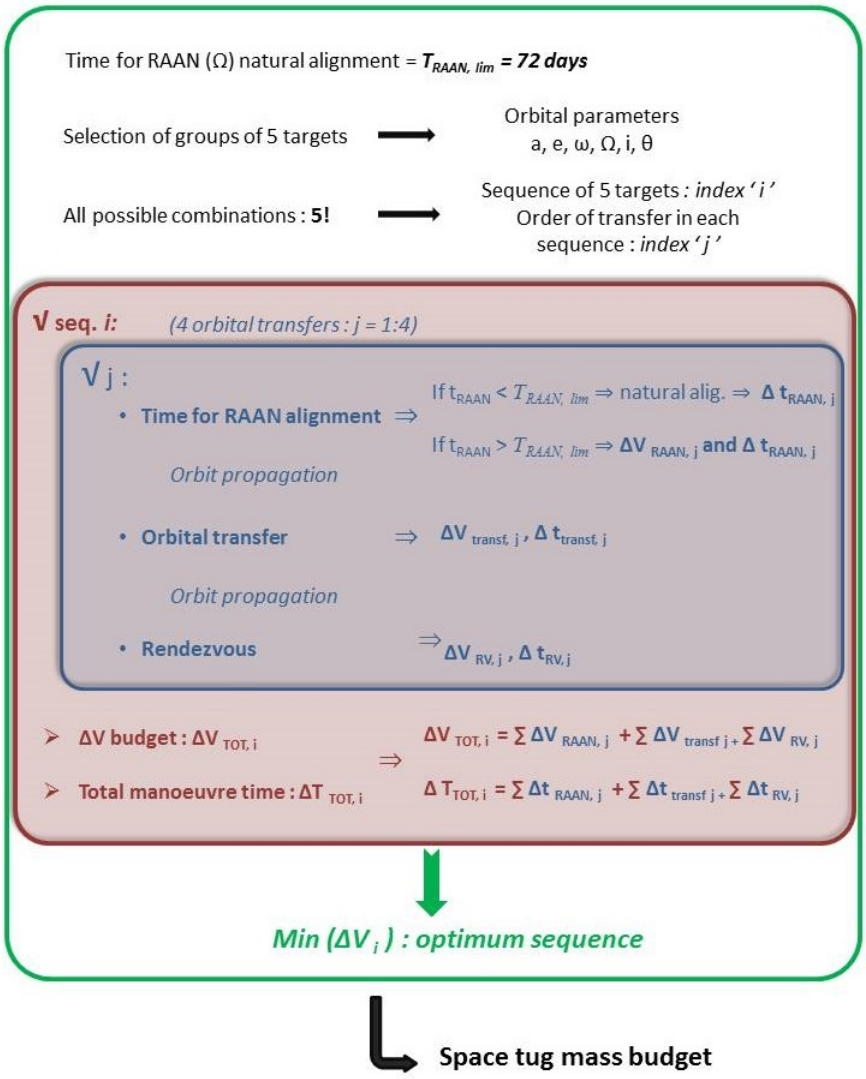

Figure 3.10: Scheme of the procedure implemented to determine the optimum sequence of orbital transfers that minimize the total ΔV budget, and so, the propellant mass required to de-orbit a set of five selected debris within 1 year. For each set of 5 debris, the total number of possible combination is 5!. For each sequence i ($\sqrt{seq.i}$ in the figure) four orbital transfers are performed. For each orbital transfer j ($\sqrt{j}$ in the figure) it is determined the time required for the RAAN alignment and the consequent ΔV, that is the sum of the ΔV for the RAAN alignment, if required, for the orbital transfer and the rendezvous maneouvre. The total ΔV budget for the i-th sequence is the sum of the ΔV determined for each transfer j, as well as the total maneouvre time is the sum of the time for the RAAN alignment, the otbital transfer and the rendezvous manoeuvre of each transfer j.

3.5 Mission Analysis and Results

Three different case studies were defined and analysed:

1. **Case study #1:** comparison between drag sails and electric propulsion performances; debris selected randomly in a wide range of mass and initial orbits.
2. **Case study #2:** comparison between electric propulsion and electrodynamic tether performances and multiple transfers optimization; debris belonging to SSO.
3. **Case study #3:** comparison between electric propulsion, electrodynamic tether and hybrid propulsion performances. Debris belonging to all the five orbital regions identified as the most critical.

The first two case studies allowed to identify some general behaviours concerning the effects of the modular architecture approach as well as the parameters that influence mostly the mission performances with the selected de-orbiting technologies. The third case is developed extending the results previously obtained to the entire debris population. Each case study is divided in three main section: I) mission scenario, II) mission assumptions and III) mission procedures. All the procedures are developed considering the requirements reported in the NASA SDT concerning the*Postmission Disposal of Space Structures* and indicated in section 1.3.1 [10] . When drag sails are employed, the limitation on the orbital lifetime of 25 years is assumed, while for all the other options it is considered the limitation of 10 years stated for the direct retrieval.

3.5.1 Case study #1: mission analysis

The main objective of this case study was to analyse the de-orbiting performances of drag sails and electric propulsion, and to study a possible hybrid solution based on the combination of both these technologies.

Mission scenario

Three main de-orbiting scenarios were considered:

1. **de-orbiting by means of drag sail only:**
   a drag sail is deployed at the beginning of the de-orbiting manoeuvre, enhancing the effect of the atmospheric drag and reducing, in this way, the orbital lifetime of the selected debris. The effective area is related to the size of the sail stowed in the drag sail unit.
2. **de-orbiting by means of electric propulsion only:**
   the orbit of the debris is lowered through a continous low thrust manoeuvre until an intermediate altitude from which the natural re-entry occured within 25 years.
3. **de-orbiting by means of electric propulsion and drag sails combined:** the de-orbiting is accomplished through a combined maneouvre that consistes of two main phases:

   I phase: the orbit of the debris is lowered through a continous low thrust manoeuvre employing a set of electric propulsion units, where the number of units depends on the debris mass and altitude;

   II phase: once the intermediate altitude is low enough to take advantage form the atmospheric drag, the thrusters are shut down and a sail is deployed and contributes to accelerate the descending phase until the final orbit is reached.

Mission assumptions

The main assumption adopted for this analysis were:

- the mission was supposed to begin with the de-orbiting kit already attached on the selected debris;
- a controlled re-entry manoeuvre is foreseen starting at an altitude of 250 km; see section 3.3 for details;

- six representative debris were selected (Table 3.1), with variable mass and from different orbital bands. One of these debris, in particular, is of the same size of ENVISAT, since it represents one of the most interesting targets at the attention of the European space community because of its dimensions. For each debris, the orbital lifetime was estimated through the software DAS to verify that it was greater than 25 years. The orbital parameters and the A/m ratio were obtained from the Celestrack on-line catalogue. The main properties are listed in table 3.1;

- four types of elementary units to assemble were sized and implemented in the calculations: 1) a main bus unit, 2) a drag sail unit, 3) an electric thruster unit and 4) a hybrid module for the controlled re-entry. The mass of each unit was estimated through the procedures presented in sections 2.3.5 2.3.1 and 2.3.2 for the first three; the mass of the hybrid module to perform the controlled re-entry manoeuvre was estimated according to the sizing procedure explained in section 2.3.3 in the paragraph *Hybrid unit for controlled re-entry*. The mass badgets for each unit are shown in Table 3.2;

- a schematic rapresentation of a possible de-orbiting kit configuration is represented in Figure 3.11. Both the solar panels of the propulsive units and the sail, when deployed, contribute to increase the cross sectional area of the object; furthermore, the attached de-orbiting kits increase the mass of the system. These parameters influence the ballistic coefficient of the de-orbited system. The *A/m ratio* was evaluated in three different cases: 1) initial debris A/m; 2) A/m due to the solar panels; 3) A/m due to the drag sail. The maximum A/m was evaluated in each de-orbiting scenario and implemented in the drag effect evaluations;

- a single unit with a drag sail was considered; this technology is quite simple and it was observed from the preliminary sizing procedure that the dimension of the unit does not change a lot if the sail area is increased. Furthermore, the mass of the case does not affect significantly the total mass budget of the unit. Three different sail area were considered: 10 m^2, 20 m^2, 30 m^2. For very massive debris, even larger sails could be needed to de-orbit within 25 years. Although the deployment of a 20x20 m^2 sail has been performed at DLR, there are still several critical aspects that have to be considered for an ADR mission: the strength and the resistance of such systems to the aerodynamical loads that act on the structures during a de-orbiting manoeuvre should be evaluated; Furthermore, large structure deployed on-orbit imply higher risks of collisions and a proper risk assessment analysis could be required for very large systems. Both these aspects were out of scope at this point of the analysis, so no more researches were done in this field. For these reasons, it was assumed to limit the sail area to 30 m^2, to simulate a more realistic and feasible scenario with the technologies available;

- the number of propulsive units assembled was varied from 1 to 10 in the following way: $n_p = [1, 2, 3, 4, 6, 8, 10]$; for each case it was evaluated the altitude reached at the end of the propulsive phase through equation 3.40;

- the maximum propellant mass stowed in a single propulsive unit was set equal to the maximum propellant mass required to de-orbit the less massive debris from the lowest orbit; among the selected debris, Debris #1 fulfils these conditions. The total propellant mass was set at 16 kg.

- the electric thruster BUSEK BHT-200-X2B was selected for the analysis. Its performances are: $I_{sp} = 1300s$, nominal power P = 200W, thrust F = 17 mN. This electric thruster is flight qualified: it was integrated on the TacSat-2 satellite, launched in 2006.

Mission procedure

A procedure was developed and implemented in *Matlab* in order to evaluate the performances in each scenario, in terms of remover configuration, i.e. total number of units assembled, and hence mass of the de-orbiting kit, and total de-orbiting time. The procedure implemented for this mission analysis is shown schematically in Figure 3.12.

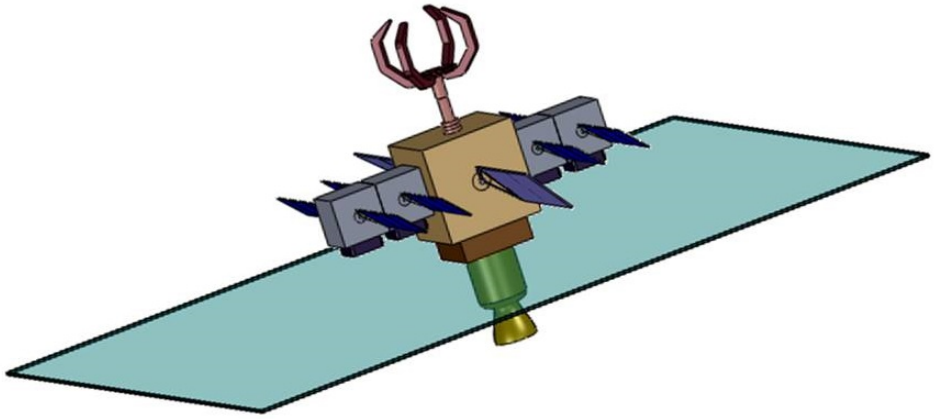

Figure 3.11: Example of a de-orbiting kit composed by both drag sail unit and electric propulsion units. An hybrid rocket (schematically represented in yellow) is foreseen for the controlled re-entry.

Debris	**mass**	h_i	**i**	**A/m**
	[kg]	**[km]**	**[deg]**	$[m^2/kg]$
#1	743	717	73.99	0.002386
#2	1030	810	98.5	0.000156
#3	1421	860	98.81	0.000257
#4	2279	751	108	0.009283
#5	3221	850	70	0.00546
#6	8050	767	98.4	0.0031

Table 3.1: Selected debris for the mission analysis: main orbital parameters (initial altitude and inclination), mass and A/m ratio.

Main Bus Unit	
Total mass [kg]	55
Drag Sail Unit	
Drag sail mass [kg] (A = [10 - 30] m^2	4 - 5
Electric Propulsion Unit	
Dry mass [kg]	35
Maximum propellant mass [kg]	14

Table 3.2: Mass budget of the main bus unit, drag sail unit and electric propulsion unit employed in case study #1. The subsystems of the main bus unit, and the relative mass, are indicated in 2.1, section 2.3.5

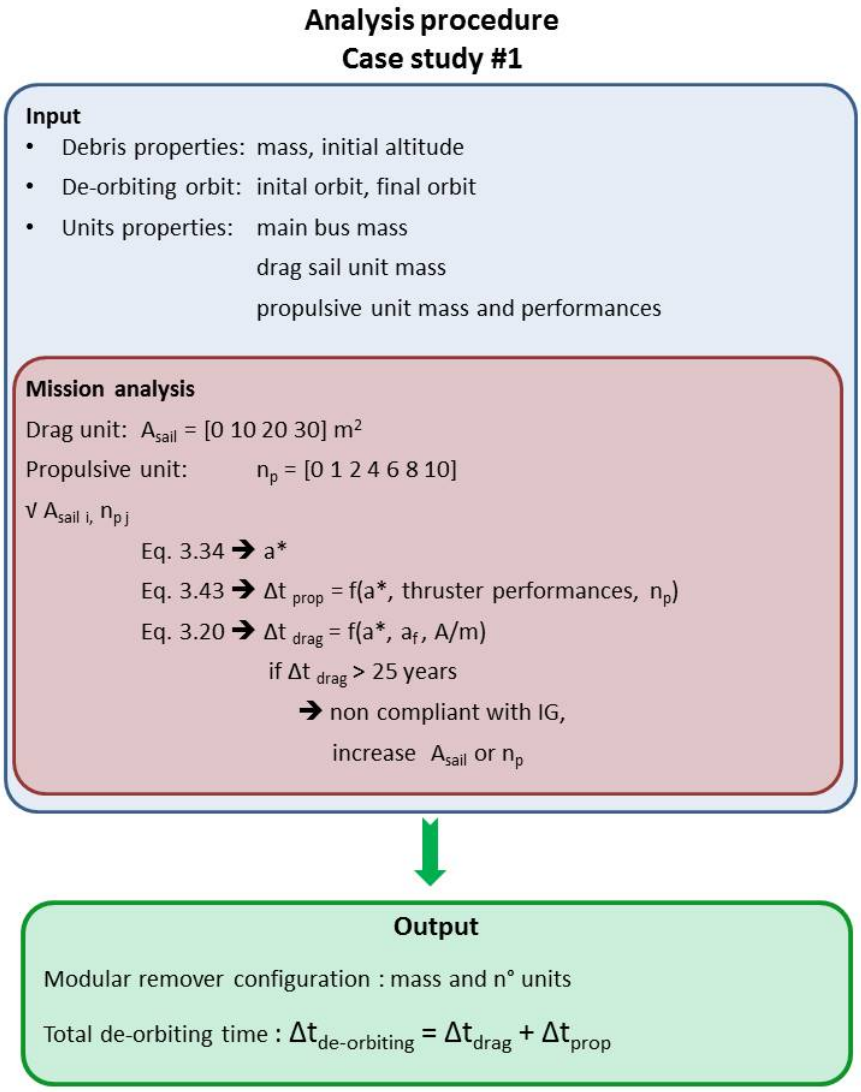

Figure 3.12: Scheme of the code developed and implemented in *Matlab* to analyse the ADR scenario emphCase study #1

3.5.2 Case study #1: results

De-orbiting by means of drag sail only

As it was expected, the employment of a drag sail only is feasible in a limited number of cases, where the debris mass and the initial altitude are quite low. In our case the only debris that respected these two conditions was the #1 (see Table 3.1. For this debris, a drag sail of 20 m^2 could allow to de-orbit from the initial altitude of 717 km within 18 years, while a sail with an area of 30 m^2 reduces the orbital lifetime to 12.5 years. These values are mean values obtained through the Equation 3.20; a more accurate estimation of the de-orbiting time could be obtained through the software DAS, which takes into account the solar flux variation during the de-orbiting manoeuvre, for a given epoch. The results of these simulations are reported in the last column of Table 3.3. As it can be seen, the analytical model underestimates the orbital lifetime respect to the values obtained with DAS. This is mainly due to the solar flux variations that are not considered in the model. A safety factor should be then considered and an increase in the sail size could be needed in case of de-orbiting through drag sail only. Anyway, from these results it emeregs that drag sails could be not efficient for the debris population considered in our study.

Debris #1				
A_{sail} $[m^2]$	m_{rem} $[kg]$	$m_{rem} \backslash m_{deb}$ %	$\Delta T_{deorbit}$ $[y]$	ΔT_{DAS} $[y]$
20	53.3	7.17	18.7	[26 - 35]
30	54	7.27	12.5	[20 - 16]

Table 3.3: De-orbiting by means of drag sail only: results. The table shows the remover configuration, the remover mass fraction (%) and the total de-orbiting time for a given sail area.

De-orbiting by means of electric propulsion only

The main results are shown in Figure 3.13 and 3.14.

The advantage of a propulsive only scenario is that the propulsive phase could be employed to lower the orbit of the debris at an altitude where atmospheric drag is more effective and allows a faster re-entry of the debris. In such way, a significant reduction in the orbital lifetime derives from the propulsive phase, respect to a drag only scenario, and mass savings are possible since the debris could continue the descending phase without any additional device. Obviously, the total orbital lifetime is influenced by the intermediate orbit at which the propulsive phase ends, as well as the A/m ratio of the debris. If this parameter becomes too high and the probability of collisions during the second phase becomes significant, it is sufficient to increase the number of assembled units in order to reduce the manoeuvre time and, hence, the collision risk. And this is one of the main advantages of the employment of the modular architecture. Anyway, it can be noted that the intermediate altitude reached with the lowest number of propulsive units, which correspond to the minimum number of units needed to lower the orbit at a level where the re-entry of the debris occurs within 25 years, is in all the cases around 600 km. The most critical orbits for the collision risk assessment are at higher altitudes, so it is reasonable to conclude that propulsion could be a promising solution for ADR. It can be observed, for the less massive objects (mass $\leq$ 2000 kg), one or two propulsive units are sufficient to lower the orbit enough to guarantee a fast re-entry of the debris: the orbital lifetime is almost always less than 4 years (well below the limit of 25 years). For more massive objects, the number of propulsive units varies between 4 and 6, for the same orbital lifetime; a numer of assembled units $n_p \geq 6$ appears to be useless and hence the remover complexity can be avoided.

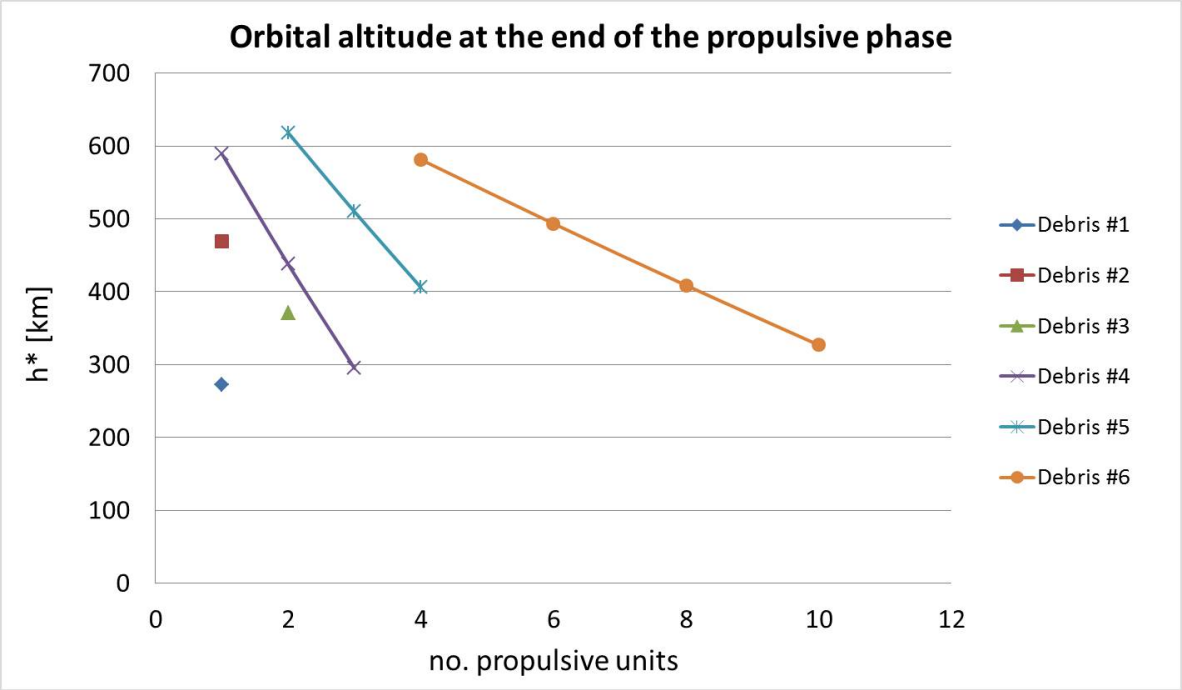

Figure 3.13: Intermediate altitude that allows a natural re-entry of the debris within 25 years, reached after the propulsive phase, in function of the number of propulsive units (propulsion only scenario).

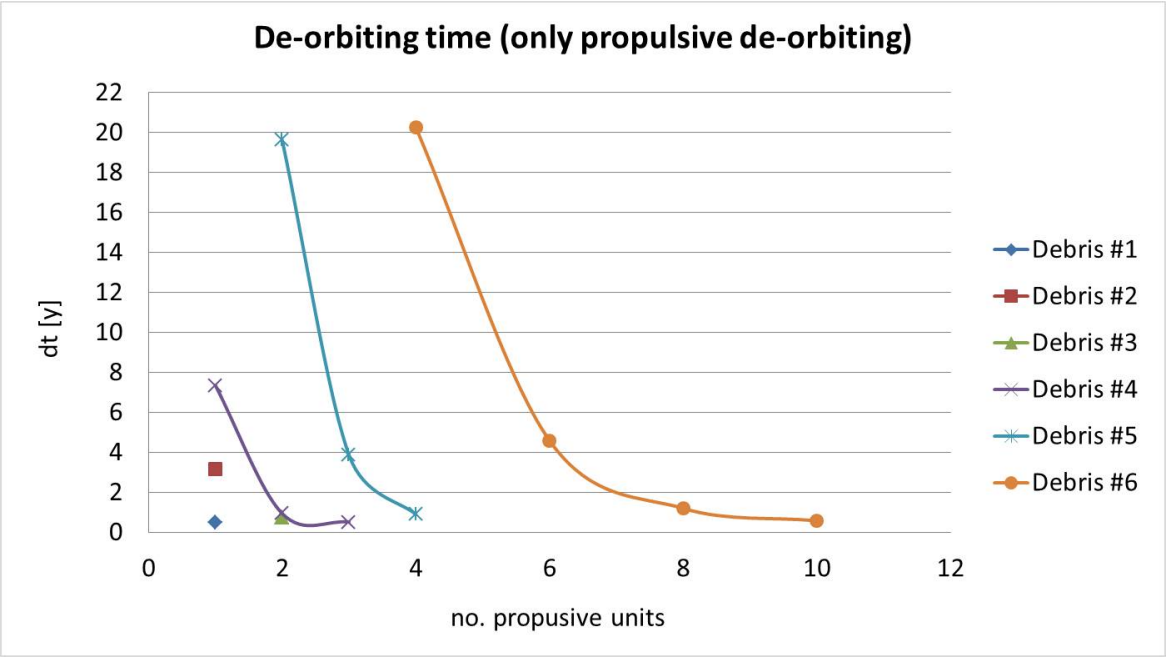

Figure 3.14: Total orbital lifetime in case of de-orbiting performed by means of propulsion only

De-orbiting by means of electric propulsion and drag sail combined

A combined manoeuvre gathers the advantages of both the propulsion only and drag only scenarios. In this case it can be determined the better remover configuration that allows to optimize both the total remover mass and the orbital lifetime. In this analysis, the total de-orbiting kit mass and orbital lifetimes obtained in case of combined manoeuvre are compared to the mass and orbital lifetime determined in the previous analysis, where only electric propulsion was implemented, considering for each debris, only the values correspondent to the minimm number of propulsive units required to allow the natural re-entry of the object within 25 years.
The results of the comparison are shown in Figures 3.15 - 3.20. The blue bars in the charts refers to propulsive mission scenario, while bar in light blu refer to the combined manoeuvre. The number of units in the latter case is the sum of the propulsive units and the drag sail unit, recalling that only one drag sail unit is always employed, regardless the sail area. Debris #1 can be excluded from this analysis: as emerged from the previous analysis, the debris can be de-orbited employing only a drag sail or elecric propulsion. In the former case the mass of the removal system is very low, being only the mass of the main bus plus the drag sail unit, but the de-orbiting time is quite high, and proper risk assessment evaluations should be performed to exclude any possible failure due to orbital impacts during the de-orbiting phase. On the other hand, electric propulsion allows a faster de-orbiting, although the mass of the de-orbiting kit is almost doubled. Figure 3.15 reveals that a combined manoeuvre is not useful, being the remover mass and the total de-orbiting time the same in both de-orbiting scenarios. The main effect of the implementation of a combined manoeuvre can be observed in Figures 3.16, 3.18, 3.19 and 3.20: simply adding a drag sail unit to the de-orbiting kit determined in the *only propulsion* scenario, with a minimal increase of the total removal system mass, the de-orbiting time can be significantly reduced. The decrease is more evident for debris with mass lower than 4000 kg, like debris #2, #4 and #5, where the change in time is between 28% and 60% respect to the de-orbiting time obtained considering a natural re-entry after the propulsive phase. For more massive debris, such as debris #6, the reduction of the orbital lifetime is less effective, being around only 16%. In this case, an increase in the number of propulsive units could be considered, both if natural re-entry or drag sails are implemented. Another effect can be observed from the results obtained for debris #3, Figure 3.17: in this case, two propulsive units were needed to lower the orbit enough so as naturally re-entry would have occured within 25 years. If a drag sail is employed, the number of propulsive units can be reduced to one, and the overall system mass, with the darg sail unit, cqan be reduced of 28%. Although the employement of the largest sail considered in this mission analysis (30 m^2), the de-orbiting time in this case increases respect to the propulsion only scenario. Risk assessment evaluations could be performed to identify the better de-orbiting scenario for debris #3. In conclusion, drag - propulsion combined scenarios resulted advantageous for debris with mass lower than 4000 kg, depending on their initial orbit: faster de-orbiting maneouvres could be performed with a minimal increase of the de-orbiting kit mass. For more massive debris, increases in the number of propulsive units or sail area should be considered to significantly accelerate the de-orbiting phase. Risk assessment evaluation are anyway needed to identify the better solution resulting as the compromise between the better combination of remover mass and orbital lifetime.

To conclude the analysis, the total de-orbiting kit mass, in case of a combined maneouvre, was compared to the debris mass. As it can be observed from Figure 3.21, the de-orbiting kit mass is a small percentage of the debris mass, lower than 15% in most of the examined cases. Furthermore, it emerged that this percentage decreases as the debris mass increases.

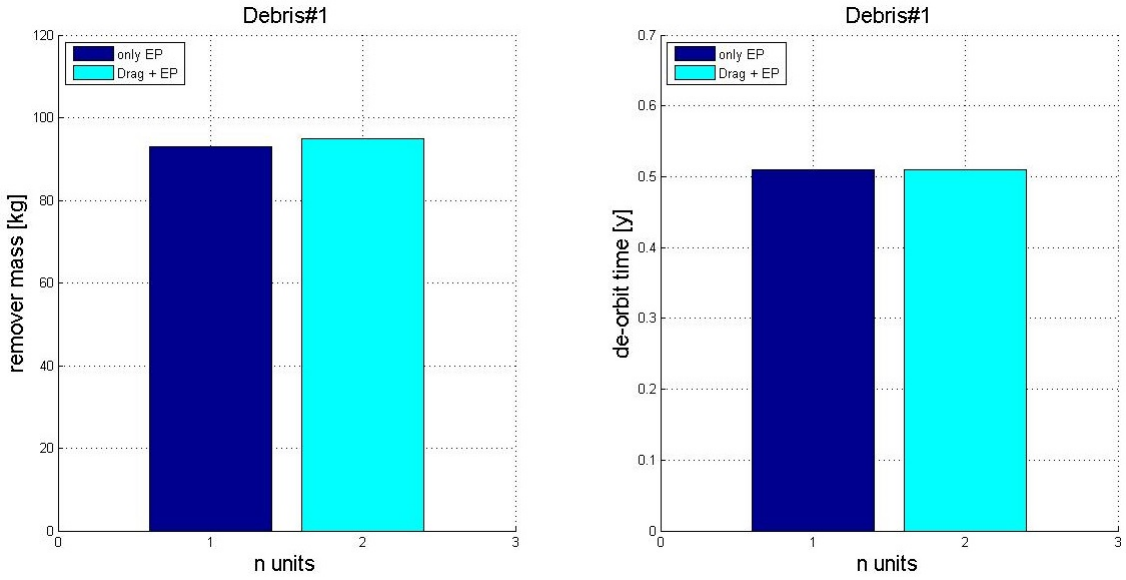

Figure 3.15: *Debris #1.* Total mass of the de-orbiting kits and total de-orbiting time: comparison between de-orbiting by means of propulsion only and combined maneouvre drag sail + electric propulsion ($A_{sail} = 10\ m^2$).

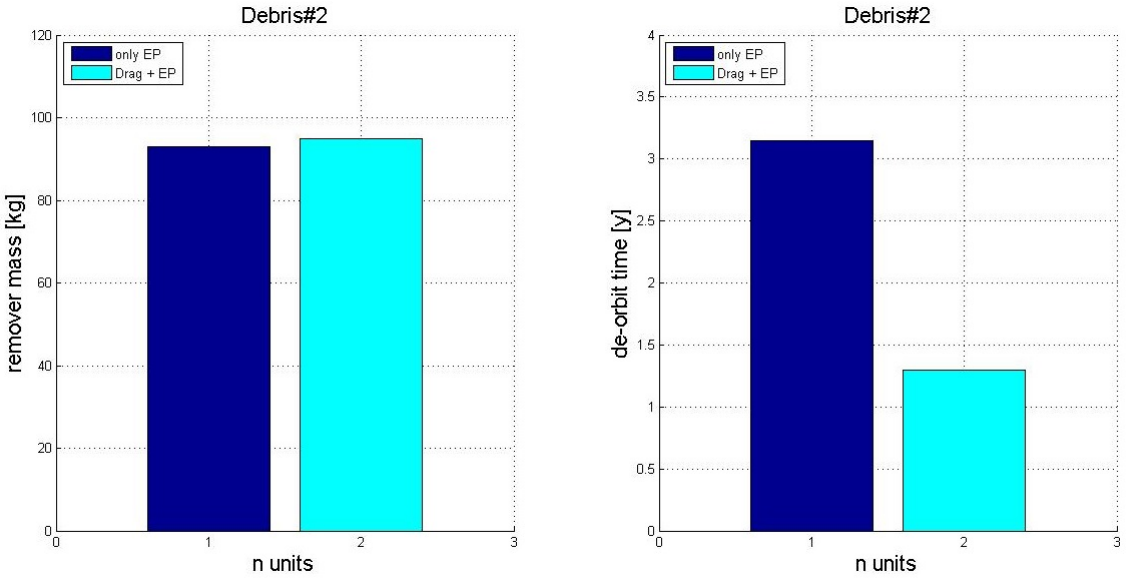

Figure 3.16: *Debris #2.* Total mass of the de-orbiting kits and total de-orbiting time: comparison between de-orbiting by means of propulsion only and combined maneouvre Drag sail + electric propulsion ($A_{sail} = 10\ m^2$).

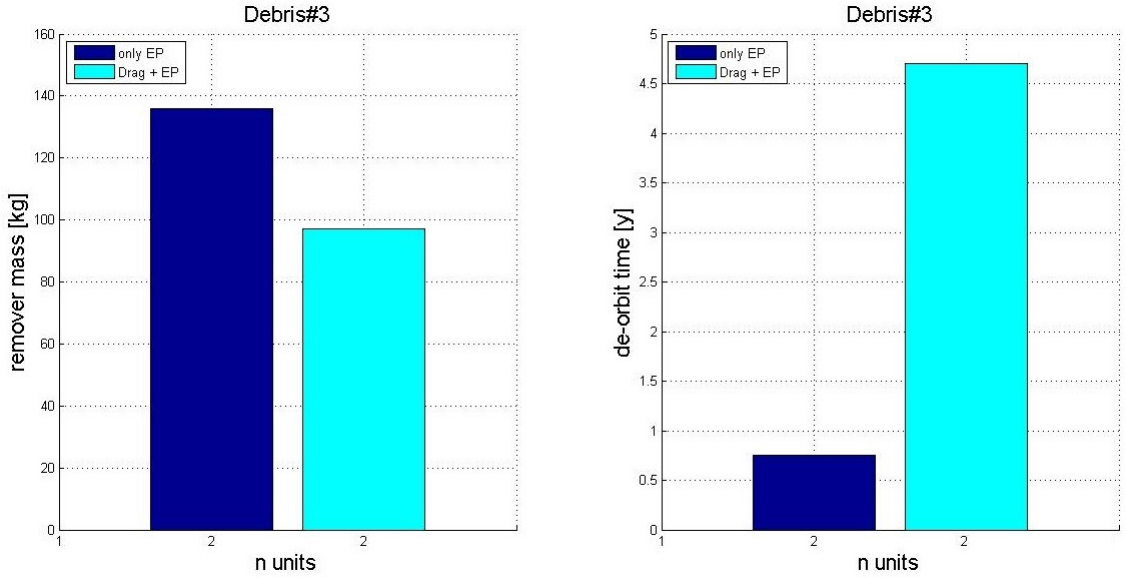

Figure 3.17: *Debris #3.* Total mass of the de-orbiting kits and total de-orbiting time: comparison between de-orbiting by means of propulsion only and combined maneouvre Drag sail + electric propulsion ($A_{sail} = 30\ m^2$).

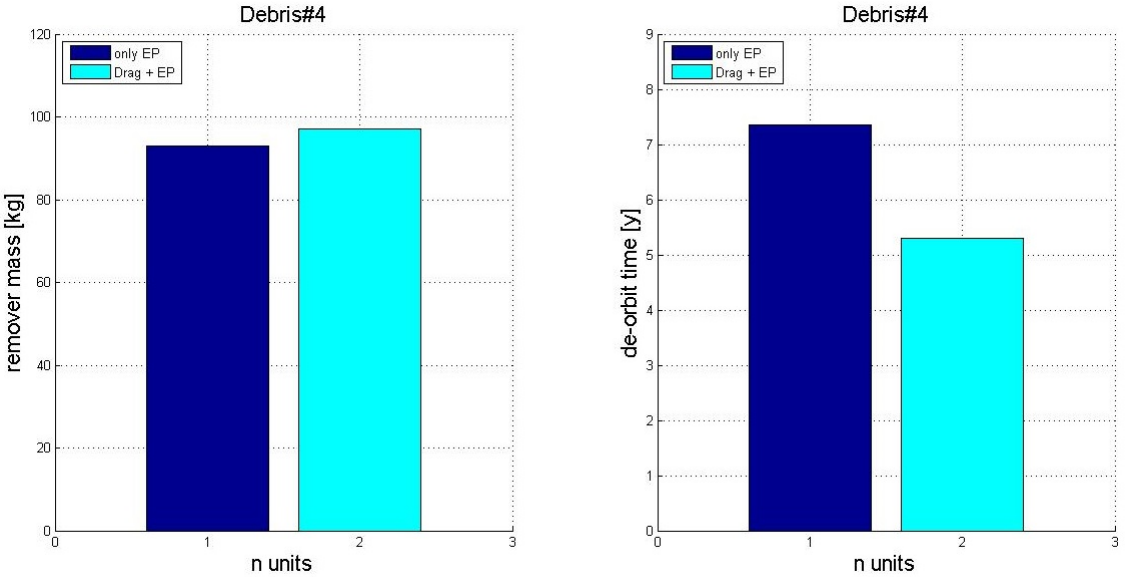

Figure 3.18: *Debris #4.* Total mass of the de-orbiting kits and total de-orbiting time: comparison between de-orbiting by means of propulsion only and combined maneouvre Drag sail + electric propulsion ($A_{sail} = 30\ m^2$).

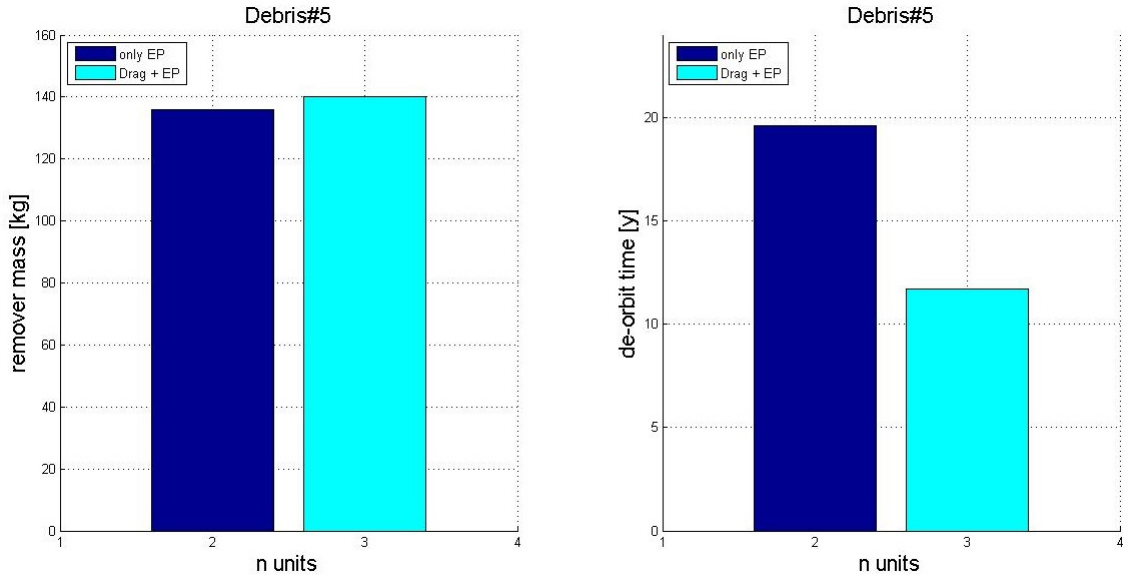

Figure 3.19: *Debris #5.* Total mass of the de-orbiting kits and total de-orbiting time: comparison between de-orbiting by means of propulsion only and combined maneouvre Drag sail + electric propulsion ($A_{sail} = 30\ m^2$).

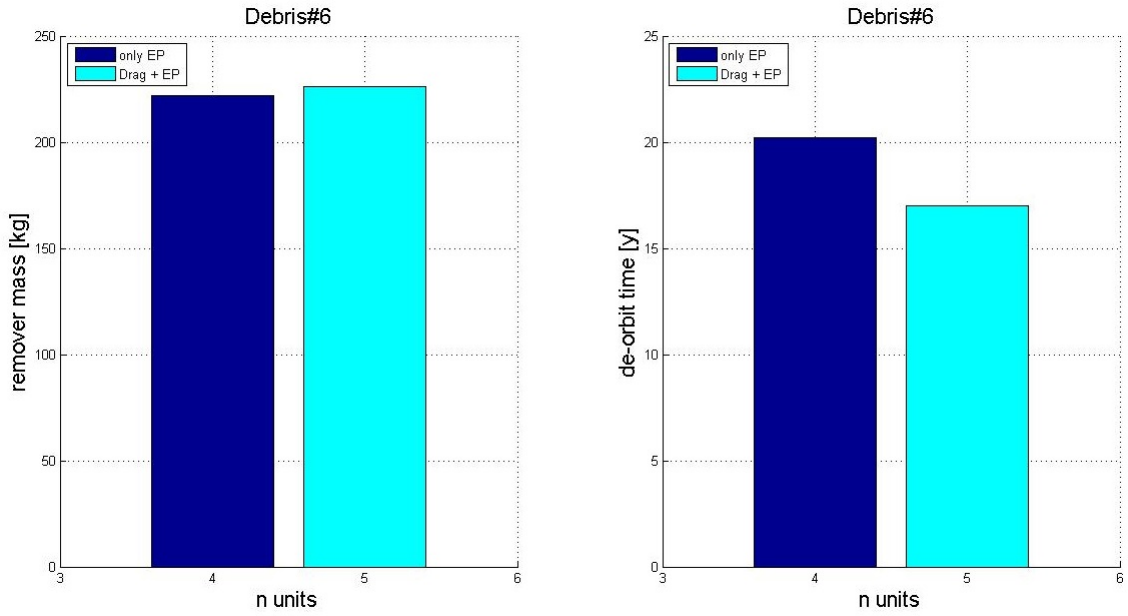

Figure 3.20: *Debris #6.* Total mass of the de-orbiting kits and total de-orbiting time: comparison between de-orbiting by means of propulsion only and combined maneouvre Drag sail + electric propulsion ($A_{sail} = 30\ m^2$).

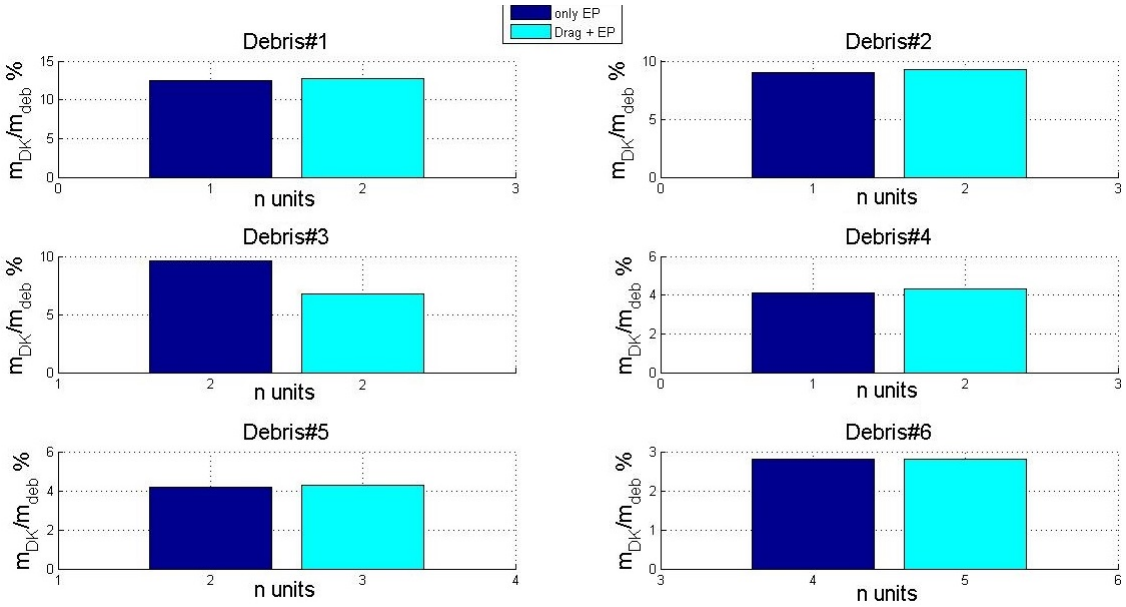

Figure 3.21: Remover mass fraction, in percentage, respect to the debris mass. As it can be observed, the mass of the remover is, in most of the cases, less then 15% of the debris mass

Controlled re-entry

The mass of the hybrid module was determined considering the final mass of the de-orbited system (debris + de-orbiting kit). As example, it was selected the most massive case among the previous analysed, i.e. the *maximum number of propulsive units - maximum drag sail area*. The results of such analysis are listed in table 3.4. As it can be observed, the hybrid unit required for the controlled re-entry is always a small percentage, around 1.3%, of the entire system mass.

Debris	m_{HPU} [kg]	$m_{HPU} \backslash m_{sys}$ [%]
#1	11	1.31
#2	14.6	1.29
#3	20.5	1.31
#4	35.1	1.43
#5	46.6	1.35
#6	110	1.29

Table 3.4: Mass of the hybrid unit required to perform a controlled re-entry from an altitude of 250 km, in function of the final mass of the de-orbited system. In the second column it is reported the percentage of the hybrid unit mass respect to the final system mass.

3.5.3 Case study #2: mission analysis

This case study focused on two main aspects: the first one was the comparison between electric propulsion and electrodynamic tether performances; the second one was the analysis and optimization of a multiple transfers maneouvre.

Mission scenario

Electric propulsion (EP) and an electrodynamic tether (EDT) were assumed as de-orbiting means. Tow main scenarios are then possibile:

1. **de-orbiting by means of electric propulsion only:**
   the debris is lowered through a continuous low thrust manoeuvre until the final altitude of 250 km is reached; then, a controlled re-entry is performed by means of a hybrid engine module;
2. **de-orbiting by means of electrodynamic tether only:**
   the orbit of the debris is lowered deploying an electrodynamic tether, 5 km long, until the final altitude of 250 km. The tether is then cut to allow the controlled re-entry maneouvre by means of a hybrid engine module.

No combined manoeuvres were considered in this case.
Concerning the orbital transfers, a servicing vehicle, indicated as space tug, was responsible to carry the de-orbiting kits in the debris orbit and to perform the rendezvous maneouvres to allow its capture.

Mission assumptions

As concern the de-orbiting manoeuvres, the following assumptions were adopted:

- the mission was supposed to begin with the de-orbiting kit already attached on the selected debris;
- a controlled re-entry manoeuvre is performed at an altitude of 250 km; see section 3.3 for details;
- two sets of five debris were selected among the objects in the SSO; in the first one was a class of homogeneous objects, listed in Table 3.5); in particular, four Ariane 40 and the Ariane 5 were selected as possible targets among the Ariane third stages class. The second set of debris, listed in Table 3.6, was composed by spent spacecraft, with mass variable between 3000 kg and 8100 kg;
- four types of elementary units to assemble were sized and implemented in the calculations: 1) a main bus unit, 2) an electric populsion unit, 3) an electrodynamic tether unit and 4) a hybrid module for the controlled re-entry. The mass of each unit was estimated through the procedures presented in sections 2.3.5, 2.3.2 and 2.3.4 for the first three; the mass of the hybrid module to perform the controlled re-entry manoeuvre was estimated according to the sizing procedure explained in section 2.3.3 in the paragraph *Hybrid unit for controlled re-entry*. The mass badgets for each unit are shown in Table 3.7;
- the total propellant mass was set equal to the maximum propellant mass that could be stowed in order to limit the total unit mass to 100 kg, that is the typical mass of a microsatellite;
- the electric thruster selected for this analysis was the model BUSEK BHT-200-X2B, the same employed in study case #1.

As concern the multile transfers manoeuvre, these main assumptions were adopted:

- a removal trend of 5 debris per mission was set: this is the minimum number of removals required to make ADR effective in long term [11] [22] [28];
- the mission was considered to start with both the space tug and the de-orbiting kits already in the same orbit and docked together;
- assuming the removal trend of 5 objects per mission, it was supposed that five remover vehicles were launched in the same orbit of the space tug, already assembled in a single larger structure. The entire system is transferred by the space tug to each selected debris, according to an optimized sequence of manoeuvres. At the end of each transfer, a remover kit is detached from the structure to accomplish the capture and de-orbiting operations of the correspondent debris, and the space tug transfers the remaining de-orbiting kits to the subsequent targets.

Debris set #1				
Debris Name & (Number)	h_{mean} **[km]**	**i [deg]**	**Ω [deg]**	**mass [kg]**
ARIANE 40 (20443)	766	98.76	35.78	1800
ARIANE 40 (21610)	756	98.76	58.85	1800
ARIANE 40 (22830)	786	98.76	15.76	1800
ARIANE 40 (25261)	780	98.34	15.80	1800
ARIANE 5 (27387)	770	98.25	27.05	3600

Table 3.5: Set of homogeneous debris selected among the thrid stages in the SSO band.

Debris set #2				
Debris Name & (Number)	h_{mean} **[km]**	**i [deg]**	**Ω [deg]**	**mass [kg]**
SPOT 5 (27421)	822	98.763	121.79	3000
METOP-A (29499)	817	98.67	111.35	4100
METOP-B (38771)	817	98.72	111.19	4424
COSMOS-2442 (33272)	719	98.11	110.30	6500
ENVISAT (27386)	764	98.44	120.53	8050

Table 3.6: Set of eterogeneous debris selected among the debris in the SSO band.

Main Bus Unit	
Total mass (with 20% margin) [kg]	50
Electric Propulsion Unit	
Dry mass [kg]	27
Maximum propellant mass [kg]	70
Electro-dynamic Tether Unit	
EDT Unit mass (debris mass $\leq$ 4000 kg) [kg]	50
EDT Unit mass (debris mass $\geq$ 4000 kg) [kg]	70

Table 3.7: Mass budget of the main bus unit, electric propulsion unit and electro-dynamic tether unit. The mass of the main bus unit, of the electric propulsion unit and of the electrodynamic tether unit were estimated according to the sizing procedure presented in sections 2.3.5, 2.3.2 and 2.3.4 respectively.

Analysis procedure

Two procedures were developed and implemented, one relative to the de-orbiting manoeuvre, shown in Figure 3.22, and the other one to otpimize the multiple transfers maneouvre. This second procedure was already presented in section 3.4

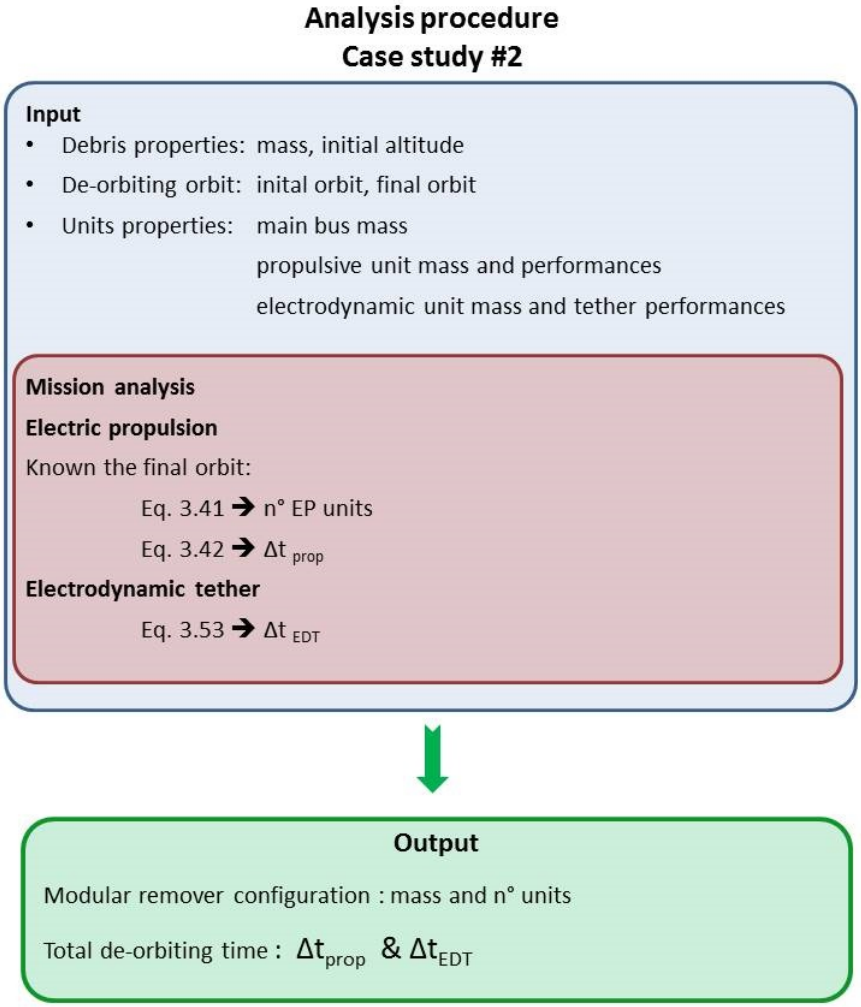

Figure 3.22: Scheme of the code developed and implemented in *Matlab* to analyse the ADR scenario *Case study #2*

3.5.4 Case study #2: results

In Table 3.8 it is shown the total number of assembled units required if electric propulsion is employed (second column) or if the de-orbiting is performed through an electro-dynamic tether (fourth column). As it can be seen, when the removal is accomplished through an electro-dynamic tether, it is required only one unit in all cases, while the number of propulsive units increases as the mass of the debris increases. In both cases, the mass of the de-orbiting kit is always a small percentage of the debris mass, as it had already emerged form the analysis in the previous section, and, furthermore, this percentage is lower in case of the electro-dynamic tether. From Figures 3.23 and 3.24 it emerges that for debris with mass lower than 2000 kg, as for example the Ariane 40 third stages, the mass of the propulsive remover kits is comparable to the values obtained with the electro-dynamic tether. This fact s also confirmed from the data reported in Table 3.9: the difference, in percentage, between the de-orbiting kit mass required for the electric propulsion and for the EDT is only 10% and considering the approximations that are

introduced in the preliminary sizing of the units, it can be neglected. For debris with mass greater than 2000 kg the EDT seems to perform better as regards the de-orbiting kit mass, being always lower than the mass obtained with the electric propulsion. This results is quite obvious since as the mass of the debris increases, more propellant mass is required to de-orbit the objects, and hence a higher number of units has to be assembled, while in case of EDT, only one unit is employed in any case. The opposite can be observed concerning the de-orbiting time; for debris with mass lower than 2000 kg, the performances are still comparable between the two technologies, although EDT seems to be slightly better; for debris mass greater than 2000 kg, electric propulsion allows a faster de-orbiting, and the difference with the EDT becomes larger as the mass of the debris increases: this is shown in the third column of Table 3.9, where it is reported the percentage difference in the de-orbiting time betwee EP and EDT, evaluated respect to EDT. For more massive objects, as the Ariane 5 third stage or the satellites in 3.6, the number of propulsive units required for the de-orbiting increases, and hence the propulsive thrust, since it was supposed that all the motors work simultaneously. This implies, on the one hand, an increased remover kit mass, but, on the other hand, the de-orbiting time could be significantly reduced with respect to that of the EDT scenario. These two parameters, the total remover kit mass and the de-orbiting time, play an important role during the removal mission design, driving the choice of which solution could be better in each specific case. The remover mass drives the estimation of the mission cost, especially regarding the launch costs, while the de-orbiting time represents a key parameter to consider for the mission risk assessment. One of the main threat for the EDT is represented by its high extension for few kilometres and its vulnerability to debris, which are very numerous in the orbital regions crossed during the descending phase. Debris flux simulations could be required to determine the risk of catastrophic collisions in both scenarios, but this aspect is out of the scope of the paper and it will not be examined in more detail. Anyway, it can be concluded that the choice of which de-orbiting solution could be better than the other depends on which one allows the best compromise between the mass and the de-orbiting time, according to the costs and risk requirements stated during the removal mission design.

The mass of the space tug was estimated according to the procedure described in Section 3.4, considering the optimal sequence of orbital transfers determined for each set of debris. EDT removal kits were considered for the Ariane 40, while propulsive kits were chosen for the Ariane 5 and all the other debris. The results obtained are reported in Table 3.10. From this analysis it emerged taht the ΔV budgets for the orbital transfers are significantly high; this significant increase in the mass budget is due to the high ΔV required for the RAAN alignment. As consequence, very massive propulsion system are required, of the order of several tons, as it can be observed form the last column of table 3.10. In all the cases, no natural alignment of the RAAN was achievable with the selected debris. If this implies a high propelant mass, on the other side the total mission time results well within one year, allowing a removal trend of five objects per year as it was stated at the beginning. Taking advantage of the natural alignment of the lines of the ascending node, the mass of the space tug could be reduced, but the mission time would exceed the limit of one year. Alternative orbital transfers could be considered to avoid the impulsive manoeuvres, as for example first lowering the orbit of the space tug in order to obtain a quite different nodal precession, and then raising it again when the orbital plane has rotated properly to match the next debris; also alternative propulsion systems could be implemented to lower the mass of the space tug. Electric propulsion could be considered another option, but longer mission time could be implied.

Conclusions

In this mission analysis both de-orbiting maneouvre and multiple transfers were analysed. Electric propulsion and electro-dynamic tether were chosen as de-orbiting solutions. Two sets of debris where selected, among the possible targets that orbit in the SSO. For each debris, a proper remover configuration was determined, one for the electric propulsion and one for the electro-dynamic tether. The total mass and the total de-orbiting time were then evaluated in both cases. From the results obtained it emerged that for low massive objects (mass $\leq$ 2000 kg), the two options are comparable in terms of removal kit mass, but the EDT performs better as regards the de-orbiting time. For quite massive debris (mass $\geq$ 2000 kg), although the mass of propulsive removal kits increases, the de-orbiting time is significantly lower compared to that of the EDT scenario. A risk assessment and a mission costs analysis should be performed to determine which solution could perform better, according to the costs and risk requirements

Debris	$N°EPU$	$m_{rem}\backslash m_{deb}$ [%]	$N°EDTU$	$m_{rem}\backslash m_{deb}$ [%]
ARIANE 40	1	12	1	10
ARIANE 5	2	10	1	7.5
SPOT 5	2	9.2	1	6.5
METOP-A	2	7.4	1	5.2
METOP-B	2	7.0	1	4.9
COSMOS-2442	3	5.1	11	3.3
ENVISAT	3	6.0	12	3.6

Table 3.8: Number of units assembled and de-orbiting kit mass ratio. in percentage, for a de-orbiting performed by means of electric propulson (EP) and electrodynamic tether (EDT) for the debris selected in SSO.

Debris	$\Delta m(\%)$	$\Delta T(\%)$
ARIANE 40	10.8	34.0
ARIANE 5	33.0	-34.4
SPOT 5	33.5	-33.4
METOP-A	28.5	-33.3
METOP-B	29.4	-32.9
COSMOS-2442	36.1	-55.8
ENVISAT	41.3	-55.2

Table 3.9: Difference, in percentage, between the de-orbiting kit mass (left column) and de-orbiting time (right) obtained with electrc propulsion and electrodynamic tether (electrodynamic tether as reference).

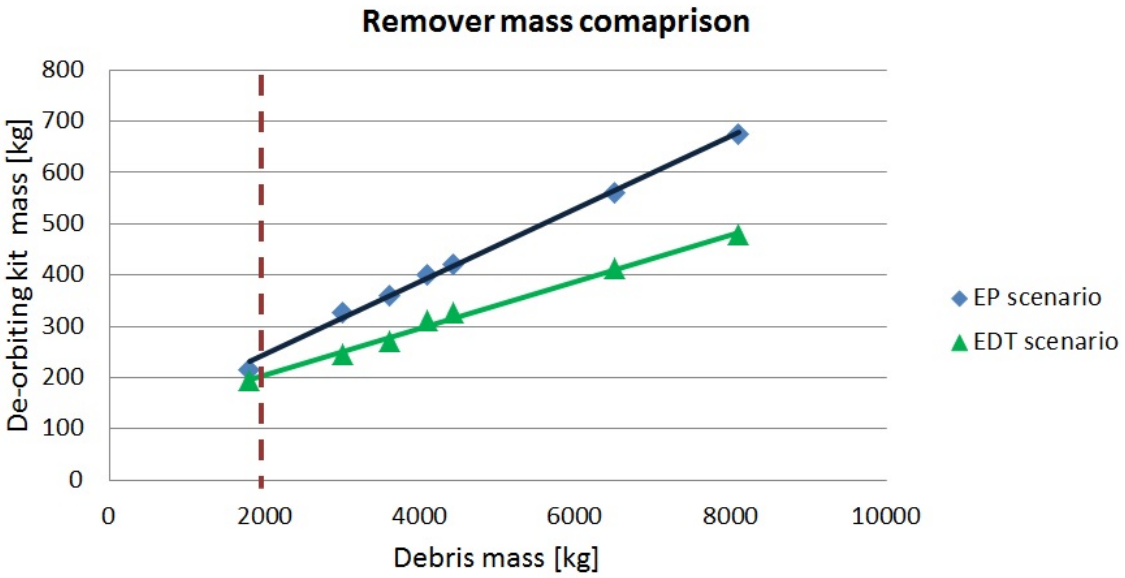

Figure 3.23: Total orbital lifetime in case of de-orbiting performed by means of propulsion only

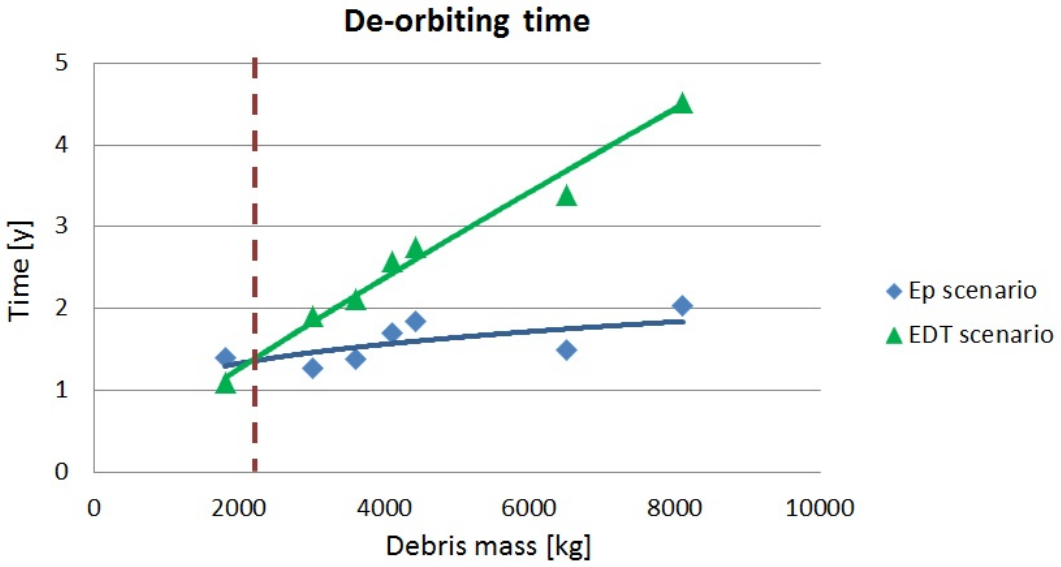

Figure 3.24: Total orbital lifetime in case of de-orbiting performed by means of propulsion only

ΔV $[km\backslash s]$	sequnce	Time [days]	Propellant mass [kg]	Wet mass [kg]
Debris set #1				
6.9	43512	54	5269	6983
Debris set #2				
4.5	51243	56	2524	3345

Table 3.10: Examples of the most efficient multiple transfers. The ΔV budget required for multiple orbital transfers is always significant and this implies a large mass of the propulsion system required to accomplish the entire mission: the mass could be of the order of some tons, depending on the maneouvres required for each sequence of debris.

stated in the removal mission design. A preliminary sizing of the space tug was performed, considering a chemical bipropellant propulsion technology. An optimal sequence of multiple removals was determined for two sets of debris. Form the results obtained, it emerged that very massive space tugs are required to accomplish this kind of mission. Alternative manoeuvres and /or propulsion systems could be considered to reduce the mass needed for the entire mission.

3.5.5 Case study #3: mission analysis

In this case study, three de-orbiting solutions were implemented: electric propulsion, electrodynamic tether and hybrid propulsion. Debris of all the five orbital bands described in section 3.1 were considered. For each mass range it was determined the correspondent de-orbiting kit configuration according to the three removal technologies implemented. The results obtained, in term of remover mass and total de-orbiting time, were then compared in order to evaluate if an optimum de-orbiting solution could be identified according to the characteristics of the debris to remove.

Mission scenario

The ADR scenarios analysed in prevous sections were useful to identify the main parameters that influence the performances in terms of remover configuration and de-orbiting manoeuvres for some selected, rapresentative targets. Three de-orbiting technologies were compared. As it emerged in the case study #1, drag sails are suitable and effective solutions at altitudes below 600 km, when the mass of the debris is less than 1000 kg. For this reason they were excluded for furhter analysis, being the greater part of the objects to de-orbit more massive and in orbital bands that are above 800 km. The second analysis (case study #2) allowed to conclude that both electric propulsion and electrodynamic tethers could be suitable solution for ADR. In this section, hybrid propulsion, previously employed only for the controlled re-entry manoeuvre, was added as third de-orbiting technology.

Thre different mission scenarios were then considered:

1. **de-orbiting by means of electric propulsion only**;
2. **de-orbiting by means of electrodynamic tether only**;
3. **de-orbiting by means of hybrid propulsion only:**
   the debris is inserted in a transfer orbit through an impulsive maneouvre, from its initial altitude to the final altitude at 250 km.

The third maneouvre is a simple impulsive manoeuvre performed by means of a hybrid engine.
All the manoeuvres end at 250 km, from which a controlled re-entry manoeuvre is foreseen by means of a hybrid engine module, as in previous analysis.

Mission assumptions

The following assumptions were adopted in the analysis:

- the mission was supposed to begin with the de-orbiting kit already attached on the selected debris;
- a controlled re-entry maneouvre is foreseen at 250 km;
- in this case, the SNECMA PPS-1350 electric thruster was chosen, thanks to its higher performances, more suitable for the wider range of targets considered. he thruster performances are shown in table 3.11;
- the electric propulsion unit and the electrodynamic tether units were sized as in the previous analysis. The mass budget for each unit is sumarized in table 3.12.
- a proper hybrid propulsion unit was developed aiming to optimize the number of units required to de-orbit the entire population, maintining the limitation of 100 kg, for the microsatellite size. The procedure is described in details below.

SNECMA PPS-1350	
Total impulse [Ms]	3.4
Specfic impulse [s]	1600
Thrust [mN]	88
Power [W]	1500
Thruster mass [kg]	5.3

Table 3.11: SNECMA PPS-1350 performances

Electric Propulsion unit	
Thruster mass [kg]	5.3
Power plant mass [kg]	23
Tank mass mass [kg]	4.5
Maximum propellant mass [kg]	54
Total dry mass [kg]	44
Inert-to-propellant-mass ratio	0.26
Total EP unit mass [kg]	98
Hybrid Propulsion Unit	
Total dry mass [kg]	36.6 kg
Propellant mass [kg]	69.6 kg
Total HP unit mass [kg]	106.2 kg
Electro-dynamic Tether Unit	
EDT Unit mass (debris mass $\leq$ 4000 kg)	50 kg
EDT Unit mass (debris mass $\geq$ 4000 kg)	70 kg

Table 3.12: Mass budget of the electric propulsion unit, the hybrid propulsion unit and the electro-dynamic tether unit. The mass of the electric propulsion unit and of the electrodynamic tether unit were estimated according to the sizing procedure presented in section 2.3.2 and 2.3.4 respectively. The mass of the hybrid unit was the result of an optimization procedure presented in this section.

The sizing procedure for the hybrid module was developed by Filippo Maggi. The information reported below are taken form the internal report [60]. The results obtained were used to determine the perfomances in case of ADR through hybrid propulsion. The size of the hybrid propulsion unit was determined through an optimization procedure that minimized the total mass of the hybrid de-orbiting kits injected in orbit to remove the entire debris propulsion (all debris in the five orbital bands). As a reference, all computations were performed by choosing a reference payload mass of 1000 kg and comparing a selection of available ΔV, spanning between 200 to 900 m/s. For each debris and for each deorbiting kit, the available ΔV is reported from nominal 1000 kg to the actual mass of the debris (the actual payload) through Tsiolkovski equation. If the performance is not accomplished, the number of kits required for the scope is incremented. By completing the analysis per each debris, it is possible to compute the number of items required to accomplish the full deorbiting and, as consequence, the total mass to launch into orbit, excluding the space platform. Table 3.13 reports the list of potential deorbiting kits that were computed using the abovementioned procedure. Due to the criterion of mass minimization, the selected design points fall on the maximum value of $L = D_{in}$. The optimal value of ox increases with the required ΔV while the resulting technological parameter of inert-to-propellant mass fraction tends to decrease and the trend can be fitted with a high degree of confidence by a power law function (Figure 3.25). When the overall number and mass of required deorbiting kits are evaluated, a minimum is found for the kit supplying 400 m/s for a nominal payload of 1000 kg (Figure fig:HybridKitsTotalMassDv). Turning to the initial debris classification, it is evident that the kit granting the lowest overall orbit mass injection exceeds the requirements of a part of the debris. However, for small ΔV missions, inert mass becomes an important factor and can impair the general convenience of a specific choice. Under the investigated constraints, it appears that the best choice for the deorbiting kit is the pack supplying $\Delta V = 400 m\backslash s$ which allows the deorbiting of the relevant population by using 726 packs (in single or multiple configuration) and injecting into orbit less than 155 tons of propellant and inerts, excluding the space platform which is assumed to be common to any other propulsion technology, not considered in this study. The rocket under consideration is a centre-perforated grain of HTPB with density of $\rho_f = 920 kg\backslash m^3$ having the following features:

- total masses: M_{prop} = 69.6 kg, M_i = 36.6 kg, $\dot{m}_{ox} = 0.7 kg\backslash s$;
- time averaged performance data: I_{sp} = 314.4, $O\backslash F_{mean}$ = 7.30, max thrust = 2455 N, firing time = 86 s, $R_f = 0.2 mm\backslash s$.
- geometric data: throat diameter 40 mm, case lenth = 1.24 m, grain lenth: 1.09 m, grain inner diameter: 109 mm;
- mass details: pressurant 3 kg, pressurant tank 5.2 kg, case 3.3 kg, oxizider tank 4.2 kg, nozzle 12.2 kg, injection plate 5.5 kg.

Mission procedures

The debris population was divided in ten classes that covered the entire mass range, from 800 kg to 11000 kg, as shown in Figure 3.3. *Matlab* codes were developed to determine the remover architecture and total mass, the de-orbiting time and the total mass injected in orbit, according to the de-orbiting technology employed, depending on the mass and the orbital band of the debris. A risk assessment analysis was also performed to determine the probability of collisions during the de-orbiting phase with the selected technologies.

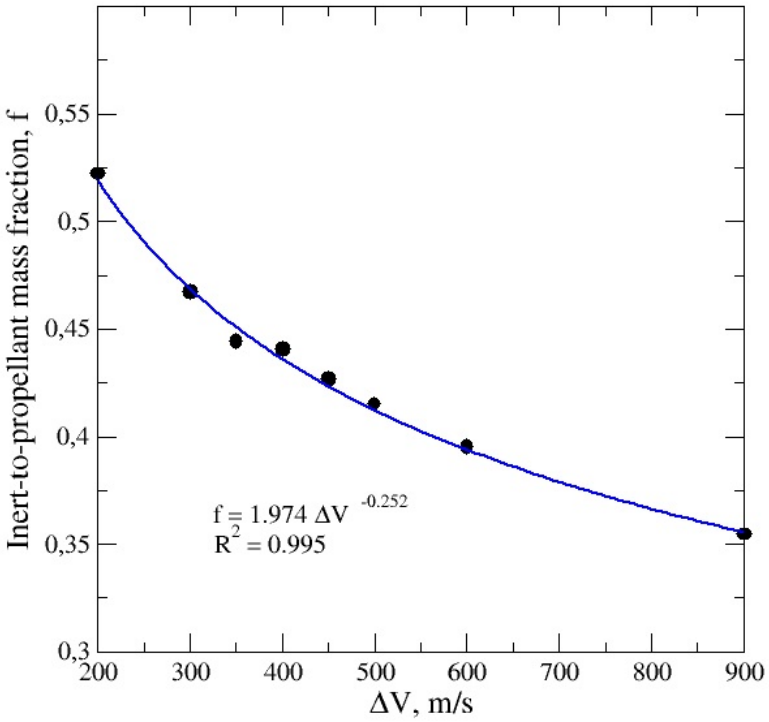

Figure 3.25: Inert-to-propellant mass fraction of hybrid rocket systems for $M_{pay} = 1000\,kg$ and variable ΔV.

ΔV m/s	Initial L/D_{in}	Initial OF ratio	$M_i + M_{prop}$ kg	Average I_s, s	$\dot{m}_{ox}$ kg/s	M_i/M_{prop}	Total kits Mass, tons	Total kits Number
200	10	7,50	106,3	313,1	0,7	0,522	247,91	2333
300	10	7,50	158,4	313,1	0,9	0,468	243,55	1538
350	10	7,75	185,6	311,7	1,0	0,445	206,70	1114
400	10	7,25	212,8	314,4	1,2	0,441	154,51	726
450	10	7,25	240,7	314,4	1,3	0,427	164,86	685
500	10	7,25	269,1	314,4	1,4	0,415	180,05	669
600	10	7,25	327,8	314,4	1,6	0,395	210,44	642
900	10	7,25	522,2	314,4	2,2	0,355	306,51	587

Table 3.13: Candidate deorbiting kits for a nominal payload mass of 1000 kg and quantification of total items for the relevant debris population. L/D_{in} and OF ratio are characteristics of the hybrid rocket derived by the sizing procedure; M_i and M_{prop} are the inert mass and the propellant mass respectively; $\dot{m_{ox}}$ is the oxidizer flow rate. The last two columns represent the total mass and the total number of unit inserted in orbit, as the ΔV provided by each single unit is varied from 200 m/s to 900 m/s.

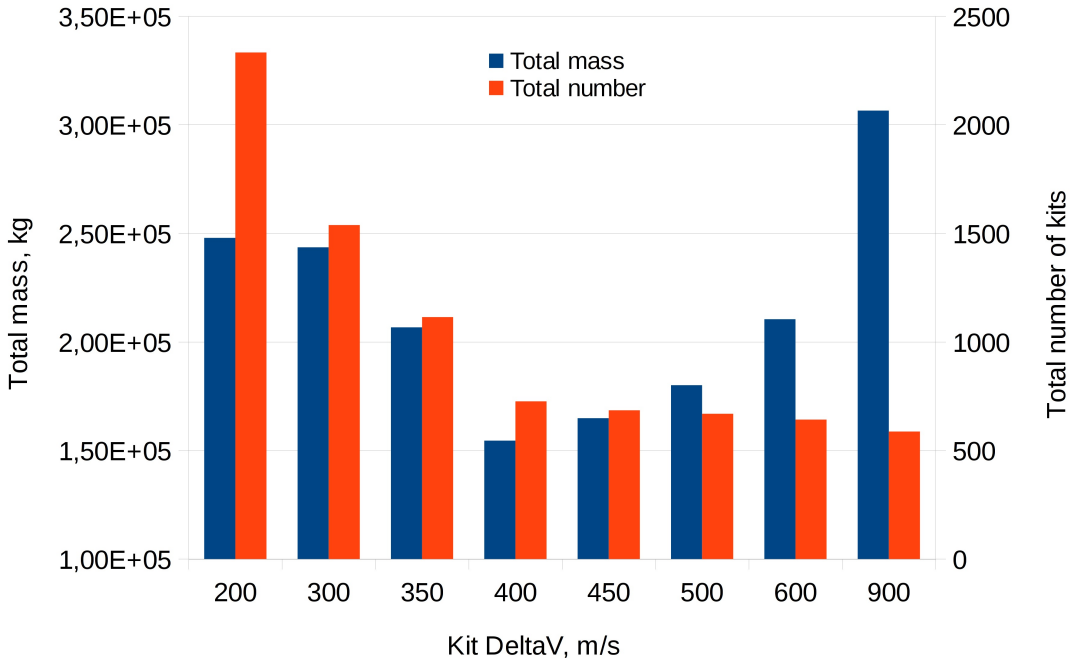

Figure 3.26: Total number and total mass for each kit required for population deorbiting.

3.5.6 Case study #3: results

Figures from 3.27 to 3.31 show the mass of the de-orbiting kits and the total de-orbiting time for each range of debris mass in the five orbital bands. The time required for the HYP scenario is not reported since it is very small, being the time to perform half of the transfer ellipse. In the graph on the left of the same figures it is also plotted the number of debris in the correspondent mass range (scale 10:1). From the analysis it emerges that in most of the cases, the EDT scenario implies the lowest remover mass and number of units, while the highest values are obtained in HYP scenario. The EP scenario represents an intermediate solution mainly for debris with mass greater than 6000 kg, while for the lower ranges it appears quite comparable with the EDT scenario. This result is quite interesting since, as it can be observed in Figure 3.3 and Figure 3.4, most of the debris lie in the mass range [800 6000] kg, with the highest concentration between 800 kg and 3000 kg, where the two solutions are almost overlapped. Concerning the de-orbiting time, the results confirmed what it was previously said concerning the strong dependence of the EDT performances from the orbital inclination: this technology is more effective for inclinations below 70°, while between 70° and 110° its effectiveness falls down, with a peak at 84° - 86°. As it can be observed, in almost all the cases, the EP allows to de-orbit more rapidly than the EDT, except for the debris that lie in the orbital band at 64° of inclination where the EDT seems to perform better for the debris in the mass range [800 2000] kg, even though the difference is very slight. Furthermore, the necessity to increase the number of EP units due to the debris mass allows to reduce the de-orbiting time since the total thrust is increased, when it is assumed that all the thrusters are operative simultaneously. For debris with mass lower than 2000 kg, the divergence between EP and EDT is very small, almost negligible, in the orbital bands with inclinations 71° and 74°; the difference is more evident at inclinations of 82° and 99°. For more massive debris the effect is amplified and the EP results to perform better than the EDT in any case. The de-orbiting time in case of EP is always around 0.5 years, while with the EDT it can be required also 6 or even 8 years, depending on the inclination of the orbit. These values are important when a risk assessment is performed; a fast de-orbiting is usually better since the collision is lower; furthermore, in case of the EDT the length of the tether could represent a critical aspect, being of the order of several kilometers.

Figure 3.32 shows the number of units assembled, depending on the debris mass and orbital band. As it can be observed, the number of units in case of electric propulsion is ≤ 5 in most of the cases; more complex systems are required in case of hybrid propulsion, where the number of assembled units grows up to 20 for the most massive objects. In case of electrodynamic tether it is obtained the simplest configuration, with only one deorbiting unit.

Figure 3.33 shows the total mass of the removers and the total number of units injected in orbit. The most evident result is that the HYP scenario implies the highest mass and number of units. This result was in part expected since hybrid propulsion required high masses and number of units for the entire debris population. The EDT scenario appears to be the most effective solutions as regards both the total mass and the number of units injected in orbit, even though the EP is of the same order of magnitude and could be considered almost comparable.

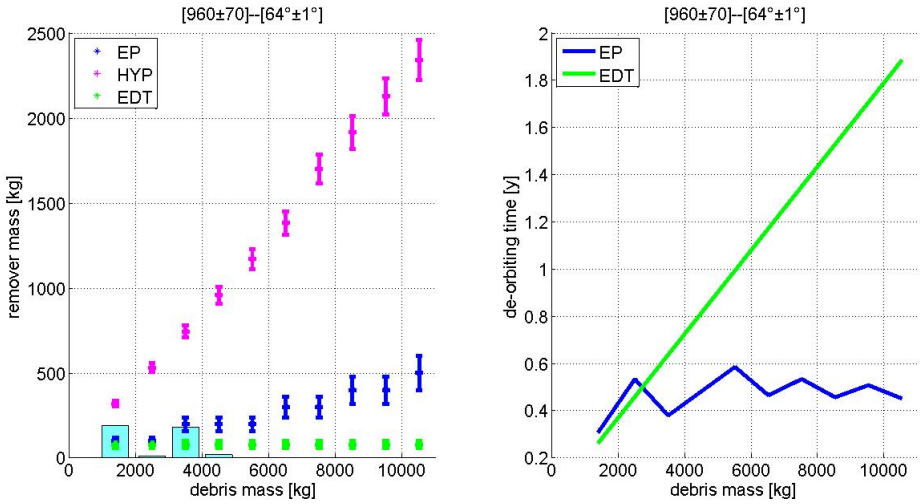

Figure 3.27: *Orbital band $h = 960$ km, $i = 64°$.* Total mass of the de-orbiting kit required to de-orbit a debris in function of its mass, when electric propulsion (blue), electrodynamic tether (green) and hybrid propulsion (magenta) are employed (on the left). Total de-orbiting time with electric propulsion (blue) and electrodynamic tether (green) (on the right). Hybrid propulsion is not reported since the orbital lifetime is very small and not visible ompared to the one obtained with the previous technologies: it is simply the semi-period of the transfer elliptical orbit.

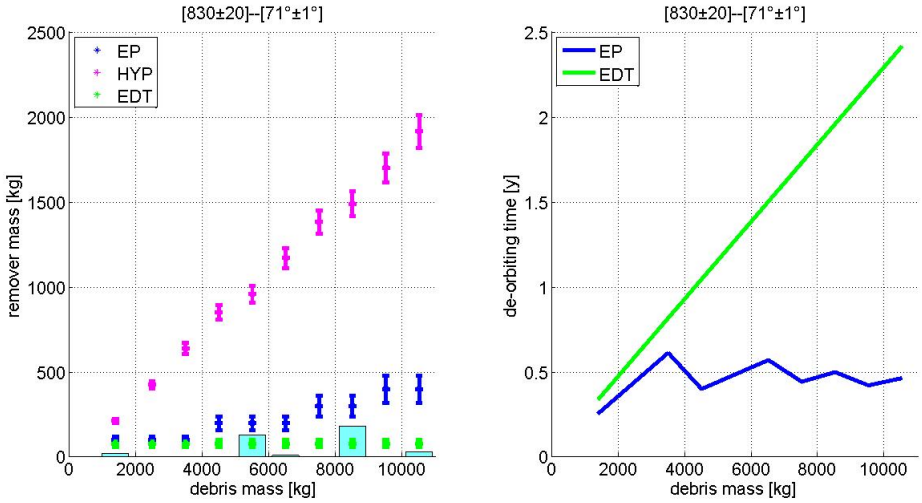

Figure 3.28: *Orbital band $h = 830$ km, $i = 71°$.* Total mass of the de-orbiting kit required to de-orbit a debris in function of its mass, when electric propulsion (blue), electrodynamic tether (green) and hybrid propulsion (magenta) are employed (on the left). Total de-orbiting time with electric propulsion (blue) and electrodynamic tether (green) (on the right). Hybrid propulsion is not reported since the orbital lifetime is very small and not visible ompared to the one obtained with the previous technologies: it is simply the semi-period of the transfer elliptical orbit.

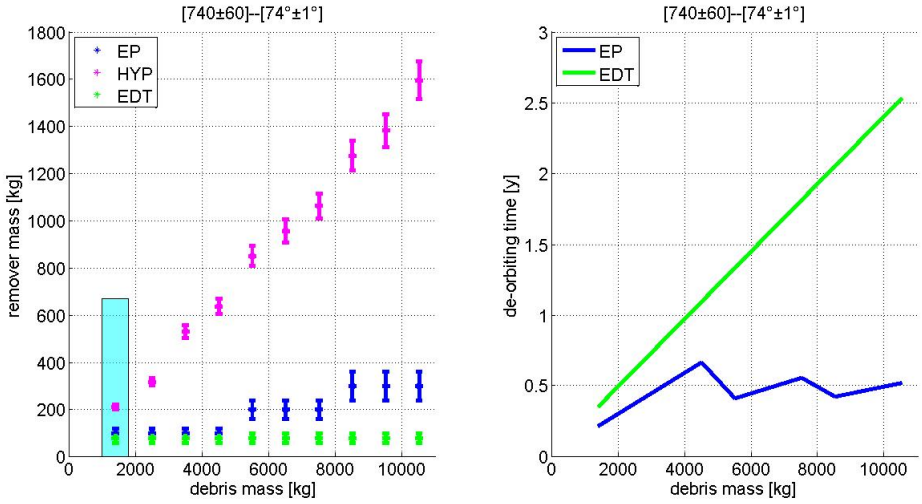

Figure 3.29: *Orbital band $h = 740$ km, $i = 74°$.* Total mass of the de-orbiting kit required to de-orbit a debris in function of its mass, when electric propulsion (blue), electrodynamic tether (green) and hybrid propulsion (magenta) are employed (on the left). Total de-orbiting time with electric propulsion (blue) and electrodynamic tether (green) (on the right). Hybrid propulsion is not reported since the orbital lifetime is very small and not visible ompared to the one obtained with the previous technologies: it is simply the semi-period of the transfer elliptical orbit.

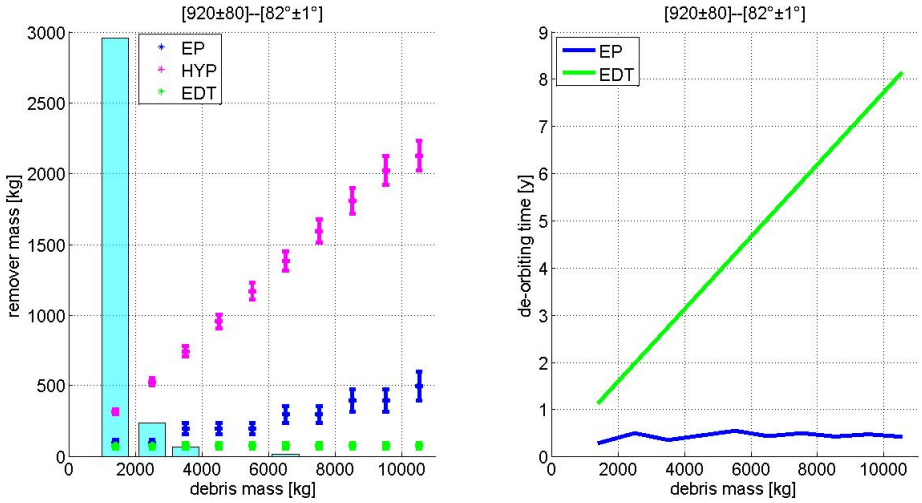

Figure 3.30: *Orbital band $h = 920$ km, $i = 82°$.* Total mass of the de-orbiting kit required to de-orbit a debris in function of its mass, when electric propulsion (blue), electrodynamic tether (green) and hybrid propulsion (magenta) are employed (on the left). Total de-orbiting time with electric propulsion (blue) and electrodynamic tether (green) (on the right). Hybrid propulsion is not reported since the orbital lifetime is very small and not visible ompared to the one obtained with the previous technologies: it is simply the semi-period of the transfer elliptical orbit.

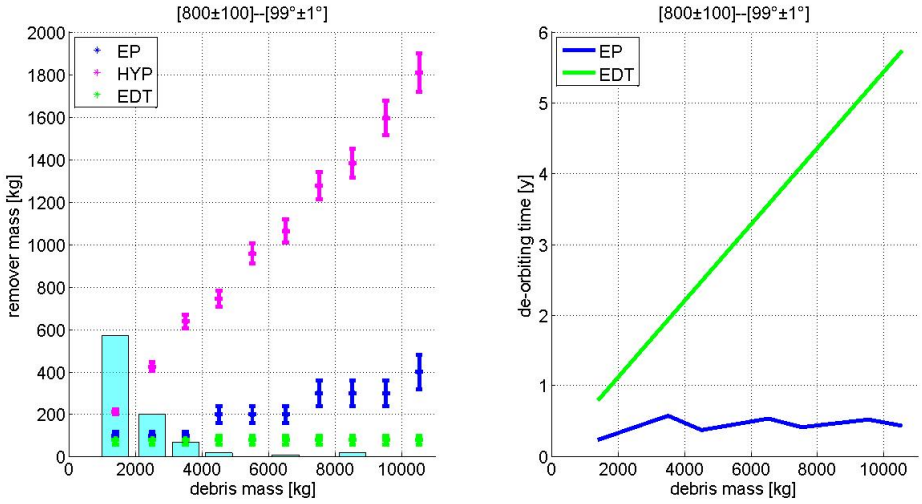

Figure 3.31: *Orbital band $h = 800$ km, $i = 99°$.* Total mass of the de-orbiting kit required to de-orbit a debris in function of its mass, when electric propulsion (blue), electrodynamic tether (green) and hybrid propulsion (magenta) are employed (on the left). Total de-orbiting time with electric propulsion (blue) and electrodynamic tether (green) (on the right). Hybrid propulsion is not reported since the orbital lifetime is very small and not visible ompared to the one obtained with the previous technologies: it is simply the semi-period of the transfer elliptical orbit.

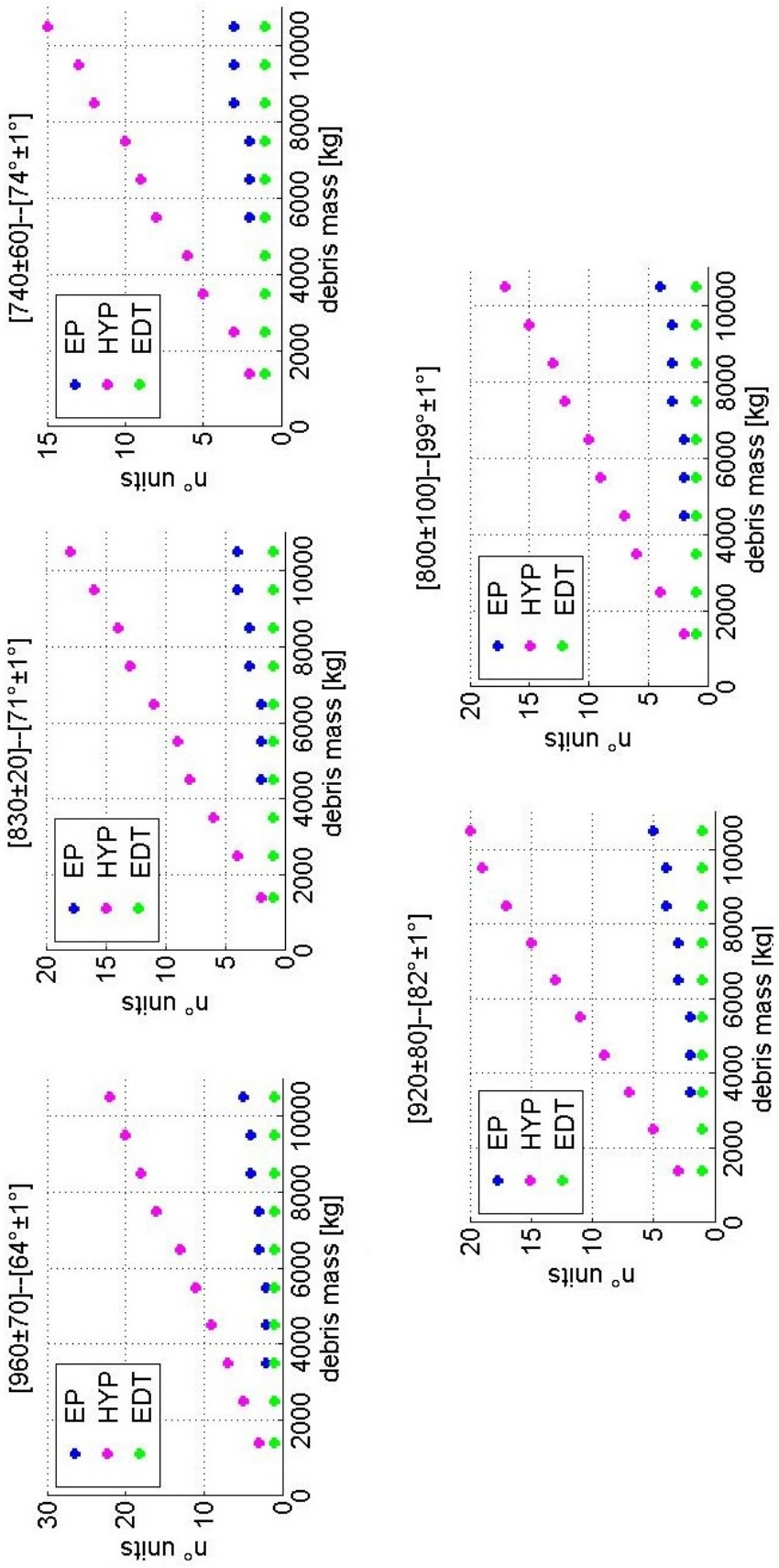

Figure 3.32: Number of the de-orbiting kits, for each orbital band, required to de-orbit a debris in a specific mass range.

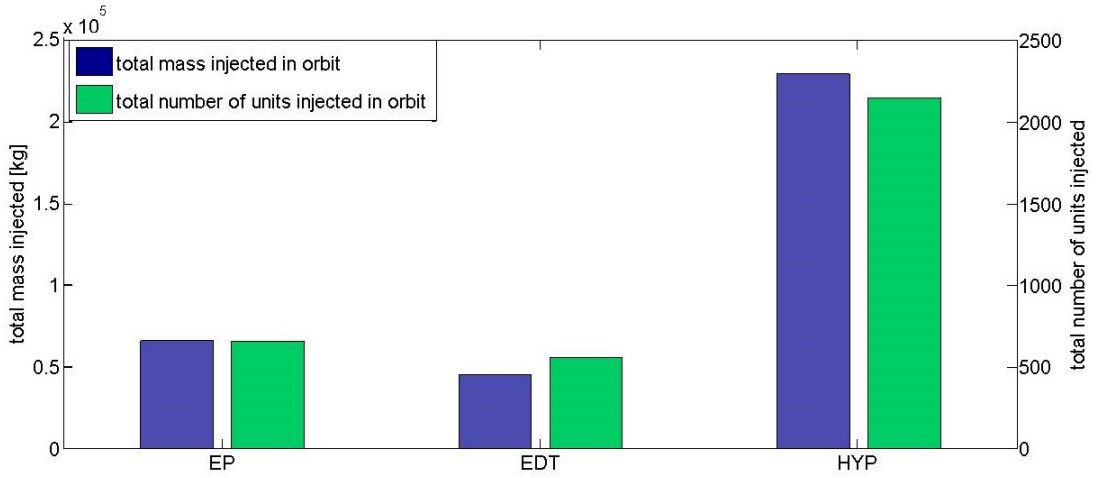

Figure 3.33: Total mass (blue) injected in orbit depending on the technology employed. The mass is evaluated considering the number of debris in each mass range for each orbital band; the mass of the de-orbiting kit is multiplied for each number and then all the values obtained for the same mass range are summed over the five orbital bands. In the same way it is evaluated the number of units injected in orbit (green) for each de-orbiting technology.

3.6 Risk assessment evaluation

One of the main issues to consider during and ADR mission analysis is the risk assessment, i.e. the estimation of the probability to have impacts with other objects during the de-orbiting phase. While for an impulsive manoeuvre the flight time is very low and the risk of impacts can be negligible, the problem arises with tethers and electric propulsion, due to the length of the tether and the de-orbiting times, that could be of the order of years. For these reasons, a preliminary risk assessment was performed for the electric propulsion and the electrodynamic tether de-orbiting scenarios, in order to verify the feasibility of the mission avoiding the risk of creating further debris.

The number of impacts expected during the de-orbiting phase is determined from the following equation:

$$n_{impacts} = Flux A_{cs} \Delta t \tag{3.61}$$

where *Flux* has dimensions of $\#/m^2/year$ and represents the environmental debris flux (function of debris size, speed and direction) in a specific orbital region, Δt is the time spent by the target debris in this region and A_{cs} is its cross-sectional area exposed to the *Flux*. The *Flux* was determined through the environmental model MASTER, which gives in output two information:

- Differential flux *f(d,v)*, i.e. $number of impacts/m^2/year$ as function of particle diameter d (down to 10^{-5} m) and speed v;
- Cumulative flux *F(d,v)*, i.e. $number of impacts/m^2/year$ as function of particle speed v, for all particle diameters from d (down to 10^{-5} m) to infinity. The cumulative flux is normally the standard output of environment models.

3.6.1 Electric propulsion: risk assessment

The risk of catastrophic collisions during the low thrust manoeuvre was evaluated considering the energy to mass ratio equation which defines the limit to determine whether a collision is catastrophic or not [108]:

$$EMR = 40\frac{kJ}{kg} = \frac{1}{2}\frac{M_p {v_p}^2}{M_{target}} \tag{3.62}$$

where M_p is the mass of the impacting particle, v_p is its velocity, M_{target} is the target mass.

The number of impacts was determined through Equation 3.61. In case of electric propulsion, the cross sectional area A_{cs} was estimated assuming a mean density of 96 kg, according to the density range reported in [57], and determining the equivalent radius of a sphere with the same mass of the object. The MASTER *Cumulative flux* was used to characterise the particles population in the 5 orbital regions previously selected: each region was divided in five sub-regions 200 km wide, starting from an altitude of 1100 km till a final orbit of 200 km. The output matrix contained 60 classes of particles of different sizes (d_{imp}), varying from 0.11e-4 m to 8.91 m in diameter, divided in 40 sub-classes of velocities (v_{imp}), ranging from 0.5 km/s to 39.5 km/s; for each size and velocity it was given the *Cumulative flux* of different classes of particles (fragments due to explosions, fragments due to collisions, debris released during launches or missions, , ejecta) and the total flux of particles of that size and velocity. Through the EMR equation it was calculated the critical diameter of a particle that could cause a catastrophic collision for each target mass range and then this was used to obtain the associated couple (d_{imp} , v_{imp}) with the correspondent cumulative flux in the MASTER matrix.

EP risk assessment: results

The number of catastrophic collisions in each orbital sub-region was evaluated considering the associated cumulative flux and summed to determine the total number of imacts during the entire mission. In all cases this value resulted ≤ 0.001 (order 10^{-7} - 10^{-9}), meaning that no catastrophic impacts would have occurred during a low thrust de-orbiting manoeuvre for the selected debris.

3.6.2 Electrodynamic tether: risk assessment

The risk assessment procedure relative to the electrodynamic tether is taken form the internal report *BETS - Passive Electric Propulsion* [109]. The results highlighted in the document were used to evaluate the probability of collision in our mission analysis, in case of de-orbiting by means of electrodynamic tether. We report as follows the main aspect of the risk assessment evaluation presented in the docment [109]. The number of impacts was determined through Equation 3.61. In this case the cross sectional area of a tape tether was determined as $L \cdot w_{eff}$, where L and w_{eff} are respectively the tether length and the effective width. In this case the flux was determined for 54 different mission profiles, derived by the combination of 6 initial orbital altitudes, three inclinations and three epochs. All the orbits were considered circular. The mission parameters are reported in Table 3.14.

Initial orbital parameter		**Range**
Initial orbital altitude	[km]	250 - 500 - 750 - 1000 - 1250 - 1500
Inclination	[°]	0 - 50 - 90
Epoch	[year]	2016 - 2021 - 2027

Table 3.14: Mission parameters considered for impact flux calculation. All orbits are circular.

The risk computation for a tape tatehr, like the one emplyed in our mission analysis, was performed using a Ballistic Limit Equation (BLE), given in the following form:

$$d_{crit} = f(v_p, \alpha_{loc}) \tag{3.63}$$

BLE provides the minimum particle diameter d_{crit} which produce a tether critical damage (cut-off) at given speed v_p and impact angle α_{loc}, measured in the tape reference frame, see Figure 3.34 (left). Figure 3.34 (right) presents the definition of edge impact: this type of impact occurs when the projectiles projection is not entirely contained in the tape surface, which is not unlikely since the size of critical debris can can be close to the tethers width.

Previous investigations had already developed some BLE, but they were mostly focused to the evalaution of the impact resistance of round-wires [110] [111] [112] [113]. These studies showed that a particle with size from 1/5 to 1/2 of the tether diameter is enough to cut the rope REF, and they indeed provide a first estimation of the ballistic limit of a tether. However, they are based on the assumption that any

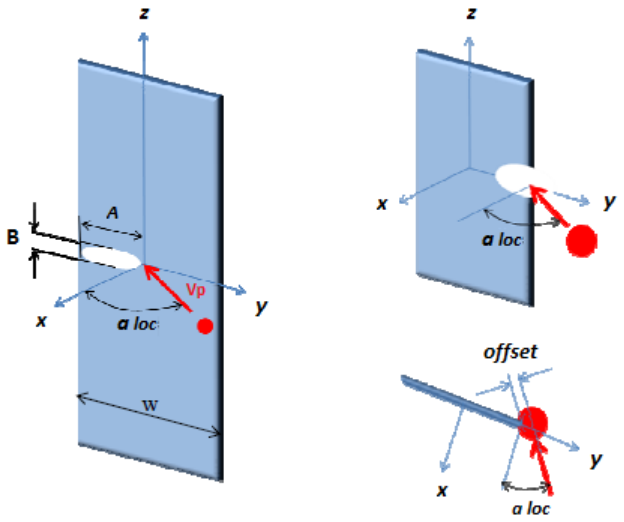

Figure 3.34: Tape tether geometry and reference frame (left); edge impact (right). A and B are the axis of the elliptic impact damage

impact on the wire excavates a crater whose volume depends on the M/OD kinetic energy, and their application is not rigorously valid for tethers whose cross section is thin, e.g. tapes. Furthermore, the damage dependence from the impact velocity and impact angle is not considered and this latter parameter could be particularly important for tethers with non-axis-symmetric cross section, like tape tether. The BLE employed for this study was then derived through a new empirical approach [114] [115] which makes it possible to estimate the uncertainty in the failure prediction. In this new method, the characteristics of the tape were also considered, such as the materials it is made of. Impact experiments were performed to preliminary derive the BLE, and simulations were used to extrapoltae the BLE outside the test range.
The assessment of the tethers survivability was carried out combining the information on debris and meteoroids fuxes to that on Ballistic Limit Equation. Specifically, for each critical particle (d^*_p, v^*_p) in the flux, BLE was used to identify the range of impact directions for which the particle is above the ballistic limit, i.e. it could brake the tether.

EDT risk assessment: results

The total number of debris critical impacts per unit length and per unit time $N_c/L\Delta t$ is represented in Figure 3.35. The debris flux has been limited to 10 cm, that is nearly the minimum size of catalogued objects. It appears that the selected tapes are very resistant to impacts with non catalogued space debris (i.e. debris smaller than 10 cm), with a maximum number of predicted failures always < 0.002 over 1 year-mission for a 5 km Al1100 + 5km PEEK tether (25.4 mm width). The NASA-STD 8719.14 [26] set the limit for the survuvability at 1%, which means 0.001, for impact with debris of 10 cm or larger. As emerged in the the mission analysis presented in section 3.5.6 the de-orbiting time is between 0.5 years and 1 year for debris with mass < 2000 kg, regardless the orbital band. In these cases, the number of predicted failures results < 0.002. Even though this value is slightly higher (1% point) than the limit imposed, the tether could still have an acceptable probability to survive during the de-orbiting phase. For more massive debris that lie in orbits at 74°, 64° and 71° (Figures 3.29 , 3.30 and 3.31), that are the inclinations where the electrodynamic tether works better, the maximum de-orbiting time in the worst case in between 2 years and 2.5 years. In these cases, the number of predicted failures is around 0.004. Also in this case the collisison risk exceeds the limit imposed, although it could be still acceptable. The situation is different for debris which lie in orbits at 82 ° and 99 °. The de-orbiting time for debris with mass > 2000 kg significantly increases: 6 years or even 8 years could be required for de-orbiting in the worst cases. The number of predicted failures grows up to 0.012 - 0.016: also in this case, the probability

for the tether to be severly damaged exceeded the limit of 0.001. This does not mean that the mission will fail, but the risk of failure should be properly evaluated.
It is worth to remind that the tethers survivability could be further reduced if catalogued objects with size $> 10cm$ are considered. In this case, however, impact events can be predicted from ground observations and collision avoidance maneuvers could be implemented, if necessary.

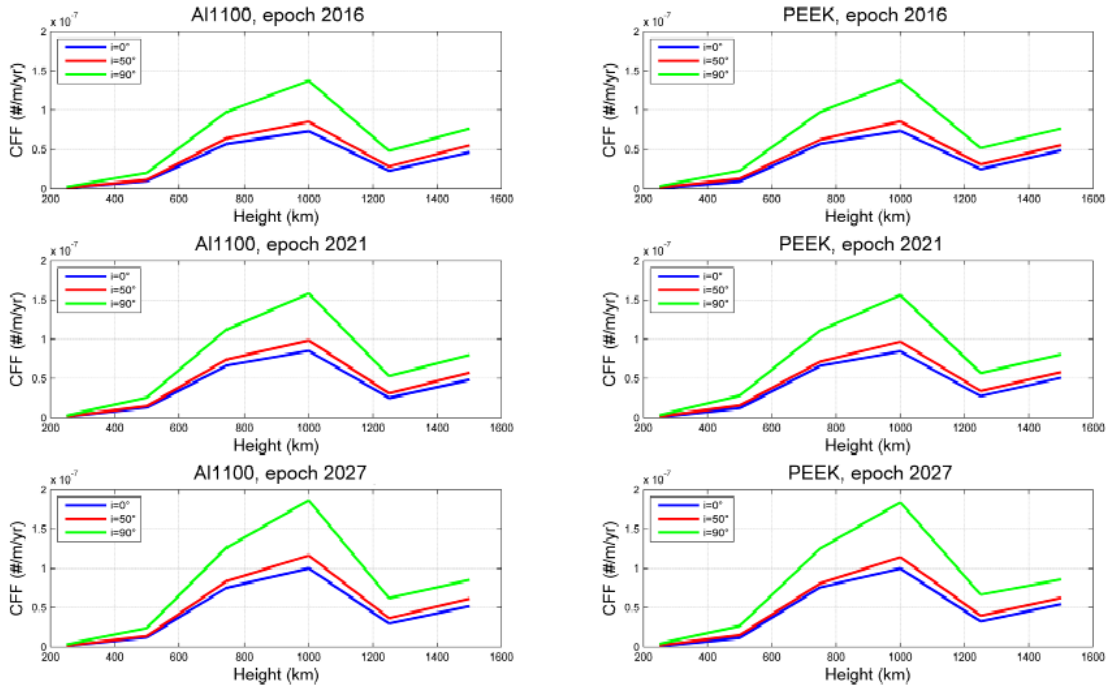

Figure 3.35: Total number of debris critical impacts per unit length for Al1100 (left) and PEEK (right), in function of the orbit altitude (250, 500, 750, 1000, 1250, 1500 [km]), inclination (0, 50, 90 [°]) and epoch (2016, 2021, 2027). The impact flux is provided for maximum debris size equal to 10 cm [109].

Chapter 4

Capture interface for uncooperative objects

4.1 On-orbit capture of uncooperative objects

The ability to manipulate and /or to join objects in space is one of the main issues the space community has been interested in to improve the operability in orbit and increase the safety of on-orbit missions. Dealing with joining between space objects, a distinction between **cooperative** and **uncooperative** objects is required. In case of *cooperative* objects, proper devices are mounted onboard the target and the chaser satellites in order to aid autonomous rendezvous and docking/capture operations (RvD). Docking operations between cooperative targets have already been successfully performed [116] [117]. The interest in the autonomous join between space objects has evolved over the years bringing to the well known *On-Orbit Servicing (OOS)*, where different orbital operations, such as satellite repair, refurbishment and refuelling, automatic assembly and maintenance of complex structures [118] [119] [120] are foreseen in order to increase operational lifetime and to improve the functionality of spacecraft already in orbit. In this way, the launch of new spacecraft to replace old ones can be limited, allowing significant cost savings and decreasing the generation of further space debris. An example of OOS is represented by the STS-74 mission in 1995, where the Shuttles robot arm was employed to help the placement of a docking module on the Russian Space Station MIR in order to make shuttles flights safer and make easier to get on board the station. One of the most significant example of space vehicle properly designed to support OOS and extravehicular activities (EVAs) is the Hubble SPace Telescope (HST): it was supposed to support periodic servicing by Space Shuttle astronauts to service, maintain, repair, and upgrade the telescope. The improvements derived by the execution of such EVAs on HST revealed to be useful for many other human spaceflight and robotic missions, such as International Space Station, satellite retrieval and servicing, and long duration spaceflight [121]. OOS missions can be easily implemented on satellites that have been sent in orbit recently or that will be launched in the future, since they could be equipped with proper devices for RVD operations. For previous satellites, if no OOS missions were foreseen, their implementation could become more complex.

In case of *uncooperative* objects, no specific feature are mounted on the target satellite to aid RvD operations. This is the case of most of the older operational satellites and, above all, of space debris. In this case, the chaser satellite should approach and perform capture manoeuvres without any help from the target satellite, determining, through proper vision based systems, the best way to make a rigid link with the object and stabilizing its motion. In 1992 the rescue mission of Intelsat V1-F3 satellite, that needed to be re-orbited after a malfunctioning of its engine that placed it in a useless orbit, posed a new problem regarding the operability in space: the Canadarm, that was supposed to be used to mount a new motor on the satellite, was not designed to manipulate uncooperative objects and a human extravehicular operation was required to install a grapple fixture to grab the satellite. This was one of the first examples of OOS of an un-cooperative object [125].
One of the main limitations to the implementation of ADR missions is represenetd by their capture. Several studies have addressed different problems related to RvD with space debris [126] [127] [128] [129],

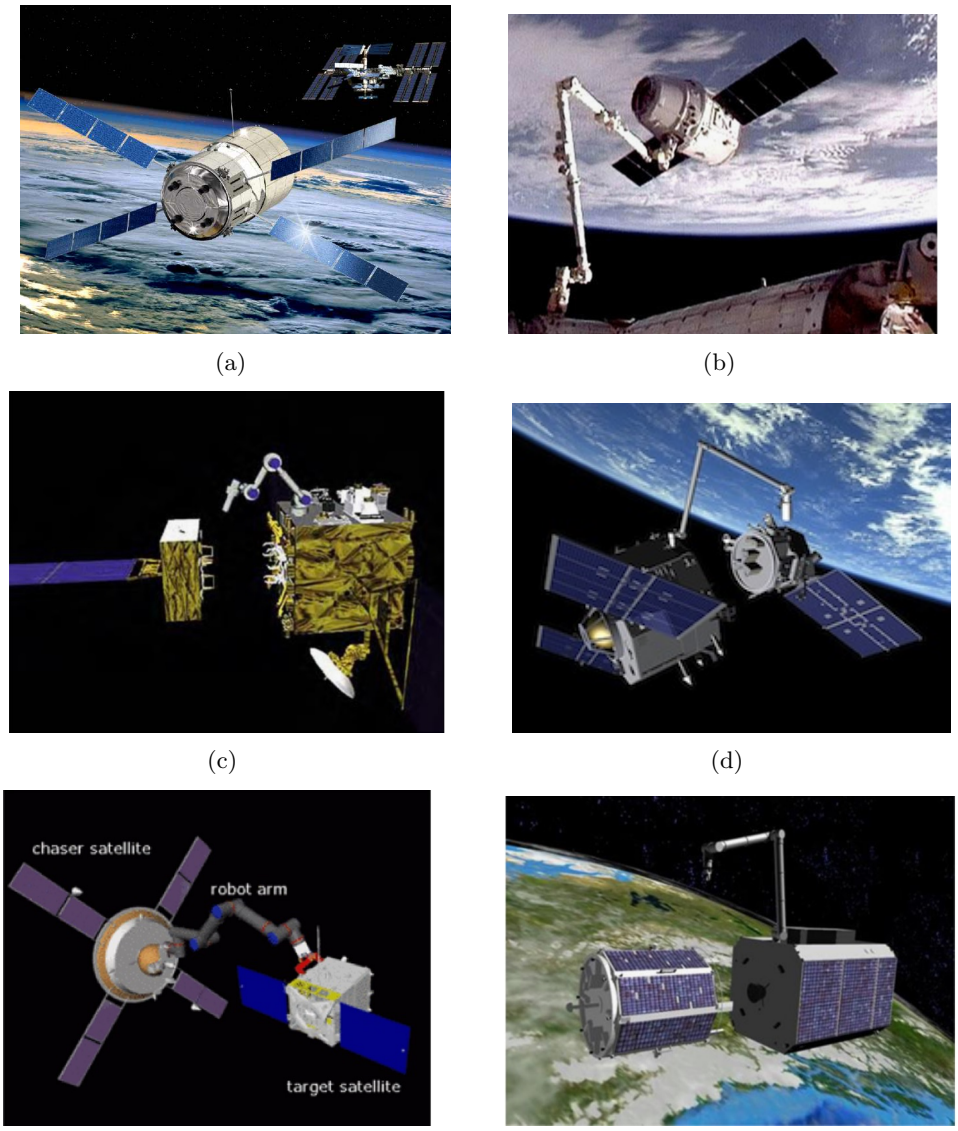

(a) (b) (c) (d) (e) (f)

Figure 4.1: On-OrbitServicing concepts: (a) ESA - ISS by ESA (*credit: ESA*), (b) SpaceX Dragon captured by the ISS robotic arm (*credit: NASA*), (c) ETS - VII by Jaxa [122], (d) Orbital Express by DARPA (*credit: Vacco*), (e) TECSAS of DLR, CSA and RKA [123] and (f) DEOS by DLR [124].

while others have focused on the dynamics and the attitude control and stabilization of the system at the beginning of the capture manoeuvre [130] [131]; finally, several robotic concepts have been proposed so far [132] [133] [134] where vision based systems, multi-degree-of-freedom manipulators and docking and latching systems are combined to simulate and analyse the behaviour of a possible robotic device during the entire capture manoeuvre. An aspect that still needs to be investigated more deeply concerns the study and development of proper interfaces to be placed as end-effectors to allow a secure capture of uncooperative objects. Most of the actual robotic systems used in space and proposed in previous studies are based on dexterous configurations [135] [136] that limit their employment mainly to cooperative objects. Several capture concepts have been proposed so far and are under investigation, such as robotic arms with proper gripping interfaces [137] [138], tethered nets [139], electrodynamic tethers [140], harpoons [141], but there are still several problems to be solved in order to make these solutions applicable in a real space mission. The main issues concern the connection with objects of unknown shapes and external features, the dynamic control during the capture phase and the stabilization of the coupled motion once the object has been grasped.

4.2 Capture interface concept

The capture interface developed in this work addresses two main issues that deal with the capture of uncooperative objects: the first is the ability to become compliant to objects of different or even unknown shapes, allowing to adhere on surfaces with microscopic irregularities, related to the surface roughness, as well as macroscopic ones, like screws, nuts, reinforcements that may be present on the external walls of spacecraft. The second issue is the capability to adhere to different materials that could be found on the external surfaces of spacecraft, varying from metals, paints, composites or blankets. A deep analysis on possible morphing and adhesion technologies to developed in order to enable grasping of a wide range of objects was carried out and some possible solutions were selected as promising candidates. A detailed description is presented in the following sections.

4.2.1 Morphing capabilites

The ability to conform to any kind of surface is important when the shape of the object to handle is irregular or unknown. Shape adaptive gripping techniques have become of particular interest since the 90s for terrestrial applications. Different morphing concepts have been investigated so far, based on electro/magnetorheological fluids, pneumatic devices, phase change materials, memory foams and polymeric substrates.

Electro/magnetorheological fluids have been studied to realize haptic interfaces , i.e. interfaces that mirror the human hands, where the stiffness of each finger can be varied by applying an electric or magnetic field [142] [143]. Although electro/magnetorheological fluids could represent promising materials to be implemented in robot grippers, they still need further investigations, especially concerning the field intensity required to reach the desired stiffness. One of the main limitations to employ these fluids for our purpose is that such materials work well mainly under shear conditions, while in a capture manoeuvre normal loads prevail.

Pneumatic techniques employ cushions that can be filled with air, when acting as passive devices, or which can be inflated with air or other gaseous/liquid means, when acting as active devices. The main disadvantages of such technologies are related to the necessity of maintaining the pressure inside the cushion, or to the risk of pressure loss due to damage to the cushion surface [144]. Furthermore, the device could be easily damaged by macroscopic elements, increasity the probability of possible fractures or perforations of the inflated cushions, with the consequent loss of the internal fluid which make unusable the device.

Another concept that was preliminary investigated was the employment of a phase change material (PCM) mixed with high concentrations of small solid particles, like metal particles, of the order of few millimeters in diameter, or even smaller, enclosed in a flexible synthetic material, belonging to the thermoplastic polymers class. When in its liquid phase, the PCM could help the compliance on the target surface, and the presence of the small particles could increase the adaptability at a microscopic scale.

Once deformed, the solidification of the PCM could freeze the deformed shape, increasing at the same time, the stifness of the interface. The concept appears to be quite simple and the power needed for the phase change precesses can be tuned employing proper PCM - dispersed particles combinations. One of the drawbacks of such concept is the vulnerability to surface irregularities that could cause perforations of the enclosing membrane, and the subsequent failure of the system.

Among the aforementioned morphing technologies, memory foams and polymeric substrates appeared to be promising solutions to be employed for our purpose, i.e. the realization of a shape adaptive interface. Since the early 90s, new polymeric materials have been investigated because of their ability to be easily deformed and maintain the deformed shape, when a proper external stimulus is applied. Although few earlier references to such materials can be found [144], it is only in the last two decades that their potential practical applications have brought an increase in the research activities related to them. A great number of studies [145] [146] [147] [148] have been conducted on memory foams and polymeric materials regarding their potential to adapt to different surfaces and several interesting and curious applications have been proposed so far.
Particular attention has been dedicated to those polymers known as *Shape Memory Polymer (SMP)*, a class of stimuli-responsive materials for which the response consists of a shape change and maintainance. This feature has made SMP very interesting for use in a wide range of both terrestrial and space applications which require the necessity of adaptive capabilities. Examples are adaptable wings for airplanes, irrigidization of dry adhesive structures to increase adhesion, self-healing membranes to be employed in structural field as well as biomedical applications [145] [148]. The environmental stimuli that cause the change in shape can be of different nature, such as heat, light, moisture or solvents, depending on the material. The capability to be deformed, maintain the deformed shape and restore the original one, under different external conditions appeared to be interesting aspect that could be advantageous for the development of the proposed gripping interface. For this reason, a detailed description of shape memory polymers is presented in the next section.

4.2.2 Shape Memory Polymers (SMP): overview and main applications

According to the conventional definition, a SMP is *a polymer that can be deformed and subsequently fixed into a temporary shape, which would remain stable unless it is exposed to an appropriate external stimulus that triggers the polymer to recover to its original or permanent shape* [145].
The main characteristic of such materials is a drastic change in the Youngs modulus if an external stimulus is applied [146], as shown in Figure 4.2 (temperature is the external stimulus).

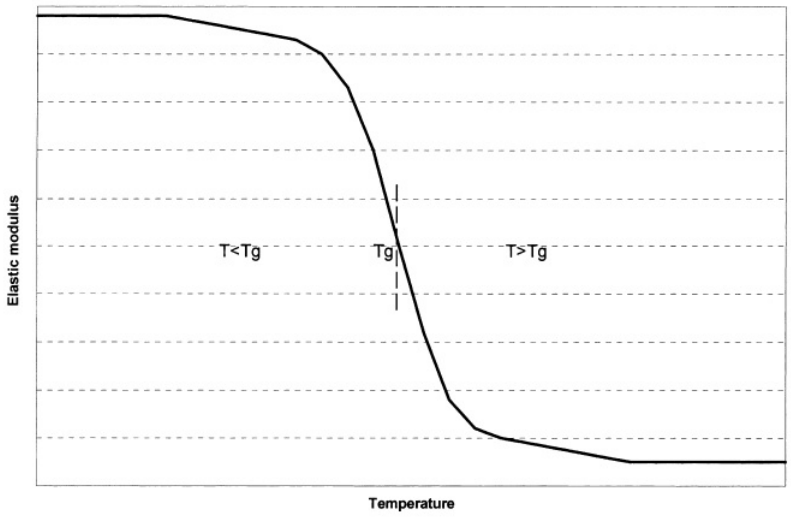

Figure 4.2: Drastic change in the Youg's modulus of a SMP, where temperature is the external stimulus [146].

SMPs were not very known until 1990s. At the beginning the research in this field had been quite

poor due to the limited applications envisaged for this kind of materials. A significant interest arose with the discovery of *segmented polyurethane based polymer* made by Mitsubishi Heavy Industries Ltd: the polyurethane based mayerials acquired a significant importance in many industrial applications thanks to the wide versatility of the urethane chemistry that could allow an easy structural tuning. In 2002, Lendlein et al. proposed the use of SMP for minimum invasive surgery in biomedical applications. Thanks to the interest in biomedical applications and the large ammount of fundings located in this field of research, SMP started to be investigated always more frequently, also for non-biomedical applications, and new efforts were dedicated to investigate more deeply the *Shape Memory Effect (SME)* [145]. Since 2000s, numerous reviews have been published expainng and covering the general aspects of SMPs, SMP composites, biomedical applications, and non-biomedical applications. Furthermore, in the last few years enormous and innovative progresses have been carried out and the conventional view of the SME have been significantly changed [145] [148].

Main advantages of SMP

SMPs present several advantages respect to other materials with similar properties, such shape memory alloys. They are lightweight (almost two order of magnitude lighter than aluminum), capable of hundreds of percent recovery strain and low cost; they are good thermal and electrical insulators. They have high compressibility, allowing high full/stowed volume ratios. They can be processed using standard polymer processing techniques, reducing the time for technology development. They present high dynamic damping properties: they can effectively absorb the energy of impact or of forces generated by deceleration without creating high damaging stresses [145] [148].

Shape Memory Effect

The *Shape Memory Effect* can be activated by several factors, as previoulsy said. The most common is heat, which corresponds to a temperature change; this is the reference case that will used to expalin the *SME*. When the material is heated above its transition temperature T_g, that is a property of the material istelf, it becomes soft and easily deformable; when the temperature is below T_g the material is quite stiff. Proper stress and strain conditions can be applied in different temperature ranges, activating the shape memory behaviour. Several SMEs can be identified [145]:

- One-way dual-shape memory effect;
- Two-way shape memory effect;
- Triple-shape memory effect;

The *one-way dual-shape memory effect* is the most common SME, and it is the most representative to expalin the working cycle of a SMP, shown in Figure 4.3 and Figure 4.4.

Three main variables can be identified: temperature, stress and strain. According to the evolution of these parameters, the SME cycle can be divided in thre main phases:

I **phase**: the material is heated at a temperature slightly above its transition temperature T_g. This determines a drastic drop of the Young's modulus and the material soften. Neither stress nor strain are registered in ths phase.

II **phase**: a load is applied, causing a deformation ε_{load}, under an isothermal loading condition. The load is then maintained constant for a certain time interval (*loading phase* section a), white the temperature is lowered gradually below T_g. When the temperature is low enough at a level where the material has the required stiffness, due to the Young's modulus change, the load is removed, while the temperature continues to be lowered (*unloading phase* section b). Upon load removal, a **temporary** shape is fixed, althoug a very small, negligible strain recovery occurs, usually of the order of 2% (red circle in the figure).

III **phase**: the material is re-heated, under a stress free condition, increasing the temperature above T_g; when the temperature crosses the T_g range, the deformation is rapidly recovered and the material comes back to its original, **permanent** shape.

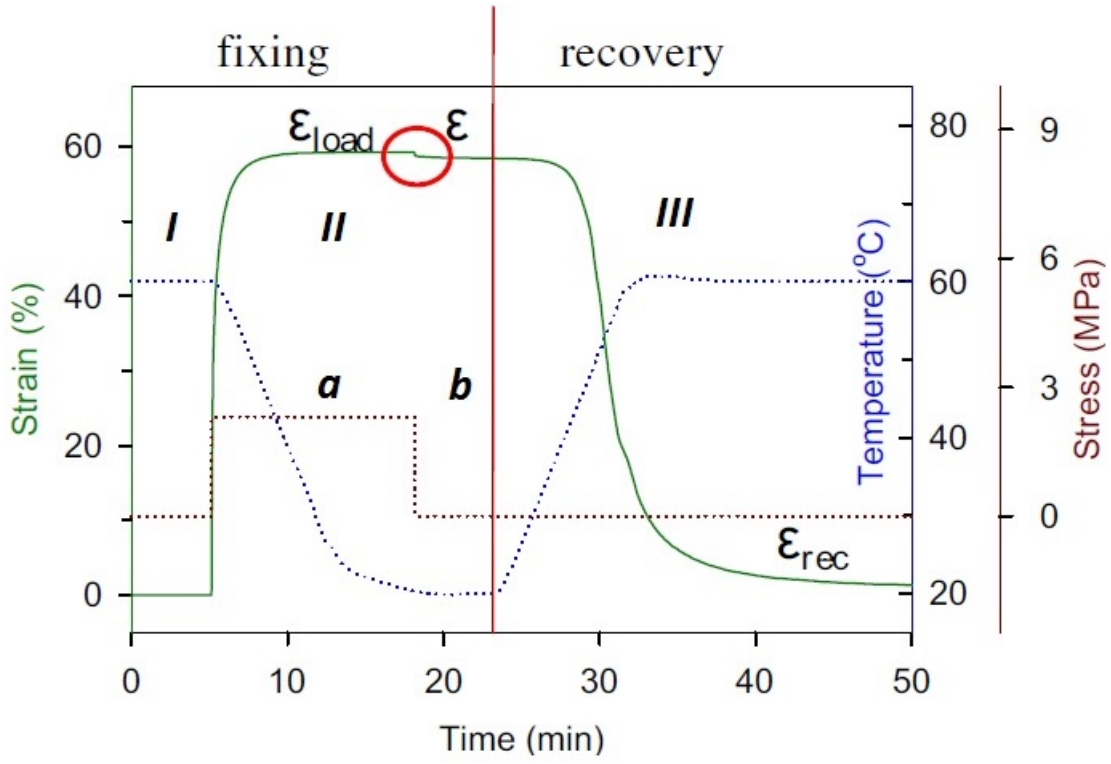

Figure 4.3: *Shape Memory Effect* cycle [145].

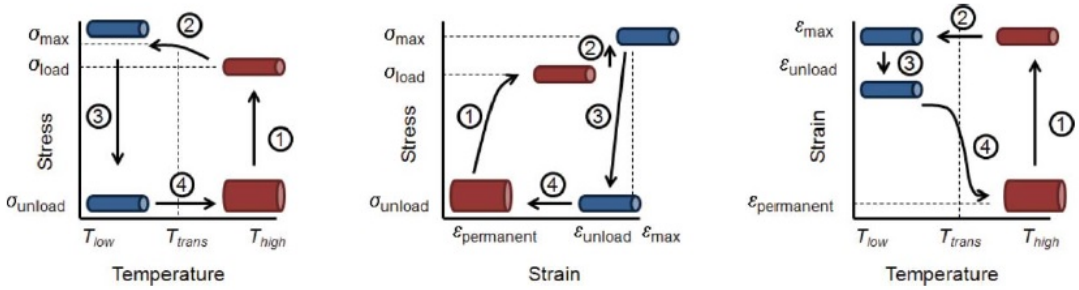

Figure 4.4: Illustration of the shape memory cycle [148]: stress/temperature plane (on the left), stress/strain plane (in the middle), and strain/temperature plane (on the right).

Phase I and II define the *shape fixing*, while phase III characterises the *shape recovery*. In the *one-way dual-shape memory effect* one transition temperature T_g and two shapes are involved: a temporary shape during the fixing phase, when $T < T_g$, and a permanent shape during the recovery phase,when $T > T_g$. The ability to fix and to recover the shape are defined by two parameters, respectively the *shape fixity* R_f and the *shape recovery* R_r [145]:

$$R_f = \frac{\varepsilon}{\varepsilon_{load}} * 100 \tag{4.1}$$

$$R_c = \frac{\varepsilon - \varepsilon_{rec}}{\varepsilon} * 100 \tag{4.2}$$

In a *one-way dual-shape memory effect* cycle, the deformations can be applied only one direction, i.e. in the order heating-cooling+deformation (temporary deformed shape)- heating (permanent shape recovery). The main difference in a *dual-shape memory effect* is that the polymer can be deformed reversibly in both cycle directions without the need of an external mechanical load. With polymers that have this characteristic, for example Liquid Crystalline Elastomer (LCE), it is possible to work under stress-free conditions but the strain is limited to 8%, although recent studies reached also 14 %. On the other hand, the range of reversible strain can be extremely high, about 300%, under non-zero stress conditions. This requirement plays a dual role: on one hand it is of practical importance since constant stress can be easily realized inside a device; on the other hand, it could limit the application of such polymers to simple elongations and contractions, if no further engineering solutions occur. The main drawback of *dual-shape memory effect* polymers is that their synthesis typically involves sophisticated chemistry and the transition temperatures cannot be easily tuned as transitional SMPs. In a *triple-shape memory effect* two thermal transitions can be applied to fix a temporary shape of a polymer, so three deformed shape states are available, including the permanent shape. The *triple-shape memory effect* cycle is then characterized by two shape fixing and two shape recoveries.
Varying the internal chemistry of SMPs, a wide range of tunable shape memory effects can be realised, spreading from dual-shape memory effect polymers to multi-shape memory effect ones.

Chemistry of SMPs

SME is mainly an entropic effect, characterised by the internal chemistry of the material, that derives from the synthesis processes [145]. SMP are urethane based materials which belong to the thermoplastic class. A polymer should present two main characteristics to display SME:

- reversible thermal transition: typical for the greater part of polmeric materials, that are in general intrinsically viscoelastic materials with at least one thermal reversible phase transition;
- **cross-linking** networks: the crosslinking prohibits the slippage between the chains when the material is deformed at temperatures greater than its transition temperature; the shape change then arises from entropy, which is recoverable, so the SME can be obtained.

As emerges, the cross-linkning is the key aspect that differentiates SMP from all the other polymeric materials, and that allows to have at least one permanent shape. The chemistry of polymers is not the subject of the present work, so the reader is invited to refer to proper materials researches. Clear treatise can be found in [145] and [148]. We will only focus on the cross-linking that characterises SMP to better explain the reasons of their particular behaviour. A *cross-link* is a bond between polymer's chains. It can be covalent or ionic. In polymeric materials, links are introduced through proper synthesis procedures to obtain different physical properties that influence then the material mechanical properties.
The cross-linking could be obtained chemically or physically.

Four SMP categories can be identified acording to the crosslinking origin, and most of the SMPs reenter in one of them:

1. chemically crosslinked glassy polymers;
2. chemically crosslinkedsemicrystalline polymers;
3. physically crosslinked glassypolymers;

4. physically crosslinked semicrystalline polymers.

Chemical crosslinking can be obtained, for example, by e-beams or UV radiation; so, most of the polymers can be chemically inverted in SMP. Physically crosslinked polymers are characterised by the presences of two or more phases with different transition temperatures. The structure of the two types of crosslinking is shown in Figure 4.5. Often, the shape memory effect is obtained physically, creating two different chain segments, one SOFT and one HARD: the soft one is responsible of the deformation, the hard one is responsible of the fixation of the permanent shape. The typical SME cycle, from the structure pont of view, is shown in Figure 4.6: the crosslinks act as springs that recall the polymer chains to their orginal configuration, restoring the permanent shape at the end of the SM cycle. The distinction between SMP and normal thermoplastic materals can be done analyzing the DMA curve of the material: in general, SMP, under heating, should present a 2-3 orders of drop in the elastic modulus, but then they have a plateau after this drop (see Figure 4.2. This plateau is an indicator of the prohibition chain slippage.

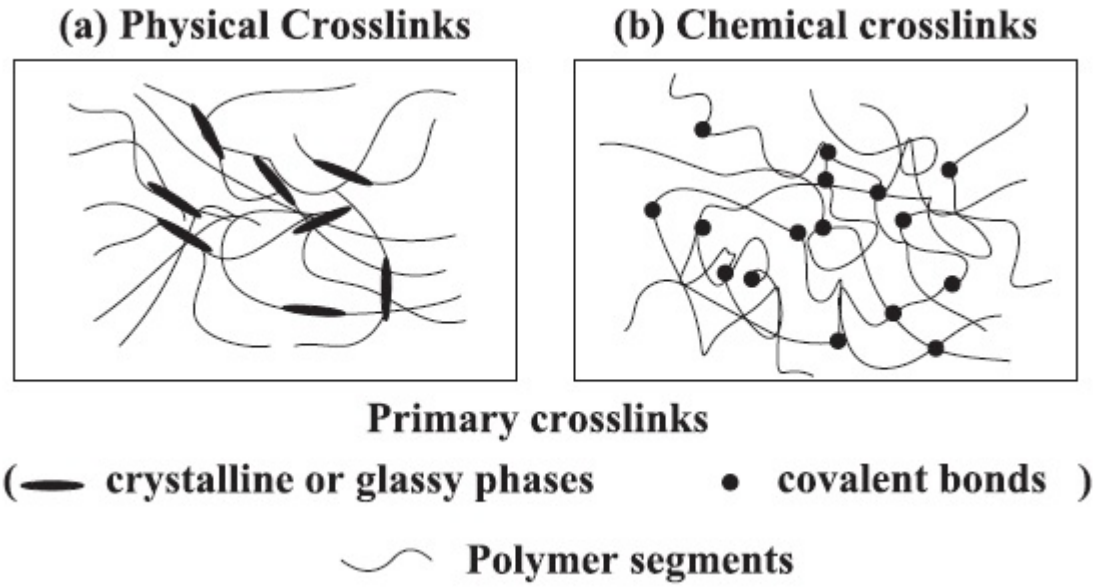

Figure 4.5: Schematics of the typical structures of a polymer network that is (a) physically cross-linked network; (b) chemically cross-linked network.

SMPs applications

SMPs can be found in a wide variety of applications, both in terrestrial and aerospace fields [148] [149]. As anticipated in the introduction, the first research field was related to biomedical applications and numerous studies have been performed over the years. More recent researches [148] proposed the employment of porous shape memory polymers mainly for embolic vascular devices, thanks to their large shape recovery, large surface area to volume ratios, and tortuous flow; an example is shown in Figure 4.7(a). Other potential biomedical applications include scaffolds for filling bone defects, hemostatic sponges, soft tissue scaffolds, and drug-delivery platforms. Cytotoxicity test were also performed by several researchers on the CHEM polyurethane foam, CHEM3520 and CHEM5520 foams to verify their compatibility with thehuman body [148]. Recently, in biomedial field, SMP have found large employment in the realization of orthopedic rehabilitation supports; an example is shown in Figure 4.7(c). These supports take advantage from the ability to fix the temporary shape of the SMP: they are produced in standardized sizes; before being applied, the material can be heated and molded around the part of the body to be supported, increasing the compliance and then the comfort. In this case, the advtange derives by the ability to fix the temporary deformed shape of the polymer.

SMPs have seen a real boom in the last years in the realization of comfort devices, such as matress,

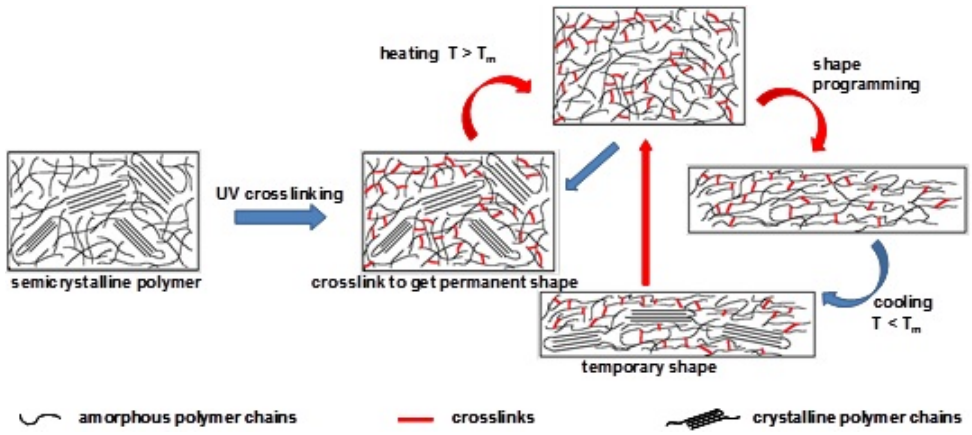

Figure 4.6: Example of SME at molecular scale: the crosslinks allow to maintain the deformed shape when the material is cooled, and they act as springs, recalling the chains to their original place, when the material is heated again, determinng the recovery of the permanent shape.

fillings elements for cushions and seats in medical, automotive, motorbike and aeronautical applications: the SMPs usually employed in such fields are characterised by transition temperatures near the human body temperature. In this way, when they get in contact with the human body, they become softer, and deform following the shape variation of the body, increasing the comfort sensation; they restore the original shape when the load is removed. As it can be observed in Figure 4.7(b) these materials are able to stand significant deformations and can follow quite precisly the shape of the body that causes the deformation. These characteristics resulted particularly attractive for our applications in adaptable interfaces to capture uncooperative objects. Other interesting terrestrial applications are related to the realization of smart technical textiles: proper SMP textiles are employed in motorbike suits, ski-boots, running shoes and many others, to enhance the adaptability to human shapes, in the same way explained for comfort devices.

Innovative applications of SMPs in the aeronautic field are related to the realization of adaptive airplane wings, even though several limitations are still present and further investigation is needed: the main concept is to change the shape of the wing by appling the required stimulus to the SMP in order to adapt the wing shape to different flight conditions, increasing in this way the general perfomances. Some studies in the *Morphing Aircraft Structures program* were sponsored by DARPA and Air Force Research Laboratorys Air Vehicles Directorate, but they were then closed. The work has been continued by the Cornerstone Reseacrh Group: CRG fabricated a subscale, carbon fiber-reinforced SMP composite wing prototype to demonstrate the feasibility of such solution: when heated, the wing can be reshaped by the internal wing structure and will maintain that shape when cooled. When reheated, the skin regains its original shape. Several practical challenges remain, like the heating of the wing inder the cooling effect of the inflight airflow; furthermore, the conventional structure of the wing of aircrafts should be re-designed since the SMP is not able to carry significant loads during the change in shape, and usually they are supported by the skin. An example of adaptive wing developed by CRG is shown in Figure 4.7(d) - 4.7(f). The U.S. Air Force has identified Unmanned Aerial Vehicles (UAVs) as possible practical candidates for the implementation of wing morphing technology.

SMPs have been considered for several other innovative applications, such as self-healing materials, flexible batteries, flexible electrodes and future LCD screens. These are only some examples of the great variety of fields that could take significant benefits from the implementation of such kind of materials.

In the space field, SMPs appeared around the second half of 1990s, when at JPL, it was established the study and development of a new kind of structures, known as *Cold Hibernated Elastic Memory (CHEM)* structures [149]. The main objective of the CHEM Structure Technology Development Program was to develop and validate the CHEM self-deployable structure technology for selected space applications. Several potential space applications were identified at that time, where the implementation of SMPs

appeared to be particularly interesting:

- support structures such as struts, beams, ...;
- robotics: rover subsystems such as wheels, chassis, insulation box, masts.
- low frequency parabolic antennas;
- power: solar array deployment device;
- sensing systems: radar structure;
- thermal control: insulation shields;
- in-situ propellant production: tanks, containers etc;
- space habitats: shelters, hangars etc;
- space electronics: insulation, boards;

Numerous research have been conducted on deployable structures [150], such as inflatable structures, large deployable structures, solar sails (example in Figure 4.7(g)). These applications could take advantages form the implementation of SMPs thanks to their relative low-cost, reliability and self-deployable properties; it has been also proven that SMPs can be stored in compressed states for long periods of time with no effect on shape recovery. They can be also employed as damping elements, absorbing energy from any striking object that would otherwise damage the structures, increasing the structures survivability in the space environment. For long booms technologies, they could be combined with carbon fiber reinforced polymers, increasing the buckling resistance of the entire structure. The polymer ribbons could improve the axial stiffness and the overall stability of the structure. Elastic energy stored in the ribbons when rolled into the stowed configuration could aid in the deployment of the truss element when the foam is heated. Possible applications as adaptable structures for nanoreovers were also foreseen, such as deformable wheels to adapt to different terrain surfaces in planetary missions (e.g. martian rovers) [149]. Monkman and coworkers investigated the use of a commercially available polyurethanebased SMP foam as an improvement on robotic gripping technology [151]: it was observed that the increase in temperature could result particularly advantageous to enhance the compliance with irregular surfaces of objects that had to be grasped. This concept is of particular interest for the capture interface developed in the present work.

Mid teaming with MITs Man Vehicle Lab (MVL) has completed a NASA Phase I study to determine the effectiveness of smart materials to provide Mechanical Counter Pressure (MCP) for MITs next generation Extra-Vehicular Activity (EVA) space suit, the Bio-Suit concept (Figure 4.7(h)) [152]. Mid produced SMP sleeves that when heat activated attempt to reach their memorized shape set state. Mid team created a hybrid material obtained by an elastomer garment impregnated with a SMP, creating a semi-flexible stretch garment at low temperature, and a highly flexible material at elevated temperature to increase the flexibility of the space suit in both conditions. Experiments on SMP are going to be carried out onboard the ISS in the near future. The Italian-Foam experiment will aim to evaluate the recovery of shape memory epoxy foam in microgravity using samples of various geometric complexities obtained by solid-state foaming on ground. The results of this study will be used to determine the shape memory properties required to manufacture new concept actuators for space applications.

Why SMPs for the capture interface

As emerges from the previous paragraph, SMPs are suitable materials for a wide range of applications. Their ability to become compliant also with complex geometries, such as human body, and the ability to fix temporary shapes make this class of polymers particularly attractive for the development of the morphing interface for the capture of uncooperative objects. In Figure 4.8 and 4.9 are shown chemical compositions, physical, and material properties of porous SMP materials: it is particularly interesting how changing the chemistry of such materials, a great variety of properties can be obtained, allowing the material to be tuned according to the working conditions.

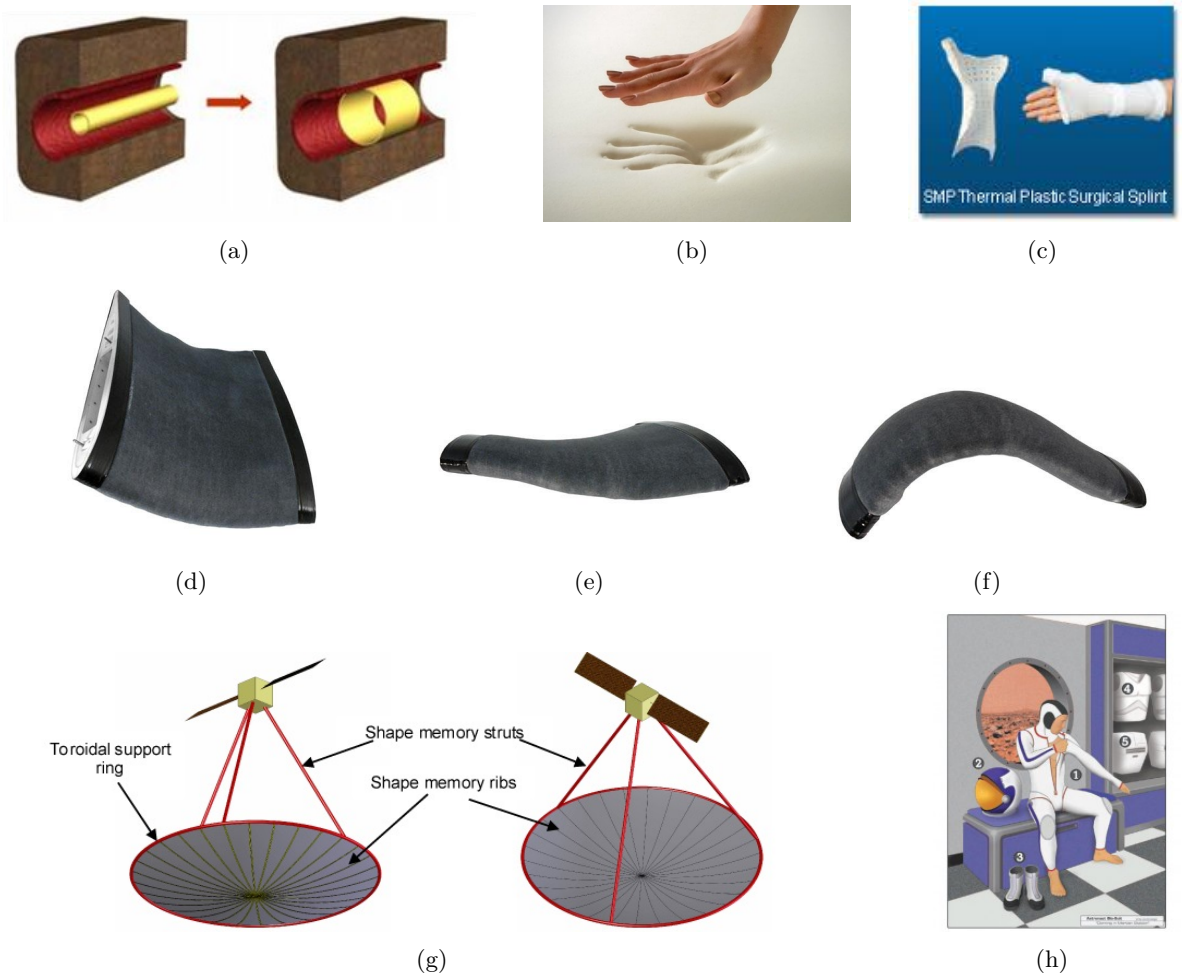

(a) (b) (c)

(d) (e) (f)

(g) (h)

Figure 4.7: Example of terrestrial and space applications where SMP are employed: (a) biomedial application for surgical operations, (b) comfort devices, like matress or cuscions fillings, (c) supporting devices for post-surgical rehabilitation, (d)(e)(f) possible configurations with adaptabe wings, (g) deployable structures for space applcations, (h) technical textures for space suits.

Material	Procured From	Density	Modulus	T_{trans}
CHEM Polyurethane Foam	Mitsubishi, Jet Propulsion Lab	0.032 g/cm^3	—	60°C (T_g)[43]
MF5520 Foam	Mitsubishi Heavy Industries	—	—	63°C (T_g),[81] 64°C (T_g)[77]
MF No. 21 Foam	Mitsubishi Heavy Industries	—	10 MPa	55°C (T_g)[12]
TEMBO® 3XE 2-part epoxy foam	Composite Technology Development (CTD)	0.20 g/cm^3	50 MPa	92 ± 3°C (T_g)[49]
TEMBO® DP5.1 2-part epoxy foam	Composite Technology Development (CTD)	RD 0.20, 0.30, 0.40	60–120 MPa	83–88°C (T_g)[53, 67]
CHEM 3520 Polyurethane Foam	Mitsubishi, Jet Propulsion Lab	0.12 g/cm^3	10–20 MPa	32°C (T_g)[36]
CaloMER 48 Foam	Polymer Technology Group, Berkeley, CA; Blowing agents Plastronfoam BSH and W16	0.85–0.91 g/cm^3	1000 MPa	61–89°C (T_g)[44]
	Polymer Technology Group, Berkeley, CA; Prepared by salt leaching 20, 50, 70 wt% NaCl	0.67–1.11 g/cm^3	1000 MPa	82–89°C[44]
Veriflex® polystyrene syntactic foam (2 part thermoset resin system: Part A has styrene, divinyl benzene and vinyl neodecanoate, Part B has benzoyl peroxide)	CRG Industries SMP, Potter's Industries glass microballoons	0.08–0.14 g/cm^3	845 MPa	64–71°C (T_g)[90]

(Continued on next page)

Figure 4.8: Comparison of chemical compositions, physical, and material properties of porous SMP materials reported in the literature [148].

Material	Procured From	Density	Modulus	T_{trans}
Polyurethane foam from MDI, diethanolamine, ester type polyols (ethylene glycol, 1–4 butane glycol, adipic acid)	Gas blowing (DC2583 silicone surfactant; BL-22, BL-11 blowing catalyst, Dabco 33LV gelling catalyst)	0.22–0.30 g/cm^3	20 MPa	20°C (T_g)[19]
Polyurethane foam (Hexamethylene Diisocyanate (HDI), Trimethyl hexamethylene diisocyanate (TMHDI), Triethanolamine (TEA), Hydroxy propyl ethylene diamine (HPED).	Gas Blowing (DC5179, DCI990 surfactants, BL-22 blowing catalyst, T-131 gelling catalyst, Enovate and water- blowing agents)	0.015–0.027 g/cm^3	0.15–0.30 MPa (shear)	44–86°C (T_g)[35]
Poly ester-urethane, from Poly caprolactone triol (M_n = 4000 Da), MDI and 1,4-butanediol	Salt leaching; PU dissolved in THF, NaCl poragen	0.11 g/cm^3	—	31°C (T_m)[27]
3M Skotchkote 206N one part heat curable epoxy resin	Solid State Foaming	0.35–0.65 g/cm^3	80–220 MPa	100–105°C (T_g)[55]

Figure 4.9: Comparison of chemical compositions, physical, and material properties of porous SMP materials reported in the literature [148].

4.2.3 Adhesion capabilities

One of the main requirements in a capture maneouvre is the maintance of the contact between the gripper and the captured object: in other words, it has to be guaranteed the adhesion at the contact interfaces. In general, the term adhesives is used to refer to substances that create a permanent bond between two contact surfaces. Solid bonds are realized by means of different kind of adhesion techniques. Several studies have been carried out over the years and many improvements have been made in the creation of new substances that allow the joining of dissimilar materials, such as metals, wood, plastics, rubbers, fiber composites, paper products and so on [153] [154].
When large and irregular contact interfaces are involved, such solutions could be less effective; more complex devices could also be needed to allow the adhesive to be spread on the entire surfaces.
Other adhesion technologies, where the adhesion forces act as surface forces, have then been considered. The basic idea came from the ability of some animals, like geckos, to generate strong adhesion and friction forces when they adhere to a surface. The adhesion and friction forces are rapidly relaxed on releasing, allowing them to climb almost any kind of surface [155] [156]. Inspired by the gecko's bioadhesive system, various structured surfaces have been fabricated suitable for robotic applications, especially in the field of the wall-climbing robots [157]. This kind of adhesion is in general referred to as dry-adhesion and is thought to rely on the Van der Waals forces that arise between the gripper surface and the substrate to which it has to adhere. For wall-climbing robots, a further evolution of dry-adhesion as means of adhesion to different kind of surfaces has been represented by the electro-adhesion, a reversible technology which uses the generation of electrostatic forces between two contact surfaces to create a temporary bond [158] [159] [160] [161]. Considering the adhesion shear pressures that can be reached and reported in literature, electroadhesion could represent a promising solution to be implemented in robot grippers which require to generate adhesion forces on a large variety of surfaces.

4.2.4 Electroadhesion

Electroadhesion was developed for robotic manipulation during clothing manufacturing in 1989 by Monkman [162]; electrostatic latching has been proposed for the creation of modular robotic systems and electrostatic chucks have been studied for a variety of micro-fabrication processes, such as lithography, ion implantation, plasma etch, film deposition, and inspection [163]. In the last decades electroadhesion has become one of the most interesting technologies in the field of wall-climbing robots [159] [160] [161]: thanks to the generation of electrostatic forces, these robots are able to climb a wide variety of surfaces, conductive but even non-concuctive, such as wood, concrete, glass. Examples are shown in the first three pictures in Figure 4.10. This characteristic makes electroadhesion particularly attractive for a great variety of applications, including robot grippers; some demonstrative concepts have already been developedby SRI International, and are shown in Figure 4.10 [164].

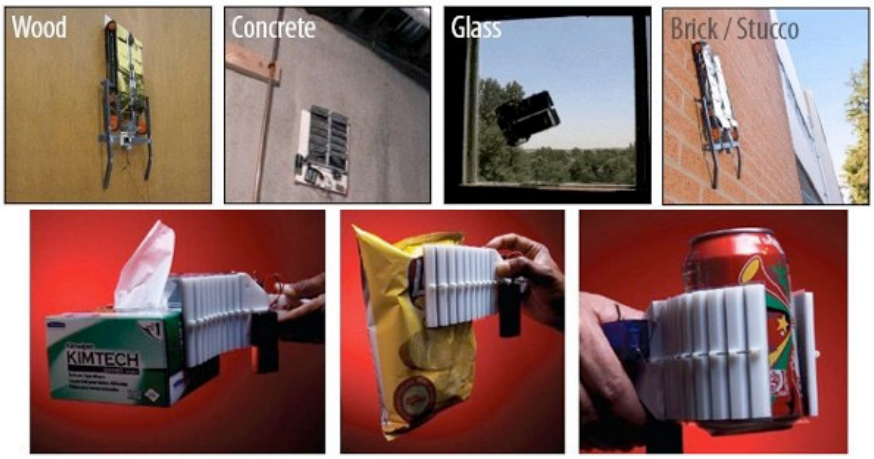

Figure 4.10: Scheme of an electroadhesive interface [164].

Working principle

The basic principle of electroadhesion is to induce the generation of *electrostatic* forces between two contact surfaces to allow them to adhere and maintain the contact. A scheme of a typical electroadhesive layer is shown in Figure 4.11. Specifically, an electroadhesive layer is made depositing a pair of independent electrodes (red and black in the figure), on an insulating material, usually a polymer (light blue in the figure). As we previously said, the electroadhesive interface can get in contact with conductive surfaces, as well as insulating ones (green substrate in the figure). In the first case, and in general for safety reasons, the electrodes are covered with a very thin layer of insulating material to avoid any direct contact with the conductive surface and to reduce the risk of possible spikes. The electrodes result then embedded in the insulator. A high voltage, between 1kV and 5kV (although higher voltages can be applied according to the charactristics of the device), is applied to the electrodes: this let an electric field to arise betwen the electrodes. The effect is similar to the capacitor working principle, with the difference that in this case, the electrodes lie on the sample plane instead of being parallel. When a second surface is moved towards the electroadhesive interface and gets in contact with it, the electric field changes its shape and the charges on the electrodes induce an opposite charge on the object surface, generating attractive electrostatic forces through the insulating layer.

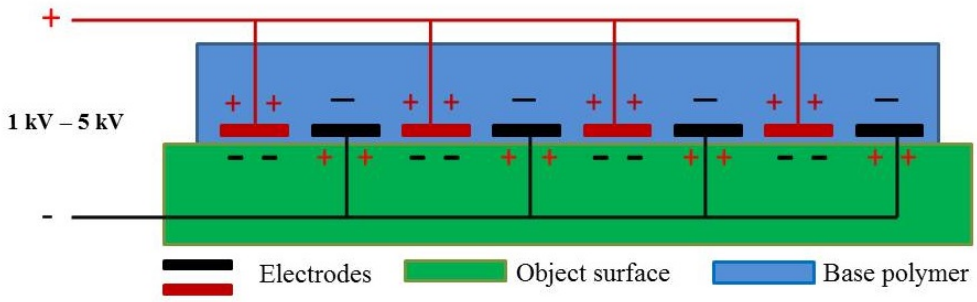

Figure 4.11: Scheme of an electroadhesive interface.

Several works [159] [160] [161] [165] have investigated the performances of such technology and it has ben demonstrated that the adhesion force achievable through electroadhesion depends on several factors, such as:

- the applied voltage:
- the thickness of the insulator and the material is made of;
- the nature and the roughness of the object surface: if it conductive or not, smoth or rough;
- the geometry of the electrodes.

Increasing the applied voltage, the intensity of the electric field increases and then, the level of electroastatic force achievable. It exists anyway a maximum voltage above which the system saturate and no significant increase of the adhesion force is observed as the voltage is further increased [166]. This happen because after a certain voltage level, the HV/DC power supply could start to supply non-zero current (as in a capacitor, no current flows in the system during its functioning). When current begins to flow, the ideal electrostatic model is no longer valid, and leakage and corona discharge phenomenons arise, determining the saturation of the device. The influence of the insulator thickness and material has been well demonstrated in several researches [160]: as the thickness increases, the adhesion force level achievable decreases. This could be in part foreseen: as in a capacitor, the intensity of the electric field, and then the attraction force between the plates, decreases as the electrodes gap becomes higher. Furthermore, in this case, the insulating material acts as dielectric, and it is known that the force between the plates depends on the dielectric properties of the material placed between them. In our specific application, an important role is also played by the surface of the object to be captured [158]. If the

surface is conductive, the mechanism of force generation can be derived from the basic electrostatic theory. In case of an insulating surface, the pricnciples of force generation are different and related to the two major types of electrical polarization: permanent polarization, due to molecule's permanent dipole moment, and induced polarization, which is the result of an applied electric field. In a very simple way, when the surface is conductive, the free electrones reorganise themselves in order to balance the charge induced by the electric field between the electrodes; if the material is insulating, there are no free electrons, so the only way to re-organise according to the electric field is by turning the molecules in a way that allow to neutralise the build up charge. In a solid, the molecules are usually rigidly bounded, and rotation and displacements are very limited. The basic equations can be derived by the main principles of polarization. In our work, only conductive surfaces were considered, so the latter case was not further investigated. The surface roughness has a direct effect on the adhesive force, at a microscopic level: it has been demonstrated that the adhesion on rough surfaces is less effective than on smooth surfaces [165]. Adhesion forces on drywall, tile or cedar, that are samples of different materials and roughness, can vary of several percentage, for the same electrodes geometry: the better performances are on a tile, 20% and 40% lower on drywall and cedar respectively for a square spiral configuration. Several works have also highlighted that the geometry of the electrodes could significantly influence the adhesion force achievable: a basic interdigitated configuration, shown in Figure 4.12(a) appears to be one of the simplest and most effective geometries [160] [161], compared to a two rectangular electrodes configuration of the same total area. It was demonstrated as configuration with alternate electrodes works better than with two single electrodes. The interdigitated geometry has been the most used configuration up to now in the realization of the adhesive devices of climbing robots (see Figure 4.12(c)). Some recent studies investigated other geometries [165] [167], shown in Figure 4.13: it emerged that a concentric circles pattern could allow the best performances; the width of the electrodes can be also optimized in each configurations, creating geometries with variable width, improving the adhesion performances. It can be also performed the gap between the electrodes with respect to the width of the electrodes.

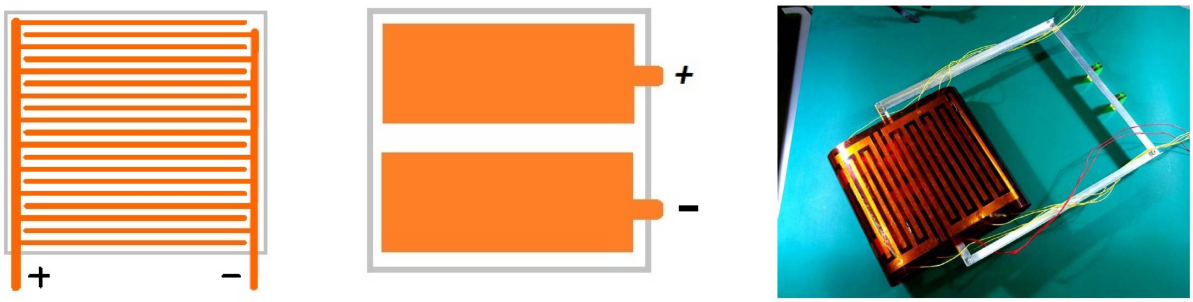

(a) (b) (c)

Figure 4.12: Example of interdigitated electrodes geometry (a) and equivalent rectangular electrodes configuration (b). In (c) it is represented the typical electroadhesive layer employed in climbing robots, with the interdigitated configuration.

Approximation of the adhesion force

A first approximation of the intensity of this force was provided by Monkman [158] in 1999, considering the parallel plane capacitor model; the attraction force between two parallel plates of a capacitor is expressed as:

$$F_{EA} = \frac{1}{2} A_{el} \varepsilon_0 E^2 \tag{4.3}$$

where A_{el} is the area of a plane electrode, ε_0 is the permittivity of free space, E is the electric field generated across the the electrodes. The electric field E depends on the voltage V applied and the distance d between the plates:

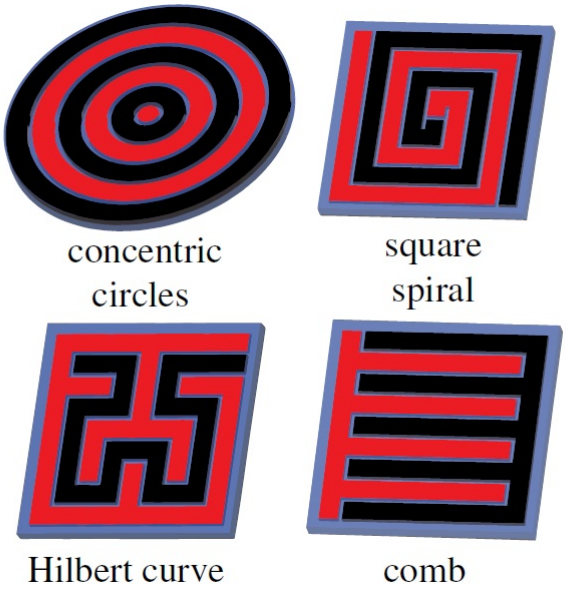

Figure 4.13: Simulation models of electrodes patterns used in [167] to optimize electrostatic adhesive geometries.

$$E = \left(\frac{V}{d}\right) \tag{4.4}$$

and the equation 4.3 can be written as:

$$F_{EA} = \frac{1}{2} A_{el} \varepsilon_0 \left(\frac{V}{d}\right)^2 \tag{4.5}$$

This expression is for a simple plane capacitor with no insulator between the plates. Furthermore, in this expression does not appear any information relative to the geometry and the configuration of the electrodes for which, on the contrary, it has been demonstrated that they could have a significant influent on the intensity of the adhesion force.

A more accurate relation can be found in [163]:

$$F_{EA} = \frac{1}{2} A_{el} \varepsilon_0 \frac{V^2}{\left(g + \frac{2d}{\varepsilon_r}\right)^2} \tag{4.6}$$

This expression is referred to an electrostatic latch where d is the thickness of the insulator and g is the gap between the electrodes and ε_r is the dielectric constant of the nsulator. In this case the gap is considered in vacuum.

In case of an electroadhesive interface, the system can be schematically rapresented as shown in Figure 4.14. When the electrodes are embedded in the insulator, the gap is filled with the same material, so it has to be considered the correspondent dielectric constant ε_r; the dielectric thickness is counted twice since the total distance between the electrodes is 2d. In our analysis, Equation 4.6 was then modified in the following way:

$$F_{EA} = \frac{1}{2} A_{el} \varepsilon_0 \frac{V^2}{\left(\frac{g}{\varepsilon_r} + \frac{2d}{\varepsilon_r}\right)^2} \tag{4.7}$$

Considering the interdigitated configuration, the total force generated is given by the product of the previous equation with the number of pairs of electrodes; the final approximated expression is then:

$$F_{EA,tot} = N_{pairs} * \frac{1}{2} A_{el} \varepsilon_0 \frac{V^2}{\left(\frac{g}{\varepsilon_r} + \frac{2d}{\varepsilon_r}\right)^2} \tag{4.8}$$

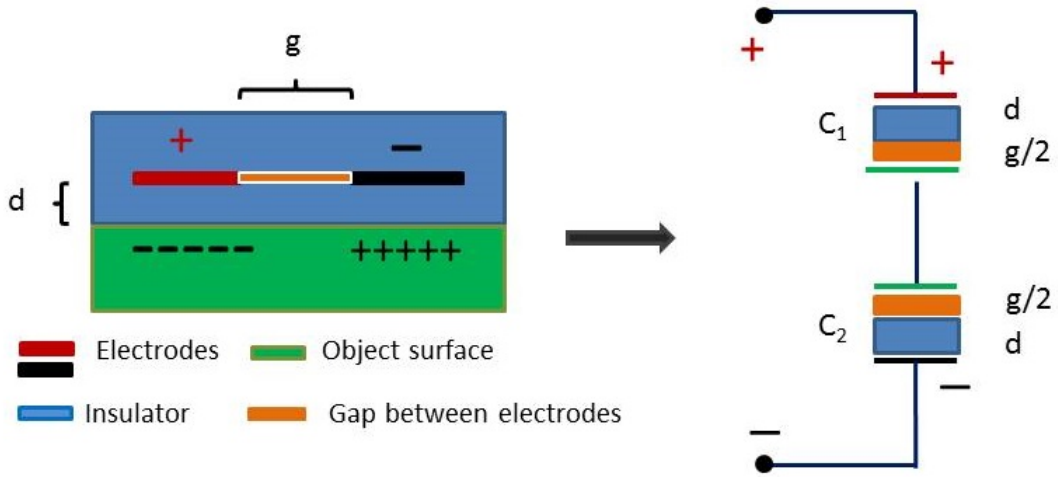

Figure 4.14: Example of interdigitated electrodes geometry (a) and equivalent rectangular electrodes configuration (b).

Equation 4.8 is otained starting from the capacitor theory. The influence of the insulator and of the electrodes geometry can be identified in the parameters ε_r and d, A_{el} and g. It has to underlined that it is only an approximation of the achievable force. As previously said, the adhesion force depends on several parameters that do not appear in the equation, such as the surface roughness. Furthermore it can be applied only when the electroadhesive interface is put in contact with a conductive surface. For more complex geomtries, FEM analysis could be required to obtaine more accurate models. Electroadhesion theory lacks of knowledge as concerns the force modelling, so no many references were available to compare the results obtained with analtycal expressions. A recent study proposed a more detailed modelling of the theoretical force that takes into account several factors, such the geometry of the electrodes and the gap between them, not considered in previous works [168]. The study is limited to the interdigitated configuration. Without describing all the theory developed, it is reported only the final expression of the normal adhesion force and normal adhesion pressure obtained by the authors:

$$F_{EA,Kho} = \frac{0.5\varepsilon_0\varepsilon_{ins} w l V^2}{g^2} + \frac{0.265\varepsilon_0\varepsilon_{ins} w^{0.5} l V^2}{g^{1.5}} \tag{4.9}$$

$$P_{EA,Kho} = \varepsilon_0\varepsilon_{ins} V^2 \frac{0.25 w d^{-2} + 0.135 w^{0.5} d^{-1.5}}{w + d}; \tag{4.10}$$

The normal adhesion pressure is obtained from Equation 4.9 considering the area (2w + 2d)*l, that is the total area on which the electrostatic froce is spread, shown in Figure 4.15. w is the width of the electrodes, l is the length of each arm of the electrodes; the other parameters are the same defined above. The difference between the adhesion pressure estimated through the capacitor theory (Equation 4.7) and the model developed by Koh in [168] (Equation 4.10) is shown in Figure 4.16, for $w = 0.5mm$, $d = 0.5mm$, $l = 4.5mm$, $\varepsilon_r = 5$ that is the dielectric constant of the silicone employed to realise the electroadhesive interface. As it emerges from the plot, the modified capacitor theory and the theory obtaind through the three dimensional model developed by Koh [168] are similar, of the same order of amgnitude. In the model developed by Kho does not appear the dielectric thickness and the adhesion pressure is slightly above the line obtained with the capacitor theory. With the second theory it has to be considered a reducing factor due to the presence of the insulator between the electrodes and the surface of the object. Anyway, both models allow to determine an approximation of the achievable adhesion force, once the geometry is known. Unfortunately, the are no references where normale tests were performed:

all the data that can be found in literature refer to shear adhesion test, which are influenced by the friction coefficient; most of the times, no precise values of such parameter are reported, so it was difficult to validate the models with experimental data. Some prelminary considerations will be reported at the end of the tests section.

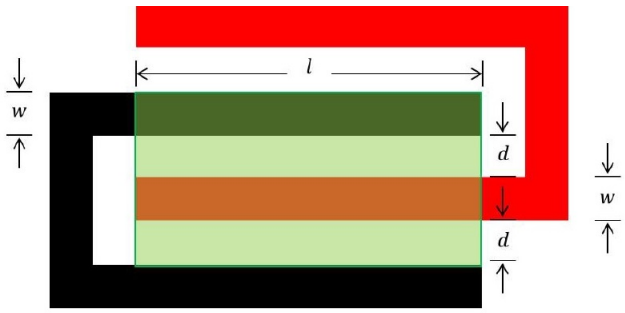

Figure 4.15: Interdigitated configuration considered to determine the adhesion performances in [168].

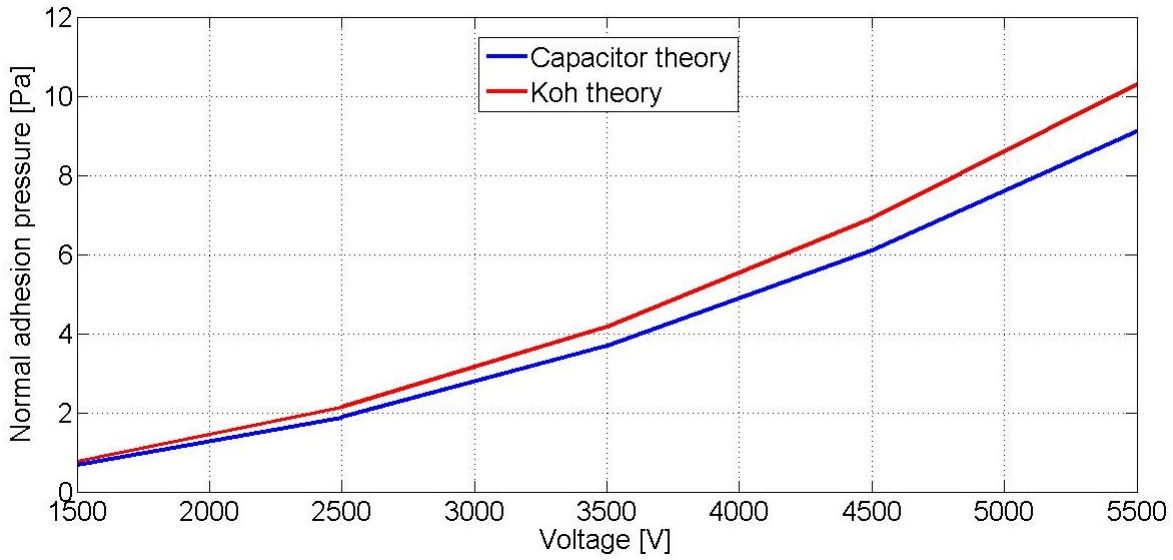

Figure 4.16: Comparison between the normal adhesion pressure evaluated with the capacitor theory and with the model developed by Koh in [168].

Concerning the shear adhesion pressure, previous studies demonstrated that it can range form few kPa to few tens of kPa, depending on the substrate: in Figure 4.17 some measured clamping pressures obtained on several materials with a 1 cm^2 sample are reported to give an idea of the force achievable [159].

Some other studies reported similar results: as it can be seen, the substrate on which the adhesion performances are tested has a significant influence. The normal adhesion pressures estimated by Prahalad [159] and the values that can be extrapolated form other studies, from the shear tests, are greater than the adhesion pressures predictied with the models presented above. This highlights that there are other paramters that cannot be included in an analytical model, but whose influence affect the overall perofrmances of an electroadhesive interface. It wil be observed that when silicones and similiar polymers are used for the insulator, adhesion effects arise due to the natural adhesion that these maerials can present. For more details, it is suggested to investigate the theory of rubber friction. In this work, the main nterest was to investigate how shape memory polymers and electroadhesion could be combined for a space gripper. The prototypes developed will be usefull for further future investigations.

MEASURED CLAMPING PRESSURES ON A VARIETY OF SUBSTRATES, MEASURED WITH 4 KV DC ACTUATION VOLTAGE

Material	Measured Lateral Force per Unit Area P_L (N/cm^2)	Measured Frictional Coefficient	Estimated Normal Pressure P_N (N/cm^2)
Finished wood (shelf wood)	0.55	0.4	1.375
Drywall	0.21	0.40 (estimated)	0.525
Paper	0.24	0.46	0.52
Glass	0.41	0.45	0.84
Concrete (dry)	0.17	0.57	0.3
Concrete (damp)	0.08	0.40 (estimated)	0.2
Steel	1.4	0.33	4.24

Figure 4.17: Shear adhesion pressures measured on different materials [159].

Origin of the adhesion force

Some tests performed on the developed interface revealed that the insulating silicone layer, when placed on a surface, was able to adhere, and a small force was required to detach it from the object in normal direction. The phenomenon was amplified in shear direction. It was found that this effect could be related to the theory of rubber friction: a clarifying interpretation of the adhesion effect can be found in [169]. Without going inside the details, we explain te main prnciple useful to understand the results obtained by tests. As reported in *"On the theory of rubber friction"* by Persson, *"For elastically hard materials, adhesion usually does not manifest itself on a macroscopic scale. The area of real contact consists of nearly randomly distributed contact areas (junctions), where surface asperities of the two surfaces "touch". The surface asperities are elastically deformed and since they have different sizes and shapes, the junctions will "pop", one after another, as the block is removed. The situation is drastically different for rubber and other elastically soft solids. In these cases, even a weak adhesive junction, e.g. resulting from Wan der Waals interaction between the surfaces, may be elongated before breaking by a distance which is larger than the "height" of the surface asperities.* As emerged from the paper [169], the adhesion between two contact surfaces is influenced by the nature of the surfaces themselves, and it is characterised by the combination of two phenomenon: the contact between the surface asperities and the generation of Wan der Waals interaction at the contact interface.
When both materials are elastically hard solid, the adhesion is mainly related to the contact between the asperities and to the real area of contact; it manifests only in shear direction and it is governed by the common friction theory; the friction coefficient is always less than 1 and in presence of smooth surfaces, the adhesion can be very low due to the low number of asperities. It is not usually observed any adhesion in normal direction.
The latter prevails when one of the two contact surfaces is an elastically soft solid, like polymers and silicones: in this case the adhesion is mainly related to the generation of Wan der Waals force between the two surfaces. In this case, the adhesion could be observed not only in shear direction, but also in normal direction. In shear direction, high loads could be required to cause the detachment between the surfaces, also when negliglible force are applied in normal direction (it could happen that if the material is placed on a vertical surface without any kind of support, it could remain attached, without sliding down). The interesting effect is that in this case, some adhesion can be observed also in normal direction. The friction coefficient μ, for such kind of materials, can be also greater than 1, reaching values around 10 or more, depending on the material. It was also observed that, because of the molecular adhesion, $\mu \longrightarrow \infty$ when $L \longrightarrow 0$, and it decreases with increasing load, becoming constant at high enough load. This second kind of adhesion is better known as *dry adhesion* and it is the main working principle of bioinspired systems [155] [156] [157] [170]. In these systems, proper surface geometries, like mushrooms cups or pillars, are employed to increase the contact surface area, enhancing the generation of Wan der Waals forces. It was

demonstrated that the adhesion increases respect to planar surfaces. The interesting effect is that the adhesion can be significantly increased by electroadhesion: the electrostatic attraction forces the surfaces to get in contact, promoting the Wan der Waals interactions. This effect can be assimilated to a kind of *electrostatic pre-load*. The overall adhesion force is a combination between the electrostatic attraction, the pre-loading effect and the resulting Wan der Waals interactions at the contact interface. These elements will be evident in the analysis performed after tests.
This is the guide principle for the development of the gripping interface. A planar surface will be selected: even though the dry-adhesion performances are expected to be lower than more complex micro-geometries, like mushrooms cups or pillars, the latters could be sensible to normal loads and deformations caused by macroscopic irregularities, decreasing the nominal adhesion capabilities. The lanar surface was assumed to be a good starting point for the preliminary study of the morphing-adhesive iterface.

4.2.5 Thermal model

A thermal model was developed to predict the electrical power required to heat the polymer sample from room temperature to $T > T_g$, where T_g is the polymers glass transition temperature. The model was then validated through experimental data obtained with proper thermal tests. This part of the activity is taken from the internal report [171].

The thermal balance is described by equation

$$mc\frac{dT}{dt} = P - Q_{rad} - Q_{cond} - Q_{conv} \tag{4.11}$$

where m and c are the mass of the sample and the specific heat of the polymer, T is temperature and t is time; P is the electrical power; Q_{rad}, Q_{cond} and Q_{conv} are the heat fluxes dissipated by the polymer sample respectively by radiation, conduction and convection. In more detail:

$$Q_{rad} = \sigma_n A_t F_v \varepsilon_t (T_t^4 - T_e^4) \tag{4.12}$$

$$Q_{cond} = 4A_s \frac{\lambda_s}{l_s}(T_t - T_e) \tag{4.13}$$

$$Q_{conv} = \alpha_{conv} A_t (T_t - T_e) \tag{4.14}$$

In the above equations, σ_n is the Stefan-Boltzmann constant, subscripts t, s and e stand respectively for polymer sample, support and environment, A is surface area, F_v is the view factor from the polymer sample to the environment, ε is emissivity, λ_s is thermal conductivity, l is length and α_{conv} is convective heat transfer coefficient. The environment is supposed to be a large black chamber held at constant temperature $T_c = 293K$. The convective heat flux is due to natural convection and α_{conv} is calculated using the McAdams empirical correlation [**?**]. For a white rectangular sample having size 100x120x2.5 mm^3, the model predicts that the electric power required to heat the polymer up to 388 K (i.e. $T_g + \Delta T$, where $\Delta T = 20K$ is a margin to ensure that the glass transition is reached throughout the material) is $P = (34.0 \pm 5.1)W$ in laboratory (with air at ambient pressure and temperature). The uncertainty in the nominal power value is related to both the model assumptions and the uncertainty in the knowledge of the models physical parameters (in particular the polymer samples emissivity ε_t and the convective heat transfer coefficient α_{conv}).

4.3 Prototypes realization and testing

This part of the research activity was performed in collaboration with Prof. Carlo Menon at MENRVA Research Group, Simon Fraser University of Burnaby (Vancouver), Canada. The activity was divided in two main parts:

I **proof of concept**:
the objective, in this phase, was to study the feasibility of an innovative technological concept

where the conductive pattern of electrodes was supposed to be responsible for controlling both the morphing behaviour and the adhesion capabilities. The idea was to design a proper electrodes geometry that allowed to connect properly the electrodes, switching between a resistive mode, in which the electrodes acted as resistors and hetaed the polymer by the Joule effect, and a capacitive mode, where the electrodes became the plates of a capacitor, allowing the adhesion through the generation of the electrostatic forces. The morphing behaviour is tested separately using a SMP available on the market.

II **combination of morphing-adhesive capabilities**:
in this phase, the electroadhesive interface and a deformable substrate were combined to test the capabilities to adhere on surface with macroscopical irregularities.

4.3.1 Prototype # 1: design and realization

The main objective of this first testing phase was to analyse and verify the possibility to employ the electrodes of the electro-adhesive interface as both capacitors and resistors, i.e. if it was feasible to integrate the electrodes in a single circuit that allows to switch between the two modes. Two parameters were identified as the main drivers to be considered in the design of the resistive-electroadhesive interface. On one hand, the electrodes pattern should ensure a certain level of heating power, due to Joule effect, when connected in a resistive mode and, on the other hand, proper geometries should be implemented to maximize the adhesion force.

The material used to realize the resistive-electroadhesive interface consisted of a copper layer, 0.07 mm thick, deposited on a Kapton layer, 0.08 mm thick (DuPont, Pyralux AC). Using a common PCB etching technique, a sample was obtained where the copper electrodes reproduced the selected geometry of the conductive pattern on the Kapton layer. Several conductive configurations were considered to determine the better compromise between the maximum electrical resistance, which determines the maximum power available based on the Joule effect, and the electroadhesion force level. A contact area approximately 10x10cm was selected as reference area. Figure 4.18 shows the geometries that were analysed. Although several studies [160] [161] demonstrated that an interdigitated configuration is the most suitable geometry to enhance electradhesion (e.g. configuration C in Figure 4.12, where positive and negative electrodes are alternated), such configuration could not be employed for our purpose since it does not allow a continuous flow of current along the entire conductive pattern when the electrodes are connected in a resistive mode. In fact, the current flows along the lowest-resistance path and in this case it would flow only along the external lines of the pattern; this could cause a short circuit when the electrodes are connected to the external power supply, because of the low resistance of the conductor, and furthermore, it would not be possible to heat the polymer over the entire surface. For all these reasons, the configurations A and B in Figure 4.12 appeared to be the most suitable for this study. At this point, the driving parameter for the final configuration was the resistance of the entire circuit. The power supply available for the experiments had a maximum current limit, and hence, using a specific output voltage line, the resistance of the pattern would have been high enough to avoid any risk of short circuit. The electrical resistance equation is:

$$R = \rho \frac{L}{A} \tag{4.15}$$

where R is the resistance in Ω, ρ is the electrical resistivity of the material in Ωm (1.67e-8 Ωm for copper), L is the total length of the conductor in meters and A is the cross-section area in m^2. As it can be seen, high values of resistance R can be obtained by either increasing the length of the conductive pattern or decreasing the cross-section area of the conductor. In our case, since the fabrication process of the electrodes limited the minimum width achievable to approximately 1 mm, the only means available to increase the resistance was to increase as much as possible the length of the conductive path, remaining within a 10x10 cm^2 area, while maintaining a safety distance between each pair of electrodes. An electrode gap of 2 mm was selected, based on the breakdown voltage of air (3 kV in vacuum, lower at ambient conditions). The dimensions of the final design are summarized in Table 4.1 and a picture of the realised resistive-electroadhesive interface is shown in Figure 4.19: in blue the capacitive line is shown, while in red it is shown the resistive connection. When one of the two modes is activated, the other one is off: this means that, when the eletrodes are connected to the HVA, all the connection of the resisitve line are open, and viceversa. This is for safety reasons, in order to avoid any damage to the HVA due to accidental

current flow, as well as to the power supply due to the built up charge on the electrodes. According to this configuration, the maximum adhesion force was expected to occur applying a voltage of about 3 kV.

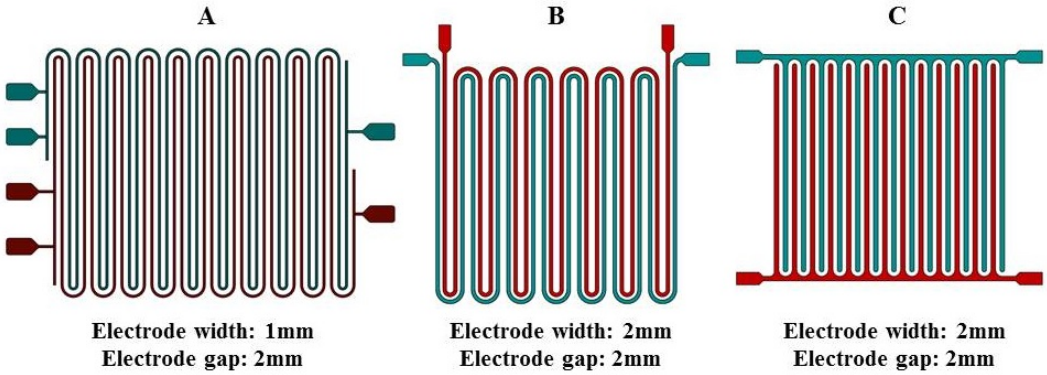

Figure 4.18: Electrodes configurations.

Configuration B: characteristics	
Electrode width $[mm]$	1
Gap between electrodes $[mm]$	2
Total length of the conductive path $[m]$	4
Total resistance of the conductive pattern $[\Omega]$	0.8

Table 4.1: Geometric and electrical characteristics of the conductive path realised for Prototype #1.

Since the resistive pattern material was made of copper, it was quite difficult to increase the resistance to higher values, copper being a good conductor. Future improvements on this aspect are foreseen. The 3.3V output line voltage of an ATX 450W power supply was used as a power supply, resulting in a total power of 13W being available to heat the polymer.

4.3.2 Prototype # 1: tests and results

Adhesion test

The experimental setup used to test the electroadhesion is shown in Figure 4.20. A DC-DC high voltage amplifier (E101CT, $EMCO^{TM}$ High Voltage) with maximum output voltages 5000V was used to charge the electrodes to the desired output voltage. The sample was rigidly connected to a $FUTEK^{TM}$ load cell, mounted on a linear stage ($Zaber^{TM}$) that allowed the sample to move along the shear direction. The adhesion force was measured against a steel plate, fixed to the base of the experimental setup. The Kapton side of the electroadhesive pad was in contact with the steel plate, while the side with the electrodes was covered with an electrically insulating tape for safety reasons (the black area in Figure 4.20). The steel plate was properly grounded. Three experiments were performed on three different days. The maximum voltage allowed, before the breakdown voltage of air was reached and some sparking between the electrodes (not across the Kapton) occurred, was found to be 2.6 kV. The test was executed for three different voltages (1.4 kV, 2 kV and 2.6 kV), with the test being repeated ten times for each voltage. Each test cycle consisted of three distinct phases: 1) high voltage amplifier (HVA) connection and electrodes charging; 2) linear stage activation and maximum shear force measurement through the load cell; 3) HVA disconnection and electrodes discharge to neutralize any built up charge.

The electroadhesive shear force was determined as the mean value of the ten measurements performed for each output voltage, with the corresponding standard deviation serving as an indicator of the experimental error. The shear pressure was determined as the ratio between the shear force and the total area of the sample, which was 100e-4 m^2. The results obtained in the three tests are shown in Figure 4.21. The

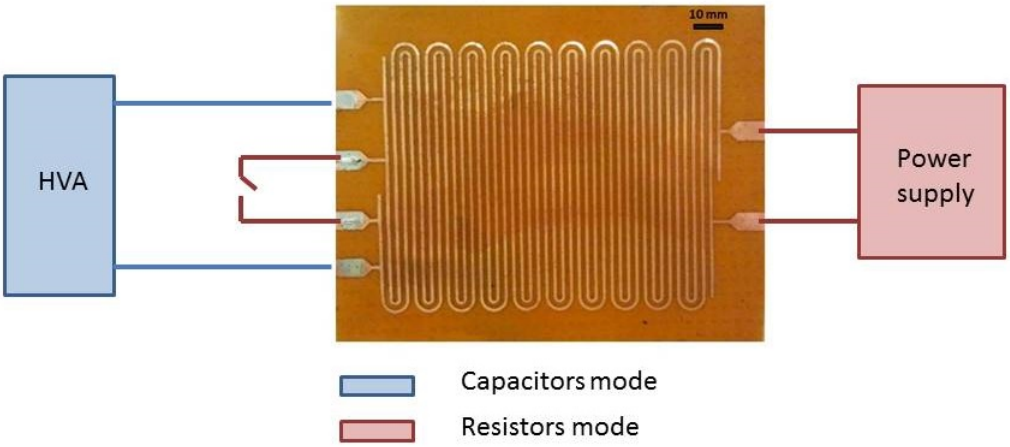

Figure 4.19: Electrodes final configuration. It is also shown how the connection as resistor (red line) and capacitors (blue line) was realised.

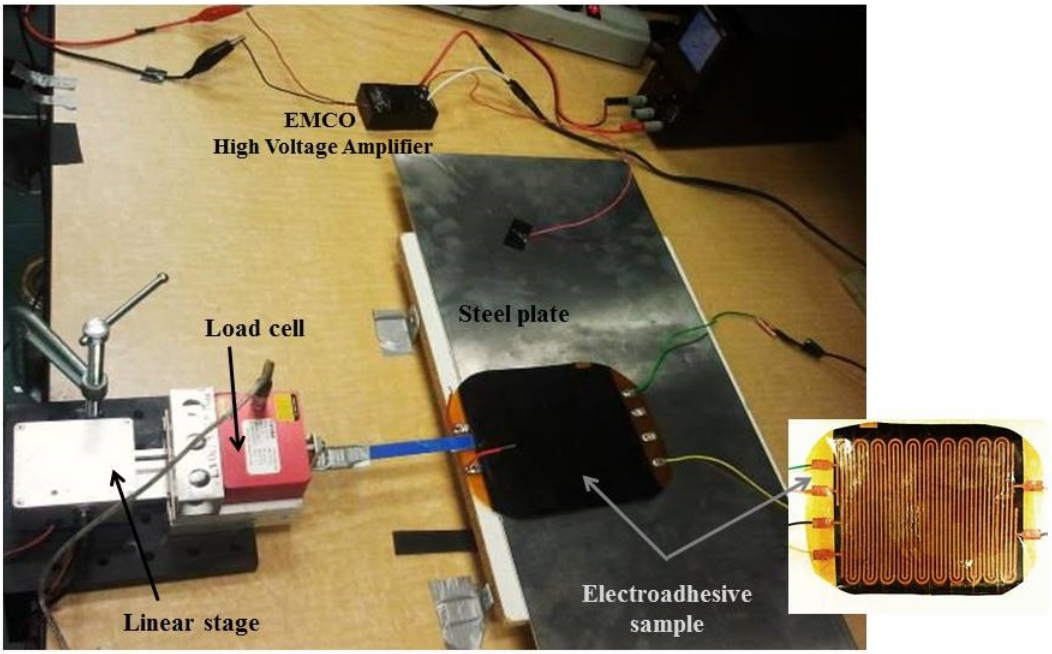

Figure 4.20: Experimental setup to test electroadhesion on Prototype # 1. The setup consisted of: a DC-DC high voltage amplifier (E101CT, $EMCO^{TM}$ High Voltage), a $FUTEK^{TM}$ load cell, a linear stage ($Zaber^{TM}$).

green line refers to the data colected the first day, the blue line to the second day and the magenta line to the last one. The red line is the adhesion shear pressure determined through Equation 4.6, that was derived by the classical capacitor theory. Since the capacitor formula refers to the normal force between two plates of a capacitor, the friction coefficient μ between the electroadhesive sample and the steel plate was determined by testing, and used to calculate the theoretical shear pressure (P_s) as: $P_s = \mu P_N$. The friction coefficient was found to be 0.25 ± 0.08. As can be seen from the graph in Figure 4.21, different shear pressure levels were obtained when performing the tests on three different days. The results of the second and third day are comparable with the theoratical ones, but they differ significantly from those of the first test. Some hypotheses have been formulated to justify these differences. Although temperature and humidity are addressed as possible factors that could influence the electroadhesion effect [158] [162], they were not supposed to be the only cause of these pressure changes. The first test was performed right after the fabrication of the sample. The procedures done to clean the surface after the etching bath could have induced some charge on the sample responsible of the increase in force between the sample itself and the steel surface, in the same way it happens when polymeric metrials show electrostatic attractions after being rubbed. For the test made later, particular attention was dedicated to eliminate any soruce of potential charge before doing the test procedure.
Only the results obtained in the last two days were considered reliable. The sample realised allowed to achieve a maximum shear adhesion pressure of 0.4 kPa for an applied voltage of 2.6 kV. The difference, in percentage, respect to the theoretical expected pressure varies between 41% and -14% for the results obtained in the second test, and between 70% and -9% for the tests peroformed the third day. Anyway, the results obtained are comparable with data found in literature, although some considereations are required: often, the total area considered to evaluate the shear pressure was set equal to the electrodes area, neglecting the space between the electrodes. In this way, the pressures obtained can be higher than in our case. The adhesion acts on the entire surface and the resulting force is spread over the entire sample surface, not only where the electrodes are. For more accurate values, it should be considered the entire sample area.

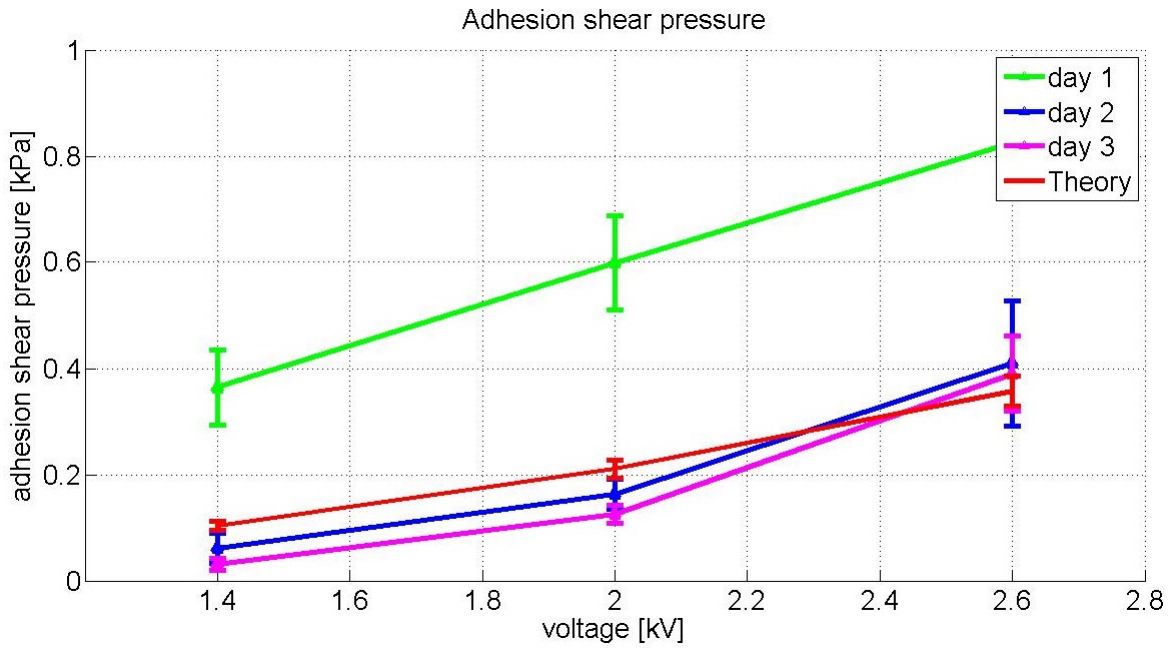

Figure 4.21: Adhesion shear pressure obtained with Prototype # 1.

Thermal tests

Three thermal tests were performed in order to validate the model developed. The experimental setup was the same for all the tests, and it is shown in Figure 4.22. The sample consisted of the resistive-

electroadhesive interface previously realised, where the side with the electrodes was attached to the polymeric substrate, while a white covering was used on the external surface of the polymer to control its thermal emissivity. A humidity and temperature sensor (SHT15, SENSIRION), was placed in contact with the external surface of the polymer (the white one in Figure 4.22) to measure the temperature trend during the entire test. The humidity and temperature data were sent to the computer through an Arduino microcontroller. An ATX power supply was employed to supply the required power, using the 3.3V output line. For the first 10 minutes of each experiment, the power supply was turned off in order to register the ambient temperature at the beginning of each the test. The power supplied by the electrodes was estimated to be 13W.

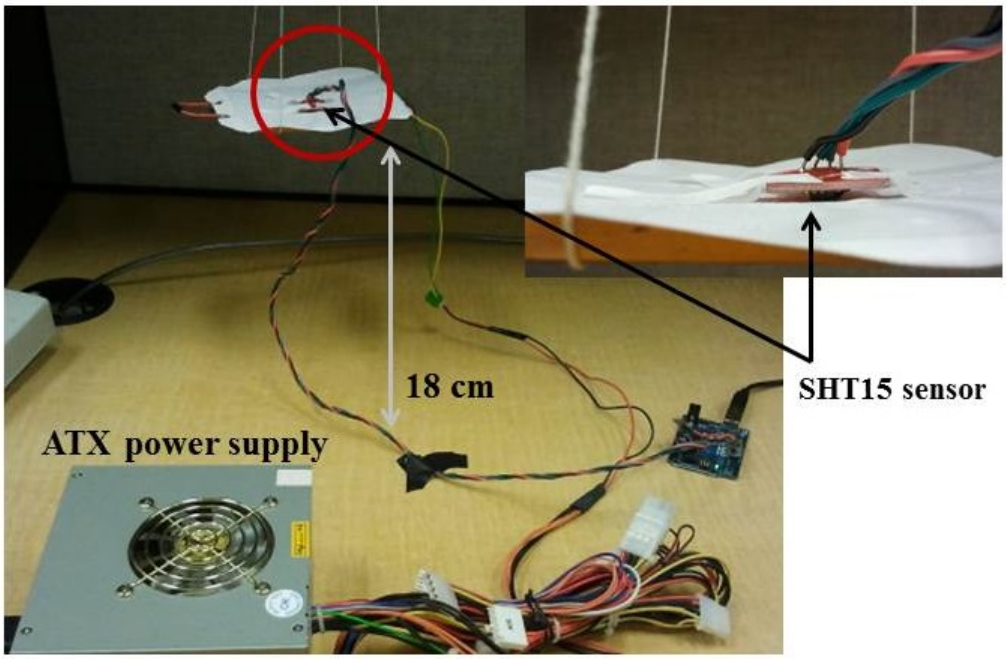

Figure 4.22: Thermal test exeprimental setup. The test setup consisted of: the electro-adhesive sample and a humidity and temperature sensor. An ATX power supply was employed to supply the required power, using the 3.3V output line.

The regime temperatures reached in each test are listed in Table 4.2.

Regime temperature	
Test # 1	50 ° C
Test # 2	48 ° C
Test # 3	48 ° C

Table 4.2: Regime temperatures reached during each one of the three heating cycles.

A comparison between experimental data (white polymer sample heated by P = 13 W) and numerical predictions is presented in Figure 4.23. The plot highlights that the model results are compatible with test data, even though the experimental curve is shifted towards the lower values of the models uncertainty range. This is probably related to the accuracy of the empirical correlation used to calculate α_{conv}, which seems to under-predict the value of the convective heat transfer coefficient. The developed model can be then implemented to predict the power required to heat samples of SMP, given their shape.

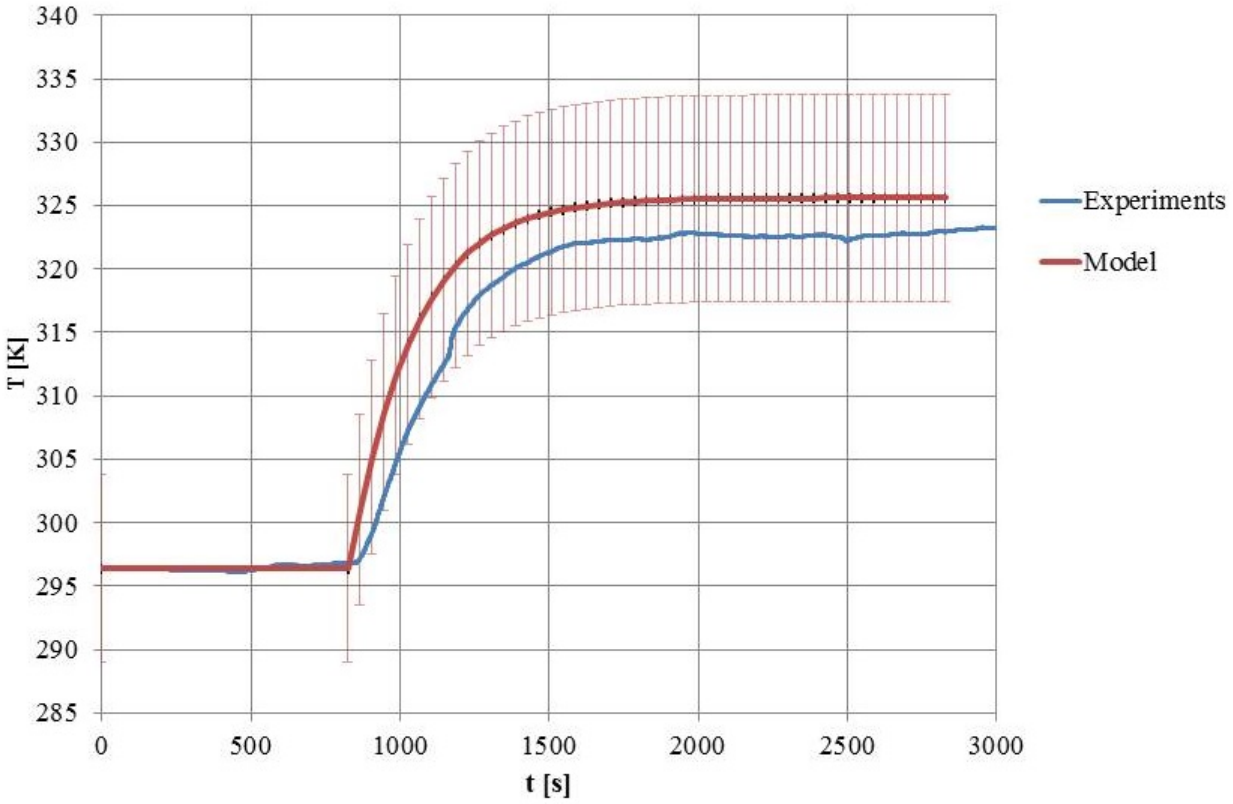

Figure 4.23: Thermal model validation through experimental data. The red line rapresents the values predicted by the developed model, while the blue line are the experimental data.

Morphing test

The objective of the morphing test was to verify the possibility of properly deforming the polymer and then to determine its strain recovery, i.e. the ability of the material to maintain the deformed shape after cooling. The test consisted of four main phases: 1) the heating phase, where the polymer was heated to a temperature slightly higher than its transition temperature (110 $°C$); 2) the deformation phase, where the polymer was deformed by applying a load that allowed it to adhere to the surface of an object with a known shape; 3) the cooling phase, in which the polymer was cooled, below its transition temperature; 4) the image acquisition phase and analysis, which consisted of taking images of the deformed polymer and analysing them to determine if any strain recovery could be observed. The polymer used to test the morphing capabilities was a shape memory polymer whose characteristics are listed in Table 4.3. The size of the sample was 100x120x2 mm^3. Three objects with different shapes were used to deform the polymer: two were cylindrical, with different radii, and one an U-shaped profile. The first image, taken just after the cooling phase, and the last one, taken after 30 minutes, were analysed in order to determine the strain recovery. In Figure 4.24 the first and last images of each test are shown: the polymer is the thin black layer on the surface of each object, whose envelope is indicated by the red arrows. No relevant differences were observed between the two images in all three tests. It was then concluded that the material was able to maintain the deformed shape, without significant strain recovery after cooling and load removal.

SMP properties

Density $[kg/m^3]$	Tensile Strength [MPa]	Tensile modulus of elasticity [GPa]	Flexile modulus of elsasicity [GPa]	Activation Temperature $°C$
1350	42	2.2	2.3	90

Table 4.3: Properties of the SMP employed to test the morphing capabilities.

Conclusions

This section was focused on an innovative concept where the electrodes employed to generate the electrostatic forces required to adhere on a surface were used as both resistors and plates of a capacitor. A proper geometry was selected in order to allow the switching between the two operative modes. A conductive path was realised on a Kapton layer: the length of the resistive path was 4 m on an area of 10x10 cm^2; the total resistance was 0.8 Ωm for a total power of 13 W. The 3.3 V output line of an ATX power supply was employed to supply the required power for heating. When the electrodes were connected in capacitor mode, they allowed to adhere on a steel plate through electro-adhesion. The maximum shear adhesion pressure achievable with the selected configuration resulted 0.4 kPa at 2.6 kV. This result was comparable with experimental data reported in previous works. When connected as resistors, the electrodes were able to provide about 13 W of power: even though it was not enough the reach the transition temperature of the SMP selected ($T_g = 90°C$), the thermal tests allowed to validate the thermal model developed to predict the power need to heat the polymer. It was then demonstrated that the concept developed could work, i.e. the electrodes could be employed as both resistors and capacitor, allowing a combination of morphing and adhesive capabilities in a single smart interface. Some improvements are however required, such as selection of proper materials that increase the resistance of the path (copper is a good conductor, so it is not the best material for heating through Joule effect), or SMPs with lower transition temperatures.

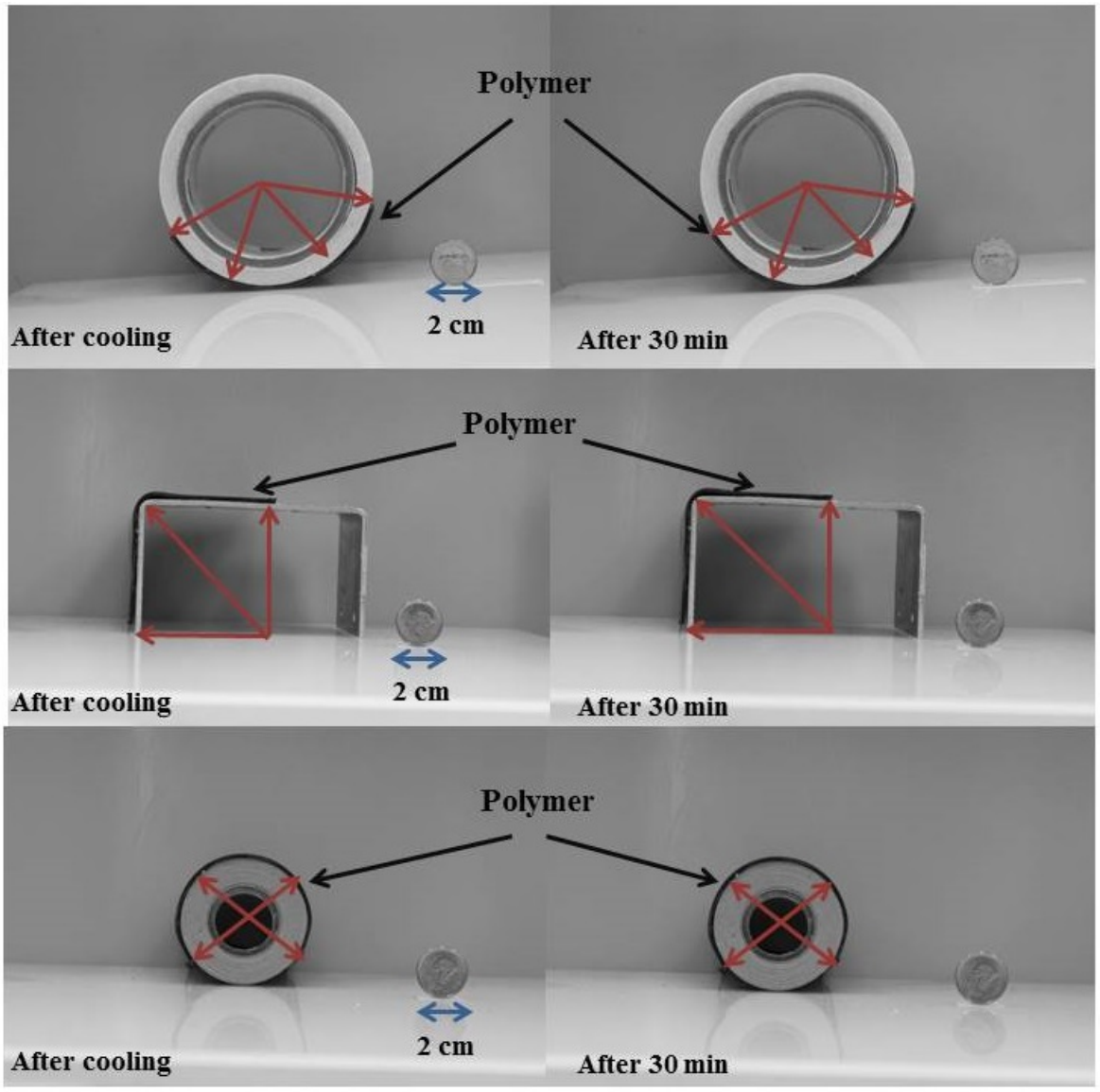

Figure 4.24: Images of the deformed polymer, after the cooling phase (left side) and after 30 minutes (right side); the polymer is the black thin layer, indicated by the red arrows in the pictures. No relevant differences can be observed regarding the strain recovery of the material.

4.3.3 Prototype # 2: design and realization

The second part of the tesing phase focused on the integration of the electro-adhesive interface and the morphing support in a single smart substrate. The electro-adhesive interface realised in the Prototype # 1 was too stiff and did not allow irregular deformations of the Kapton layer. Furthermore, residual deofrmations were observed on the surface, decreasing the adhesion performances of the interface. New solutions were then implemented in order to realise a more compliant interface, where both the electrodes and the insulator were flexible enough to allow the compliance with irregular surfaces. To simplfy the test procedure, it was selected a polymer that was already soft at ambient temperature, so no heating power was required. This assumption simplified the design of the electrodes, for which the typical interdigitated geometry was chosen.

Morphing-adhesive interface: fabrication process

The interface was composed by two main layers: the first one was the electroadhesive layer, composed by the insulator - with the embedded electrodes - while the second one was the foam support. Two different solutions were considered to fabricate flexible electrodes, required to allow a good deformability of the interface: the first pair of electrodes was obtained by cutting the interdigitated configuration from a very thin layer (0.08 mm) of pure copper polyester taffeta fabric (provided by LessEMF), with a resistivity of 0.05 Ω/sq; the second pair of electrodes was cut from a conductive silicone foil, made in laboratory. In the specific case, 20% of conductive carbon black (CB) particles were mixed in a 10:1 silicone matrix of PDMS (Sylgard 184). The homogeneous mixture obtained was spread onto a mould and cured at 80 $°C$ for about 2 hours. The interdigitated geometry was then cut from the foil of conductive silicone obtained. The electrodes had a mean thickness of about 1.3 mm and a mean resistance of 2.5 $k\Omega$, determined measuring the resistance between different points of the electrodes with a multimeter. In both cases, the total area of the electrodes was 16 cm^2 (each electrode was 8 cm^2). The objective of adopting two different solutions for flexible electrodes was to determine if the nature of the electrodes could influence the electroadhesion performances, as well as to propose alternative fabrication processes to realise the adhesive interface. The insulating layer in which the electrodes were embedded was made of TC-5005, a silicone provided by BJB Enterprise; this material was chosen because of its good dielectric properties [172] (dielectric constant $\varepsilon \sim 4.5$) and its high elongation properties that allow great deformations of the material. The electroadhesive layer was realized by spreading the TC-5005 (A/B = 10:1.5) onto a mould to obtain a thin layer of silicone, around 400 μm. After a curing period of 1 day, the electrodes were placed and covered with a second thicker layer of silicone, obtaining an electroadhesive interface of about 1mm with the electrodes made of conductive fabric, and around 2 mm with the conductive silicone electrodes. The total area of the sample was 63 cm^2. The electroadhesive samples are shown in Figure 4.25, with the electrodes in conductive fabric on the left and in conductive silicone on the right. A third thin layer of TC-5005 was used to connect the electoadhesive interface to the polymeric foam support. The entire morphing-adhesive substrate is shown in Figure 4.26.

4.3.4 Prototype # 2: tests and results

Different adhesion and morphing tests were performed in order to evaluate the adhesion performances and the morphing capabilities of Prototype # 2, i.e. the adhesion levels achievable and the ability to become compliant to objects with macroscopic irregularities, and how this compliance could aid the adhesion. All the adhesion tests were performed in normal direction. The experimental setup is shown in Figure 4.27; it consisted of: a supporting structure, a DC-DC high voltage amplifier ($EMCO^{TM}$ High Voltage, model E101CT) connected to the power supply, a linear stage ($ZABER^{TM}$, model T-LS28-SMV), a load cell ($FUTEK^{TM}$, model LCM 300 FSH02700) mounted on a support rigidly connected to the moving base of the linear stage, and a conductive plate (steel), connected to the load cell, used to simulate the surface of the object to capture; finally the electroadhesive sample was attached on a plate rigidly fixed to the base of the supporting structure. A Labview code was used to control the linear stage and to record the output data from the load cell.
Three experimental procedures were defined, two related with the adhesion and one with the morphing behaviour.

I The first test procedure aimed to evaluate the influence of a mechanical pre-load on the normal

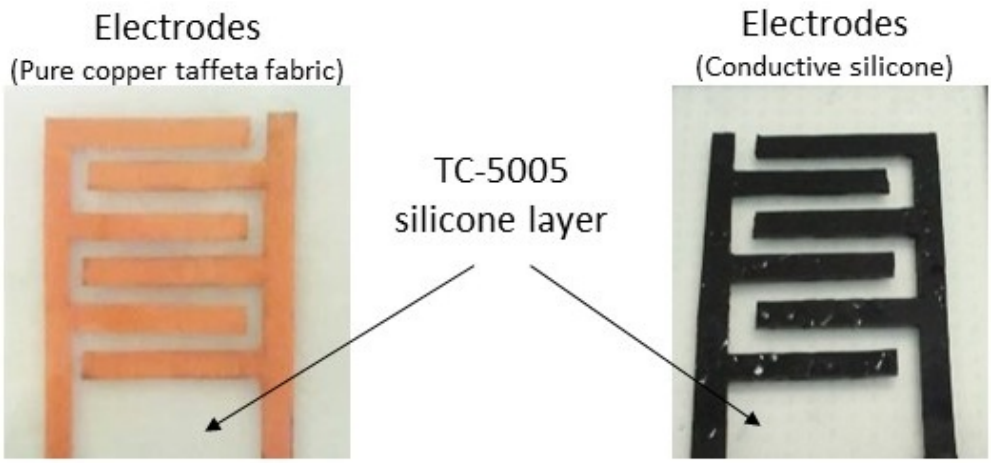

Figure 4.25: Electro-adhesive layers. On the left, the sample with electrodes otained from a conductive fabric texture; on the right, the layer with the electrodes made fabricating a conductive silicone in laboratory.

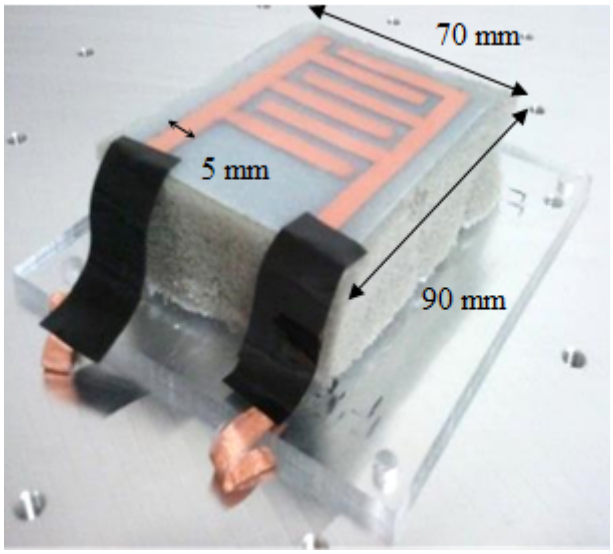

Figure 4.26: Morphing electro-adhesive sample with electrodes made of conductive fabric. The electro-adhesive interface was connected to the polymeric foam support through a thin layer of TC-5005.

adhesion capabilities of the silicone layer itself, when no voltages were applied (see section 4.2.4, *Origin of the adhesion force* for details).

II The second test procedure aimed to determine the increase in the normal adhesion force due to the electrostatic forces.

III The third test procedure aimed to determine how the presence of a foam substrate could enhance the normal adhesion when macroscopic irregularities are present on the surface of the target object.

The first and the second procedures were performed with both prototypes, the one with the electrodes made of conductive fabric and the one with the electrodes in coductive silicone; the results obtained were then compared to verity if the nature of the conductors could influence the electro-adhesion performances. Each test procedure is described in details in the following sections.

Adhesion tests

Influence of a mechanical pre-load

The first set of tests was performed without applying any voltage, determining in this way the dry-adhesion capabilities of the TC-5005 layer itself. The speed of the linear stage was set in all tests at 500 $\mu m/s$. The test consisted in two main phases: I) the linear stage was moved towards the surface of the sample, allowing the contact between the testing plate (steel plate) and the sample itself; II) after about 30s, the linear stage was pulled, causing the detachment of the testing plate from the sample. The force data were continuously recorded during the entire test. Four different preloads (compression load during the contact phase) were applied: 1.5N, 5N, 10N, 15N, and for each preload condition, 5 trials were performed. The mean adhesion force was determined considering the peak in force registered in each trial and for each set of test it was aslo determined the standard deviation to monitor the error trend. In Figure 4.28 it is shown the mean adhesion force due to the TC-5005 layer only, at different mechanical pre-loads. From the graph it turns out that increasing the mechanical pre-load, the natural adhesion of the silicone increases until a certain value, above which it becomes almost constant although the pre-load is further increased. This effect is better clarified in Figure 4.29, where the percentage increase in the adhesion between two different pre-load condictions is shown: passing from 1.5N to 5N of mechanical pre-load, the percentage increase in the adhesion force registered was 128%, while from 5N to 10N, and from 10N to 15N this percentage is drastically reduced to 16% and 4% respectively. This means that a mechanical pre-load could increase the adhesion performances of the silicone layer itself until a certain level, above which the adhesion capabilities *saturate* and cannot be significantly increased even if a higher pre-load is applied. The possible reason of such saturation could be the maximization of the contact area and hence of the Wan der Waals interaction that can be established at the interface.

Influence of electrostatic forces

This set of tests aimed to determine the influence of the electrostatic forces on the adhesion capabilities of the sample. The tests were performed applying two voltage levels of 2.5 kV and 4.5 kV at three different mechanical preloads of 1.5N, 5N and 10N. As emerged from the previous analysis, no significant increase in the adhesion was observed for pre-loads greater than 10 N. For each voltage and pre-load condition, two different procedures were followed:

I **Continuous voltage applied**:

- the linear stage was moved towards the surface of the sample, allowing the contact between the testing plate (steel plate) and the sample itself;
- the high voltage was applied for about 30s;
- the linear stage was pulled, causing the detachment of the testing plate from the sample.

II **Voltage removed before pulling: electrostatic pre-lad**:

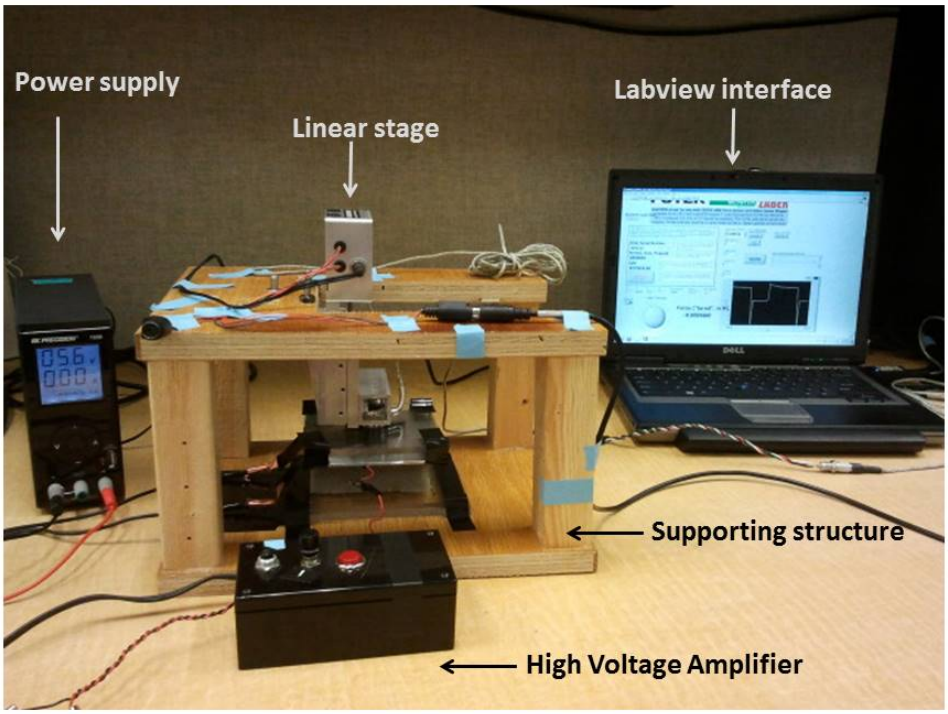

(a)

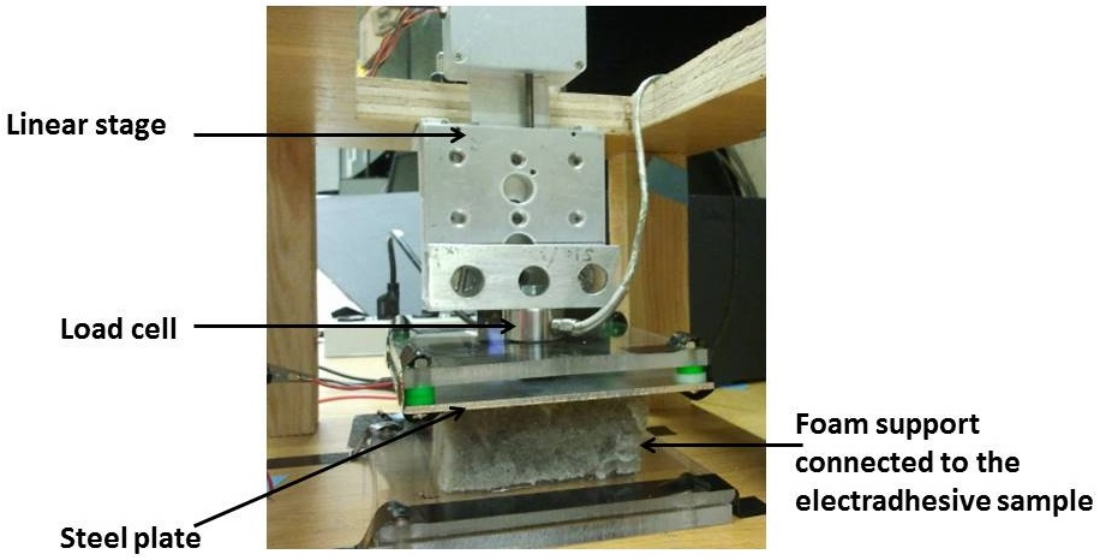

(b)

Figure 4.27: Experimental setup to test normal adhesion and morphing capabilities of Prototype # 2. The test setup consisted of: a supporting structure, a DC-DC high voltage amplifier, a linear stage, a load cell and a conductive plate (steel). An enlargement of the linear stage, the load cell and the steel plate assemply, and the sample is shown in (b).

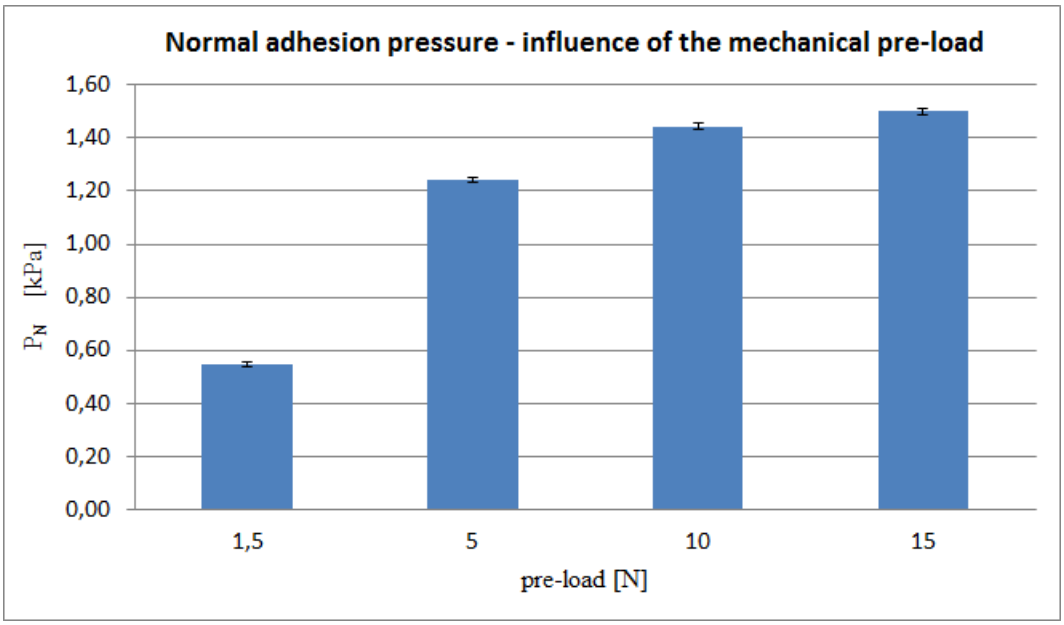

Figure 4.28: Influence of a mechanical pre-load on the normal adhesion performances when no voltage is applied.

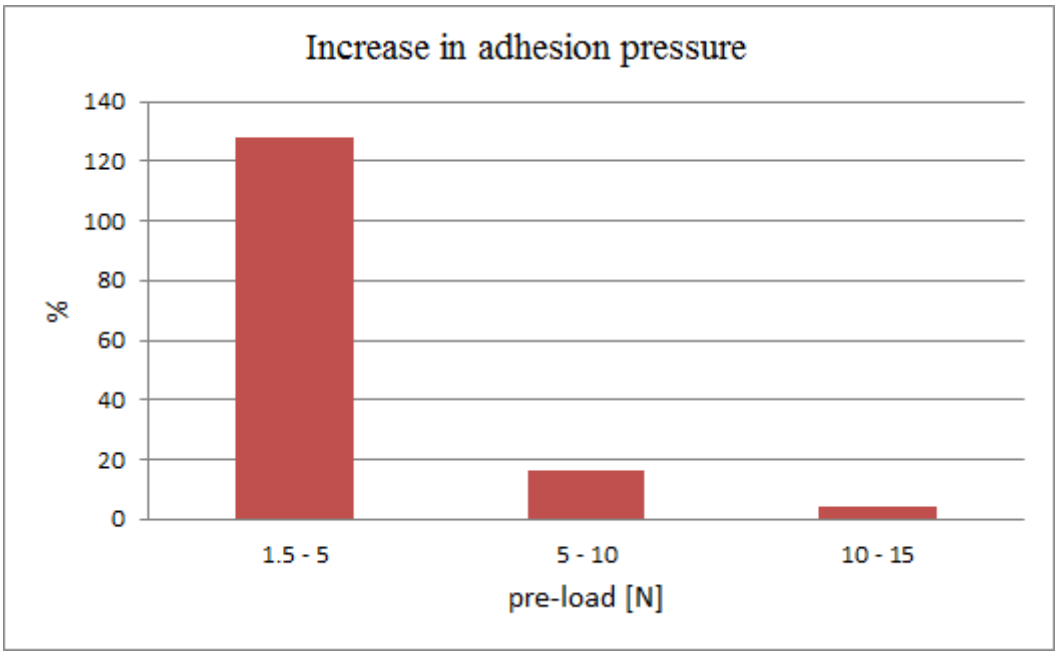

Figure 4.29: Percentage increase of the adhesion force as the mechanical re-load is increased.

- the linear stage was moved towards the surface of the sample, allowing the contact between the testing plate (steel plate) and the sample itself;
- the high voltage was applied for about 30s;
- the high voltage was removed, waiting 30 s before activating the linear stage (**electrostatic pre-load effect**);
- the linear stage was pulled, causing the detachment of the testing plate from the sample.

For each pre-load and voltage condition, five trials were performed. As done before, the mean adhesion force was calculated considering the peaks in the adhesion force registered in each test. The results obtained are reported in Figure 4.30 for the prototype with electrodes in conductive fabric and Figure 4.32 for the prototype with electrodes in conductive silicone. In the plot, it is reported the normal adhesion pressure, in $[kPa]$, evaluated as the ratio between the adhesion force measured through the load cell and the total area of the sample, that was 64 cm^2. Let's focus on Figure 4.30. The blue bar rapresents the normal dry-adhesion pressure (the same of the previous analysis), for comparison with the values obtained applying the voltage. The red and violet bars rapresent the normal adhesion pressure obtained applying 2.5 kV continously, while the green and the light blue bars correspond to the adhesion pressure measured in case of electrostatic pre-loading, i.e. when the voltage was removed before activating the linear stage to allow the detachment. It can be observed that the generation of electrostatic forces increases the adhesion respect to dry-adhesion condition. From the plot is evident that this increase is greater for low mechanical pre-loads, while it decreases at higher pre-loads. The increase in percentage, in the normal adhesion obtained when the voltage is applied, respect to the dry-adhesion, are reported in Table 4.4. As it can be observed, with a 1.5 N of pre-load, it was registered an increase in adhesion of 157% at 2.5 kV and 183% at 4.5 kV, while only 26% and 32% are obtained with 5 N and 19% and 24% with 10 N, at the two voltages.

% increase in adhesion - conductive fabric		
pre-load [N]	V = 2.5 kV	V = 4.5 kV
1.5	157 %	183%
5	26%	32%
10	19%	24%

Table 4.4: % increase in normal adhesion pressure respect to dry-adhesion condition, when 1-5 N, 5 N and 10 N of pre-load are applied at 2.5 kV and 4.5 kV (electrodes in conductive fabric). The greater increase is registered at low mechanical pre-loads, while the electrostatic effect decreases for higher pre-loads.

Another interesting result is the comparison between the adhesion pressures obtained when the voltage is applied continously and when it is used as electrostatic pre-loading. Even though the mean value of the adhesion pressure is slightly different in the two cases, considering the errors, the results are overlapped, except at low mechanical pre-loads (1.5 N). This means that the two pre-loading conditions are not independent and act in the same way: for example, the same adhesion pressure can be obtained or through the electrostatic pre-loading at 2.5 kV, or applying a mechanical pre-load of 10 N, with no voltage. In the first case the two surfaces get closer because of an electrostatic attraction force, while in the second one the mechanical compression is responsible of the greater contact; as it was described in section 4.2.4 (*Origin of the adhesion force*) both these conditions have the effect to enhance Wan der Waals interactions, that are the main responsibles of the increase in adhesion. From these observations, it emerges that the greater contribution in the increase in adhesion is not mainly related to the electrostatic forces themselves, but to the effect that they determined at microscopic level. These conclusions are valid in this case, in presence of the silicone insulating layer that determines the rising of the second adhesion mechanism described in 4.2.4 (*Origin of the adhesion force*).

The experimental data obtained with the lowest mechanical pre-load, where the electrostatic effect prevailed, were cmpared with the theoretical ones estimated through the capacitor theory and the theory

developed in [168]. The adhesion pressure attributed to the electrostatic effect only was determined as the difference in the adhesion pressure between the case when the voltage was applied continously and the case when it was removed before the detachment. In this case it should be excluded the effects due to the both mechanical and electrostatic pre-load. The result is shown in Figure 4.31. As it can be observed, both models underestimate the adhesion capabilities. As previously said, there are several parameters that could significantly influence the adhesion performances that are not taken into account in analytical models. In our case, the adhesion effect related to the Wan der Waals interactions established through the insulating silicone layer could act increasing the adhesion mechanisms related to electrostatic forces.

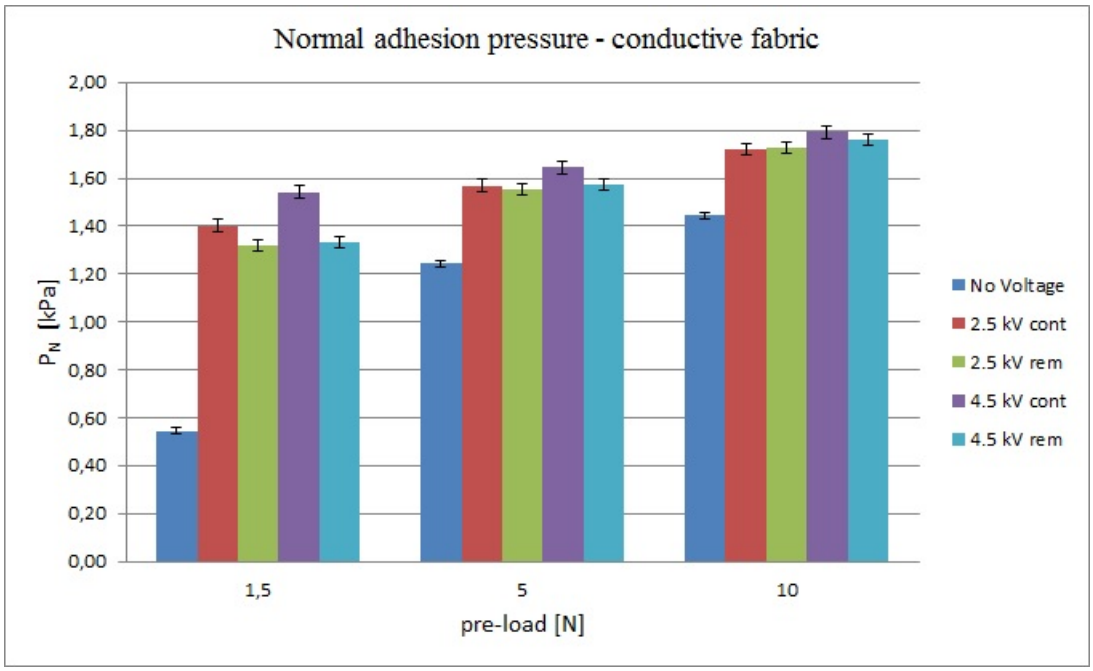

Figure 4.30: Normal adhesion pressure obtained on a steel plate, and electrodes made of conductive fabric. The blue bars rapresent the dry-adhesion pressure (no voltage applied). The red and violet bars are the adhesion pressures obtained applying respectively 2.5 kV and 4.5 kV continously; the green and light blue bars are the adhesion pressures achieved removing the voltage 30 s before the activation of the linear stage for the detachment.

The same testing procedures (I and II) were performed on the sample with the electrodes in conductive silicone. The results are shown in Figure 4.32. As it can be observed, the adhesion behaviour is similar to the previous case. The percentage increase in adhesion, respect to the dry case, is reported in Table 4.5. The increase in adhesion pressure with this second sample is greater than the values otained with the previous one. However, it cannot be concluded that conductive silicone electrodes could perform better. The results are affected by some uncertainties related to the fabrication processes of the two prototypes and the testing conditions: the perfect planarity of the sample surfaces, as well as the relative position between the sample and the steel plate during the testing, were variables difficult to control with high precision, and these parameters could influenced the general results. The general performances of the second sample (conductive silicone) were lower than the performances of the first one, concerning dry-adhesion as well as electro-adhesion. Anyway, the important result is that both prototypes showed the same behaviour. This means that also the employment of conductive polymers could be a viable solution to realize flexible electrodes. At the moment, the printing of electrical circuits on polymeric materials is an expensive and not yet common process; furthermore it is done mainly on small surfaces. Flexible polymeric electrodes could be done easily in laboratory, with no high costs, as demonstrated with the second prototype realised in this work. Further improvements should be foreseen to make the fabrication process more accurate.

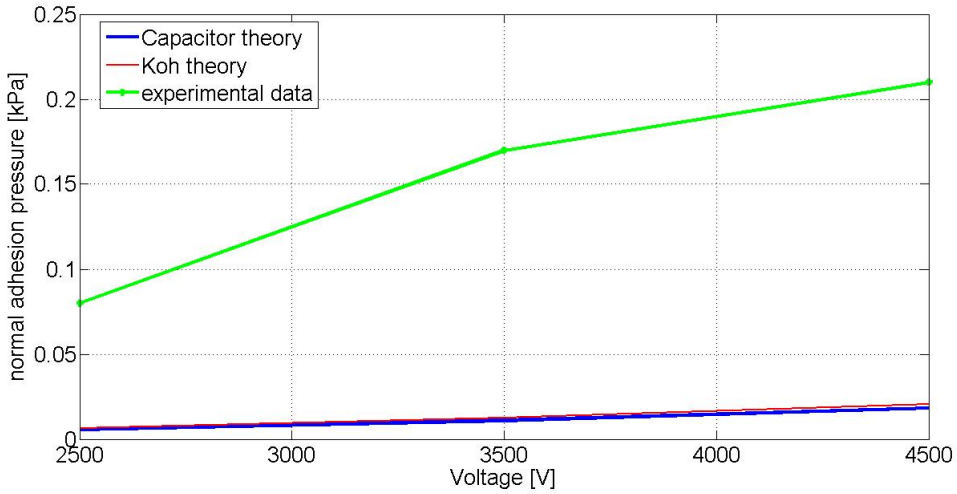

Figure 4.31: Comparison between theoretical normal adhesion pressure estimated through Equations 4.8 and 4.10 and experimental data obtained with 1.5 N of mechanical preload. As it can be observed, theoretical models underestimate the adhesion pressure achievable. This could depends on the presence of the silicone layer, responsible of some adhesion phenomenon that are not taken into account in analytical models, such as the Wan der Waals interactions that arise at the contact interface.

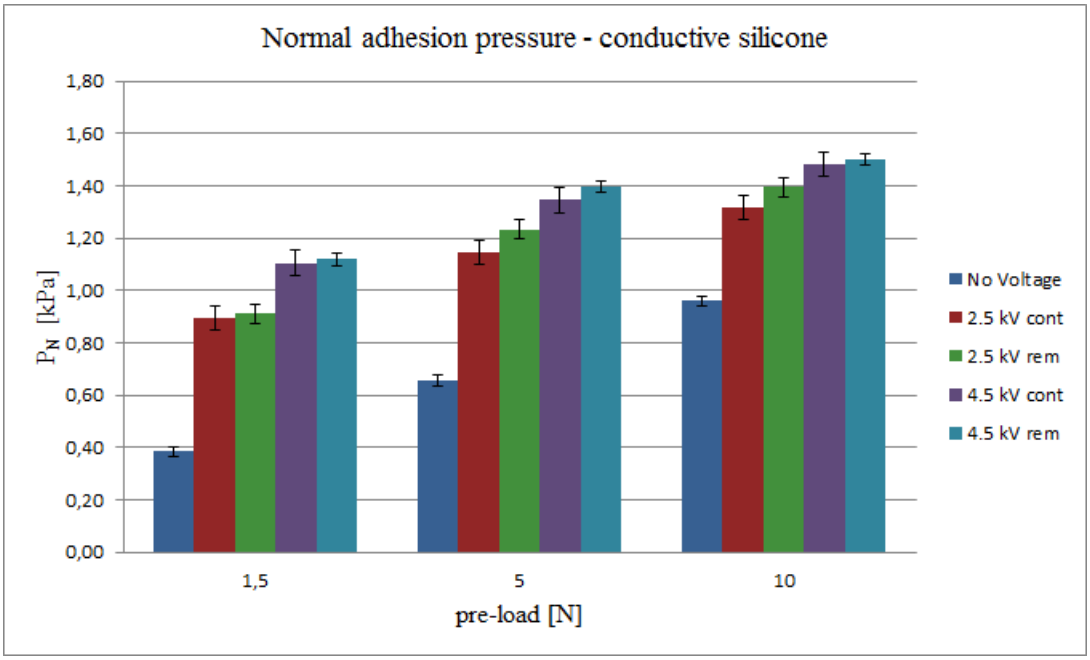

Figure 4.32: Normal adhesion pressure obtained on a steel plate, and electrodes made of conductive silicone. The blue bars rapresent the dry-adhesion pressure (no voltage applied). The red and violet bars are the adhesion pressures obtained applying respectively 2.5 kV and 4.5 kV continously; the green and light blue bars are the adhesion pressures achieved removing the voltage 30 s before the activeton of the linear stage for the detachment.

% increase in adhesion - conductive silicone		
pre-load [N]	V = 2.5 kV	V = 4.5 kV
1.5	133 %	188%
5	74%	105%
10	37%	55%

Table 4.5: % increase in normal adhesion pressure respect to dry-adhesion condition, when 1-5 N, 5 N and 10 N of pre-load are applied at 2.5 kV and 4.5 kV (electrodes in conductive silicone). The greater increase is registered at low mechanical pre-loads, while the electrostatic effect decreases for higher pre-loads.

Influence of test conditions: linear stage speed

It was observed that varying the speed of the linear stage, the values of adhesion force registered by the load cell varied. Three test campaigns were then performed, considering three different speeds: 100 $\mu m/s$, 500 $\mu m/s$ (the same set for previous tests) and 800 $\mu m/s$. The sample with the electrodes in conductive fabric was employed for these tests.
The results obtained at 100 $\mu m/s$ and at 800 $\mu m/s$ were compared to the reference values obtained at 500 $\mu m/s$, that was the typical linear speed set in other previous studies. The final results are reported, in terms of normal adhesion pressure, in Figure 4.33 and 4.34. The difference, in percentage, between the adhesion force measured at 100 $\mu m/s$ and 800 $\mu m/s$, respect to the reference values measured at 500 $\mu m/s$, are shown in Table 4.6 and 4.7. As it can be observed, as the speed of the linear stage is increased, the adhesion force measured by the load cell increases. This result is interesting since no influence of the test conditions had never been highlighted in previous reseraches. This means that it is important to specify in which test conditions the results relatve to the electro-adhesive performances are obtained, since they could be signifincantly different as some test conditions change. However, the pre-loading effects, mechanical and electrostatic, are similar at any speed condition.

% difference in adhesion at 100 $\mu m/s$ respect to 500 $\mu m/s$ speed condition			
pre-load [N]	0 kV	V = 2.5 kV	V = 4.5 kV
1.5	- 51	- 46	- 44
5	- 62	- 54	- 56
10	- 67	- 56	- 64

Table 4.6: % difference in normal adhesion pressure at 100 $\mu m/s$ respect to 500 $\mu m/s$ speed condition. As it can be observed, it was registered a decrease in the adhesion force measured as the speed of the linear stage was decreased from 500 $\mu m/s$ to 100 $\mu m/s$.

Morphing-adhesion tests

The morphing tests aimed to determine how the presence of a foam support could aid the adhesion capabilities in presence of macroscopic irregularities on the surface of the object to capture. Two irregularities of different sizes were simulated; specifically, two washers 1.7 mm high and two nuts 4.65 mm high were chosen for these tests (see Figure 4.36). The tests were performed according to the following procedure:

I the testing plate was pushed towards the sample surface, applying a very small pre-load, to allow the contact between the sample and the top surface of the irregularitiies (washers first and nuts later); in this phase there was no deformation of the foam substrate.

II A series of test was performed, before without applying any voltage and then at 2.5kV and 4.5kV.

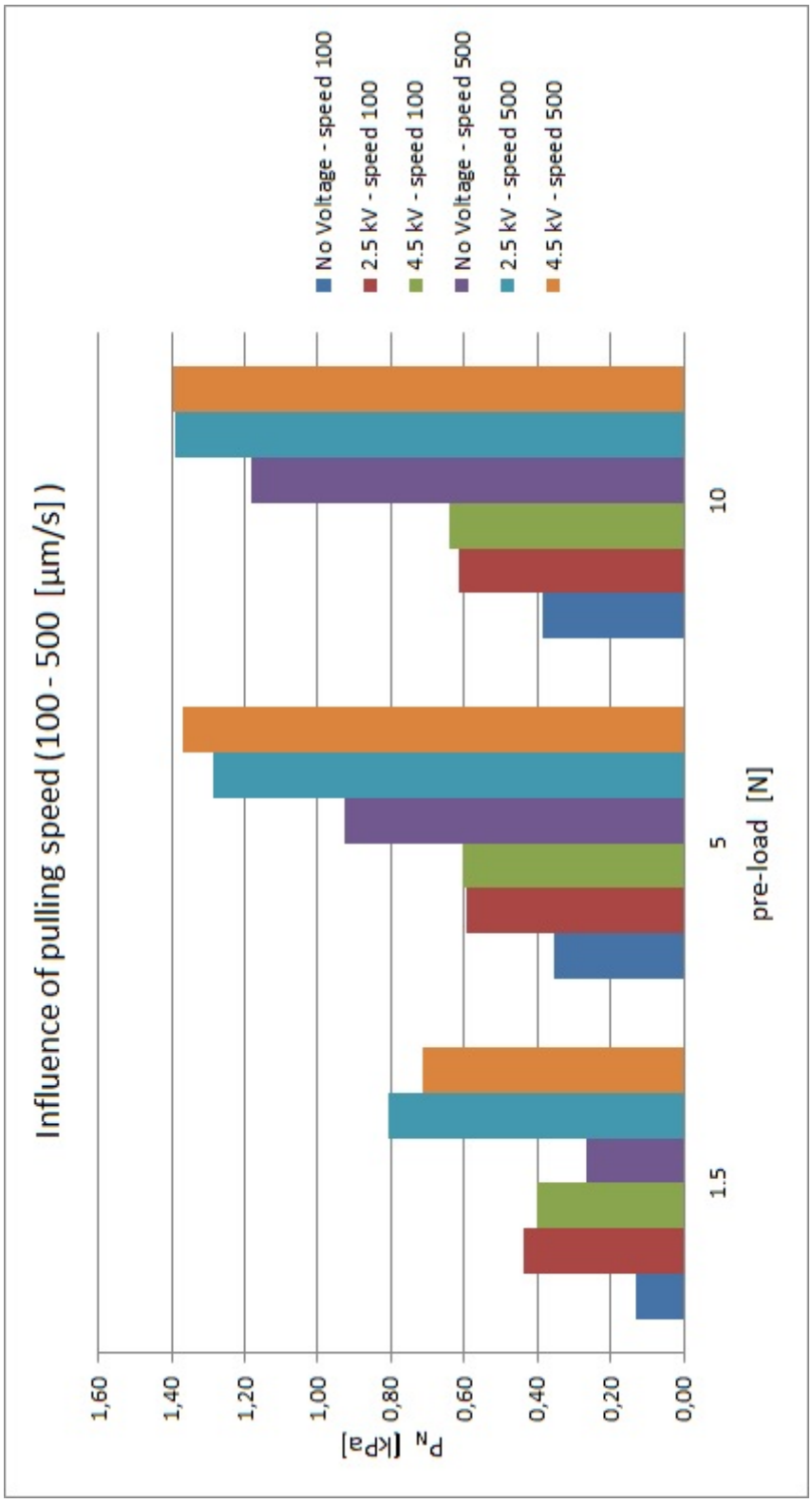

Figure 4.33: Comparison between the normal adhesion pressure obtained with a linear speed of 100 $\mu m/s$ and 500 $\mu m/s$.

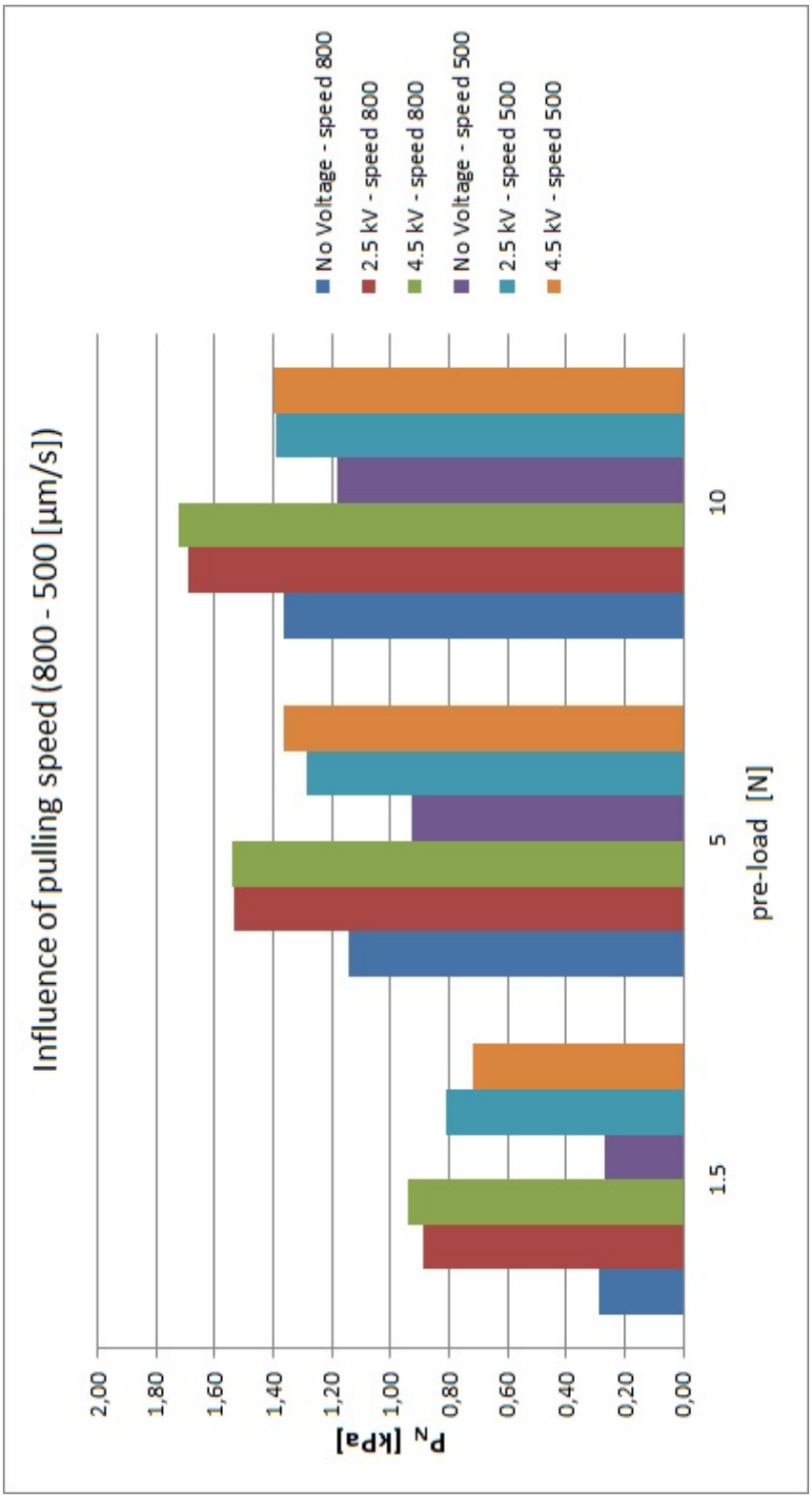

Figure 4.34: Comparison between the normal adhesion pressure obtained with a linear speed of 800 $\mu m/s$ and 500 $\mu m/s$.

% difference in adhesion at 800 $\mu m/s$ respect to 500 $\mu m/s$ speed condition			
pre-load [N]	0 kV	V = 2.5 kV	V = 4.5 kV
1.5	7	10	31
5	23	19	13
10	16	21	23

Table 4.7: % difference in normal adhesion pressure at 100 $\mu m/s$ respect to 500 $\mu m/s$ speed condition. As it can be observed, it was registered an increase in the adhesion force measured as the speed of the linear stage was increased from 500 $\mu m/s$ to 800 $\mu m/s$.

III A second series of test was then performed forcing the deformation of the foam support and allowing the contact between the surface of the steel plate and the sample.

IV As done in the previous tests, the adhesion force was first evaluated without applying any voltage, and then with 2.5kV and 4.5kV.

An example of the test cycle with a complete deformation of the sample is shown in Figure 4.35. Two peaks can be observed: the first one is due to the detachment from the surface of the steel plate, while the second one, smaller, corresponds to the detachment from the washers surface. The normal adhesion pressures obtained in the two cases (washers and nuts) are shown in Figure 4.37 and 4.38. For comparison, the results obtained with previous tests, when no irregularities were placed on the steel plate, are shown in Figure 4.39.
As emerged in the previous tests, also in presence of macroscopic irregularities, the electrostatic forces enhance the adhesion between the contact surfaces, ranging from 37% to 46% at 2.5kV and 4.5kV respectively in case of complete deformation (surface contact). It can be also observed that the adhesion pressures registered with the deformation of the foam substrate caused by the presence of the washers, are in the same range of the pressures obtained in the tests where no irregularities were present. The decrease in the adhesion pressure ranges between 35% and 53%. Similar tests were performed with the two nuts, 4.7 mm high, in order to evaluate the deformation and the adhesion with greater surface features. Also in this case, the presence of the electrostatic forces determined an increase in the adhesion force of 22% and 38% at 2.5kV and 4.5kV respectively, with respect to the adhesion of the silicone when no voltage applied, in case of complete deformation of the substrate. In this second case, the decerase in the adhesion pressure, respect to the case with no deformation of the faom, was greater, varying between 50% and 80%. Although the decrease in the adhesion pressure due to the presence of the macroscopic irregularities, these results show that the presence of a deformable substrate such as the polymeric foam, allows the compliance between two contact surfaces and preserve the adhesion capabilities even when the target surface has some irregularities.

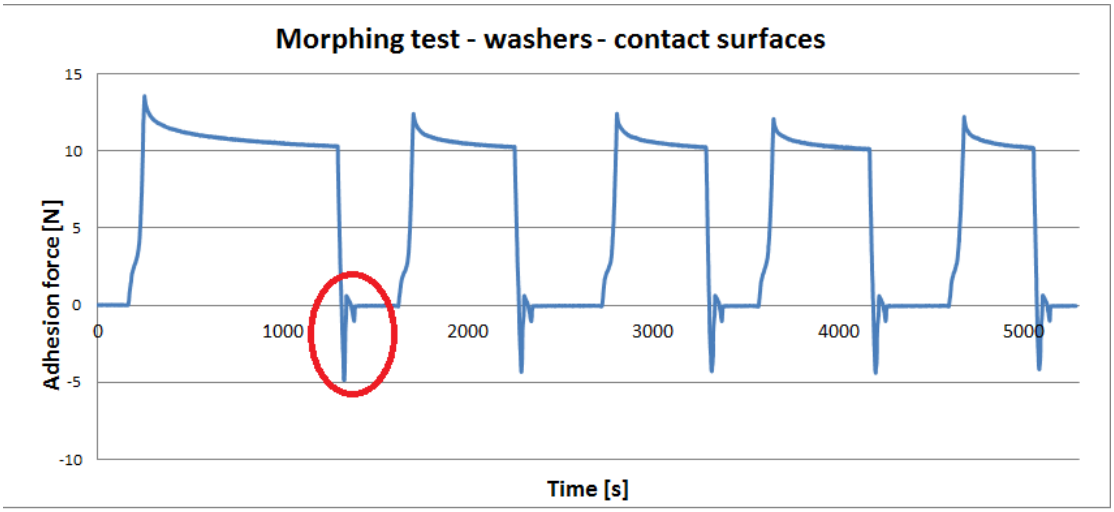

Figure 4.35: Example of a complete morphing test cycle: two peaks can be observed, the first referred to the detachment from the steel plate and the second one form the external surface of the irregularities, washers in this case.

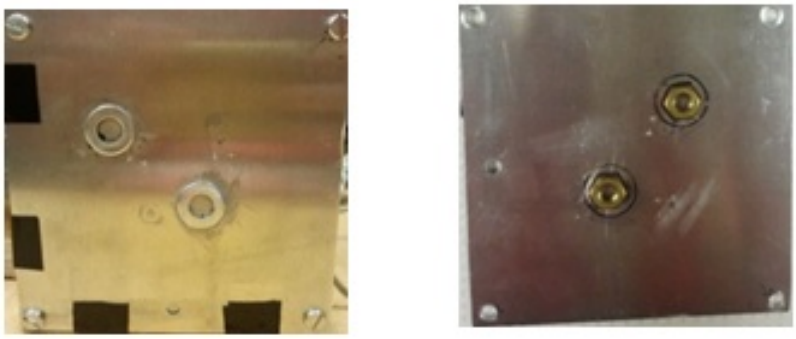

Figure 4.36: Surface irregularities: on the right, it is shown the steel plate with two washers, 1.7 mm hugh, attached on it; on the left the washers are replaced with two nuts, 4.65 mm high.

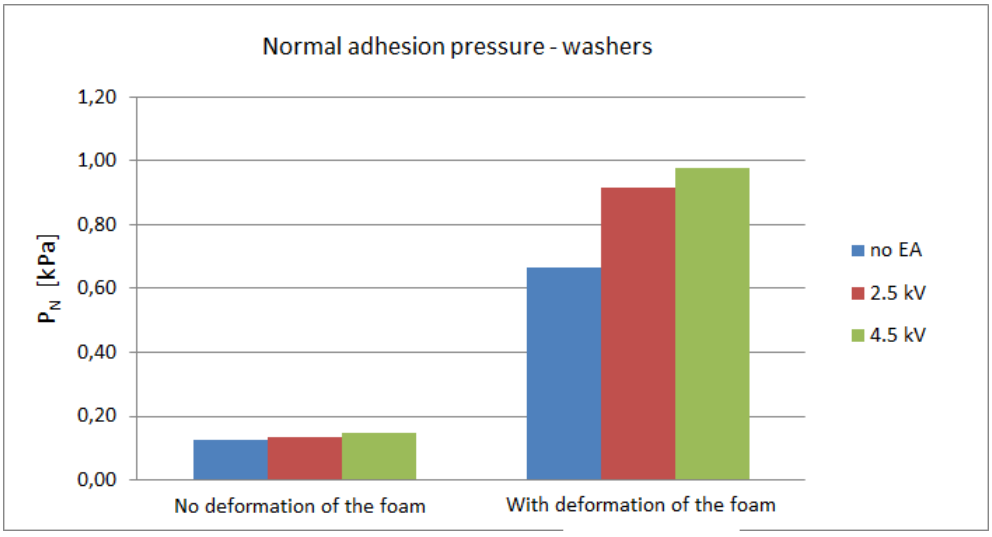

Figure 4.37: Normal adhesion pressure obtained with two washers to simulate macroscopical irregularities on the steel plate.

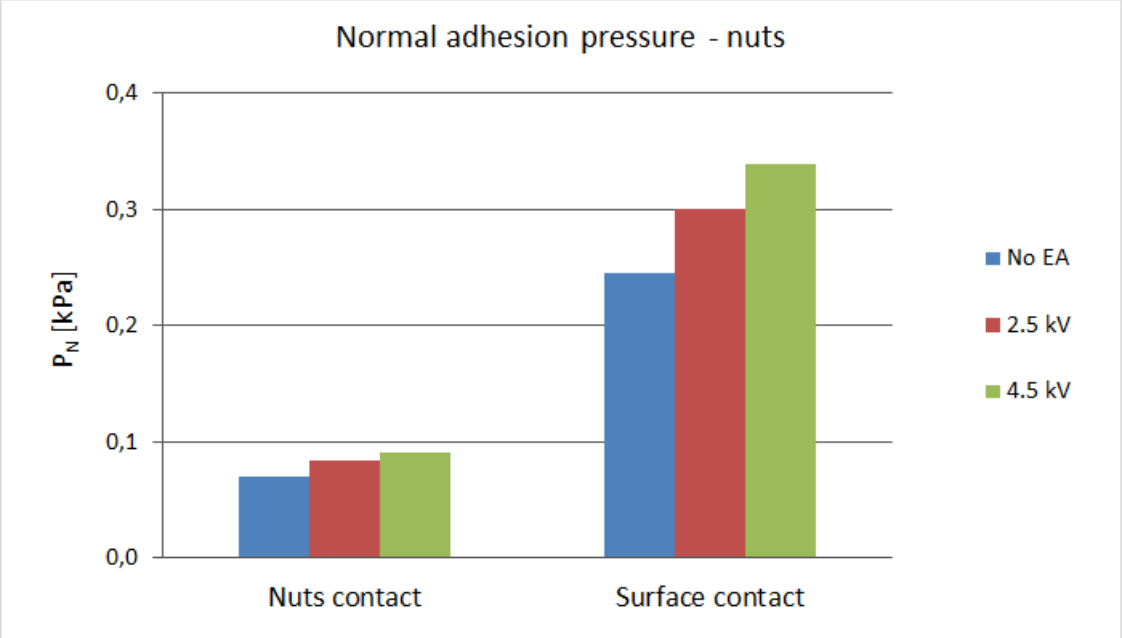

Figure 4.38: Normal adhesion pressure obtained with two nuts to simulate macroscopical irregularities on the steel plate.

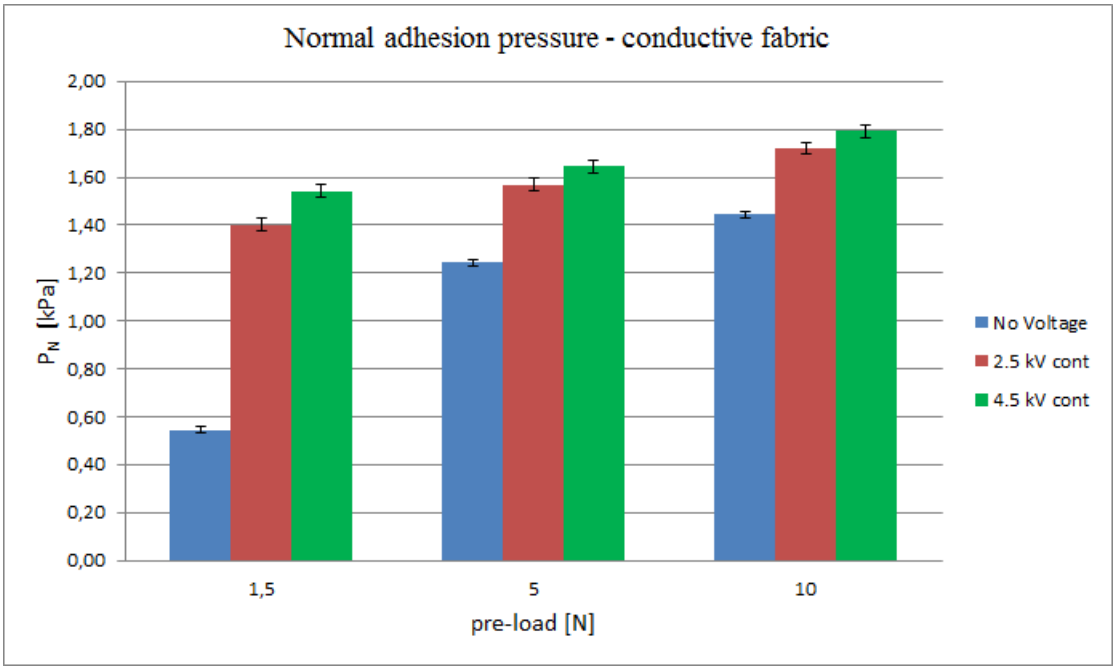

Figure 4.39: Normal adhesion pressure obtained with no irregularities on the surface of the steel plate.

Chapter 5

Final conclusions and future work

The research developed in this thesis dealt with two main aspects related to Active Debris Removal (ADR):

- ADR mission analysis;
- developement of an enabling technology for ADR; in the specific case, the development of a morphing adhesive interface to capture uncooperative ojects.

As regards the ADR mission analysis, an innovative approach was developed, based on a *multiple vehicles mission* where orbital transfers and de-orbiting operations are accomplished by distinct vehicles. The former were performed by a single large spaceraft, properly sized in order to carry proper de-orbiting vehicles to the correspondent debris, assuming to remove a certain number of objects per year before refuelling or replacement operations. As concerns the de-orbiting vehicles, an innovative solution was adopted: each de-orbiting kit was based on a modular architecture, where a certain number of *microsatellite* units, equipped wth proper de-orbiting devices, were assembled, according to the characteristics of the debris to be removed (its mass and initial orbital altitude). Microsatellites rapresent an emerging generation of satellites that have arosen in recent years. New technological solutions have been developed in several fields, like propulsion, communications, attitude control, power, in order to scale the performances typical of larger spacecraft at their small scale. The main outcomes are reliable, high performance and inexpensive designs of space systems, that make them more accessible to a larger community. For these reasons they appeared to be good candidates to implement the modular approach proposed in this work. Several advantages were expected from the implementation of a *multiple vehicles mission*, like high fault tolerance and mission reliability, greater system flexibility, scalablity derived by the modular architecture; mass and costs savings, as well as the possibility to optimize independetly orbital transfers and de-orbiting manoeuvres.
Four main de-orbiting technologies were selected for the mission analysis: drag sails, electric propulsion, electrodynamic tethers and hybrid propulsion. Controlled re-entry manoeuvres and risk assessment evaluations were also performed, to complete the analysis.
Three main study cases were defined, each one with proper mission operations.

From the results obtained it emerged:

- The mass of the de-orbiting kit is always a small fraction of the debris mass, being lower than 20% in most of the cases.
- Although drag sails are low cost and simple solutions for de-orbiting, they do not appear suitable to de-orbit the primary targets selected for the implementation of ADR, which have masses greater than 1000 kg and that orbit at altitudes above 800 km. The sail area required for such debris would be too large and collissions risk and survivability issues would not be negligible.
- Electric propulsion and electrodynamic tethers are comparable solutions, in terms of de-orbiting kit mass and de-orbiting time, for debris with mass $\leq$ 2000 kg; for more massive debris, electrodynamic tether is a more mass effective solution, but it requires longer for de-orbiting maneouvres, while electric propulsion is more effective for a fast de-orbiting, even though higher de-orbiting kit mass

is obtained. The de-orbiting time in case of electric propulsion is always lower than 1 year; the electrodynamic tether allows to de-orbit in 1 - 3 years, if the debris lie in orbits where it works better; longer orbital lifetimes, between 6 and 8 years, are required for the most massive debris at inclinations disadvantageous for the tether.

- The time limit of 10 years, suggested by International Guidelines for direct retireval, is guaranteed for each one of the selected de-orbiting technologies (electric propulsion, electrodynamic tether, hybrid propulsion).
- Hybrid propulsion allows the fastes de-orbiting, but it is the most massive de-orbiting solution among those selected. Hybrid propulsion is a suitable technology to perform a controlled re-entry manoeuvre. Its impact on the overall system mass (debris + de-orbiting kit) is only few percentage, lower than 1.5%.
- It was demonstrated that the modular architecture approach allows to create proper de-orbiting kits depending on the debris characteristics; the number of units assembled varies according to the de-orbiting solution adopted. Hybrid maneouvres could also be implemented simply assembling different de-orbiting units.
- Risk assessment evaluations demonstrated that in case of electric propulsion no catastrophic collisions are predicted to occur during the de-orbiting phase: the probability of catastrophic collisions is always of the order of 10^{-7} - 10^{-9}, well below the limit of 0.001 indicated in the NASA-STD 8719.14 [26]. The situation is more critical for the electrodynamic tether. For debris with mass lower than 2000 kg, the number of possible failures is around 0.002, taht is slightly above the limit imposed. In any case it could be still acceptable. For more massive debris, especially those at inclinations disadvanatgeous for the electrodynamic tether (82° and 99°), the probability of failure increases to mach, at values around 0.012 - 0.016 (12% - 16%), that are unacceptable. It has also to be considered that the analysis was limited to debris of 10 cm or smaller. Higher probability of failure are expected if larger debris are considered in the analysis, even though impact events could be predicted from ground observations and collision avoidance maneuvers could be implemented, if necessary.

In can be concluded that it does not exists the best solution to accomplish the de-orbiting manoeuvres, but proper evaluations, in terms of maturity of the technologies, mass of the de-orbiting kits, maneouvre time and risk assessment, are required to select the more suitable de-oriting technology that rapresent the better compromise for a specific class of debris, according to their mass and initial orbit.
More accurate models could be developed in the future to predict the de-orbiting performances of the solutions proposed, for example including orbital perturbations in the analytical models developed. Technological improvements are still required as regard the functionality of drag sails and electrodynamic tethers in space. Deeper investigation are also required concerning the implementation of electric propulsion and hybrid propulsion for ADR although, at the moment, they appear to be among the most promising solutions feasible in the near future, since they have already been proven in space. Costs analysis are also required to identify the parameters that influence most the effectiveness of ADR missions.

As regards the development of the capture interface, an innovative solution was developed, based on the combination of morphing and adhesive capabilities in a single smart interface. This solution addressed two main issuesrelated to the capture of uncooperative objects: the first one was the ability to become compliant to objects of different, or even unknown, shapes, allowing to adhere also in presence of macroscopic irregularities, like screws, nuts, structural reinforcements. The second aspect was the capability to adhere on surfaces made of different materials, like those that can be found on the external walls of spacecraft, such as metals, paints, composites or blankets. After a general overview on the possible technologies available, two were selected for the research: Smhape Memory Polymers (SMP) for the morphing behaviour, and electroadhesion for the adhesion capabilities. Two different prototypes were developed and tested.

With the first prototype it was verified the possibility to employ the conductive elements needed for electroadhesion to also activate the shape memory behaviour of the polymer. It was studied and realised a proper electrodes geometry that allowed to switch between two working modes: a restitor one, to generate the heating power required by means of Joule effect, and a capacitor one, for electroadhesion.

A conductive path was realised on a Kapton layer: the length of the resistive path was 4 m on an area of 10x10 cm^2; the total resistance was 0.8 Ωm.
The maximum shear adhesion pressure achievable with the selected configuration resulted 0.4 kPa at 2.6 kV, the maximum allowed voltage to avoid any breakeup of the dielectric. This result was comparable with experimental data reported in previous works [159] [160] [161]. When connected as resistors, the electrodes were able to provide about 13 W of power. Thermal tests were also performed to validate the thermal model developed to predict the power need to heat the polymer. It was then demonstrated that the developed concept could work, i.e. the electrodes could be employed as both resistors and capacitor, allowing a combination of morphing and adhesive capabilities in a single smart interface.
Some improvements are however required on this research, such as the selection of proper materials that increase the resistance of the path (copper is a good conductor, so it is not the best material for heating through Joule effect), or SMPs with lower transition temperatures.

The electro-adhesion tests on prototype #2 revealed that electro-static pre-load and mechanical pre-load act in the same way, enhancing Wan der Waals interaction at the contact interfaces, which are the main responsibles of the adhesion effect. The normal adhesion pressure achieved with the fabricated sample varied between 0.55 kPa - 1.40 kPa at rspectively 1.5 N and 10 N of mechanical pre-load, with no voltage applied. For the same pre-load, the normale adhesion pressure were about 1.40 kPa and 1.55 kPa at 2.5 kV and 4.5 kV respectively (1.5 N) and 1.75 kPa and 1.80 kPa at at 2.5 kV and 4.5 kV respectively (10 N). According to these values, and considering the sample area of 64 cm^2, the normal adhesion force could vary between 3.5 N and 9 N with no voltage applied and different mechanical pre-load conditions, while the maximim values achievable through electristatic forces vary between 9 N and 11.5 N. Considering the electric trusters employed in the mission analysis, BUSEK-BHT-200-X2B (thrust 17 mN) and SNECMA PPS-1350 (thrust 99 mN), it can be observed that the adhesion force are well above the thrust level; it can be concluded that the developed prototype could be able to support the loads induced by the electric units during the de-orbiting phase. It has anyway to be considered that a capture device could be more complex than the developed prototype, and larger contact surfaces would be available, increasing the adhesion force provided. The situation is different with hybrid propulsion, whose thrust levels are significantly higher than electricpropulsion. In this case a proper mechanism could be developed, composed by several elements like prototype #2, to increase the total contact area and, then, the total adhesion force achievable. However, more efficient adhesion solutions should be evaluated in case of de-orbiting through hybrid propulsion.
Finally, the morphing tests demonstrated how the presence of a foam substrate could be advantageous as regards the capture of uncooperative objects, allowing a good compliance between two contact surfaces even in presence of macroscopical irregularities, enhancing the adhesion between them.

Appendix A

Solar radiation pressure perturbation

Like drag, solar radiation pressure is a nonconservative perturbation which affects satellite orbits. It is induced by the incoming radiation from the Sun (photons) which exerts a force on the satellite, determining a perturbative acceleration on it.
The effect on satellite's motion depends on relative position between the Sun and satellite, orbital altitude, effective cross-sectional area exposed to the radiation, satellite's reflectivity and intensity of the solar flux.
The force due to solar radiation pressure is:

$$F_s = p_s K A_s \cos\gamma \tag{A.1}$$

where:

- $p_s = 4.5 \times 10^{-6}\ N/m^2$ is the solar pressure; it equals the change in momentum of the incoming radiation;
- γ is the angle between the incoming radiation and the normal to the surface;
- K is the reflectivity of the satellite and values 1 for black body, 2 for totally reflective body, 0 for translucent body;
- A_s is the cross-sectional area exposed to radiation.

The main effect of solar radiation pressure on satellite orbit is a long term sinusiodal variation of eccentricity. Orbital decay is less influenced by this perturbation.
Let now consider:

- circular, sunsychronous orbits
- Sun vector in the orbital plane
- surface always perpendicular to the incoming radiation ($\gamma = 0$)

The orbital energy variation due to solar radiation pressure equals the work of F_p:

$$dE = \frac{\overrightarrow{F_p}}{m} \cdot d\overrightarrow{s} = \frac{F_p}{m} \cos\beta \, ds \tag{A.2}$$

where β is the angle between $\overrightarrow{F_p}$ and $d\overrightarrow{s}$.

The force F_p acts on the satellite only when it is illuminated by Sun; when orbit is partially obscured by Earth's shadow, the perturbation due to solar pressure is absent. Considering the hypothesis of circular, sunsynchronous orbits, with Sun in the orbital plane, the angle of eclipse results [**?**]:

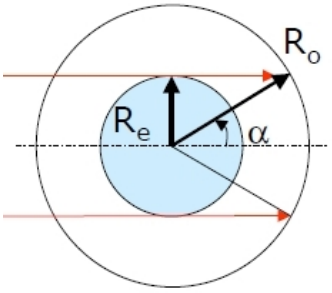

$$\alpha = \arcsin\sqrt{\frac{R_\oplus^2}{R_0}}$$

Figure A.1: Angle of eclipse

From (3.3), the orbital decay rate due to solar pressure is:

$$\begin{aligned}\frac{da}{dt} &= \frac{2a^2}{\mu}\frac{dE}{dt} = \frac{2a^2}{\mu}F_p\cos\beta\,\frac{ds}{dt}\\ &= \frac{2a^2}{\mu}F_p\cos\beta\,v_{sat} =\\ &= \frac{2a^2}{\mu}F_p\cos\beta\,na\\ &= \frac{2}{n}F_p\cos\beta\end{aligned} \tag{A.3}$$

For circular orbits it can be considered:

$$\frac{d\beta}{dt} = \omega_{sat} = \frac{v_{sat}}{R_0} \tag{A.4}$$

$$dt = \frac{R_0}{na}d\beta \tag{A.5}$$

Substituting in equation (A.3) it yields:

$$da = \frac{2}{n^2a}F_pR_0\cos\beta\,d\beta \tag{A.6}$$

Integrating previous equation for one orbit, it obtains the semimajor axis variation per orbit:

$$\Delta a_{1orbit} = \int \frac{2}{n^2a}F_p\,R_0\,\cos\beta\,d\beta = \frac{2}{n^2a}F_p\,R_0\,\sin\beta \tag{A.7}$$

The extremes of integration can be determined observing figure A.2.
The integral can be divided in two terms:

$$\Delta a_{1orbit} = \int_0^{\frac{\pi}{2}-\alpha}\frac{2}{n^2a}F_p\,R_0\,\cos\beta\,d\beta + \int_{\frac{\pi}{2}+\alpha}^{2\pi}\frac{2}{n^2a}F_p\,R_0\,\cos\beta\,d\beta \tag{A.8}$$

Solving, it is obtained:

$$\Delta a_{1orbit} = \frac{2}{n^2a}F_p\,R_0\,\left([\sin\beta]_0^{\frac{\pi}{2}-\alpha} + [\sin\beta]_{\frac{\pi}{2}+\alpha}^{2\pi}\right) = 0 \tag{A.9}$$

Under the initial assumptions, it results that solar radiation pressure has no effect on satellite orbital decay. This conclusion can be verified observing the figure A.2: when F_p and $ds\cos\beta$ have the same direction ($\cos\beta \geq 0$), the semimajor axis and the orbital energy increase, and viceversa when they are opposite; these two effects compensate each other in one orbit, resulting a semimajor axis variation per orbit equal zero.

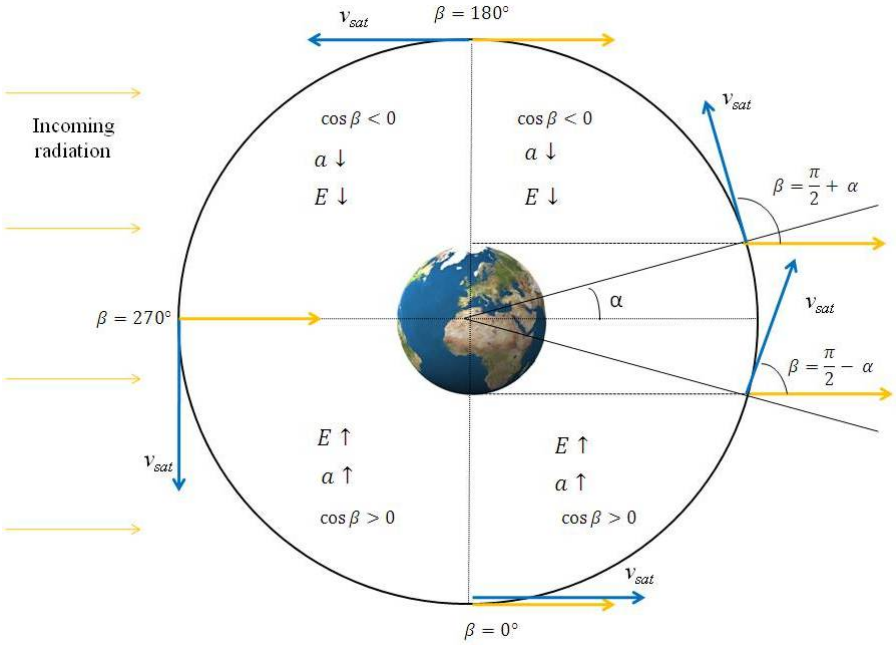

Figure A.2: Schematic representation of the effect of solar radiation pressure on satellites in circular orbits. The integration terms are obtained form the figure.

Bibliography

[1] *Active Debris Removal An Essential Mechanism for Ensuring the Safety and Sustainability of Outer Space, A Report of the International Interdisciplinary Congress on Space Debris Remediation and On-Orbit Satellite Servicing*, Committee on the Peaceful Uses of Outer Space, Scientific and Technical Subcommittee, A/AC.105/C.1/2012/CRP.16., (2012).

[2] *Position Paper Space Debris Mitigation, Implementing Zero Debris Creation Zones*, ESA SP-1301, (2005).

[3] Anon., SATCAT Boxscore, https://celestrak.com/, (Visited: September 2014)

[4] *Position paper on Orbital Debris*, updated edition, IAA, 1999.

[5] Kessler, Donald J., and Burton G. CourPalais, *Collision frequency of artificial satellites: The creation of a debris belt*, Journal of Geophysical Research: Space Physics (19782012) 83.A6, 2637-2646, (1978).

[6] Johnson, N. L. *History and consequences of on-orbit break-ups*, Advances in Space Research 5.2, 11-19, (1985).

[7] Kessler, Donald J., *Collisional Cascading: The Limits of Population Growth in Low-Earth Orbits*, Advance in Space Research, Vol. 11, No 12, pp. (12)63 - (12)66, (1991).

[8] Klinkrad, H. and Johnson, N.L., *Space debris environment remediation concepts*, 5^{th} European Conference on Space Debris, ESA SP-672, (2009).

[9] *Mitigation Guidelines*, IADC-02-01

[10] Anon., *Guidelines and Assessment Procedures for Limiting Orbital Debris*, NASA Safety Standard 1740.14, Office of Safety and Mission Assurance, (1995).

[11] Liou, J.C., Johnson, N.L., *A sensitivity study of the effectiveness of active debris removal in LEO*, 58^{th} International Astronautical Congress, IAC-07-A6.3.05, (2007).

[12] Liou, J.C., *An active debris removal parametric study for LEO environment remediation*, Advances in Space Research, Vol. 47, pp. 18651876, (2011).

[13] Liou, J.C., Anilkuma, A.K., Bastida Virgili, B., Hanada, T., Krag, H., Lewis, H., Raj, M.X.J., Rao, M.M., Rossi, A., Sharma, R.K., *Stability of the future LEO environment - An IADC Comparison study*, 6^{th} European Conference on SPace Debris, ESA SP-723, (2013).

[14] *NATIONAL SPACE POLICY of the UNITED STATES of AMERICA*, June 28, (2010).

[15] Anon., ESA - Space Debris section, http://www.esa.int/Our_ Activities/Operations/Space_ Debris/Analysis_ and_ prediction, (Oct. 2014).

[16] Anon., Center for Orbital and Reentry Debris Studies, Annual Reentry Data, http://www.aerospace.org/cords/reentry-data-2/annual-reentry-data/ , (Feb. 2014).

[17] Chobotov, Vladimir A., *Orbital Mechanics*, 3^{rd} Edition, AIAA Education Series.

[18] Anon., *HANDBOOK FOR LIMITING ORBITAL DEBRIS - Measurement System Identification: Metric*, NASA-HANDBOOK 8719.14, (2008).

[19] Anon., *Orbital Debris Management and Risk Mitigation*, Academy of Program/Project and Engineering Leadership.

[20] Rossi, A., *The Earth orbiting space debris*, Serb. Astronomy Journal, Vol. 170, pp. 1-12, (2005).

[21] Krisko, B.H., *The predicted growth of the low Earth orbit space debris environment: an assessement of future risk for spacecraft*, Proceedings of the Institution of Mechanical Engineers, Part G: Journal of Aerospace Engineering, Vol. 221, pp. 975985, (2007).

[22] Liou, J.C., Johnson, N.L., Hill, N.M., *Controlling the growth of future LEO debris populations with active debris removal*, Acta Astronautica, Vol. 66, pp. 648-653, (2010).

[23] Wright, D., *The Current Space Debris Situation*, Orbital Debris Mitigation Workshop, Beijing, (2010).

[24] Pardini, C., Anselmo, L., *Assessment of the consequences of the Fengyun-1C breakup in low Earth orbit*, Advances in Space Research, Vol. 44, pp. 545557, (2009).

[25] Anselmo, L., Pardini, C., *Analysis of the consequences in Low Earth Orbit of the collisison between COSMOS 2251 and IRIDIUM 33*, 21^{st} International Symposium on Space Flight Dynamics, France, (2009).

[26] Anon., *Process for Limiting Orbital Debris*, NASA-STD-8719.14, (2009).

[27] Bastida Virgili, B., Krag, H., *Strategies for active debris removal in LEO*, 5^{th} European Conference on SPace Debris, ESA SP-672, (2009).

[28] Liou, J.C., Johnson, N.L., *Instability of the present LEO satellite populations*, Advances in Space Research, Vol. 41, pp. 10461053, (2008).

[29] Brisibe, T.C., Pessoa-Lopes, I., *The impact of orbital debris on commercial space systems*, Proceedings of the 44^{th} colloquium on the law of outer space, AIAA, IISL-01-IISL.4.04, (2001).

[30] Braun V., *Lüpken*, A., Flegel, S., Gelhaus,J., *Möckel*, M., Kebschull, C., Wiedemann, C., *Vörsmann*, P., *Active debris removal of multiple priority targets*, Advances in Space Research, vol. 51, pp. 16381648, (2013).

[31] Martin, T., Perot, E., Desjean, M.C., and Bitetti, L., *Active Derbis Removal Mission Design in Low Earth Orbit*, Progress in Propulsion Physics, Vol. 4, pp. 763-788 (2013). DOI: 10.1051/eucass/201304763.

[32] Barbee, B.W., Alfano, S., *Piñon*, E., Gold, K., and Gaylor, D., *Design of Spacecraft Missions to Remove Multiple Orbital Debris Objects*, 35^{th} Annual AAS Guidance and Control Conference, AAS 12-017, Colorado, (2012).

[33] Castronuovo, M.M., *Active space debris removal A preliminary mission analysis and design*, Acta Astronautica,Vol. 69, pp. 848859, (2011).

[34] Quinlan, J.R., Jones, C.A., Vittaldev V., and Wilhite, A., *On the Design of an Active Debris Removal Architecture for Low Earth Orbit Space Debris Remediation*, AIAA SPACE Conference & Exposition, California, AIAA 2011-7250, (2011).

[35] http://www.esa.int/TEC/Robotics/SEMTWLKKKSE_ 0.html (visited: October 2014)

[36] Starke, J., Bischof, B., Gunter, H., David, E., *ROGER, a Potential Orbital Space Debris Removal System*, NASA-DARPA International Conference on Orbital Debris Removal, Chantilly, (2009).

[37] Pfisterer, M., Schillo, K., Valle, C., and Lin, K.C., and Ham, C., *The Development of a Propellantless Space Debris Mitigation Drag Sail for LEO Satellites*

[38] Maessen, D.C., van Breukelen, E.D., Zandbergen, B.T.C., Bergsma, O.K., *Development of a generic de-orbit device for cubesat*, International Astronautical Congress, IAC-07-A6.3.06, (2007).

[39] Mueller, J., *Thruster Options for Microspacecraft: A Review and Evaluation of Existing Hardware and Emerging Technologies*, 33^{rd} AIAA/ASME/SAE/ASEE Joint Propulsion Conference and Exhibit, AIAA 97-3058, (1997).

[40] Scharfe, D.B., Ketsdever, A.D., *A Review of High Thrust, High Delta-V Options for Microsatellite Missions*, 45^{th} AIAA/ASME/SAE/ASEE Joint Propulsion Conference & Exhibit, Colorado, AIAA 2009-4824, (2009).

[41] Janson, S.W., Helvajian, H., Hansen, W.W. and Lodmell, Lt. J., *Microthrusters for nanosatellites*, The Second International Conference on Integrated Micro Nanotechnology for Space Applications (MNT99), (1999).

[42] Covello, F., *Application of electrical propulsion for an active debris removal system: a system engineering approach*, Advances in Space Research, Vol. 50, pp. 918931, (2012).

[43] Busek, Space Propulsion and Systems, *Low Power Hall Effect Thrusters datasheet*. Available on www.BUSEK.com .

[44] Beiting, E.J., Pollard, J.E. and Pote, B., *Electromagnetic Emissions from a BHT-200 Hall Thruster*, 27^{th} International Electric Propulsion Conference, IEPC-01-342, (2001).

[45] SNECMA Safran Group, *PPS 1350 Stationary Plasma Thruster datasheet*. Available on www.snecma.com .

[46] Vial, V., Godard, L., Cornu, N., Coulaud, E., and Arrat, D., *PPS 1350-G Performance assessment with permanent magnets*, 32^{nd} International Electric Propulsion Conference, IEPC-2011-119, (2011).

[47] Vial, V., Godard, L., Cornu, N., Coulaud, E., and Arrat, D., *PPSNG: Hall Effect thruster for next generation spacecraft*, 32^{nd} International Electric Propulsion Conference, IEPC-2011-120, (2011).

[48] Sanmartin, J.R., Charro, M., Chen, X., Lorenzini, E.C., et. al., *A Universal System to Deorbit Satellites at End of Life*, Journal of Space Technology and Science, Vol. 26, No. 1, pp. 21-32, (2012).

[49] US Patent # 6.830.222., *Balloon device for lowering space objects orbit*, Dec. 14, 2004.

[50] Global Aerospace Corporation website, http://gaerospace.com/projects/GOLD/index.html

[51] Dupuy, C., and Le Couls, o., *Gossamer Technology to Deorbit LEO Non-Propulsion Fitted Satellite*, Proceedings of the 40^{th} Aerospace Mechanisms Symposium, NASA Kennedy Space Center, (2010).

[52] Whorton, M., Heaton, R., Pinson, G.L. and Adams, C., *NanoSail-D: The First Flight Demonstration of Solar Sails for Nanosatellites*, Small Satellite Conference, SSC08-X-1, (2008).

[53] Onishi, S., Funakoshi, K., Nakajima, S., *Orbital Decay Accelerator: A case of QSAT-EOS*, 3^{rd} Nano-Satellite Symposium, (2011).

[54] Romagnoli, D., Theil, S., *De-orbiting satellites in LEO using solar sails*, Journal of Aerospace Engineering, Vol. 4.2, p. 49, (2012).

[55] Burkhardt, H., Sippel, M., Krlle, G., Janovsky, R., Kassebom, M., Lbberstedt, H., Rmoberg, O., Fritsche, B., *Evaluation of propulsion systems for satellite end-of-life de-orbiting*, AIAA Journal 2002-4208, (2002).

[56] Sutton, G.P., Biblarz, O., *Rocket Propulsion Elements*, Seventh Edition, A Wiley-lnterscience Publication, (2001).

[57] Larson, W.J., Wertz, J.R., *Space Mission Analisys and Design*, Space Technology Library, Third edition.

[58] Hoskins, W.A, Cassady, R.J., *30 Years of Electric Propulsion Flight Experience at Aerojet Rocketdyne*, 33^{rd} International Electric Propulsion Conference, Paper IEPC-2013-439, (2013).

[59] *Electric Propulsion - Technology Programs*, ESA Publications Division, BR-187, (2002).

[60] Maggi, F., *Deorbiting of a population through hybrid propulsion*, Internal Report SPLab - PoliMi, (2013).

[61] Altman, D., and Holzman, A., *Fundamentals of hybrid rocket combustion and propulsion*, Progress in astronautics and aeronautics, Vol. 218, Chapter 1, Overview and history of hybrid rocket propulsion, pages 1-36, AIAA, (2007).

[62] Story, G., Zoladz, T., Arves, J., Kearney, D., Abel, T. and Park, O., *Hybrid propulsion demonstration program 250 k hybrid motor*, 39^{th} AIAA/ASME/SAE/ASEE Joint Propulsion Conference and Exhibit, AIAA Paper No. 2003-5198, (2003).

[63] Evans, B., Boyer, E., Kuo, K.K., Risha, G. and Chiaverini, M., *Hybrid rocket investigations at penn state university's high pressure combustion laboratory: Overview and recent results*, 45^{th} AIAA/ASME/SAE/ASEE Joint Propulsion Conference and Exhibit, AIAA Paper No. 2009-5349, (2009).

[64] Risha, G.A., Evans, B.J., Boyer, E., and Kuo, K.K., *Fundamentals of hybrid rocket combustion and propulsion*, Progress in astronautics and aeronautics, Vol. 218 , Chapter 10, Metals, energetic additives, and special binders used in solid fuels for hybrid rockets, pages 413-456, AIAA, (2007).

[65] Maggi, F., Gariani, G., Galfetti, L., and DeLuca, L.T., *Theoretical analysis of hydrides in solid and hybrid rocket propulsion*, International Journal of Hydrogen Energy, Vol. 37, pp. 1760-1769, (2012).

[66] DeLuca, L.T., Galfetti, L., Maggi, F., Colombo, G., Merotto, L., Boiocchi, M., Paravan, C., Reina, A., Tadini, P., and Fanton, L., *Characterization of htpb-based solid fuel formulations: Performance, mechanical properties, and pollution*, Acta Astronautica, IN PRESS, (2012).

[67] Shark, S.C., Sippel, T.R., Son, S.F., Heister, S.D., and Pourpoint, T.L., *Theoretical performance analysis of metal hydride fuel additives for rocket propellant applications*, 47^{th} AIAA/ASME/SAE/ASEE Joint Propulsion Conference and Exhibit, AIAA Paper No. 2011-5556, (2011).

[68] DeLuca, L.T., Galfetti, L., Colombo, G., Maggi, F., Bandera, A., Boiocchi, M., Gariani, G., Merotto, L., Paravan, C., and Reina, A., *Time-resolved burning of solid fuels for hybrid rocket propulsion*, Progress in Propulsion Physics, Vol. 2, pp. 405-426, EDP Sciences, (2011).

[69] DeLuca, L.T., Galfetti, L., F. Maggi, Colombo, G., Paravan, C., Reina, A., Tadini, P., Sossi, A. and Duranti, E., *An optical time-resolved technique of solid fuels burning for hybrid rocket propulsion*, 47^{th} AIAA/ASME/SAE/ASEE Joint Propulsion Conference and Exhibit, AIAA Paper No. 2011-5753, (2011).

[70] Hoyt, R., *Systems for satellite deployment and disposal*, 51^{st} International Astronautical Congress, (2000).

[71] Nishida, S., Kawamoto, S., Okawa, Y., Kitamura, S., *A study of active debris removal system of space debris*, Acta Astronautica, Vol. 65, pp. 92-102, (2009).

[72] *DuPont^{TM} Kapton®* B, Technical bulletin, available on www.dupont.com (Feb. 2012).

[73] Visagie, L., Theodorou, T., *Hybrid Sail - Hybrid Solar Sails for Active Debris Removal, Final Report*, Ariadna ID: 10-6411b, (2011).

[74] Straubel, M., Hillebrandt, M., Belvin, W.K., *Results on Research Study - Evaluation of deployable space mast concepts*, NASA LaRC Final presentation, (2011).

[75] Rehnmark, F., Pryor, M., Holmes, B., Schaechter, D., Pedreiro, N., Carrington, C., *Development of a deployable nonmetallic boom for reconfigurable systems of small spacecraft*, 48^{th} AIAA/ASME/ASCE/AHS/ASC Structures, Structural Dynamics, and Materials Conference, (2007).

[76] *Coilable Boom Systems Datasheet*, available on www.atk.com (Feb. 2012).

[77] Fatemi, N.S., Pollard, H.E.,. Hou, H.Q., and Sharps, P.R., *Solar array trades between very high-efficiency multi-junction and Si space solar cells*, 28^{th} IEEE Photovoltaic Specialists Conference, p. 1083, (2000).

[78] Gordon, S. and McBride, B., *Computer Program for Calculation of Complex Chemical Equilibrium Compositions and Applications*, NASA Technical Report, RP-1311, (1994).

[79] Casalino, L., and Pastrone, D., *Optimal Design of Hybrid Rockets for Small Satellites*, AIAA Paper No. 2002-3579, (2002).

[80] Casalino, L., and Pastrone, D., *Optimal design of hybrid rocket motors for launchers upper stages*, Journal of Propulsion and Power, Vol. 26(3), pp. 421-427, (2010).

[81] Schoonover, P. L., Crossley, W. A. and Heister, S. D., *Application of a genetic algorithm to the optimization of hybrid rockets*, Journal of Spacecraft and Rockets, Vol. 37(5), pp. 622-629, (2000).

[82] AA.VV., *Space Propulsion Analysis and Design*, McGraw Hill, Lrst revised edition, (1995).

[83] Heister, S. and Wernimont, E., *Fundamentals of hybrid rocket combustion and propulsion*, Progress in astronautics and aeronautics, chapter 11, Hydrogen peroxide, hydroxyl ammonium nitrate, and other storable oxidizers, Vol. 218 pp. 457-487, AIAA, (2007).

[84] Chiaverini, M., *Fundamentals of hybrid rocket combustion and propulsion*, Progress in astronautics and aeronautics, chapter 2, Review of solid-fuel regression rate behavior in classical and nonclassical hybrid rocket motors, Vol. 218, pp 37-125, AIAA, (2007).

[85] Yetter, R.A., Yang, V., Wu, M., Wang, Y., Milius, D., Aksay, I.A. and Dryer, F.L., *Combustion issues and approaches for chemical microthrusters*, International Journal of Energetic Materials and Chemical Propulsion, Vol. 6(4), (2007).

[86] Tam, W., Debreceni, M., Hersh, M. and Nye, C., *Low cost derivative tanks for spacecraft and launch vehicles*, 35^{th} Joint Propulsion Conference and Exhibit, AIAA Paper No. 99-2831, (1999).

[87] Anon., *Ihi pressurant and propellant tank*, http://www.ihi.co.jp/ia/en/product/satellite03.html, (July 2013).

[88] Anon. *Mt aerospace spacecrft tanks*, http://www.mtaerospace.de/en/products/space/tanks.html, (May 2013).

[89] Bombardelli, C., Zanutto, D., Lorenzini, E., *Deorbiting Performance of Bare Electrodynamic Tethers in Inclined Orbits*, Journal of Guidance, Control, and Dynamics, DOI: 10.2512/1.58428, (2013).

[90] Grahn, S., Rathsman, A., *Astrid-An attempt to make the microsatellite a useful tool for space science*, 11^{th} Annual AIAA/USU Conference on Small Satellites, XP009029828, pp. 1-11, (1995).

[91] Zee, R. E. and Stibrany, P., *The MOST Microsatellite: A Low-Cost Enabling Technology for Future Space Science and Technology Missions*, Canadian Aeronautics and Space Journal, Vol. 48, No. 1, pp. 1-11, (2002).

[92] Ravanbakhsh, A., Franchini, S., *Preliminary Structural Sizing of a Modular Microsatellite Based on System Engineering Considerations*, Third International Conference on Multidisciplinary Design Optimization and Applications, France, (2010).

[93] Anon, *NORAD Catalogue*. http://satellitedebris.net/Database/ (May 2013).

[94] Savioli., L., Francesconi, A., Maggi, F., Olivieri, L., Lorenzini, E., Pardini, C., *Space debris removal using multi-mission modular spacecraft*, 6^{th} European Conference on SPace Debris, Germany, (2013).

[95] Space Track Organization, Satellite Catalog Data. https://www.space-track.org, (2013).

[96] Union of Concerned Scientists, UCS Satellite Database 12-1-12. http://www.ucsusa.org., (2012).

[97] De Luca, L.T., Bernelli, F., Maggi, F. et al., *Active Space Debris Removal by Hybrid Engine Module*, 63^{rd} International Astronautical Congress, Paper IAC-12-A6.5.8, DVD, ISSN 1995-6258, International Astronautical Federation (IAF), (2012).

[98] Utzmann, J., Oswald, M., Stabroth, et al., *Ranking and Characterization of Heavy Debris for Active Removal*, 63^{r}d International Astronautical Congress, Paper IAC-12-A6.2.8, DVD, ISSN 1995-6258, International Astronautical Federation (IAF), (2012).

[99] Pardini, C., Anselmo, L., *Performances of atmospheric density models during satellite reentry prediction campaigns at sunspot minimum*, 21^{st} International Symposium on Space Flight Dynamics (ISSFD-2009), ACM 2009-294 (CD-ROM), (2009).

[100] King-Hele, D., *Satellite orbits in an atmosphere. Theory and applications*, Blackie Academic & Professional; (1987).

[101] Vallado, D. A., *Fundamentals of astrodynamics and applications*, Second Edition, Space Technology Library, (2001).

[102] Zanutto, D., *De-orbiting performances*, Internal report, (2012).

[103] Neuenfeldt, B.D. and Henderson, W.K., *A survey of uncontrolled satellite reentry and impact predictions*, PhD Thesis. Monterey, California. Naval Postgraduate School, (1993).

[104] Sgobba, T., *Safety Design for Space Operations*, Eds. Firooz Allahdadi, Isabelle Rongier, and Paul Wilde, Butterworth-Heinemann, First Edition, (2013).

[105] Pardini, C., Anselmo, L., *Re-entry predictions for uncontrolled satellites: Results and challenges*, 6^{th} IAASS Conference Safety is Not an Option, (2013).

[106] Ziniua, W., Ruifenga, H., Xib, Q., Xiangb, W., Zhea, W., *Space Debris Reentry Analysis Methods and Tools*, Chinese Journal of Aeronautics, Vol. 24, pp. 387-395, (2011).

[107] Burkhardt, H., Sippel, M., Krlle, G., Janovsky, R., Kassebom, M., Lbberstedt, H., Fritsche, B., *Evaluation of propulsion systems for satellite end-of-life de-orbiting*, AIAA Journal 2002-4208, (2002).

[108] Liou, J.C., *Collision activities in the future orbital debris environment*, Advances in Space Research, Vol., 38, pp. 21022106, (2006).

[109] Internal report, *BETS - Passive Electric Propulsion*, University of Padova-CISAS (UPD-CISAS).

[110] Anz-Meador P.D., *Tether-debris interactions in low Earth orbit*, AIP Conference Proceedings, Vol. 552, pp. 525, (2001).

[111] Pardini, C., Hanada, T., Krisko, P.H., *Benefits and risks of using electrodynamic tethers to deorbit spacecraft*, 57^{th} International Astronautical Congress, (2006).

[112] Pardini, C., Hanada, T., Krisko, P.H., Anselmo, L., Hirayama, H., *Are de-orbiting missions possible using electrodynamic tethers? Task review from the space debris perspective*, Acta Astronautica, Vol. 60 (10-11), pp. 916-929, (2007).

[113] Pardini, C., Hanada, T., Krisko, P.H., *Benefits and risk of using electrodynamic tethers to de-orbit spacecraft*, Acta Astronautica, Vol. 64, pp. 571-588, (2009).

[114] Francesconi, A., Giacomuzzo, C., Kibe, S., Nagao, Y., Higashide, M., *Effects of high speed impacts on CFRP plates for space applications*, Advanced Space Research, Vol. 50-5, pp.539-548, (2012).

[115] Francesconi, A., Giacomuzzo, C., Grande, A.M., Mudric,T., Zaccariotto, M., Etemadi, E., Di Landro, L., Galvanetto, U., *Comparison of self-healing ionomer to aluminium-alloy bumpers for protecting spacecraft equipment from space debris impacts*, Advanced Space Research, Vol. 51(5), pp.930-940, (2013).

[116] Oda, M., *Space Robot Experiment on NASDAs ETS-VII satellite*, IEEE International Conference on Robotics and Automation, pp. 13901395, (1999).

[117] Ogilvie, A., et al., *Autonomous satellite servicing using the orbital express demonstration manipulator system*, 9^{th} International Symposium on Artificial Intelligence, Robotics and Automation in Space, i-SAIRAS, pp. 25-29, (2008).

[118] Zimpfer, D., Kachmar, P., Tuohy, S., *Autonomous rendezvous, capture and in-space assembly: past, present and future*, 1^{st} Space Exploration Conference: Continuing the Voyage of Discovery, Vol. 1, pp. 234-245, (2005).

[119] Hastings, D. E. et al., *On-Orbit Upgrade and Repair: The Hubble Space Telescope Example*, Journal of Spacecraft and Rockets, Vol. 43, No. 3, pp. 614-625, (2006).

[120] Polites, M.E., *Technology of Automated Rendezvous and Capture in Space*, Journal of Spacecraft and Rockets, Vol. 36, No. 2, pp. 280-291, (1999). doi: 10.2514/2.3443.

[121] Werneth, R., *Lessons Learned from Hubble Space Telescope ExtraVehicular Activity Servicing Missions*, 31^{st} International Conference on Environmental Systems, Society of Automotive Engineers, (2001).

[122] Oda, M., Kibe, K., Yamagata, F., *ETS-VII, space robot in-orbit experiment satellite* IEEE International Conference on Robotics and Automation, Vol.1, pp. 73944, (1996).

[123] Sommer, B., *Automation and robotics in the german space program - unmanned on orbit servicing (OOS) & the TECSAS mission* 55^{th} International Astronautical Congress, Canada, (2004).

[124] Artigas, J., Borst, C., Landzettel, K., Hirzinger, G., *Telerobotics enabling On-Orbit Servicing A DLR perspective*, 2^{nd} European Workshop on Active Debris Removal, CNES HQ, (2012).

[125] Hadfield, C., *An Astronaut's Guide to Life on Earth*, Random House of Canada, (2013).

[126] Xu, W., et al., *Autonomous rendezvous and robotic capturing of non-cooperative target in space*, Robotica 28.05, pp. 705-718, (2010).

[127] Du, X., et al., *Pose measurement of large non-cooperative satellite based on collaborative cameras*, Acta Astronautica, Vol. 68.11, pp. 2047-2065, (2011).

[128] Boge, T. and Benninghoff, H., *Rendezvous Simulation for On-Orbit Servicing Missions Using Advanced Robotic Technology*, Automatic Control in Aerospace, Vol. 19, No. 1, (2013).

[129] Sellmaier, F., et al., *On-orbit servicing missions: Challenges and solutions for spacecraft operations*, Space Ops Conference, (2010).

[130] Nguyen-Huynh, T., et al., *Adaptive Reactionless motion with joint limit avoidance for robotic capture of unknown target in space*, Intelligent Robots and Systems (IROS), IEEE/RSJ International Conference, (2012).

[131] Yoshida, K.., et al., *Dynamics, control and impedance matching for robotic capture of a non-cooperative satellite*, Advanced Robotics 18.2, pp. 175-198, (2004).

[132] Flores-Abad, A., et al., *A review of space robotic technologies for on-orbit servicing*, Progress in Aerospace Science 68, pp. 1-26, (2014).

[133] Branz, F., Savioli, L., Sansone, F., Francesconi, A., *Innovative technologies for non-cooperative targets close inspection and grasping*, 63^{rd} International Astronautical Congress, IAC 12.D1.2.7, (2012).

[134] Aghili, F., *Pre-and post-grasping robot motion planning to capture and stabilize a tumbling/drifting free-floater with uncertain dynamics*, IEEE International Conference on Robotics and Automation (ICRA), (2013).

[135] Piedbouef, J.C. and Dupuis, E., *Recent Canadian Activities in Space Automation and Robotics - An Overview*, 6^{th} International Symposium on Artificial Intelligence and Robotics and Automation in Space: i-SAIRAS, (2001).

[136] Bonivento C., et al., *A dexterous gripper for space robotics*, 5^{th} International Symposium on Artificial Intelligence, Robotics and Automation in Space, (1999).

[137] Branz, F., Savioli, L., Francesconi, A., Sansone, F, Krahn, J, Menon, C., *Soft docking system for capture of irregularly shaped , uncontrolled space objects*, 6^{th} European Conference on Space Debris, (2013)

[138] Nishida, S., and Yoshikawa, T., *Space debris capture by a joint compliance controlled robot*, Advanced Intelligent Mechatronics, IEEE/ASME International Conference, Vol. 1, pp. 496-502, (2003).

[139] Guang, Z., and Jing-rui, Z., *Space Tether Net System for Debris Capture and Removal*, Intelligent Human-Machine Systems and Cybernetics (IHMSC), 4^{th} International Conference, Vol. 1, pp. 257-261, (2012).

[140] Pearson, J., et al., *Active debris removal: EDDE, the electrodynamic debris eliminator*, 61^{st} International Astronautical Congress, (2010).

[141] Reed, J. and S. Barraclough., *Development of Harpoon System for Capturing Space Debris*, 6^{th} European Conference on Space Debris, (2013).

[142] Mavroidis, C., Pfeiffer, C., Lennon, J., Paljic, A., Celestino, J., and Bar-Cohen, Y., *Modeling and design of an electro-rheological fluid based haptic system for tele-operation of space*, 4^{th} International Conference and Exposition/Demonstration on Robotics for Challenging Situations and Environments, 174-180, (2000).

[143] Mavroidis, C., Pfeiffer, C., Celestino, J. And Bar-Cohen, Y., "*ontrolled Compliance Haptic Interface Using Electro-rheological Fluids*, SPIE 7^{th} Annual International Symposium on Smart Materials and Structures Conference on Electro-Active Polymer Actuators and Devices, (2000).

[144] Monkman, G.J., *Memory foams for robot grippers*, 5^{th} International Conference on Advanced Robotics, Robots in Unstructured Environments 91, (1991).

[145] Xie, T., *Recent advances in polymer shape memory*, Polymer, Vol. 52, pp. 4985-5000, (2011).

[146] Monkman, G.J., *Advances in shape memory polymer actuation*, Mechatronics, Vil. 10, p. 489-498 (2000).

[147] Liu, C. and Mather, P.T., *A Shape Memory Polymer with Improved Shape Recovery* Materials Research Society Symposium 855E, 112, (2005).

[148] Hearon, K., Singhal, P., Horn, J., Small, W., Olsovky, C., Maitland, K.C., Wilson, T., Maitland, D., *Porous Shape-Memory Polymers*, Polymer Reviews, Vol. 53(1), 41-75, (2013).

[149] Sokolowski, W.M., Shunichi, H., "Applications of cold hibernated elastic memory (CHEM) structures," Proc. SPIE Smart Structures and Materials 2003: Smart Structures and Integrated Systems 5056, 534-544 (2003).

[150] Darooka, D.K., Scarborough, S.E., Cadogan, D.P., *An evaluation of inflatable truss frame for space applications*, AIAA-2001-1614 (2001).

[151] Monkman, G.J., *Robotic Compliance Control Using Memory Foams*, Industrial Robot, Vol. 18(4), pp. 31-32, (1991).

[152] Anon., Mid Technologies, Research and development, http://www.midetechnologies.com/ (2014).

[153] Kinloch, A. J., *Adhesion and adhesives: science and technology*, Springer, (1987).

[154] Pizzi, A., Mittal, K. L., *Handbook of Adhesives Technology*, Revised and Expanded], CRC Press, (2003).

[155] Reddy, S., Artz, E., del Campo, A., *Bioinsipred Surfaces with Switchabke Adhesion*, Advanced Materials, Vol. 19(2), 3833-3837, (2007).

[156] Del Campo, A., Greiner, C. and Artz, E., "Contact Shape Control Adhesion of Bioinspired Fibrillar Surfaces," Langmiur, 23, 10235-10243, (2007).

[157] Yu, J., Chary, S., Das, S., Tamelier, J., Pesika, N.S., Turner, K.L., Israelachvili, J.N., *Gecko-Inspired Dry Adhesive for Robotic Applications*, Advanced Functional Materials, Vol. 21(16), 3010-3018 (2011).

[158] Monkman, G.J., *An analysis of Astrictive Prehension*, The International Journal of Robotics Research, Vol. 16(1), 1-10, (1997).

[159] Prahlad, H., Pelrine, R., Stanford, S., Marlow, J. and Kornbluh, R., *Electroadhesive Robots-Wall Climbing Robots Enabled by a Novel, Robust, and Electrically Controllable Adhesion Technology*, IEEE International Conference on Robotic and Automation, (2008).

[160] Daz Tllez, J.P., Krahn, J. and Menon, C., *Characterization of Electro-adhesives for Robotic Applications*, IEEE International Conference on Robotics and Biomimetics, (2011).

[161] Cui, G., Liang, K., Guo, J., Li, H. and Gu, D., *Design of a Climbing Robot Based on Electrically Controllable Adhesion Technology*, International Coference on Solid State and Materials 22, (2012).

[162] Monkman, G.J., Taylor, P.M. and Farnworth, G.J., *Principals of electroadhesion in clothing robotics*, International Journal of Clothing Science and Technology 1(3), 14-20, (1989).

[163] Karagozler, M. E., Campbell, J.; Fedder, Gary K.; Goldstein, Seth C., Weller, M. P., and Yoon, B. W., *Electrostatic Latching for Inter-module Adhesion, Power Transfer, and Communication in Modular Robots*, Computer Science Department 745, (2007).

[164] Pelrine, R., *Microrobot Inspectors - Electroadhesive wall Climbing Robots and more*, SRI International, (2009).

[165] Ruffatto III, D., et al., *Increasing the adhesion force of electrostatic adhesives using optimized electrode geometry and a novel manufacturing process*, Journal of Electrostatics, Vol 72.2, pp. 147-155, (2014).

[166] Koh, K.H., Sreekumar, M., and Ponnambalam, S.G., *Experimental Investigation of the Effect of the Driving Voltage of an Electroadhesion Actuator*, Materials, Vol. 7, pp. 4963-4981, (2014).

[167] Ruffatto III, D., Shah, J., Spenko, M., *Optimization and Experimental Verification of Electrostatic Adhesive Geometry*, IEEAC Paper # 2266, (2013).

[168] Koh, K.H., Ramanathan, K.C., Ponnambalam, S.G., *Modeling and Simulation of Electrostatic Adhesion for Robotic Devices*, International Conference on Electronics, Information and Communication Engineering, (2012).

[169] Persson, B.N.J., *On the theory of rubber friction*, Surface Science, Vol. 401, pp. 445-454, (1998).

[170] Autumn, K., Sitti, M., Liang, Y.A., Peattie, A.M.,Hansen, W.R., Sponberg, S., Kenny, T., Fearing, R., Israelachvili, J.N. and Full, R.J., *Evidence for van der Waals adhesion in gecko setae*, National Academy of Sciences, Vol. 99(19), pp. 12252-12256, (2002).

[171] Sguotti, G., Francesconi, A., *Thermal model*, (2014).

ref: BonacinaThermalTest Bonacina, C., Cavallini, A., Di Filippo, P., Mattarolo, L., *Lezioni di trasmissione del calore*, Cleup Ed, (1975).

[172] Carpi, F., *Folded dielectric elastomer actuators*, Smart Materials and Structures 16.2, S300, (2007).

Acknowledgements

Anche questi tre anni di dottorato stanno volgendo a termine. E un altro piccolo pezzo andrá ad aggiungersi al puzzle della mia vita.
Volgendo indietro lo sguardo al sentiero percorso non posso non notare che accanto alle mie impronte ce ne sono molte altre...sono quelle di chi é presente da sempre, o di chi ha incrociato la sua strada con la mia, magari solo di passaggio, o per poi continuare con me, o di chi é dall'altra parte dell'oceano fisicamente, ma sempre presente nei miei pensieri. Senza queste persone il mio sentiero non sarebbe stato cosí speciale, ed é per questo che vorrei rivolgere a loro il mio grazie.

Un grazie speciale va in primis ai miei genitori per esseri sempre stata accanto, per avermi sostenuta nelle mie scelte, per avermi incoraggiata ad inseguire le mie aspirazioni. Grazie per avermi insegnato ad affrontare la vita col sorriso, a non abbattermi mai ed ad inseguire ció in cui credo.
Un affettuoso grazie va a mio fratello Lorenzo: mi fai vedere le cose da angolature diverse, arrotondi i miei spigoli e mi dai consigli che mi aiutano a migliorarmi sempre di piú come persona.
Sarete sempre le mie stelle fisse!!

Un ringraziamento particolare va al mio supervisore Prof. Alessandro Francesconi, che mi ha seguita in questi tre anni di ricerca. Mi ha dato la possbilitá di continuare a coltivare quello che per me é la passione di una vita: il mio amore per lo spazio e le attivitá ad esso correlate. Le esperienze fatte in questi tre anni mi hanno fatta crescere professionalmente, ma soprattutto come persona.
Un sentito ringraziamento va al Prof. Carlo Menon, per avermi dato la possibilitá di svolgere parte della mia ricerca nel suo gruppo di ricerca MENRVA Research Group, presso la Simon Fraser University di Burnaby (Vancouver) in Canada. É stata una delle esperienze piú belle e significative che abbia mai fatto.
Un ringraziamento va anche alle persone con cui ho avuto la possibilitá di collaborare in questi tre anni: Filippo Maggi, Cinzia Giacomuzzo, Denis, Prof. Enrico Lorenzini, Dott.ssa Carmen Pardini. Grazie per la vostra disponibilitá; ogni vostro contributo mi ha dato la possibilitá di approfondire le mie conoscenze e di migliorare l'attivitá di ricerca.

E ora é giunto il momento dei ringraziamenti ai miei compagni di avventure...e devo notare che sono state molte!!!
Un grazie va ai miei compagni di dottorato: Lorenzo (é sempre stato un piacere rilassarsi dopo ore e ore di congressi facendo maratone in giro per le cittá ...a volte senza sapere bene dove si stesse andando!!), Fren e Franz, (che mi hanno accettata nonostante le mie malriuscite battute che non facevano ridere!!), Marco, il nostro elettronico (grazie per la tua disponibilitá anche oltreoceano!!!), e gli altri ragazzi che con noi hanno condiviso le varie edizioni di ARCADE: Alessandro, Fabio, Asiago, Andrea, Jacopo. Grazie a Riccardo, per la tua sensibilitá ; a Francesca e Mitch: la vostra semplicitá e determinazione sono state di esempio per me.
Un grande, affettuoso grazie va al gruppo "Girls" e ai rispettivi "Boys": con voi il divertimento é all'ordine del giorno; ci siete sempre, nei momenti belli per condividere le gioie, e in quelli piú difficili per offrire una spalla su cui trovare conforto. Siete un tesoro raro e prezioso.
Un affettuoso grazie va alla compagnia del treno: Angela, Matteo, Anna, Sara e Riccardo. Con voi la vita da pendolare é diventata una divertente e spensierata passeggiata, un appuntamento giornaliero che faceva iniziare e terminare la giornata con il sorriso!! Un grazie va a Martina, Chiara, Marina, Stella e Anna: le uscite con voi sono sempre rigenerative!!

Ho sempre pensato che lo sport potesse essere una fonte da cui attingere valori da mettere in pratica nella vita quotidiana. Ne ho avuto la conferma dalle persone stupende che ho avuto modo di incontrare in questi anni attraverso la pratica di arti marziali. Un grazie di cuore va ai maestri e istruttori Lauro, Pietro, Stefano, Gabriele, a tutto il gruppo del Ju-Jitsu, il gruppo Krav e agli amici di combattimento della My Olympus Gym: abbiamo coltivato insieme il valore del rispetto, fatto esperienze che ci hanno insegnato a conoscere i nostri limiti, abbiamo imparato a superarli insieme, a non mollare mai e a rialzarci dopo le cadute...ma soprattutto ho trovato degli Amici con cui vivere esperienze indimenticabili!!

Now I would like to send my heartfelt thanks to the opposite side of the Earth, Where I left really nice and lovely people. Special thanks to my friend Zhen: for your help in the lab, for the beautiful journeys around Vancouver, for your enthusiasm. Many thanks to the friends of the MENRVA group: Ahmed, Jill, Ausama, Nezam (and your sister), Xin, Jeff, and all the others. I miss our funny, long lunch breaks. I spent really beautiful moments with all of you. You have been so nice and kind with me...I had never received a surprise birthday cake, and the first time was thanks to you!! I will treasure all the moments spent with you in my heart!!
A really special thanks to all 'Police Judo' people that I met at SFU. Thanks to the instructors Tobi, Al, Brian, Chin-I, Joe, Mark, and all the guys I met there: I didn't expect so much affection. You accepted me, I found respect, friendship, the will to grow up together... I am really proud to have trained with you!! Thanks for your teachings!
Special thanks to Julia and Olya: you are beautiful women, but first of all, beautiful friends!!
I cannot forget my lovely roommate Anita: I still recall the first time I met you when I came to see the apartment. And I knew from the first moment that it would have been the right one!! Thanks for our nice conversations and for your kindess. I have been really lucky to have found you! And finally, Jimmy, my Italian-Canadian friend: it was amazing to meet someone whose origins were so close to mine. Thanks for your help and for the nice conversations in our dialect...they made me feel home!!

Un grazie a tutti coloro che hanno lasciato una pennellata di colore nella mia vita!

La mia vita é come un quadro pieno di colori vivaci!
Finché vivró il dipinto non sará completo
perché ciascuno di voi, Amici,
ciascuno di voi che ho amato,
contribuirá a dipingerlo con me.
Le vostre parole, le vostre idee
cambieranno le armonie di quei colori,
alcune faranno risaltare i chiari,
altre gli scuri.
Questo puzzle di tinte diventerá cosí piú bello!
Per questo oggi dico GRAZIE
a Voi Pittori, a Voi Artisti
che ogni giorno mi firmate.
Anon.

My life is like a painting full of bright colors!
As long as I live the painting won't be completed
as each of you, Friends,
each of you I've loved,
will contribute to paint it with me.
Your words, your ideas
will change the harmonies of those colors,
some of them will let the bright colors stand out,
some other the dark ones.
This puzzle of dyes will then become nicer!
So I say THANKS to you
to You Painters, to You Artists
that every day sign me.
Anon.